

HARVARD UNIVERSITY
Graduate School of Arts and Sciences



DISSERTATION ACCEPTANCE CERTIFICATE

The undersigned, appointed by the
School of Engineering and Applied Sciences
have examined a dissertation entitled

“Structure and Thermoelectric Properties of ZnO Based Materials”

presented by : Xin Liang

candidate for the degree of Doctor of Philosophy and here by
certify that it is worthy of acceptance.

Signature François Spaepen
Typed name: Prof. F. Spaepen

Signature S. Ramanathan
Typed name: Prof. S. Ramanathan

Signature Z. Suo
Typed name: Prof. Z. Suo

Signature D. Clarke
Typed name: Prof. D. Clarke

Date: August 29, 2013

Structure and Thermoelectric Properties of ZnO Based Materials

A dissertation presented

by

Xin Liang

to

The School of Engineering and Applied Sciences

in partial fulfillment of the requirements

for the degree of

Doctor of Philosophy

in the subject of

Applied Physics

Harvard University

Cambridge, Massachusetts

August 2013

UMI Number: 3600200

All rights reserved

INFORMATION TO ALL USERS

The quality of this reproduction is dependent upon the quality of the copy submitted.

In the unlikely event that the author did not send a complete manuscript and there are missing pages, these will be noted. Also, if material had to be removed, a note will indicate the deletion.



UMI 3600200

Published by ProQuest LLC (2013). Copyright in the Dissertation held by the Author.

Microform Edition © ProQuest LLC.

All rights reserved. This work is protected against unauthorized copying under Title 17, United States Code



ProQuest LLC.
789 East Eisenhower Parkway
P.O. Box 1346
Ann Arbor, MI 48106 - 1346

© 2013 – Xin Liang

All rights reserved.

Structure and Thermoelectric Properties of ZnO Based Materials

Abstract

The present dissertation investigates the relationship between the structure and thermoelectric properties of ZnO based materials, with a focus on trivalent element doping on engineering the microstructure and altering the electrical and thermal transport properties. Within the solubility range, the addition of trivalent elements, such as In^{3+} , Fe^{3+} and Ga^{3+} , is observed to increase the electrical conductivity of ZnO and decrease the thermal conductivity.

As the solubility is exceeded, the consequent structure and thermoelectric properties varies with dopant species. The ZnO-In₂O₃ binary system, which we have chosen as one of the model systems, is of particular interests as it contains a variety of phase equilibria and microstructures. The In₂O₃(ZnO)_k superlattice structures, which form as the indium solubility is reached, are observed to strongly scatter phonons while relatively permissive to electrons, resulting in a low thermal conductivity of about 2 W/mK and improved electrical conductivity. The thermal (Kapitza) resistance of In₂O₃(ZnO)_k superlattice interfaces is found to be $5.0 \pm 0.6 \times 10^{-10} \text{ m}^2\text{K/W}$ by fitting the modified Klemens-Callaway's thermal conductivity model to the experimental data. Across the phase diagram, the materials behave as n-type free-electron semiconductors at high temperatures. An effective medium approximation model is for the first time successfully tested on the thermoelectrics of two-phase regions.

Both Fe_2O_3 -ZnO and Ga_2O_3 -ZnO binary systems are also investigated. In the Fe doped ZnO system, a highly Fe concentrated ZnO solid solution phase as well as the significant grain refinement are observed after high temperature annealing. The $\text{Ga}_2\text{O}_3(\text{ZnO})_9$ homologous superlattices in Ga_2O_3 -ZnO system is also found to strongly scatter phonons and induces a drastic reduction in thermal conductivity.

Thermal conductivity, as one of the key factors in thermoelectrics, is highly sensitive to material defects. In this dissertation, I also present my work on recasting Callaway and von Baeyer's thermal conductivity model by introducing a minimum phonon relaxation time. The modeling calculation results, as compared with experimental data, illustrate the significance of phonon scattering by various types of defects, and thereby provide the basis for the nanostructure engineering as an efficient approach to enhancing thermoelectric properties.

Dedicated to my parents

Contents

Abstract.....	iii
Contents	vi
Acknowledgements	ix
List of Figures.....	xii
List of Tables	xix
Chapter 1 Introduction.....	1
1.1 Fundamentals and Applications of Thermoelectrics	1
1.2 Nanostructure Engineering for Thermoelectrics	12
1.3 ZnO Based Oxide Thermoelectrics	18
1.4 Objectives and Structure of the Thesis.....	26
Chapter 2 Experimental.....	30
2.1 Chemical Synthesis of Oxide Powders.....	30
2.2 Sintering and Post-annealing Treatment.....	31
2.3 Structural Characterization.....	33
2.4 Thermoelectric Properties Measurement and Analysis	34
Chapter 3 Recasting the Thermal Conductivity Physics Model with Numerical Evaluations	37
3.1 Introduction	38
3.2 Recasting Callaway and von Baeyer's Thermal Conductivity Model.....	47
3.3 Pure and Perfect Materials.....	49
3.4 High Temperature Thermal Conductivity Limit	52
3.5 Materials with Point Defects	56
3.6 Materials with Point Defects and Interfaces.....	68
3.7 Conclusions	72
Chapter 4 Thermal (Kapitza) Resistance of Interfaces in Compositional Dependent ZnO-In₂O₃ Superlattices	74
4.1 Introduction	74
4.2 Experiments.....	76
4.3 Results and Discussions	78

4.4 Conclusions	87
Chapter 5 Relation between Thermoelectric Properties and Phase Equilibria in the ZnO-In₂O₃ Binary System.....	88
5.1 Introduction	89
5.2 The ZnO-In ₂ O ₃ Binary System.....	90
5.3 Experimental Details	93
5.4 Observations and Results	95
5.4.1 ZnO Solid Solution Compositions.....	99
5.4.2 ZnO Solid Solution Containing Planar Crystallographic Interfaces.....	99
5.4.3 The Modular Compounds.....	101
5.4.4 Indium-rich Two-phase Regions	102
5.5 Discussions.....	104
5.5.1 ZnO Solid Solution Region – Point Defect Phonon Scattering.....	105
5.5.2 ZnO Solid Solution Containing Planar Interfaces	106
5.5.3 Modular Compounds	107
5.5.4 Electrical Transport Properties	108
5.5.5 Two-phase Thermoelectrics	114
5.5.6 Attaining Compositional and Structural Homogeneity	116
5.6 Conclusions	118
5.7 Appendix: Conversion between Molar and Volume Fractions	119
Chapter 6 Thermoelectric Properties of Fe doped ZnO with High Temperature Grain Refinement.....	121
6.1 Introduction	121
6.2 Experimental	123
6.3 Results	124
6.3.1 Structural Characterization.....	124
6.3.2 Thermal and Electrical Transport Properties.....	133
6.4 Discussions.....	135
6.4.1 Phase Equilibria and ZnO Solid Solution.....	135
6.4.2 Microstructural Evolution of 18 m/o FeO _{1.5} Sample	138
6.4.3 Thermal Conductivity.....	140
6.4.3 Thermoelectric Properties	141
6.5 Conclusions	146

Chapter 7 Thermoelectric Properties of Ga Doped ZnO with Natural Nanostructures	148
7.1 Introduction	149
7.2 Experiments.....	150
7.3 Results	151
7.4 Discussions.....	159
7.4.1 Solid Solution and Nanostructures of Ga doped ZnO	159
7.4.2 Thermal Transport Properties.....	161
7.4.3 Electrical Transport Properties	164
7.4.4 Thermoelectric properties.....	167
7.5 Conclusions	169
Chapter 8 Conclusions and Outlook	171
8.1 Phase Equilibria, Nanostructure and Thermoelectric Properties of Trivalent Elements Doped ZnO Oxides.....	171
8.2 Achieving Low Thermal Conductivity by Nanostructure Engineering.....	175
8.3 Comments on Electrical Conductivity and Seebeck Coefficient.....	176
8.5 Outlook for the Future Work.....	177
Appendix: Combined X-ray Diffraction and Raman Spectroscopy Characterization of $\text{In}_2\text{O}_3(\text{ZnO})_k$ Natural Superlattice Structures	179
References	186

Acknowledgements

As probably the most senior graduate student in my office (Gordon McKay 405) now, I still clearly remember when I just came here as a first year PhD student. In retrospect of the past five years at Harvard, I was enriched with vast amount of knowledge and skills; but the most important education I gained is the methodology and approach of deeply, thoroughly and systematically thinking, exploring and investigating an issue – the true wisdom, not just knowledge.

During the course of my PhD study and research, there are a number of people who have taught and helped me on my learning and making progress in my research. My first and foremost thanks go to my thesis advisor Professor David R. Clarke, who inspired and guided me through my PhD research. David is not only a truly admired material scientist and physicist, but a great mentor as well. I am deeply grateful for countless discussions he had with me with patience. He taught me how to apply what I have learned to explore and understand the unknown world; he educated me how to think deeply from the fundamentals of materials science and capture the physical picture behind the observations. By writing scientific papers with him, I learned from him on the way of structuralizing the content in an academic style and his rigorousness is highly respected. I also greatly appreciate David for his care and support on helping me to widen my horizon of learning, such as sending me to the ICMR (International Center for Materials Research) Summer School at UCSB, which is an unforgettable learning experience of two week's intensive lectures on the cutting-edge research of energy materials. He deserves much more thanks than what I have expressed here. It has been a great honor and fortune to be his student!

I am also thankful for all my thesis committee members: Professor Frans Spaepen, Professor Zhigang Suo and Professor Shriram Ramanathan, who are kindly willing to serve in PhD committee. Frans, as my academic advisor in my first year here, gave me many helpful guidance and advices; several courses he encouraged me to take turn out to be the most useful ones in initiating and carrying on my PhD research. It is also a great pleasure to be the teaching fellow with Shriram. He taught me the effective way of exciting students' interests in the subject and how to prepare session lectures, which is a great training to be a good instructor.

There are also a number of people who helped me on the technical development of my research skills and capabilities. I am truly thankful to Dr. Andi Limarga, a great colleague and friend, who generously transfer several central lab skills to me, including the CADPro system, thermal diffusivity measurement system, and confocal Raman and luminescence spectroscopy system with the spectral analysis program. I also appreciate Andi's kind advices on my future career development. Many thanks are given to Dr. Mor Baram, who is an expert on electron microscopy and atom probe tomography (APT), for not only her assistance with HRTEM and APT that helps me understand the complex oxide superlattice structures, but also her teaching me on how to properly and correctly conduct the high resolution TEM lattice imaging as well as perform the post-analysis. I like to thank Dr. David C. Bell and Adam Graham at Center for Nanoscale Systems (CNS) at Harvard for their teaching and assisting me on the use of both aberration corrected TEM and STEM. Sincere acknowledgements go to our group members, the past and present. I like to thank our faculty assistant Sarah Lefebvre for her help on academic affairs.

I would also like to express my gratitude to my Master's thesis advisor Professor J. David Embury, who continuously cared about my PhD progress and provides me with advices on my career development. I am also especially thankful to several senior graduate students here: Changhyun Ko, Han Li, Charbel Madi, Masaru Tsuchiya, Hongtao Wang and Xi Wang, etc., for their kind help and advices especially at the early stage of my PhD studies and research at Harvard.

In addition to the people mentioned, I also obtained numerous help from people inside and outside of the lab. In particular, I am grateful to William Bonificio, Jing Feng, Tao Feng, Chenhui Hu, Jiangshui Huang, Laetitia Laversenne, Yunzhuo Lu, Feilong Niu, Yang Shen, Samuel Shian, Taylor Sparks, Kejie Zhao, and Shijie Zhu for their kind help on various aspects of my study, research, career as well as living here.

My deep gratitude goes to my parents. They give me never-ending care and understanding, while leaving me with great freedom of achieving my dreams. Without their love, I could not have gone so far.

List of Figures

Figure 1.1: Illustration of Seebeck effect [2]. (a) Electrons at hot side possessing higher energy and migrate towards the cold side; (b) Equilibrium is reached as that internal electric field is built up due to the migration of electrons from hot to cold side, which depress the further diffusion.	3
Figure 1.2: Illustration of Seebeck and Peltier effects for thermoelectric applications in power generation and green cooling modes. Figure from Bell, Science 2008 [8].....	7
Figure 1.3: Calculation and plot of power generation efficiency with the figure of merit ZT. Calculations were made according to equation 1.11 with $Th = 1273$ K and $Tc = 500$ K. The energy conversion efficiency corresponding to a ZT value of 1.0 is indicated on the plot.	8
Figure 1.4: Illustration of the carrier concentration dependence of electrical conductivity σ , Seebeck coefficient α , thermal conductivity κ , power factor $\alpha^2\sigma$ and ZT. Figure taken from the work by Snyder and Toberer [6].	9
Figure 1.5: Benefit for the thermoelectric figure of merit by reducing lattice thermal conductivity. Figure from the work by Snyder and Toberer [6].....	12
Figure 1.6: Temperature dependence of thermal conductivity for STO polycrystalline ceramics for different grain sizes and a bulk single crystal [17].	15
Figure 1.7: TEM images of $ZnMnGaO_4$ [46]. (a) Coexisting nanoscale checkerboard and herringbone domains. The inset is the expanded view of the herringbone structure. (b) Expanded view of the checkerboard structure; the white arrows present the cubic axes. (c) Diffraction pattern of the herringbone domains (circle region), showing the diffuse and superlattice spots. The red arrow points to the first order superlattice peak.....	16
Figure 1.8: Thermal conductivity of $Bi_4Ti_3O_{12}$ for randomly oriented material and perpendicular to the layer structure[47]. Also shown is the in-plane thermal conductivity.	17
Figure 1.9: Atomic-resolution Z-contrast of image taken along the [1120] zone axis showing the inverse domain boundaries in $In_2O_3(ZnO)_2$ thin films [91].....	21
Figure 1.10: $ZnO-In_2O_3$ binary phase diagram, adapted from Moriga et al.'s work [92].	22
Figure 1.11: HRTEM image of $Ga_2O_3(ZnO)_9$ taken with the incident electron beam parallel to the [100] direction [42].	25

Figure 1.12: TEM image of $\text{Fe}_2\text{O}_3(\text{ZnO})_{15}$ showing the modulated defect structures [72].	26
Figure 2.1: Illustration of a typical CADPro sintering profile.....	32
Figure 2.2: Illustrative scheme (a) and picture (b) of configuration for electrical resistivity and Seebeck coefficient measurements. Illustrative drawing is taken from ULVAC Riko manual.....	35
Figure 3.1: Illustration of typical four stages of thermal conductivity with temperature [118]. Data points are experimental values of single crystal germanium from 3 K to its melting temperature from Glassbrenner and Slack's work [120].....	40
Figure 3.2: Modeling fit of measured thermal conductivity of pure ZnO synthesized by CADPro and further annealed at 1150 °C for 1 day. The thermal conductivity model developed in the present work (equation 3.38) demonstrates better description of experimental data than the Callaway and von Baeyer's model (equation 3.13).....	52
Figure 3.3: Thermal conductivity of ZnO solid solutions of indium with temperature for different indium concentrations (0.02 – 0.40). Calculations based on equation 3.63 or 3.64 are shown as red solid curves. Calculations based on Callaway and von Baeyer's model (equation 3.11) are shown as blue dashed curves. Measured values of $[\text{In}] = 0.02$, 0.05 and 0.08 doped ZnO annealed at 1150 °C for 1 day are also presented.	63
Figure 3.4: Numerical calculations of the thermal conductivity of 0.02 indium doped ZnO, with evaluations of three terms in equation 3.63 or 3.64. Thermal conductivity of fully dense materials obtained from measured results for two sets of annealing conditions (shown as scattered symbols) are also presented.	65
Figure 3.5: Significance of phonon-phonon scattering ($C_2 T^2 \tau_{\min}$) and point defect scattering ($4A$) over temperature and indium concentration in ZnO.	66
Figure 3.6: Calculations of thermal conductivity of indium doped ZnO based on equation 3.63 or 3.64 for the indium concentration range of 0.02 to 0.10 and in the temperature range of 300 K to 1073 K. Experimental results of two different annealing conditions (scattered symbols) are also shown for comparison. The Debye temperature of ZnO, $\theta = 370$ K, is shown as a dashed line on the figure.....	67
Figure 3.7: Calculated thermal conductivity of indium doped ZnO with different superlattice interface spacing ($L = 2.5 \sim 5000$ nm). Also shown is the measured thermal conductivity of indium doped ZnO with superlattice structure.	70

Figure 3.8: Calculated thermal conductivity of indium doped ZnO as a function of interface or boundary spacing at different temperatures, shown as connected open symbols. Also shown are experimental results for comparison..... 72

Figure 4.1: Thermal conductivity as a function of temperature for the indium concentrations indicated. The solid lines through the data correspond to the equation 4.3 in the text incorporating both point defect and interface scattering..... 79

Figure 4.2: Room temperature thermal conductivity as a function of indium concentration. The two curves correspond to the Klemens-Callaway model with (equation 4.3) and without phonon scattering (equation 4.1) from superlattice compositionally-dependent superlattice spacing. The data point represented by * is that of pure, polycrystalline ZnO processed in the same way as the compositions containing indium. 80

Figure 4.3: ZnO basal plane {0002} spacing measured by X-ray diffraction as a function of indium concentration. Below $x = 0.1$, the lattice parameter varies linearly with indium concentration, as consistent with Vegard's law, suggesting a random solid solution range. An abrupt change at $x = 0.1$ was observed, indicating the onset of InO_2 sheets formation. 81

Figure 4.4: TEM and atom probe tomography (APT) images of ZnO containing 10 at. % indium ($\text{Zn}_{0.9}\text{In}_{0.1}\text{O}$). The TEM image indicates the presence of an almost periodic superlattice. The APT image (middle) reveals the existence of indium ions in solid solution in the ZnO blocks as well as the indium ions forming irregular InO_2 sheets. The yellow and blue dots representing indium and zinc ions, respectively (For clarity, the oxygen ions are not shown. Also the magnification is not the same as the TEM image). The compositional profile (right), obtained from the APT image perpendicular to the superlattice, quantifies the solubility of the indium ions in the ZnO blocks and the zinc ions in the InO_2 sheets..... 82

Figure 5.1: The compositions of the materials studied superimposed on the $\text{ZnO}-\text{In}_2\text{O}_3$ binary phase diagram [92]. Two sets of materials were annealed at 1150 °C for one day (circles) and at 1250 °C for seven days (squares). Phase regions of interests include In_2O_3 -rich two-phase regions, two-phase regime of $\text{In}_2\text{O}_3(\text{ZnO})_5$ and $\text{In}_2\text{O}_3(\text{ZnO})_7$ modular compounds, and the ZnO solid solution phase with individual InO_2 interfaces. In this and subsequent diagrams, the superlattice repeat value, k , is indicated along the top axis for phases stable below 1300 °C. 92

Figure 5.2: Room temperature thermal conductivity as a function of indium concentration for samples heat treated at either 1150 °C for 1 day (blue squares) or 1250 °C 7 days (red filled circles). In this and succeeding figures the compositions of the modular superlattice compounds $k = 4, 5, 7, 9$ stable below 1300 °C are indicated by the vertical dashed lines. 96

Figure 5.3: Thermal conductivity at 800 °C, for two sets of thermal treatments, 1150 °C 1 day (blue squares) and 1250 °C 7 days (red circles), respectively.	97
Figure 5.4: Electrical conductivity of ZnO-In ₂ O ₃ oxide system as a function of indium concentration. Data presented are measurements made at 800 °C. The lines through the data points are guides to the eye.	98
Figure 5.5: Seebeck coefficient at 800°C as a function of indium concentration.....	98
Figure 5.6: TEM micrographs of 10 m/o InO _{1.5} , after the post-annealing for (a) 1150 °C for 1 day and (b) 1250 °C for 7 days (b). The latter has a “chessboard” type pattern consisting two sets of superlattice structures of InO ₂ sheets.	100
Figure 5.7: HRTEM image of 22 m/o InO _{1.5} after the post-annealing of 1150 °C for 1 day, showing the almost constant superlattice spacing; the inset is the selected area diffraction pattern taken with zone axis <1010> where superlattice reflection spots are clearly captured. Both HRTEM image and indexing of diffraction pattern confirm the observed structure as In ₂ O ₃ (ZnO) _k phase.....	102
Figure 5.8: SEM image and elemental mapping of the cross-section microstructure of the 50 m/o InO _{1.5} after 1250 °C 7 days annealing: (a) SEM micrograph revealing the grain microstructure, (b) The corresponding EDS mapping showing the distribution of zinc (red) and indium (green).	103
Figure 5.9: Jonker plot (Seebeck coefficient against natural logarithm of electrical conductivity) of ZnO-In ₂ O ₃ materials measured 800 °C. The best fit of the data with a slope of + 86.15 μV/K is shown as the dashed line.	110
Figure 5.10: Thermoelectric power factor at 800 °C after annealing at 1150 °C for 1 day (blue squares) and 1250 °C for 7 days (red circles). Also shown are literature measurements for the k = 5, 7, 9 compounds measured at 800 °C [31, 32]. The dashed lines correspond to the Bergman effective medium model for two phase thermoelectrics [175, 176].	112
Figure 5.11: Thermoelectric figure of merit at 800 °C. Also shown are values from the literature for the k = 5, 7, 9 compounds measured at 800 °C [31, 32]. The dashed lines correspond to the Bergman effective medium model for two phase composite thermoelectrics [175, 176].	113
Figure 6.1: ZnO – FeO _{1.5} binary phase diagram adapted from Degterov et al.’s work[73]. The compositions of the material with different annealing temperatures are indicated on the figure.	123

Figure 6.2: X-ray diffraction results of Fe doped ZnO with pure ZnO data also presented. Characteristic peaks of each phase are labeled.	126
Figure 6.3: Cross-section microstructure of 18 m/o $\text{FeO}_{1.5}$ doped ZnO annealed at 1150 °C for 1 day: (a) SEM micrograph; (b) EDS mapping with green and red colored data points representing Zn and Fe, respectively.	127
Figure 6.4: TEM observations of microstructure in 18 m/o $\text{FeO}_{1.5}$ doped ZnO annealed at 1150 °C for 1 day: (a) TEM micrograph of grains; (b) HRTEM lattice image of ZnO {002} basal planes.	128
Figure 6.5: SEM micrographs of cross-section microstructure of 18 m/o $\text{FeO}_{1.5}$ doped ZnO annealed at 1350 °C for 3 days: (a) Fine grain structures; (b) Platelet structures.	129
Figure 6.6: Cross-section microstructure of 18 m/o $\text{FeO}_{1.5}$ doped ZnO annealed at 1350 °C for 3 days. (a) SEM image; (b) EDS mapping with green and red colored data points representing Zn and Fe, respectively.	129
Figure 6.7: TEM micrographs of typical microstructures in 18 m/o $\text{FeO}_{1.5}$ doped ZnO annealed at 1350 °C for 3 days. (a) Bright field image of lamellar structure; (b) Bright field image of fine grain structure.	130
Figure 6.8: STEM image and elemental mapping of lamellar structure in 18 m/o $\text{FeO}_{1.5}$ doped ZnO annealed at 1350 °C for 3 days. (a) STEM dark filed image with an arrow showing the line scan direction; (b) STEM EDS map with Zn and Fe represented by green and red colored data points, respectively.	131
Figure 6.9: STEM EDS line scan across several platelets showing the Zn and Fe profile. Clearly, the thin lamellar structures are highly enriched in Fe, and the ratio of Fe to Zn is about two, in correspondence to ZnFe_2O_4 spinel phase.	132
Figure 6.10: Aberration corrected STEM image and elemental mapping of fine grain structures in 18 m/o $\text{FeO}_{1.5}$ doped ZnO annealed at 1350 °C for 3 days. (a) STEM dark field image; (b) STEM EDS map with Zn and Fe represented by green and red colored data points, respectively.	132
Figure 6.11: Thermal conductivity of Fe doped ZnO samples measured from room temperature up to 800 °C. The solid lines are for visual guide.	133
Figure 6.12: Electrical conductivity of Fe doped ZnO samples measured with temperature.	134

Figure 6.13: Seebeck coefficient of Fe doped ZnO samples measured with temperature.	135
Figure 6.14: ZnO basal plane (002) spacing or c_2 measured by X-ray diffraction plotted as a function of actual m/o $\text{FeO}_{1.5}$ in ZnO lattices. The Vegard's law was determined based on the undoped ZnO, 2 and 4 m/o $\text{FeO}_{1.5}$ doped ZnO. The actual Fe content of ZnO solid solution in 18 m/o $\text{FeO}_{1.5}$ sample annealed at 1150 °C and 1350 °C were then estimated.	138
Figure 6.15: Room temperature thermal conductivity of Fe doped ZnO with actual m/o $\text{FeO}_{1.5}$ in ZnO lattices. Each sample's composition and annealing temperature is indicated beside the symbol.	141
Figure 6.16: Jonker plot (Seebeck coefficient against natural logarithm of electrical conductivity) of Fe doped ZnO (including pure ZnO) measured at 800 °C. The best fit of the data with a slope of +86.15 $\mu\text{V/K}$ is shown as the dashed line.	144
Figure 6.17: Power factor of Fe doped ZnO with temperature.	145
Figure 6.18: Figure of merit for Fe doped ZnO samples with temperature.	146
Figure 7.1: X-ray diffraction of Ga doped ZnO after 1150 °C 1 day thermal treatment. The characteristic peaks of $\text{Ga}_2\text{O}_3(\text{ZnO})_9$, ZnGa_2O_4 spinel and ZnO phases are indicated at the bottom of the figure. A few ZnGa_2O_4 spinel X-ray diffraction peaks as distinguished from other phases are indicated.	152
Figure 7.2: Raman spectra of Ga doped ZnO annealed at 1150 °C for 1 day; pure ZnO data was also enclosed. The characteristic Raman modes for ZnO and ZnGa_2O_4 spinel phase (s) are indicated by olive and red colored labels, respectively. Raman modes of significant interests in the present work are also indicated by the dashed lines across all the spectra.	154
Figure 7.3: SEM image and corresponding EDS elemental mapping of cross-sectional microstructure in 18 m/o $\text{GaO}_{1.5}$ doped ZnO. (a) SEM image; (b) Zn map; (c) Ga map.	155
Figure 7.4: HRTEM image and the corresponding diffraction pattern (shown in the inset) of superlattice structures with nanotwins in 18 m/o $\text{GaO}_{1.5}$ doped ZnO. The HRTEM image reveals the nanotwin boundary with a crystallographic angel of about 60 °. The electron diffraction pattern was taken along the [1210] direction, which consists of two sets of lattices; in addition, diffuse superlattice reflection streaks were also observed..	156

Figure 7.5: Thermal conductivity measured with temperature for Ga doped ZnO samples with date of undoped ZnO well as 18 m/o FeO _{1.5} doped ZnO shown for comparisons, all represented by scattered symbols. All the samples presented on this figure were annealed at 1150 °C for 1 day. The blue and red solid curves represent the calculation results for the 2 m/o and 18 m/o GaO _{1.5} doped ZnO samples, respectively.	157
Figure 7.6: Electrical conductivity of Ga doped ZnO measured with temperature up to 800 °C. Pure ZnO data are also indicated. The lines through the data points are guides to the eye.	158
Figure 7.7: Seebeck coefficient of Ga doped ZnO measured with temperature up to 800 °C. The experiment results are shown as scattered symbols, and the modeling fits of the measured data are represented by dashed lines with the same colors of the measurement data symbols.	158
Figure 7.8: Power factor of Ga doped ZnO as a function of temperature; the undoped ZnO data are also enclosed. The lines through the data points are guides to the eye....	168
Figure 7.9: Figure of merit of Ga doped ZnO with temperature, with the undoped ZnO data also enclosed. The lines through the data points are guides to the eye.....	169
Figure A.1: X-ray diffraction results of ZnO-In ₂ O ₃ binary system annealed at 1150 °C for 1 day. The 2θ range of 10 – 30 degree where most of In ₂ O ₃ (ZnO) _k superlattice reflections lie are presented. The InO _{1.5} concentration is indicated to right of the figure. The characteristic diffraction peaks of different In ₂ O ₃ (ZnO) _k superlattices are indicated by the dashed lines of different colors with k values shown on the top of the figure....	180
Figure A.2: X-ray diffraction results of ZnO-In ₂ O ₃ binary system annealed at 1250 °C for 7 days.	181
Figure A.3: Raman spectra of ZnO-In ₂ O ₃ binary system annealed at 1150 °C for 1 day; InO _{1.5} concentration is indicated on the right of the figure. The characteristic Raman modes of ZnO and In ₂ O ₃ are labeled by the dashed lines of green and red colors, with vibration modes indicated on the top of the figure.	183
Figure A.4: Raman spectra of ZnO-In ₂ O ₃ binary system annealed at 1250 °C for 7 days.	184

List of Tables

Table 1.1: List of structure information on $\text{In}_2\text{O}_3(\text{ZnO})_k$ modular (superlattice) phases, including symmetry, lattice parameter, molecular weight (M), unit cell volume (Ω), mass density (ρ) and band gap (Eg). The two end materials, ZnO and In_2O_3 are also enclosed.	24
Table 3.1: Summaries of high temperature thermal conductivity limit κ_{limit} calculated from different models.	56
Table 3.2: Calculated point defect scattering strength factor (SI units) for different indium concentrations based on equation 3.70 and 3.71	61
Table 4.1: Examples of interfacial thermal resistances	86
Table 5.1: Calculated room temperature thermal conductivity of $\text{In}_2\text{O}_3(\text{ZnO})_k$ modular compounds based on InO/ZnO interface scattering (according to equations 5.10 and 5.11). Also shown are the room temperature measurements in the present work (annealed at 1150 °C) and literature reported values.	108
Table 5.2: Electrical conductivity and Seebeck coefficient of $\text{In}_2\text{O}_3(\text{ZnO})_k$ modular compounds measured at 800 °C. Also shown are literature reported values.	111
Table 8.1: Summaries of band gap for several zinc spinel phases	173

Chapter 1 Introduction

In this chapter, the background and applications of thermoelectrics, normally known as the Seebeck and Peltier effect, are first provided. I will then describe the fundamentals of thermoelectrics which involves a few central physical parameters characterizing the electrical and thermal transport properties. The conflict among electrical and thermal conductivity as well as Seebeck coefficient in achieving large thermoelectric figure of merit is also discussed. Nanostructure engineering, as an effective approach to lower the lattice thermal conductivity and thereby improve the overall thermoelectric properties, is introduced and discussed with selected examples. ZnO based thermoelectric materials with the benefits of inexpensiveness and earth abundance, chemical and high temperature stability as well as non-toxicity are highlighted. A few examples of ZnO related oxide systems are briefly reviewed and proposed as useful model system to investigate and understand the correlations between chemical composition, phase equilibria, structure and thermoelectric properties. At the end of the chapter, the structure and organization of the present dissertation is provided.

1.1 Fundamentals and Applications of Thermoelectrics

It has been found that about 60% of energy production in the United States is wasted in the form of heat [1]; accordingly, power generation to convert the waste heat into electrical energy, which is one of the major thermoelectric applications, becomes of significant importance. In addition, thermoelectric energy conversion also provides other benefits such as reducing the reliance on fossil fuels to reduce the greenhouse gas

emissions. Other benefits of thermoelectric energy conversion include quietness and compactness as compared to the traditional systems such as heat engines [2].

A well-established application is the radioactive thermoelectric generators for deep-space probes (NASA's Voyager and Cassini missions) [3]. Nowadays, thermoelectric energy conversion devices can be installed on vehicles to recover the automobile exhaust heat into useful electrical energy and thereby increases the fuel efficiency [2]. On the other hand, solid state refrigerating devices, which utilizes the thermoelectric or Peltier cooling function, has been widely applied in small-scale cooling in computers, infrared detectors and optoelectronic devices [2]; Thermoelectric car seat climate control system has also been commercialized [1]. Recent applications including the TE-solar hybrid systems for energy conversion and power generation [4].

One of the most fundamental phenomena of thermoelectrics is the Seebeck effect, in which a voltage difference ΔV is developed and proportional to the temperature difference ΔT between two ends of a material. The voltage developed to the temperature difference ($\Delta V / \Delta T$) is defined as the Seebeck coefficient S^1 , also known as thermopower especially in physics community. In the current dissertation, I will stick to the term “Seebeck coefficient” to avoid getting confusing with another term “thermoelectric power factor” which will be introduced in a later content. The physical picture is that the charge carriers at hot side are more energetic and therefore diffuse to the cold side and then accumulate there, until an internal electrical field is built up that depress the further migration, as described in Figure 1.1. In the case of electrons as the dominant charge carriers, the internal built electrical field is opposite to the temperature gradient, and

¹ Also commonly denoted as α in literatures

therefore the Seebeck coefficient has a negative sign for electrons. For the case of holes, a positive sign is assigned for Seebeck coefficient. The opposite phenomenon is the Peltier effect in which heat sink is developed when an electrical current passes through the material and carrying the heat from one end to the other.

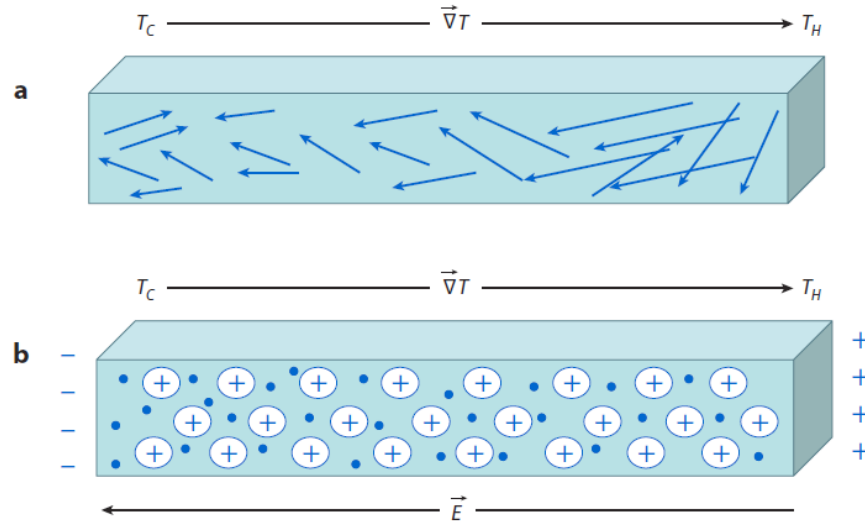


Figure 1.1: Illustration of Seebeck effect [2]. (a) Electrons at hot side possessing higher energy and migrate towards the cold side; (b) Equilibrium is reached as that internal electric field is built up due to the migration of electrons from hot to cold side, which depress the further diffusion.

The physical meaning of the Seebeck coefficient is the heat carried by carriers per charge per temperature, or simply the entropy per carrier. In the following content, I will show my derivation of both the units and the physical parameters involved in Seebeck coefficient, from which several Seebeck coefficient expressions in the literature can be clarified and unified.

The Seebeck coefficient is known to have the unit of V/K, from which we can start,

$$S \sim \frac{V}{K} \sim \frac{eV}{eK} \sim \frac{\text{Specific heat (eV/K)}}{\text{Carrier charge (e)}} \quad (1.1)$$

which is consistent with its physics expression,

$$S \approx \frac{c_{el}}{e} = \frac{1}{e} \frac{C_{el}}{N} \quad (1.2)$$

where e is the electronic charge, c_{el} and C_{el} are the electronic heat capacity for one electron and the whole system, respectively, and N is the number of electrons in the system. Using the free electron model for metals and degenerated semiconductors, the electronic heat capacity is given by [5]

$$C_{el} = \frac{\partial U_{el}}{\partial T} \quad (1.3)$$

where U_{el} is the total electronic thermal kinetic energy. In the case of a classical electron gas, each electron has the energy of $\frac{3}{2}k_B T$; one can immediately see the Seebeck coefficient of a classical electron gas is approximately as $\frac{k_B}{e} \approx 87 \mu\text{V/K}$.

For metals or degenerated semiconductors, since only those electrons with an energy range $k_B T$ of the Fermi level are thermally excited, the number of electrons that can be thermally excited at temperature T and participate in the conduction process is then approximately $N \left(\frac{T}{T_F} \right)$ where T_F is the Fermi temperature [5]. Accordingly, the total electronic thermal kinetic energy can be written as,

$$U_{el} \approx \left(N \frac{T}{T_F} \right) k_B T \quad (1.4)$$

Substituting the above equation back to equation 1.3, one obtains,

$$C_{el} \approx Nk_B \frac{T}{T_F} \quad (1.5)$$

Noting that the Fermi temperature is related to Fermi energy by

$$E_F = k_B T_F \quad (1.6)$$

Combining the above two expressions and substituting back to equation 1.2, we obtain

$$S \approx \frac{1}{e} \frac{k_B^2 T}{E_F} = \frac{k_B}{e} \left(\frac{k_B T}{E_F} \right) \quad (1.7)$$

which is commonly seen in literatures for the Seebeck coefficient expression for metals[2]. Equation 1.7 suggests that only the $\left(\frac{k_B T}{E_F} \right)$ fraction of electrons participate in the conduction process and contribute to the Seebeck coefficient.

Also noting that the Fermi energy is related to the effective mass m^* and carrier concentration n as,

$$E_F = \frac{\hbar^2}{2m^*} (3\pi^2 n)^{\frac{2}{3}} \quad (1.8)$$

Another expression for Seebeck coefficient is then obtained,

$$S \approx \frac{2k_B^2}{e\hbar} m^* T (3\pi^2 n)^{-\frac{2}{3}} \quad (1.9)$$

which is commonly used for degenerate semiconductors [6]. Equation 1.9 explicitly suggests that large Seebeck coefficient requires large effective mass and small carrier concentration. It also has temperature T clearly shown in the expression, although the dependence may not be as that simple since other parameters such as carrier concentration n are also dependent on temperature.

In the case of non-degenerate semiconductors, charged carriers need to be excited across the bandgap E_g to participate the conduction. Accordingly, the Seebeck coefficient for semiconducting material can be approximately expressed as [2],

$$S \approx \left(\frac{k_B}{e}\right) \frac{E_g}{k_B T} = \frac{E_g}{eT} \quad (1.10)$$

where $\left(\frac{k_B}{e}\right)$ is the Seebeck coefficient for a classical electron gas.

In practice, thermoelectric applications are achieved by making a device consisting of many modules and a single module basically is composed of a pair of n-type and p-type thermoelectric material usually called TE couple, as illustrated in Figure 1.2. In the cooling mode, electrical field forces a current flowing through the TE couples. Since holes drift along the current flow direction whereas electrons drift in the opposite direction, both holes and electrons are moving away from top side towards the base side, as shown in Figure 1.2(a). Recalling these charge carriers also carry heat, the top side which is losing electrons and holes is under cooling, where the heat sink is developed. In the case of power generation mode as illustrated in Figure 1.2(b), electrons and holes gain more energy at heat input side and therefore diffuse to the base side. Accordingly, a flow of current is going through the TE couple and there will be power output at the base side. In real applications, a TE module or device consists of many arrays of such TE couples, and there are a few applicable geometric configurations for the purpose of increasing the overall efficiency of the whole TE system. However, this is not the focus of the present dissertation work but can be found in a couple of related literatures [7, 8].

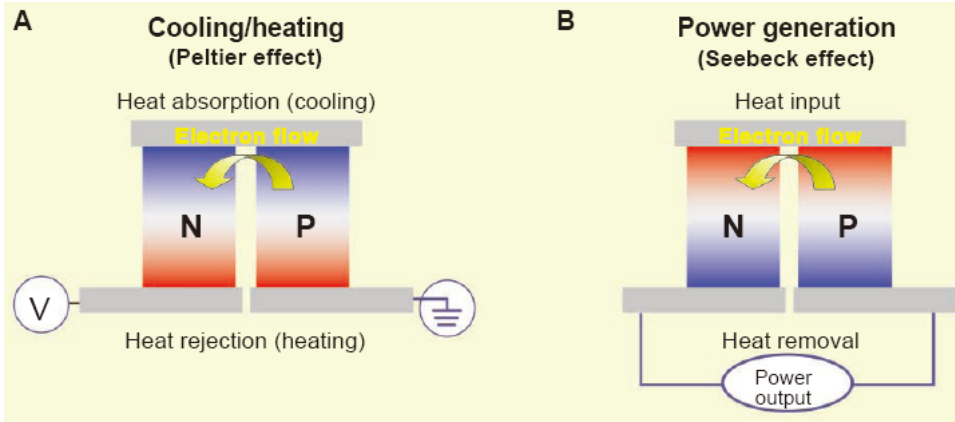


Figure 1.2: Illustration of Seebeck and Peltier effects for thermoelectric applications in power generation and green cooling modes. Figure from Bell, Science 2008 [8].

In the case of power generation, the idealized maximum energy conversion efficiency is given by [9],

$$\eta = \frac{\Delta T}{T_h} \frac{\sqrt{1 + ZT_h} - 1}{\sqrt{1 + ZT_h} + T_c/T_h} \quad (1.11)$$

where ΔT is the temperature difference and ZT is the dimensionless figure of merit of the material which characterizes the intrinsic thermoelectric properties of a material and will be discussed in details in the later content. T_h is the temperature at which ZT is maximized and therefore mostly corresponds to the maximum operating temperature of the TE devices. Accordingly, $\Delta T/T_h$ basically corresponds to the Carnot efficiency which is the maximum efficiency of a heat engine operating between two temperatures. With the input values of $T_h = 1273$ K and $T_c = 500$ K, equation 1.11 was calculated and plotted as a function of ZT as shown in Figure 1.3. Materials with ZT of ~ 1.0 are thought of possessing excellent thermoelectric properties, and the corresponding energy conversion efficiency is about 12.3 %. One important piece of information from equation 1.11 and Figure 1.3 is that energy conversion efficiency monotonically increases with ZT ,

which is the focus of thermoelectric research from the materials science perspective. Clearly, maximizing of ZT values is required for the best energy conversion performance.

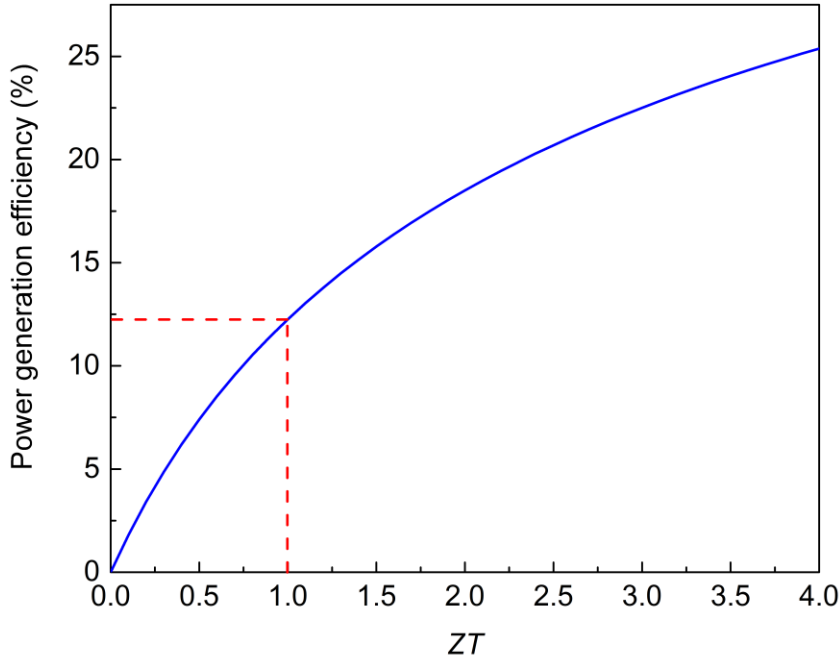


Figure 1.3: Calculation and plot of power generation efficiency with the figure of merit ZT . Calculations were made according to equation 1.11 with $T_h = 1273$ K and $T_c = 500$ K. The energy conversion efficiency corresponding to a ZT value of 1.0 is indicated on the plot.

The figure of merit ZT is a central parameter characterizing the thermoelectric properties of a material and is determined by the electrical and thermal transport properties of the material. It is given by

$$ZT = \frac{S^2 \sigma}{\kappa} T \quad (1.12)$$

where S is the Seebeck coefficient introduced in the previous content, σ is the electrical conductivity, κ is the thermal conductivity and T is the absolute temperature. σ depends on both carrier concentration n and mobility μ as,

$$\sigma = ne\mu \quad (1.13)$$

where e is the electronic charge. The product $S^2\sigma$ is usually named as “thermoelectric power factor” or simply “power factor” which characterizes the electrical transport properties and is widely used in literatures. As seen from equation 1.12, large power factor $S^2\sigma$ is desired for high figure of merit. However, electrical conductivity σ increases while Seebeck coefficient S decreases with carrier concentration, as seen in equation 1.13 and 1.9. Accordingly, there exists an optimized value of carrier concentration at which power factor reaches the maximum as illustrated in Figure 1.4.

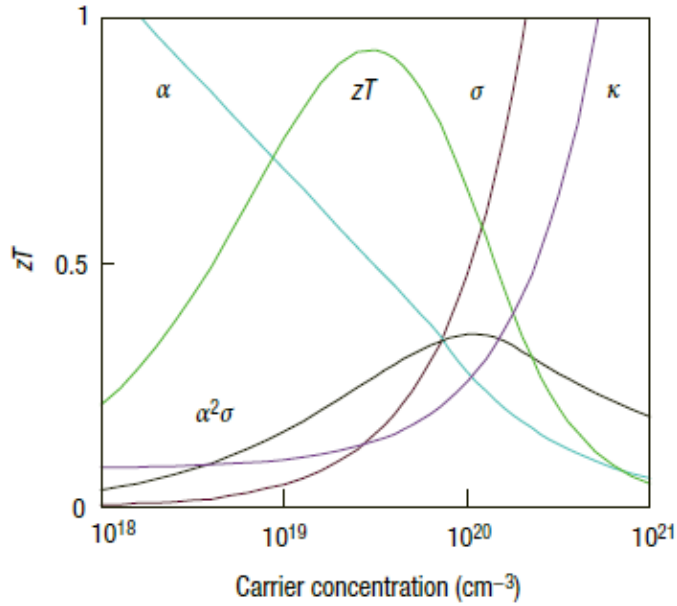


Figure 1.4: Illustration of the carrier concentration dependence of electrical conductivity σ , Seebeck coefficient α , thermal conductivity κ , power factor $\alpha^2\sigma$ and ZT . Figure taken from the work by Snyder and Toberer [6].

The trade-off between electrical conductivity and Seebeck coefficient can also be understood from the electronic density of states [1]. Large Seebeck coefficient requires the high asymmetry of density of states (or differential electrical conductivity) with respect to the Fermi level; however, such asymmetry is reduced when doping in the

material increases, which moves the Fermi level deeper into the band of 3D crystal. In addition, to make the balance between electrical conductivity and Seebeck coefficient in search of good thermoelectric materials, the semiconductor must have one dominant type of charge carriers, being either electrons or holes. Otherwise, if both similar density of electrons (above the Fermi level) and holes (below the Fermi level) contribute to electrical conduction, the asymmetry of differential conductivity is reduced and so is the Seebeck coefficient.

The thermal conductivity κ is desired to be minimized for high thermoelectric performance. Fundamentally, both phonons and electronic charge carriers (electrons or holes) are responsible for thermal transport, and the corresponding contributions are lattice or phonon thermal conductivity κ_l and electronic thermal conductivity κ_e , respectively, as written in the expression below,

$$\kappa = \kappa_l + \kappa_e \quad (1.14)$$

where the electronic contribution is related to electrical conductivity via Lorentz factor L ,

$$\kappa_e = L\sigma T = ne\mu LT \quad (1.15)$$

where L is typically taken as $2.48 \times 10^{-8} \text{ J}^2\text{K}^{-2}\text{C}^{-2}$ for metals and $2.0 \times 10^{-8} \text{ J}^2\text{K}^{-2}\text{C}^{-2}$ for degenerated semiconductors [2]. With equation 1.14 and 1.15, one immediately sees that thermal conductivity κ increases with carrier concentration. According to equation 1.12, the possible highest thermoelectric figure of merit ZT is obtained when the ratio of power factor $S^2\sigma$ over thermal conductivity κ is maximized with respect to the carrier concentration n , which results in a peak value of ZT as shown in Figure 1.4. The carrier

concentration corresponding to the maximum of ZT is generally in the range of 10^{19} to 10^{21} carriers per cm^3 [6].

Since high electrical conductivity requires large carrier concentration whereas low thermal conductivity demands small values for large ZT , one of the most efficient approaches is to bring down the lattice or phonon thermal conductivity. This has been one of the major focuses on improving the overall thermoelectric properties over the past decade [10-17]. As illustrated in Figure 1.5, reducing lattice thermal conductivity κ_l has a two-folds benefit for the thermoelectric figure of merit. On one hand, the ZT optimized with a κ_l of 0.8 W/mK, shown as the point (1) on the figure, increases up to point (2) as κ_l decreases down to 0.2 W/mK. Furthermore, lowering the lattice thermal conductivity re-optimize the carrier concentration n (reduced), leading to a smaller electronic thermal conductivity κ_e and a larger Seebeck coefficient S . The figure of merit ZT is also re-optimized to a larger value shown at point (3).

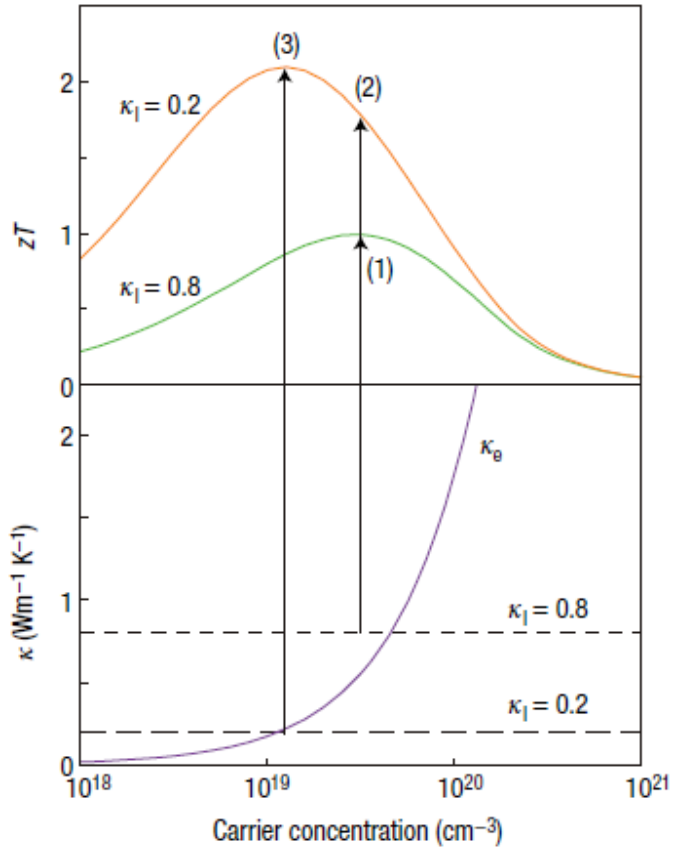


Figure 1.5: Benefit for the thermoelectric figure of merit by reducing lattice thermal conductivity.
Figure from the work by Snyder and Toberer [6].

1.2 Nanostructure Engineering for Thermoelectrics

Lattice thermal conductivity is very sensitive to microstructure as lattice vibrations can be affected by structural defects such as point defects, dislocations, interfaces and precipitates and so on [18], which offers opportunities of reducing thermal conductivity and therefore enhance thermoelectric performance by structural engineering. Accordingly, most of the recent research focus and success in obtaining high thermoelectric performance is achieved by the reduction of lattice thermal conductivity while remaining reasonably good electrical conductivity [1]. A traditional but viable

approach to reduce the lattice thermal conductivity of polycrystalline bulk materials is through alloying which introduces the atomic-scale defects to scatter phonons [19]. However, point defects due to alloying normally scatter short-wavelength phonons, leaving the transport of medium- to long-wavelength phonons mostly unaffected, which implies room for further reducing thermal transport. Nanostructure engineering, which mostly exists in the form of planar defects such as nano-grain boundaires, nano-phase boundaries and superlattice structure and so on, could effectively scatter these medium- and long-wavelength phonons [20].

In the past decade, the nanostructure approach has been found to be helpful in terms of lowering thermal conductivity by introducing the interfacial phonon scattering without significantly compromising the power factor to yield an increased figure of merit [10, 11, 16-18, 21-23]. However, effectiveness of reducing thermal conductivity of bulk materials by nanostructure engineering has only been practiced in recent a few years [10, 16, 21, 22, 24]. One of the major approaches is to decrease the grain size down to nanoscale, usually in the order of several ten nanometers. One such example is the synthesis of bulk n-type strontium titanate (SrTiO_3 or STO) oxides with nanometer-size grains [25, 26]. Figure 1.6 presents the effect of grain size on the thermal conductivity of STO polycrystalline ceramics with temperature. A significant drop in thermal conductivity was observed when the grain size decreases from the micrometer to nanometer length scale. However, there are a few major limitations for the grain boundary scattering approach. First, the thermal conductivity reduction with decreasing grain size is mostly apparent at room temperature and becomes much less significant approaching high temperatures, as is also found in yttria-stabilized zirconia system [27].

In addition, even with the grain size as small as 50 nm the thermal conductivity does not yet go down to the alloy limit since this length scale is still far larger than the phonon mean free path [17]. More importantly, grain growth is generally inevitable for high temperature prolonged operations during which the benefit of thermal conductivity reduction by grain boundary scattering of phonons is compromised or even lost with time. It is therefore of significance to seek coarsening-resistant nanostructures with length scale close to the unit cell scale.

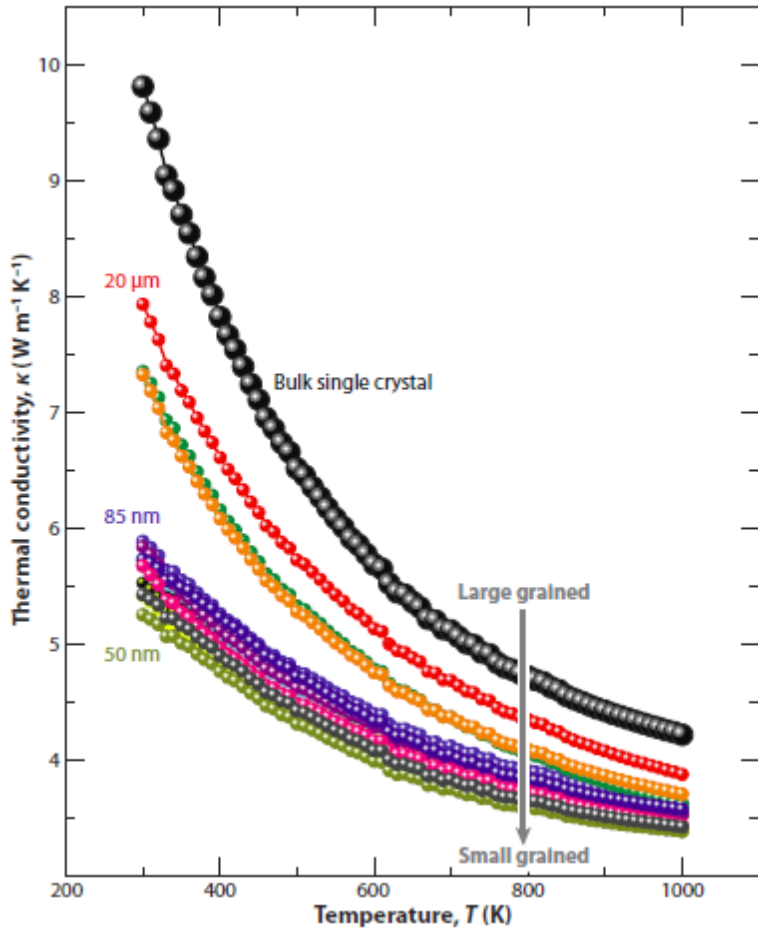


Figure 1.6: Temperature dependence of thermal conductivity for STO polycrystalline ceramics for different grain sizes and a bulk single crystal [17].

Recent special interests of thermoelectrics also lie in the material systems that could form self-assembly nanostructures, for instance, by spinodal decomposition [28-30] or natural superlattice structures in some oxide systems [31-45]. One example is the $\text{Zn}(\text{Mn},\text{Ga})\text{O}_4$ system in which a spontaneous phase separation can occur under certain thermal treatment, and the consequent two phases are the Mn-rich tetragonal phase ($\text{ZnMn}_{1.7}\text{Ga}_{0.3}\text{O}_4$) and the Ga-rich cubic phase ($\text{ZnMn}_{0.5}\text{Ga}_{1.5}\text{O}_4$) that are alternatively stacked, forming the nanoscale “checkerboard” and “herringbone” structures if observed with cross-sectional and side views, respectively[46]. The TEM micrographs of the domain structures in $\text{Zn}(\text{Mn},\text{Ga})\text{O}_4$ system with nanometer building blocks are shown in

Figure 1.7. Such self-assembly nanostructure is found to significantly reduce the thermal conductivity even much below the theoretical minimum limit of the two-phase mixture [24], suggesting the effectiveness of complex nanostructures on scattering phonons.

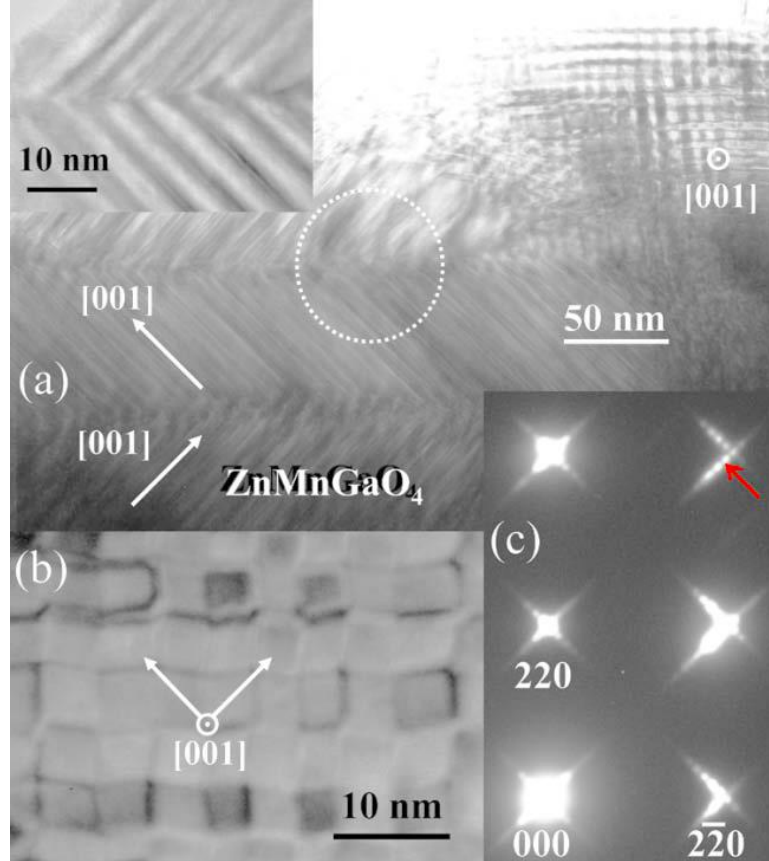


Figure 1.7: TEM images of ZnMnGaO_4 [46]. (a) Coexisting nanoscale checkerboard and herringbone domains. The inset is the expanded view of the herringbone structure. (b) Expanded view of the checkerboard structure; the white arrows present the cubic axes. (c) Diffraction pattern of the herringbone domains (circle region), showing the diffuse and superlattice spots. The red arrow points to the first order superlattice peak.

In addition to phase separation, self-formed nanostructures can also be produced in a natural superlattice system. One of such examples is the Aurivillus phase of bismuth titanate $\text{Bi}_4\text{Ti}_3\text{O}_{12}$, which consists of alternating layers of pseudoperovskite $(\text{Bi}_2\text{Ti}_3\text{O}_2)^{2-}$ and fluorite $(\text{Bi}_2\text{O}_2)^{2+}$ blocks. Strong anisotropy of thermal conduction was found that the *c*-axis thermal conductivity is about a half of the *a-b* plane conductivity [47], as shown in

Figure 1.8. This suggests a strong interface scattering of phonons due to the mass difference between the pseudoperovskite and fluorite blocks in the unit cell, which brings down the overall or effective thermal conductivity of the polycrystalline materials as well.

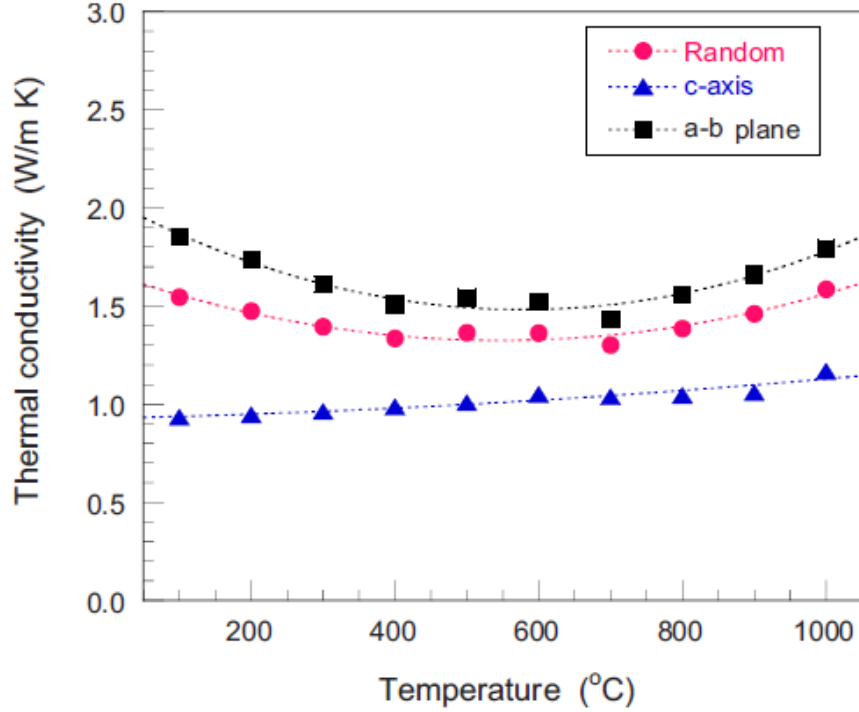


Figure 1.8: Thermal conductivity of $\text{Bi}_4\text{Ti}_3\text{O}_{12}$ for randomly oriented material and perpendicular to the layer structure[47]. Also shown is the in-plane thermal conductivity.

One major perspective of nanostructure engineering to enhance thermoelectric properties is to design and create the (defect) structure with appropriate length scale, which is smaller than the mean free path of phonons but larger than that of electrons or holes [48]; the consequent effect is to reduce the thermal conductivity without the significant degradation of the electrical transport properties. Superlattice structures, normally created by artificial approaches such as MBE deposition (Molecular Beam Epitaxy), has been a renowned success in thermoelectrics due to the achievement of ultralow thermal conductivity [49-54]; one such example is the $\text{W}/\text{Al}_2\text{O}_3$ nanolatminates

demonstrating the thermal conductivity as low as 0.6 W/mK [52]. The effect of superlattice structures on reducing thermal conductivity has been attributed to various mechanisms, including the modification of phonon spectrum [55], phonon localization, phonon scatterings at interfaces due to acoustic mismatch or defects formed arising from lattice mismatch [56] etc. It is also quite intriguing to search for natural superlattice material systems in which superlattice structure or compounds are thermodynamically stable phases; under certain heat treatment, the material can therefore self-develops into coarsening-resistant nanostructures.

1.3 ZnO Based Oxide Thermoelectrics

Recent research interests in thermoelectrics vary from semiconductor or semimetals to ceramic oxides in classes of materials, and from nanowires to thin films to polycrystalline bulk materials in dimensions [2]. The most utilized state-of-the-art thermoelectric materials are Bi_2Te_3 , PbTe and related materials due to their superior figure of merit [21, 57]. However, the constituent elements are mostly toxic, naturally rare and therefore expensive, and can be oxidized or volatized or even melt during high temperature operations in air [17, 58]. Accordingly, seeking environmental friendly, earth abundant, cheap, chemical and high temperature stable thermoelectric materials become necessary, especially for large scale production and high temperature applications. Oxide materials generally meet these needs and become the highly promising candidate thermoelectric materials.

In addition, although low dimensional materials such as thin film superlattice materials [59] or even nanowires [60, 61] demonstrate extraordinary thermoelectric properties, they are only appropriate in small load applications such as cooling or power generation in electronic and optoelectronic devices. Large scale power generation or refrigeration in civil and industrial applications still requires the development of high performance bulk materials [2]. Homm and Klar [9] compared several classes of thermoelectric materials in terms of efficiency and material abundance, including the base materials of Bi_2Te_3 , PbTe , SiGe , FeSi_2 and ZnO etc., and concluded that ZnO related oxide materials are ideal for stationary mass production and applications due to their large earth abundance (thereby low cost) and environmental friendliness. It should also be noted that in a number of practical cases, energy cost is more important than energy conversion efficiency [1].

In this dissertation, ZnO based materials are chosen as the model system to investigate and understand the correlation among chemical compositions, processing (mainly thermal treatment conditions), phase equilibria, microstructure including defect structure, and electrical and thermal transport properties. The beauty of the ZnO based oxide system is that there are a variety of doping elements available to tune its electrical transport properties and engineering its phase equilibrium and microstructure by which the thermal transport properties can be altered. There has been numerous studies on the doping effect on the structure and/or properties of ZnO with the following elements: Al [62-67], Bi [68], Co [69], In [31, 32, 34-36, 40, 41, 70, 71], Fe [72-79], Mn [80], Ni[81, 82], Sb [83], Sn [84] and even dual doping [85-87]. These research works provide valuable and rich information, but lack a systematic and comprehensive investigation on

the connection between chemical compositions, phase equilibria, structure and thermoelectric properties.

ZnO-In₂O₃ is one of the most interesting binary oxide systems in that compositionally dependent natural superlattice nanostructures can be formed under certain thermal treatment. This was first discovered and observed with electron microscopy by Cannard and Tilley [88]. A later study with combined experiments and atomic simulation work by McCoy *et al.* [89, 90] suggests that the type of defect structure is dependent on the indium concentration. A low concentration, indium ions are incorporated on zinc sites with creation of zinc vacancies to maintain the charge balance, forming the defect cluster consisting of two indium substitutional ions surround a zinc vacancy. With increasing concentration, layered or superlattice structure develops with In-O sheets stacked along the *c*-axis of the hexagonal wurtzite structure separating ZnO slabs. Such layered oxide structures can also be considered as planar defects associated with the inverse domain boundaries (IDBs), as Yan *et al.* [91] characterized by high resolution transmission electron microscopy (HRTEM) as shown in Figure 1.9.

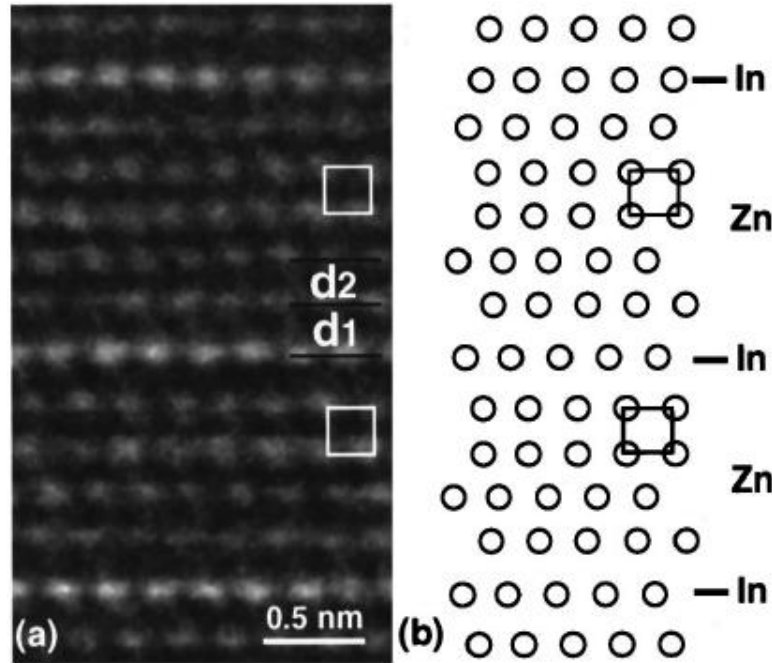


Figure 1.9: Atomic-resolution Z-contrast of image taken along the $[11\bar{2}0]$ zone axis showing the inverse domain boundaries in $\text{In}_2\text{O}_3(\text{ZnO})_2$ thin films [91].

Almost at the same time, Moriga *et al.* [92] constructed the equilibrium phase relationships in the ZnO - In_2O_3 binary system based on solids state reaction techniques and X-ray diffraction phase analysis. They discovered and identified a series of $\text{In}_2\text{O}_3(\text{ZnO})_k$ homologous compounds on the phase diagram with indium concentration, as shown in Figure 1.10. For a specific $\text{In}_2\text{O}_3(\text{ZnO})_k$ compound or phase, the chemical formula suggests a structure in which $(k + 1)$ number of ZnO layers are sandwiched between In-O sheets along the c -axis of the hexagonal unit cell. The phase diagram shown in Figure 1.10 suggests the following significant interesting features of the ZnO - In_2O_3 binary system. First, the natural superlattice structure, which is compositionally dependent, can be created under certain heat treatment. In addition, by tuning the chemical composition and controlling the annealing temperature, a variety of phase equilibria and microstructure can be produced, including simple solid solution, solution

phase with planar defects associated with IDBs, modular or superlattice compounds and two-phase composite. Accordingly, the ZnO-In₂O₃ binary system enables us to study and understand the effect of phase equilibria and microstructure on thermoelectric properties. Some of our special interests include the superlattice effect on thermal transport properties and the test of mean-field mathematic modeling on describing the two-phase composite thermoelectrics.

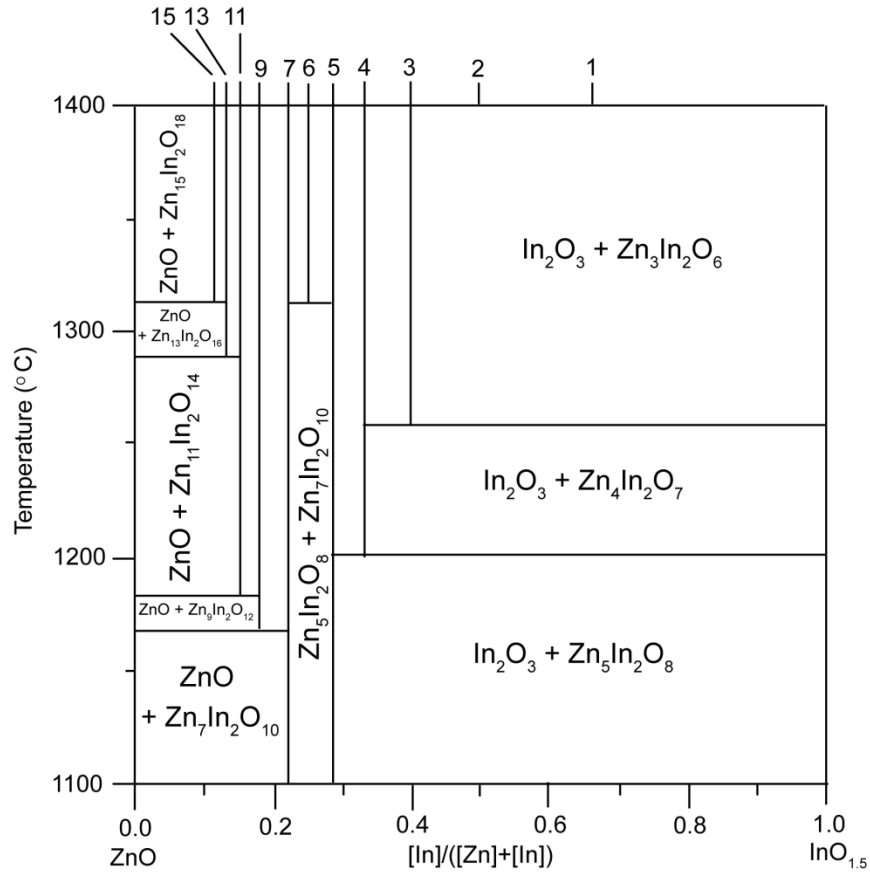


Figure 1.10: ZnO-In₂O₃ binary phase diagram, adapted from Moriga et al.'s work [92].

Table 1.1 lists the crystal structure information of $\text{In}_2\text{O}_3(\text{ZnO})_k$ modular (superlattice) phases with two end oxides, ZnO and In₂O₃. The crystal structure

information (symmetry and lattice parameters etc.) are obtained from literatures [31, 92], based on which the mass density can be calculated. References for band gap values are indicated in the table for each phase. ZnO and In₂O₃ have the hexagonal (*P*63_{*m*}*c*) and bixbyite cubic (*Ia*) crystal structures, respectively. The crystal structure of In₂O₃(ZnO)_{*k*} modular (superlattice) phase depends on the *k* value: rhombohedral (*R*3*m*) and hexagonal (*P*63/*mmc*) for odd and even values of *k*, respectively. In addition, the number of chemical formula per unit cell, represented by the *z* value in Table 1.1, is taken as 3 and 2 for odd and even values of *k*, respectively.

Table 1.1: List of structure information on $\text{In}_2\text{O}_3(\text{ZnO})_k$ modular (superlattice) phases, including symmetry, lattice parameter, molecular weight (M), unit cell volume (Ω), mass density (ρ) and band gap (E_g). The two end materials, ZnO and In_2O_3 are also enclosed.

k	Symmetry	Lattice parameter, Å			M, g/mol	Ω , Å ³	ρ , g/cm ³	E_g , eV
		a	c	c/z				
0 (In_2O_3)	Ia-3	8.762	8.762	8.762	277.64	517.91	7.179	2.93 [93]
3	R-3m	3.353	42.51	14.17	521.864	137.965	6.280	2.72 [94]; 2.81 [92]
4	P63/mmc	3.338	33.52	16.76	603.272	161.725	6.193	2.85 [92]
5	R-3m	3.326	58.11	19.37	684.68	185.569	6.126	2.75 [94]
6	P63/mmc	3.316	43.96	21.98	766.088	209.309	6.077	-
7	R-3m	3.311	73.68	24.56	847.496	233.173	6.035	2.82 [94]; 2.87 [92]
9	R-3m	3.300	89.25	29.75	1010.312	280.573	5.979	2.83 [94]
11	R-3m	3.291	104.94	34.98	1173.128	328.100	5.936	2.95 [92]
13	R-3m	3.284	120.36	40.12	1335.944	374.712	5.919	-
15	R-3m	3.278	135.99	45.33	1498.76	421.827	5.899	-
∞ (ZnO)	P63mc	3.250	5.207	5.207	81.408	23.810	5.677	3.3 [95]

In addition to ZnO-In₂O₃ system, gallium doped ZnO is also found to form nanostructures consisting of superlattice and nanotwins [42-45]. One typical example from the HRTEM work done by Li *et al.* [42] is shown in Figure 1.11, in which both the superlattice structures and nanotwins with a crystallographic orientation angle of 60° is clearly revealed. Besides the significant change of the structure, it is also found that addition of gallium into ZnO could improve the electrical conductivity [96-98]. Nevertheless, neither the thermal conductivity nor the Seebeck coefficient of gallium doped ZnO have been reported, nor the information on structure and transport properties

have been combined and correlated. It is of thereby interests to explore the structure and thermoelectric properties of gallium doped ZnO, especially on the effect of defect structure such as nanotwins on the transport properties.

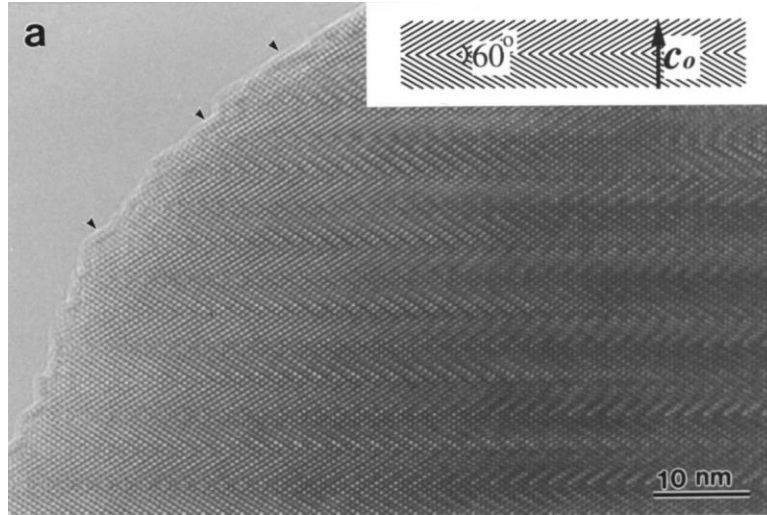


Figure 1.11: HRTEM image of $\text{Ga}_2\text{O}_3(\text{ZnO})_9$ taken with the incident electron beam parallel to the [100] direction [42].

Complex nanoscale defect structure has also been observed in iron doped ZnO [72, 76], one example of TEM observations is shown in Figure 1.12. Whereas in a different study of iron doped ZnO by Liu *et al.* [77], no such defect structure but simple solid solution phase was observed. Since the intricate pattern of planar defect structures is expected to affect the electron and phonon transport properties, it is of interest to explore and investigate the phase equilibria and microstructural evolution of iron doped ZnO. In addition, electrical and especially thermal conductivity of iron doped ZnO, which have not been systematically studied and reported, need to be collected for the investigation of its thermoelectric properties.

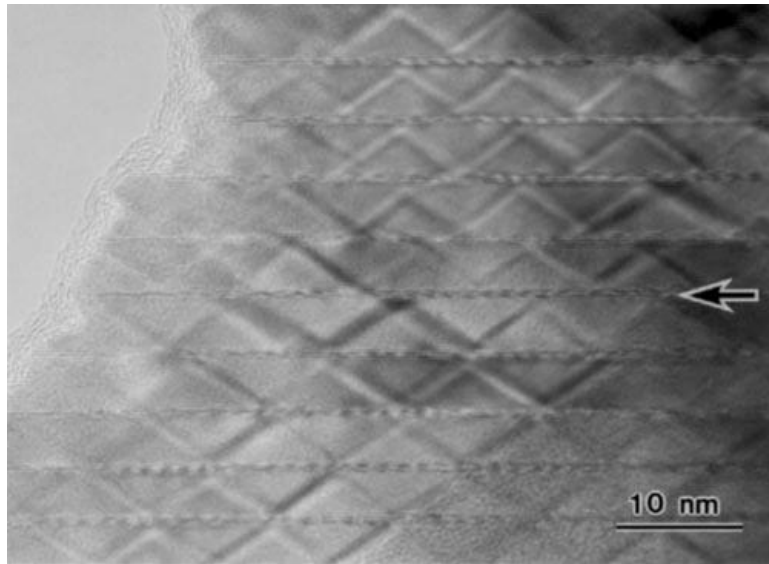


Figure 1.12: TEM image of $\text{Fe}_2\text{O}_3(\text{ZnO})_{15}$ showing the modulated defect structures [72].

Besides the above, there are a variety of doping choices for ZnO materials in terms of modifying the structure and/or improving electrical transport properties. Although there have been a number of studies, yet insufficient research have placed emphasis on the thermoelectric properties. It is of interests to attempt and explore some doping elements such as Al, Ni, Co etc., which might give intriguing results of thermoelectric performance.

1.4 Objectives and Structure of the Thesis

With ZnO based oxide materials as a model system, the present dissertation is aimed to investigate and understand how the thermoelectric properties (including electrical and thermal transport properties) can be affected and tuned by the chemical composition control and structural engineering which are realized through materials synthesis and processing. ZnO is a viable base material as there are a variety of doping

elements which can be used to improve its electrical conductivity by increasing the carrier concentration, which has primarily been of interest for transparent conductors [39, 70, 97, 99, 100]. In addition, natural superlattice nanostructure can be created with the addition of certain elements into ZnO; these nanoscale structures, sometimes forming intricate patterns, can effectively reduce the lattice thermal conductivity through constraining the phonon propagations. In the main body of this dissertation, I examine and evaluate the structure and thermoelectric properties of several doped ZnO oxide systems with experiments as well as physical and mathematical modeling.

Chapter 2 will be devoted to the description of the methods and techniques that I employed through my experimental work, including the synthesis of oxide powders, sintering, structural characterization at different length scales and thermoelectric properties measurement and analysis.

As has been introduced, a large number of recent research works in thermoelectrics focus on reducing the lattice or phonon thermal conductivity. Accordingly, a detailed understanding of thermal transport physics is essential. Chapter 3 presents my modeling work on thermal conductivity physics. An introduction on thermal transport physics of pure material as well as defect scattering physics is first given. The major part of the chapter is recasting the Callaway and von Baeyer's thermal conductivity model by taking into account the minimum phonon relaxation time. The modified model will then be applied to three cases with numerical calculations: pure and preface materials, materials with point defects, and materials with both point and planar defects.

Both Chapter 4 and 5 will focus on the ZnO-In₂O₃ binary system. Chapter 4 mainly focuses on the thermal (Kapitza) resistance of compositional dependent ZnO-In₂O₃ superlattice interfaces. The thermal conductivity as a function of both temperature and indium concentration is successfully described using the modified Klemens-Callaway model incorporating the superlattice interface scattering of phonons. The thermal conductivity anisotropy is taken into account and the Kapitza resistance is derived. Chapter 5 presents the comprehensive investigation and the results of the phase equilibria, microstructure and thermoelectric properties in the full range of ZnO-In₂O₃ phase diagram. Changes of phase equilibria and structure with chemical compositions and temperature will be presented and discussed in detail. The thermoelectric properties of two-phase composites as a function of phase compositions are also successfully described using a mean-field mathematical model.

In Chapter 6, I will present my results of Fe heavily doped ZnO, based on observed high temperature grain refinement. This phenomenon, which is explained on the basis of Fe₂O₃-ZnO phase equilibria, has significant applications, especially in the search for high temperature thermoelectric materials. Chapter 7 will present the effect of nanotwins and superlattice structure observed in Ga heavily doped ZnO. The electrical and thermal transport properties will be also reported and discussed.

Superlattice structures possess nanosized features which can be captured by transmission electron microscopy and possibly X-ray diffraction analysis. However, there has been a lack of efforts on identifying these nanostructures using Raman spectroscopy. In the Appendix, I will present the interesting findings of superlattice structures by Raman spectroscopy correlated with X-ray diffraction results. As a final chapter to

conclude the thesis, I will summarize and discuss my findings mainly on trivalent doping of ZnO and propose an outlook for the future research in oxide thermoelectrics.

Chapter 2 Experimental

In this chapter, chemical synthesis of oxide powders and sintering of solid pellet samples will be described in details, followed by the structural characterization methods and techniques employed in my Ph.D. research work, including X-ray diffraction, Raman spectroscopy, electron microscopy with Energy-dispersive X-ray Spectrometer (EDS) and atom probe tomography technique etc. The measurements of thermal conductivity, electrical conductivity and Seebeck coefficient with temperature will be also described in details, from which the thermoelectric figure of merit ZT can be obtained.

2.1 Chemical Synthesis of Oxide Powders

As a start, commercial high purity nitrate powders were used to prepare oxide powders. Nitrate solutions were then prepared by dissolving them in deionized and distilled water and the ionic concentration of each solution was then determined by drying the solutions and then decomposing the nitrate salts at 900 °C. Solutions were weighted according to the desired compositions, and were then mixed together and stirred uniformly. The mixed solutions were heated up and held at 80 °C. A few organic fuels were added into the mixed solutions, which are as follows: acrylamide as monomer, N,N'-Methylene-bisacrylamide as cross-linking agent, 2,2'-Azobisisobutyro-nitrile and ammonium persulfate as catalysts. These chemicals eventually converted the mixed solution liquid into gel in which different species of ions were kept to the designated ratios. These gels were then dried in the low temperature drying furnace for 12 hours at 120 °C. The dried gels were crushed and ground into small particles and sent to

combustion furnace at 600 °C at which self-assisted chemical reactions occur. After fully reacted, the powders became a mixture of very fine oxide and carbon particles. They were further calcined at 825 °C for 2 hours to remove the residual carbon and organic chemicals. The calcined powders were then oxide powders with desired compositions. This wet chemistry method allows a uniform mixture of different ions in the atomic or molecular level, and the gel-combustion approach freezes the ratios of different types of ions, which provides a good control of the chemical composition.

2.2 Sintering and Post-annealing Treatment

The calcined oxide powders were wrapped in graphite foil and placed in a set of graphite die and punch. The powders were pre-compressed in a cold press machine and then sintered into solid pellets using our home-made current assisted densification processing system (CADPro) normally at 900 °C for 5 min with an applied load of 125 MPa. This sintering technique is also well known and referred as spark plasma sintering (SPS) in literatures [101-110]. All the sintering processes were performed under the vacuum level of 30-40 mTorr. An illustration of CADPro sintering profile is shown in Figure 2.1. The intermediate step at 600 °C is designed for decomposition that occurs in some powders. In most cases, a controlled cooling rate of 20 °C/min was applied to avoid the cracking arising from thermal stress.

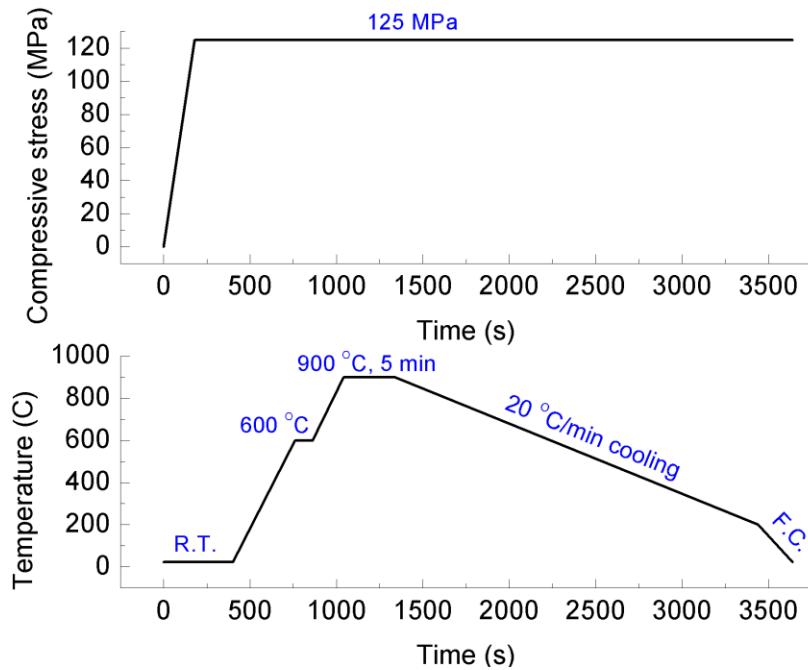


Figure 2.1: Illustration of a typical CADPro sintering profile.

The actual sintering parameters such as target temperature and holding time depends on the sinterability of specific oxide powders which could vary among materials and compositions. The solid pellets sintered from CADPro was further annealed in air at 1000 °C for 2 hours to compensate the oxygen deficiency that results from the reducing atmosphere inside the CADPro chamber. Various post-annealing treatments in air were also made to obtain and investigate the specific phase equilibria and microstructures of different oxide systems, which will be described in the following chapters. To avoid preferential evaporation of certain elements, the pellets were embedded in oxide powders of the same composition and kept in covered crucibles during annealing.

2.3 Structural Characterization

X-ray diffraction analysis was performed on a Philips® PANalytical Multipurpose Diffractometer at Massachusetts Institute of Technology (MIT) and Bruker® D8 Discover System at Harvard University. The phases were analyzed and identified with PANalytical X’Pert HighScore Plus software with 2011 ICDD PDF database [111] at MIT X-ray lab.

Raman spectroscopy was made on a LabRAM Aramis Raman system (Horiba Jobin Yvon, Edison, NJ) equipped with a HeCd laser operating at 325 nm, a solid state laser at 514 nm and a solid state laser at 785 nm. All the Raman spectra were collected at room temperature with 10 μm diameter laser beam and in most cases with a 10 X objective lens to sample sufficiently large area for acquiring global statistic information of the material. All the recorded spectra were calibrated by monitoring the laser Raleigh line at 0 cm^{-1} and were analyzed using commercial peak-fitting software (GRMS, Thermo Electron Corp., Philadelphia, PA).

Microstructures of sintered oxide pellets were examined under Field Emission Gun Scanning Electron Microscopy (FEG-SEM) with Energy-dispersive X-ray Spectrometer (EDS). The cross-sections of samples were prepared and ground and polished down to 0.5 μm . They were further either etched in dilute HCl acid or thermally etched at 1050 °C for 30 min in air to reveal the grain boundaries and other defect structures. SEM observations and EDS elemental analysis were conducted on Zeiss® FEG-SEM Super 55VP, Ultra 55 and Ultra-Plus systems. Variable pressure mode was applied in some cases when conducting is an issue.

Both conventional and high resolution transmission electron microscopy (TEM) imaging with electron diffraction analysis were also made on selected samples to observe the fine structures such as superlattice structures. Part of the TEM work was assisted with Dr. M. Baram. Plan view of the pellets was chosen for TEM observations and 3 mm diameter disks were prepared from the bulk sample using an ultrasonic cutting machine. The disk specimens were then preliminary thinned by finely polishing the both sides until the thickness was reduced down to about 60 – 80 μm , followed by ion-beam milling on a Fischione® 1010 Dual Beam Ion-Mill machine till a hole appeared in the center of the specimen. To ensure the quality of the specimen, plasma cleaning was conducted on Fischione® 110 Plasma Cleaner and the TEM observations were made on several microscopy facilities including JEOL® 2100 TEM, JEOL® 2010 FEG-TEM and Zeiss® Libra 200 Cs-TEM Aberration Corrected TEM at the Center for Nanoscale Systems (CNS) at Harvard University. The EDS elemental mapping was also performed on a Cs-STEM Aberration Corrected Zeiss® Libra 200 MC with the assistance from Dr. David C. Bell.

Samples for 3D atom probe tomography (APT) were prepared by Dr. M. Baram using focused ion beam milling and shaping from bulk samples. The atom probe tomography was subsequently carried out in a Cameca LEAP 4000X HR microscope using 355 nm pulsed laser excitation.

2.4 Thermoelectric Properties Measurement and Analysis

Thermal conductivity (κ) was determined by the following standard relation

$$\kappa = \alpha \cdot \rho \cdot C_p \quad (2.1)$$

in which the measurements of thermal diffusivity (α) are made from room temperature to 800 °C in flowing Argon gas on a NETZCH Micro Flash® LFA 457 instrument. Heat capacity C_p (per unit mass at constant pressure) were calculated using the Kopp-Neumann rule from literature data [112] and the mass density ρ measured using Archimedes method.

Specimens were cut into about $2 \times 2 \times 8$ mm shape for electrical resistivity and Seebeck coefficient measurements, which were conducted on a ULVAC RIKO® ZEM 3 M10 unit, from room temperature to 800 °C in air environment. Figure 2.2(a) is an illustrative scheme of the configuration for measuring electrical resistivity and Seebeck coefficient and Figure 2.2(b) is the picture of the real experimental setup.

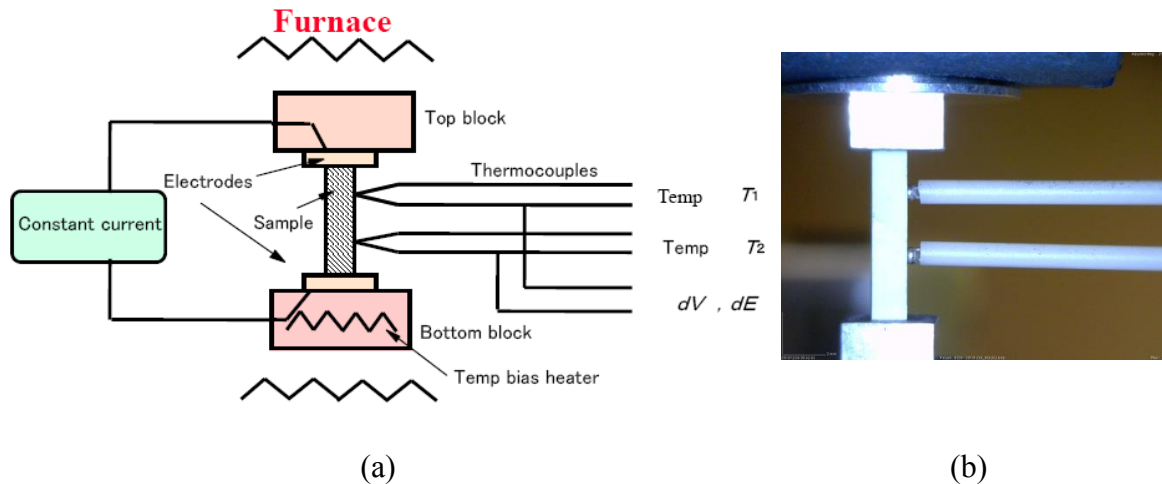


Figure 2.2: Illustrative scheme (a) and picture (b) of configuration for electrical resistivity and Seebeck coefficient measurements. Illustrative drawing is taken from ULVAC Riko manual.

The temperature of the system is under an infrared furnace and a local heater at the bottom electrode provides the temperature bias. A constant current is supplied to the sample and the potential difference dV is measured between the two thermocouples wires

of the same kind, from which the electrical resistivity is measured. Seebeck coefficient is obtained by the voltage drop dV and the temperature difference dT measured by the two thermocouples. The slope of the voltage drop against the temperature difference gives the Seebeck coefficient. Both electrical resistivity and Seebeck coefficient at each measuring temperature were averaged from three to four measurements. The figure of merit is calculated according to its definition relation,

$$ZT = \frac{S^2 \sigma}{\kappa} T \quad (2.2)$$

where S is the Seebeck coefficient, σ is the electrical conductivity and T is the absolute temperature.

Chapter 3 Recasting the Thermal Conductivity Physics Model with Numerical Evaluations

Thermal conductivity, a physical parameter characterizing thermal transport, is an important factor in many research fields as well as applications such as thermal barrier coatings and thermoelectrics. The Debye model provides a classical description of heat transfer by phonons which is treated as by analogy with classical gas where phonons are thought of a gas of particles. Unlike an ideal gas where there are no collisions between gas molecules, phonon mean free path is limited by collisions between phonons themselves or with lattice imperfections. Based on this physical picture, Debye [113] proposed the classical model for thermal conductivity κ in which the full phonon frequency spectrum is considered,

$$\kappa = \int \kappa(\omega) d\omega = \frac{1}{3} \int C(\omega) v_s l(\omega) d\omega \quad (3.1)$$

where $C(\omega)$ is the specific heat, v_s is the sound velocity and $l(\omega)$ is the phonon mean free path. Based on the Debye model, Callaway and von Baeyer [114] cast the expression 3.1 in terms of phonon relaxation time $\tau(\omega)$ which characterizes the time between phonon collision or scattering events, by either other phonons or material defects. Several follow-up works on modifying or applying the model are also present in literature [27, 49, 115-118]. Nevertheless, a drawback exists in equation 3.1 that there are no explicit integral limits of phonon frequency or phonon mean free path, as it is physically meaningless to perform the integration when phonon mean free path is smaller than the interatomic distance. It is of thus importance to modify the model by introducing a cut-off phonon frequency that corresponds to the Debye temperature.

In this chapter, I shall first provide an introduction and background on thermal transport physics, from the thermal conductivity of pure materials and several influential factors such as mean atomic mass, temperature, lattice parameters etc. towards the physics of defect scattering and various models on describing them. In the following sections, I shall then recast Callaway and von Baeyer's model by introducing a minimum phonon relaxation time τ_{min} that corresponds to the minimum phonon mean free path which is set by the interatomic distance; this modification can be treated by breaking down the integral (equation 3.1) into two parts. I will then make detailed discussions and derivations for specific cases, namely, pure or perfect materials, materials with point defects, and materials with both point and planar defects. Comparisons between my derived expressions and Callaway-von Baeyer's work [114] will be made and discussed; the additional correction terms in my derived equations arise from the consideration of minimum phonon relaxation time. Numerical calculations were also made where parameters were chosen for the indium doped ZnO system and modeling calculation results were compared with experimental data. Calculations and discussions of the length scale effect of planar interfaces on thermal conductivity will be also presented.

3.1 Introduction

As has been described in Chapter 1, both electrons and phonons are responsible for thermal transport. However, as for semiconducting and electrically insulating materials which are the materials dealt with in this current dissertation work, electronic

contribution is negligible and ignored. Using a classical gas model based on equation 3.1, a simplified Debye model for thermal conductivity is given as,

$$\kappa = \frac{1}{3} C_V v_s l \quad (3.2)$$

where C_V is the heat capacity at constant volume, v_s is the phonon velocity and is identified with the sound speed[18] and l is the phonon mean free path that is a characteristic length of phonons scatterings by themselves or lattice imperfections of various kinds (dislocations, grain boundaries, etc.). It should be noted that phonon mean free path depends on both temperature and microstructural features, since temperature determines density of states of phonons and thereby affects phonon-phonon interactions/ Lattice imperfections introduce defect scatterings of phonons. The latter one also opens up the opportunities of altering thermal transport property by structural engineering. Assuming the scattering mechanisms are additive, the total phonon mean free path can be written as [119],

$$\frac{1}{l_{tot}} = \frac{1}{l_{ph-ph}} + \sum \frac{1}{l_{ph-def}} \quad (3.3)$$

where l_{ph-ph} is phonon mean free path limited by phonon-phonon scattering and l_{ph-def} is the one limited by defect scattering processes.

The thermal conductivity expression in equation 3.2 is simple but discloses the physical picture of the temperature dependence of thermal conductivity. Figure 3.1 presents the thermal conductivity of singly crystal germanium measured from 3 K to its melting temperature [120], which possesses four typical regions characteristic of

crystalline materials, as labeled as I to IV [118]. I shall discuss each stage and clarify the physical processes behind the phenomena in the following content.

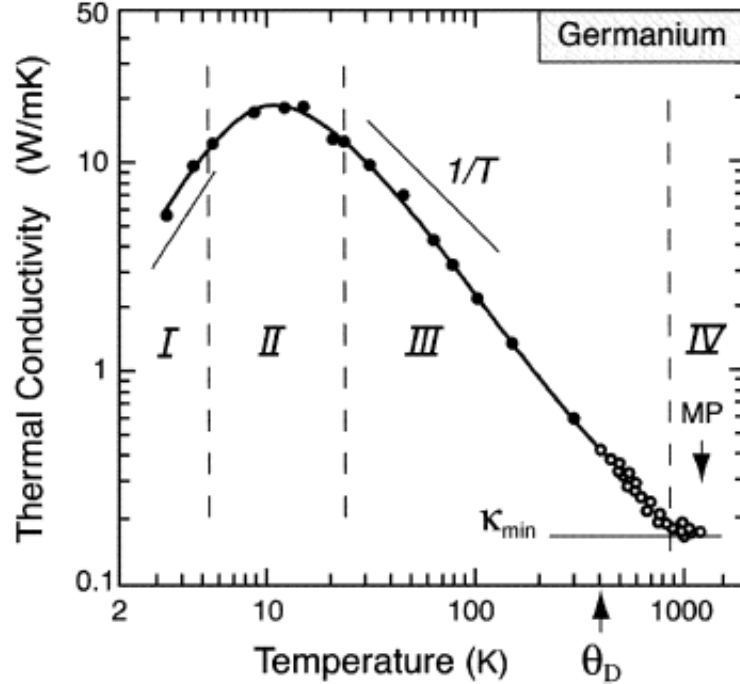


Figure 3.1: Illustration of typical four stages of thermal conductivity with temperature [118]. Data points are experimental values of single crystal germanium from 3 K to its melting temperature from Glassbrenner and Slack's work [120].

In Region III, it is normally observed that thermal conductivity decreases with temperature. This trend is mainly controlled by the phonon-phonon scattering process and therefore is dependent on the number of phonons present. In equilibrium, the number of phonons present is given by the Bose-Einstein statistical factor and the leading high-temperature term is taken for above Debye temperature [119],

$$n = \frac{1}{\exp\left(\frac{\hbar\omega}{k_B T}\right) - 1} \approx \frac{k_B T}{\hbar\omega} \quad (3.4)$$

This suggests that the number of phonons $n \sim T$ at high temperature. Since the three-phonon processes dominate phonon scattering at high temperature, one can well

approximate that the phonon mean free path $l \sim 1/T$ [119]. The heat capacity at high temperatures is well approximated by its classical values of $3k_B$ per atom; hence, the thermal conductivity κ varies with temperature as T^{-1} . Experimental observed powers of T lies in the range of $0.9 \sim 1.3$ [18]. The variation in the power of T arises from the fact that thermal conductivity is also affected by the types and density of defects, the crystal structure, the atoms in the structure, as well as the thermal expansion [118].

In Region I, thermal conductivity κ varies with temperature as $\kappa \sim T^n$, where typically $n \sim 3$. In this regime where the temperature is low and few phonons are excited, therefore phonon-phonon scattering events are rare. The phonon mean free path l is mainly limited by the size of the sample, grain boundary and defect spacing [118]. Accordingly, l is basically independent of T and mostly determined by grain boundary scattering or sample surface. The heat capacity C_V varies as T^3 for crystalline solids, according to Debye T^3 law [5]. As a consequence, $\kappa \sim T^3$.

The maximum thermal conductivity occurs in Region II which is at the crossover of Region I and III. This suggests the phonon mean free path controlled by defects is comparable to that limited by phonon-phonon scattering processes, i.e $l_{ph-ph} \sim l_{ph-def}$. Since l_{ph-def} depends on the types and densities of defects, the temperature regime of Region II is dependent on specimen and is not intrinsically characteristic of materials [119].

With increasing temperature, thermal conductivity decreases less rapidly and tends saturates to a constant value, as seen in the Region IV. As has been discussed for Region III, the phonon mean free path l decrease with T , but l cannot be smaller than the

interatomic distance as it would be physically meaningless otherwise [119]. Accordingly, there is a minimum phonon mean free path which sets the lower limit of l . Experimentally, a high temperature thermal conductivity limit κ_{limit} is observed. There have been a few discussions and derivations for κ_{limit} in literature [115, 116, 118, 121].

It is also useful to review a few thermal conductivity models which disclose the role of physical parameters on thermal transport. Dugdale and McDonald [122] proposed the phonon mean free path as

$$l = \frac{a}{\alpha\gamma T} \quad (3.5)$$

where a is the interatomic distance and γ is the Gruneisen parameter. Based on this work, Lawson further proposed the thermal conductivity expression in Region III [123],

$$\kappa = \frac{aK^{\frac{3}{2}}}{3\gamma^2\rho^{\frac{1}{2}}T} \quad (3.6)$$

where K is the bulk modulus and ρ is the mass density. Berman [124] also expressed the thermal conductivity in a practical way in which most of the physical parameters can be obtained by experiments or calculations,

$$\kappa \propto \frac{\bar{M}a\theta^3}{\gamma^2 T} \quad (3.7)$$

where \bar{M} is the average atomic weight which is the atomic weight of the molecule, M , divided by the number of the atoms in the molecule, m . θ is the Debye temperature at which the wavelength of the shortest wavelength phonon corresponds to the size of the unit cell, given by [118]

$$\theta_D = \frac{2\hbar v_s}{a_0 k_B} \quad (3.8)$$

where a_0 is the unit cell parameter. The above expressions reveal the effect of mean atomic mass, temperature and lattice parameter on the thermal conductivity of pure materials.

Defect scattering is important in controlling thermal conductivity, either in the case of reducing it for thermal barrier coatings and thermoelectric applications, or for enhancing thermal management as heat sink functions. Typical material defects include point defects, dislocations, interface or specimen boundaries etc. The scattering cross section has different dependences on the phonon wavelength λ depending on the type of the defect. For instance, the scattering cross section for a point defect varies as $1/\lambda^4$ whereas is practically independent of λ for interface boundaries. Since only those phonons with energy $\hbar\omega$ smaller than $k_B T$ are excited, the phonon frequency ω can be well approximated to be linear with the phonon wave vector q , which leads to the approximation of $\omega \sim 1/\lambda$. It follows that the scattering cross section varies with ω^n , and the corresponding phonon relaxation time τ varies with the phonon frequency as ω^{-n} , where the power n depends on the type of defects [119].

In the presence of point defects, the phonon propagation is disturbed due to the change in the atomic mass and the interatomic forces as well as the displacement of atomic positions. Ziman [125] attributed the phonon scattering to the difference or change in the mass density $\Delta\rho/\rho$ and the shear modulus $\Delta G/G$, the latter of which relates to the sound velocity. He proposed the phonon scattering (or relaxation) time due to point defect scattering as

$$\frac{1}{\tau} = n_{\text{def}} \left(\frac{AG}{\lambda^4} \right) V^2 \left[\left(\frac{\Delta\rho}{\rho} \right)^2 + 6 \left(\frac{\Delta G}{G} \right)^2 \right] \quad (3.9)$$

where n_{def} is the number of defects per volume, V is the volume of a single defect and A is a dimensionless constant of the order of $4\pi^3$. In most cases, it is well approximated that the mass mismatch or change, $\Delta M/M$, is the dominant factor [126]. Klemens derived an expression for the phonon relaxation time for point defect scattering [127],

$$\frac{1}{\tau} = c_{\text{def}} \frac{V\omega^4}{4\pi N v_g^3} \left(\frac{\Delta M}{M} \right)^2 \quad (3.10)$$

where c_{def} is the defect concentration in the lattice (i.e. site fraction occupied by defects), V/N is volume per atom, and v_g is the group velocity.

Assuming high temperatures ($T > \theta$) and a Debye spectrum, Klemens [128] first and then later Callaway [114] derived a model for the lattice thermal conductivity of crystalline solids containing point defects,

$$\begin{aligned} \kappa &= \frac{k_B}{2\pi^2 v_s (ACT)^{\frac{1}{2}}} \tan^{-1} \left[\frac{k_B \theta}{\hbar} \left(\frac{A}{CT} \right)^{\frac{1}{2}} \right] \\ &= \frac{k_B \sqrt{v_s}}{\sqrt{\pi^3}} \frac{1}{\sqrt{\Omega_0 C \Gamma}} \frac{1}{\sqrt{T}} \tan^{-1} \left(\frac{k_B \theta}{\hbar} \left(\frac{\Omega_0 \Gamma}{4\pi v_s^3 CT} \right)^{\frac{1}{2}} \right) \end{aligned} \quad (3.11)$$

Klemens [127] gives an expression for A ,

$$A = \frac{\Omega_0}{4\pi v_s^3} \Gamma \quad (3.12)$$

where Ω_0 is the unit cell volume, constant C is the inverse time coefficient for phonon-phonon scattering processes in pure and perfect materials and Γ is the point defect

scattering strength parameter introduced by solid solution alloying and depends on the types and fractions of defects at each atomic site. In the following content, we shall consider the thermal conductivity behavior at three limits or special cases based on Klemens – Callaway's model as shown in equation 3.11.

(I) In the case of perfect crystal or in the limit of small defect scattering which suggests $A \rightarrow 0$, equation 3.11 becomes,

$$\kappa_{KC-pure} = \frac{k_B^2 \theta}{2\pi^2 v_s \hbar C T} \quad (3.13)$$

This suggests that thermal conductivity of perfect crystal decreases with temperature as $\propto T^{-1}$ which is consistent with a number of experiments; however, discrepancy occurs when approaching high temperatures since equation 3.13 suggests thermal conductivity goes down endlessly with temperature whereas real materials tend to saturate to a constant value that is invariant of temperature.

(II) In the limit of infinitely high temperature, i.e. $T \rightarrow \infty$, equation 3.11 suggests that $\kappa \rightarrow 0$. Apparently, this has not been observed in any measurements.

(III) The last case of interest, especially in the studies of thermal conductivity of solid solutions [128], is the large defect scattering at high temperatures. In this case, the term $\tan^{-1} \left[\frac{k_B \theta}{\hbar} \left(\frac{A}{CT} \right)^{\frac{1}{2}} \right] \cong \pi/2$, and one may rewrite equation 3.11 as

$$\kappa = \frac{k_B}{4\pi v_s (ACT)^{\frac{1}{2}}} \quad (3.14)$$

The important implications of equation 3.14 are that the thermal conductivity falls off with temperature as $T^{-\frac{1}{2}}$ and goes down with defect concentration as $A^{-\frac{1}{2}}$. The Klemens – Callaway's model (equation 3.11) with their special cases (equation 3.13 and 3.14) has been found of successful in describing and interpreting the measurement results; however, the weakness in describing high temperature thermal conductivity behavior limits their applications, and therefore there is a need of solving this issue and improving the model for a more general applications, which is one of the major focus of this Chapter.

Dislocation scattering of phonons is complex and controversial, and the theoretical calculations are in poor agreement with experiments. As there is a strain field surrounding a dislocation, the scattering of phonons by dislocations does not behave like linear defects. Also, it has been found of importance of dislocation scattering only at very low temperatures $T < \theta/10$ and in heavily deformed materials [119].

If there are several scattering mechanisms acting simultaneously, the central relation to start from is find out the total or combined phonon relaxation time contributed by different scattering processes, as given in equation 3.3. For a relatively simple case where two scattering mechanisms are active, one may apply the Matthiessen's rule,

$$\frac{1}{\kappa_{tot}} = \frac{1}{\kappa_1} + \frac{1}{\kappa_2} \quad (3.15)$$

where κ_{tot} is the effective thermal conductivity, and κ_1 and κ_2 are those controlled by two different phonon scattering mechanisms.

3.2 Recasting Callaway and von Baeyer's Thermal Conductivity Model

The general expression for thermal conductivity is the integration over the entire phonon frequency spectrum as seen in equation 3.1. Introducing the dimensionless parameter $x = \hbar\omega/k_B T$, Callaway further derived the following general expression for thermal conductivity,

$$\kappa = \frac{k_B}{2\pi^2 v_s} \left(\frac{k_B T}{\hbar} \right)^3 \int_0^{\theta/T} \tau_c(x) \frac{x^4 e^x}{(e^x - 1)^2} dx \quad (3.16)$$

where θ is the Debye temperature. The combined phonon relaxation time $\tau_c(\omega)$ is characteristic of average period time of phonon scattering events including phonon-phonon interactions and defect scatterings of phonons, and is given by Callaway and von Baeyer,

$$\tau_c^{-1} = \tau_P^{-1} + \tau_D^{-1} + \tau_B^{-1} \quad (3.17)$$

where τ_P is the relaxation time due to phonon-phonon scattering process, and is expressed as

$$\tau_P^{-1} = S(T)\omega^2 \quad (3.18)$$

In the case of defective materials at high temperatures,

$$S(T) = CT \quad (3.19)$$

where C is a temperature independent constant.

The second term τ_D is the phonon relaxation time associated with point defect scattering, and its dependence on the phonon frequency is as follows,

$$\tau_D^{-1} = A\omega^4 \quad (3.20)$$

where A has been defined in equation 3.12, and Γ is the point defect scattering strength parameter,

$$\Gamma = \sum_i f_i \left(1 - \frac{M_i}{M}\right)^2 \quad (3.21)$$

where M_i is the mass of a unit cell and f_i is the fraction of the unit cells with mass M_i , and M is the average mass of all cells.

The last term in the equation 3.17 τ_B , is the boundary scattering phonon relaxation time, and is given by the sound velocity v_s and a characteristic length L .

$$\tau_B^{-1} = \frac{v_s}{L} \quad (3.22)$$

Accordingly, the combined phonon relaxation time can be expressed in terms of the introduced dimensionless variable $x = \hbar\omega/k_B T$,

$$\tau_c^{-1} = \tau_D^{-1} + \tau_P^{-1} + \tau_B^{-1} = Dx^4 + Ex^2 + \frac{v_s}{L} \quad (3.23)$$

where

$$D = A(k_B T / \hbar)^4 \quad (3.24)$$

$$E = CT(k_B T / \hbar)^2 \quad (3.25)$$

Physically, the thermal conductivity cannot endlessly go down with temperature when the phonon mean free path reaches its lower limit l_{min} which is the order of magnitude of interatomic distance. This was recognized by Roufosse and Klemens [115], and to account for this, they introduced the minimum phonon mean free path l_{min} . Similarly, a minimum phonon relaxation time τ_{min} can be introduced which corresponds to l_{min} as

$$\tau_{min} = \frac{l_{min}}{v_s} \quad (3.26)$$

Taking this limit into account, we have different expressions or values for the phonon relaxation time depending on the relaxation time, i.e.

$$\tau(x) = \frac{1}{Dx^4 + Ex^2 + v_s/L}, \quad \text{if } \tau(x) > \tau_{min}; \quad (3.27)$$

$$\tau(x) = \tau_{min}, \quad \text{if } \tau(x) < \tau_{min} \quad (3.28)$$

Accordingly, the thermal conductivity integration can be expressed in two parts,

$$\kappa = \frac{k_B}{2\pi^2 v_s} \left(\frac{k_B T}{\hbar} \right)^3 \left(\int_0^{x_1} \tau(x) \frac{x^4 e^x}{(e^x - 1)^2} dx + \int_{x_1}^{\theta} \tau_{min} \frac{x^4 e^x}{(e^x - 1)^2} dx \right) \quad (3.29)$$

where x_1 is set such that

$$\tau(x_1) = \tau_{min} \quad (3.30)$$

In the following sections, I shall derive the thermal conductivity functions for the cases of pure or perfect materials, materials with point defects and materials with both point and planar defects. Modeling calculations are performed and compared with experimental results of indium doped ZnO. Discussions on the thermal transport physics of defective materials are then made.

3.3 Pure and Perfect Materials

For pure and perfect materials in the absence of any type of defect, phonon-phonon interaction is the only phonon scattering mechanism. Accordingly, the combined phonon relaxation time is given by,

$$\tau_c^{-1} = \tau_P^{-1} = Ex^2 \quad (3.31)$$

Introducing the minimum phonon relaxation time τ_{min} and with the following conditions,

$$\tau(x) = \frac{1}{Ex^2}, \quad \text{if } \tau(x) > \tau_{min}; \quad (3.32)$$

$$\tau(x) = \tau_{min}, \quad \text{if } \tau(x) < \tau_{min} \quad (3.33)$$

The integral was broken into two parts,

$$\kappa_{pure} = \frac{k_B}{2\pi^2 v_s} \left(\frac{k_B T}{\hbar} \right)^3 \left(\int_0^{x_1} \frac{1}{E} \frac{x^2 e^x}{(e^x - 1)^2} dx + \int_{x_1}^{\theta} \tau_{min} \frac{x^4 e^x}{(e^x - 1)^2} dx \right) \quad (3.34)$$

Since the upper limit is less than unity, we could set the following approximation[114],

$$\frac{x^2 e^x}{(e^x - 1)^2} = 1 \quad (3.35)$$

where x_1 is determined by

$$\tau(x_1) = \frac{1}{Ex_1^2} = \tau_{min} \quad (3.36)$$

and we obtain

$$x_1 = \frac{1}{\sqrt{E\tau_{min}}} \quad (3.37)$$

Calculating the integral and substituting the above expressions, we obtain the expression for thermal conductivity of pure and perfect materials,

$$\kappa_{pure} = \frac{1}{3\pi^2} \frac{k_B}{C^{3/2} \sqrt{\tau_{min} v_s}} T^{-3/2} + \frac{1}{6\pi^2} \frac{\theta^3 k_B^4 \tau_{min}}{\hbar^3 v_s} \quad (3.38)$$

The derived temperature dependence of thermal conductivity for pure material is exactly the same as the one reported in literatures [115, 116]. Noting the second T -independent term is the high temperature thermal conductivity limit κ_{limit} ,

$$\kappa_{limit} = \frac{1}{6\pi^2} \frac{\theta^3 k_B^4 \tau_{min}}{\hbar^3 v_s} \quad (3.39)$$

Expression for pure materials shown in equation 3.38 is in contrast with the commonly accepted expression in which $\kappa \propto T^{-1}$; one of such examples is the derivation made by Callaway and von Baeyer [114] for pure and perfect materials as has been shown in equation 3.13. Equation 3.38 makes up the drawback of the Callaway and von Baeyer's model (equation 3.13) that thermal conductivity goes to zero when the temperature is sufficiently high --- which is inconsistent with observations. The reason is that Callaway and von Baeyer did not introduce a cut-off phonon frequency or wavelength which is related to the saturation of thermal conductivity with temperature; as a result, equation 3.13 does not have the high temperature saturation term which is the minimum thermal conductivity κ_{limit} .

Now, the derived function for pure material thermal conductivity in equation 3.38 was used to fit our pure ZnO experimental data (CADPro sintered and then annealed at 1150 °C for 1 day). Inputting all the values for the parameters in above equation, and leaving C as the only fitting parameter, we obtained an excellent fit with R^2 of 0.99, as shown by the solid red curve in Figure 3.2. C was derived as 1.30×10^{-18} (SI units) which is characteristic of phonon-phonon scatterings in pure, un-doped ZnO. As a comparison, Callaway and von Baeyer's model for pure materials, as shown in equation 3.13, is also applied to the measured results, as represented by dashed blue curve on the

figure. Apparently, it has much less satisfactory description of the experimental data ($R^2 = 0.93$) than the one I derived.

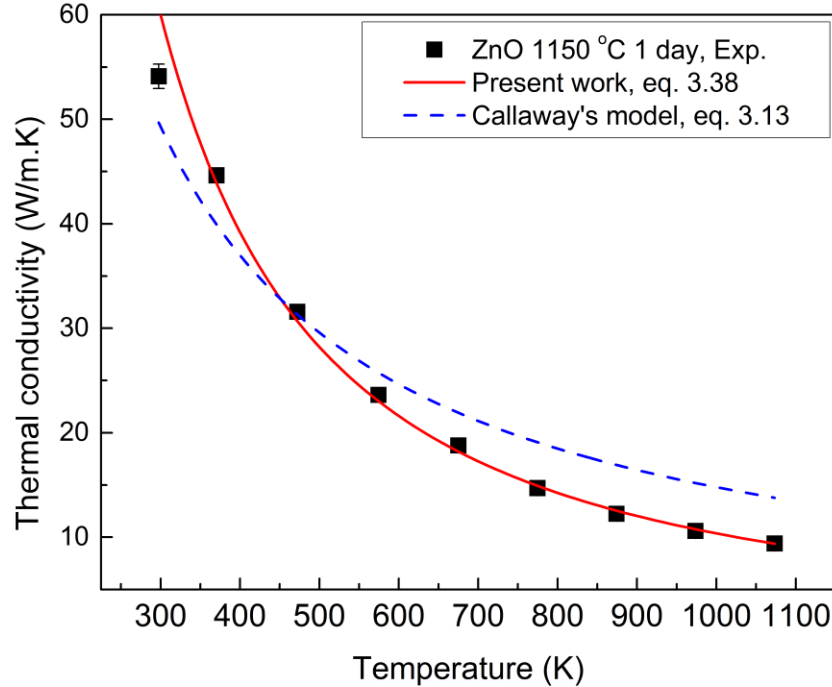


Figure 3.2: Modeling fit of measured thermal conductivity of pure ZnO synthesized by CADPro and further annealed at 1150 °C for 1 day. The thermal conductivity model developed in the present work (equation 3.38) demonstrates better description of experimental data than the Callaway and von Baeyer's model (equation 3.13).

3.4 High Temperature Thermal Conductivity Limit

In this section, we shall unify the different expressions for high temperature thermal conductivity limit κ_{limit} , starting from the derivation of κ_{limit} in Roufosse and Klemens' work. In their work, the thermal conductivity for pure materials with temperature is given as

$$\kappa = \frac{B}{T} \left[\frac{2}{3} \left(\frac{T_0}{T} \right)^{1/2} + \frac{1}{3} \left(\frac{T}{T_0} \right) \right] \quad (3.40)$$

where the second term is temperature independent and is the high temperature limit, i.e.

$$\kappa_{limit-RK} = \frac{1}{3} \frac{B}{T_0} \quad (3.41)$$

in which the parameter B is defined as,

$$B = \frac{3k_B}{Aa(6\pi^2)^{\frac{2}{3}}} \quad (3.42)$$

where a^3 is the atomic volume, and A is given by the following expression,

$$A = \frac{3\pi\sqrt{2} \left(\frac{a}{v_s} \right) \gamma^2 k_B}{M v_s^2} \quad (3.43)$$

The definition for T_0 is as follows: T_0 is the temperature at which $l(\omega_D) = l_{min}$, where the Debye frequency ω_D is defined as

$$\left(\frac{a\omega_D}{v_s} \right)^3 = 6\pi^2 \quad (3.44)$$

and a is the interatomic distance. In Roufosse and Klemens' work, $l_{min} \approx a$ where a is the interatomic distance. The phonon frequency dependence of phonon mean free path is given by,

$$l(\omega) = v_s / (A\omega^2 T) \quad (3.45)$$

Using the condition that $l(\omega_D) = l_{min}$, we derived the expression for T_0 ,

$$T_0 = v_s / (a A \omega_D^2) \quad (3.46)$$

in which the expression for A is already provided in one of the previous equations.

Substituting the expression for B and T_0 into the equation 3.26 for $\kappa_{limit-RK}$, we obtain

$$\kappa_{limit-RK} = \frac{1}{(6\pi^2)^{\frac{2}{3}}} \frac{k_B^3 \theta^2}{v_s \hbar^2} \quad (3.47)$$

The above expression, as based on and derived from Roufosse and Klemens' approach, appears different from our expression shown in equation 3.24 in which both Debye temperature θ and minimum phonon relaxation time τ_{min} are present. Since Debye temperature is the temperature at which phonon wavelength is of the order of interatomic distance a , and minimum phonon relaxation time corresponds to the minimum phonon mean free path which is also of the order interatomic distance a , there should be a correlation between the two physical parameters which could unify the different expressions for κ_{limit} . This relationship is sought in the following content.

Since the interatomic distance a is usually set as the lower limit of phonon mean free path, i.e. l_{min} , one can replace a with l_{min} in equation 3.44. Accordingly, one obtains,

$$\left(\frac{l_{min}}{v_s} \omega_D\right)^3 = (\omega_D \tau_{min})^3 = 6\pi^2 \quad (3.48)$$

which gives

$$\omega_D \tau_{min} = 6^{\frac{1}{3}} (\pi^2)^{\frac{1}{3}} \quad (3.49)$$

With the relationship between Debye temperature θ and frequency ω_D ,

$$\frac{k_B \theta}{\hbar} = \omega_D \quad (3.50)$$

Accordingly, we obtain the relation between Debye temperature θ and minimum phonon relaxation time τ_{min} :

$$\theta^3 = \frac{6\pi^2\hbar^3}{k_B^3\tau_{min}^3} \quad (3.51)$$

Expressing the minimum phonon relaxation time τ_{min} in terms of θ , our expression for κ_{limit} (equation 3.39) is converted to the expression derived from Roufosse and Klemens' work (equation 3.47). The two expressions obtained using different manners were converged and unified. Furthermore, if expressing the Debye temperature θ in terms of minimum phonon relaxation time τ_{min} , a simple function for κ_{limit} is obtained,

$$\kappa_{limit} = \frac{k_B}{v_s\tau_{min}^2} \quad (3.52)$$

Since Debye temperature θ is better recognized physical parameter than τ_{min} , we may rewrite the equation 3.38 in terms of θ ,

$$\kappa_{pure} = \frac{6^{5/6}}{18\pi^{7/3}} \frac{k_B^{3/2}\sqrt{\theta}}{C^{3/2}\sqrt{\hbar}v_s} T^{-3/2} + \frac{1}{(6\pi^2)^{2/3}} \frac{k_B^3\theta^2}{v_s\hbar^2} \quad (3.53)$$

Considering the minimum phonon mean free path as half of the c -axis of the ZnO unit cell, i.e. $l_{min} = \frac{c}{2} = \frac{0.5207}{2} = 0.26$ nm, we obtain $\kappa_{limit} = 0.61$ W/m.K. If using the interatomic distance between Zn and O ions as the minimum phonon mean free path, i.e. $l_{min} = 0.2$ nm, we obtain $\kappa_{limit} = 0.47$ W/m.K. It is of interests to compare the above model calculations with the literature models. Clarke [118] developed a model on high temperature thermal conductivity limit in terms of elastic modulus E and mass density ρ as follows,

$$\kappa_{Clarke-limit} = 0.87 k_B \Omega^{-\frac{2}{3}} \left(\frac{E}{\rho} \right)^{\frac{1}{2}} \quad (3.54)$$

and Cahill and Pohl [121] derived an expression for κ_{limit} with transverse (v_t) and longitudinal (v_l) sound velocities,

$$\kappa_{Cahill-limit} = \frac{k_B}{2.48} n^{\frac{2}{3}} (2v_t + v_l) \quad (3.55)$$

where n is the number of atoms per unit cell. Substituting numerical values into the above equations, we obtain the values of high temperature thermal conductivity limit from different models, as summarized in the Table 3.1.

Table 3.1: Summaries of high temperature thermal conductivity limit κ_{limit} calculated from different models.

Model	Present work	Clarke model	Cahill model
κ_{limit} , W/m.K	0.47 ~ 0.61	1.05	1.21

3.5 Materials with Point Defects

Doping of material can introduce several types of point defects such as interstitial or substitutional atoms or ions depending on the size of the dopant atoms or ions with respect to the host atoms or ions. In the case where doping ions possess different valences from host ones, vacancies of host ion can be formed for the charge balance. A local strain field and thereby a lattice distortion is created around each point defect due to the mass and/or size mismatch between the host and doping ions, which act as the barrier for

phonon propagation [127]. In other words, point defects are phonon scattering centers and expected to reduce the thermal conductivity as compared to the pure and perfect material [114, 128].

With contributions from both phonon-phonon interactions and point defect scattering, the combined phonon relaxation time is given by,

$$\tau_c^{-1} = \tau_D^{-1} + \tau_P^{-1} = Dx^4 + Ex^2 \quad (3.56)$$

With the lower limit of phonon relaxation time τ_{min} ,

$$\tau(x) = \frac{1}{Dx^4 + Ex^2}, \quad if \tau(x) > \tau_{min}; \quad (3.57)$$

$$\tau(x) = \tau_{min}, \quad if \tau(x) < \tau_{min} \quad (3.58)$$

The integral for the thermal conductivity of point defective materials is

$$\kappa_{pd} = \frac{k_B}{2\pi^2 v_s} \left(\frac{k_B T}{\hbar} \right)^3 \left(\int_0^{x_1} \frac{1}{Dx^4 + E} \frac{x^2 e^x}{(e^x - 1)^2} dx + \int_{x_1}^{\theta} \tau_{min} \frac{x^4 e^x}{(e^x - 1)^2} dx \right) \quad (3.59)$$

which yields after integration,

$$\kappa_{pd} = \frac{k_B}{2\pi^2 v_s} \left(\frac{k_B T}{\hbar} \right)^3 \left(\frac{1}{D \cdot E} \arctan \left(\sqrt{\frac{D}{E}} \cdot x_1 \right) + \frac{1}{3} \tau_{min} \left(\frac{\theta^3}{T^3} - x_1^3 \right) \right) \quad (3.60)$$

where x_1 is determined by

$$\tau(x_1) = \frac{1}{Dx_1^4 + Ex_1^2} = \tau_{min} \quad (3.61)$$

from which the expression for x_1 is obtained,

$$x_1 = \frac{1}{\sqrt{2}} \sqrt{\frac{\sqrt{E^2 \cdot \tau_{min}^2 + 4D \cdot \tau_{min}} - E \cdot \tau_{min}}{D \cdot \tau_{min}}} \quad (3.62)$$

where D and E are both temperature dependent functions given in equation 3.24 and 3.25, respectively. The thermal conductivity function for point defective material thermal is thus derived as below,

$$\begin{aligned} \kappa_{pd} = & \frac{1}{2\pi^2} \frac{k_B}{v_s \sqrt{A} \sqrt{C}} T^{-1/2} \arctan \left(\frac{1}{\sqrt{2}} \sqrt{\sqrt{1 + \frac{4A}{C^2 T^2 \tau_{min}}} - 1} \right) \\ & - \frac{\sqrt{2}}{24\pi^2} \frac{k_B \tau_{min}^{1/4}}{v_s A^{3/2}} \left(\sqrt{C^2 T^2 \tau_{min} + 4A} - CT \sqrt{\tau_{min}} \right)^{3/2} \\ & + \frac{1}{6\pi^2} \frac{\theta^3 k_B^4 \tau_{min}}{\hbar^3 v_s} \end{aligned} \quad (3.63)$$

Expressing τ_{min} in terms of Debye temperature θ according to their relationship derived as shown in equation 3.51, the above expression for the thermal conductivity of point defective materials can be rewritten as

$$\begin{aligned} \kappa_{pd} = & \frac{1}{2\pi^2} \frac{k_B}{v_s \sqrt{A} \sqrt{C}} T^{-1/2} \arctan \left(\frac{1}{\sqrt{2}} \sqrt{\sqrt{1 + \frac{2}{3} \frac{6^{2/3} A k_B \theta}{C^2 T^2 \hbar \pi^{2/3}}} - 1} \right) \\ & - \frac{\sqrt{2}}{24} \frac{6^{1/2} k_B^{3/4} \hbar^{1/4}}{\pi^{11/6} v_s A^{3/2} \theta^{1/4}} \left(\sqrt{\frac{6^{1/3} C^2 T^2 \hbar \pi^{2/3}}{k_B \theta} + 4A} - CT \sqrt{\frac{6^{1/3} \hbar \pi^{2/3}}{k_B \theta}} \right)^{3/2} \\ & + \frac{1}{(6\pi^2)^{2/3}} \frac{k_B^3 \theta^2}{v_s \hbar^2} \end{aligned} \quad (3.64)$$

Noting that A , as defined by equation 3.12, describes the point defect scattering strength. In comparison with Callaway and von Baeyer's derivation as shown in equation 3.11, the temperature dependence is similar while my derivations have a second correction term as well as a temperature independent term which arise from the consideration of minimum phonon relaxation time. The temperature independent term which is the high temperature thermal conductivity limit has exactly the same form as the one derived for pure, perfect materials, as seen in both equation 3.38 and 3.53.

Below I shall discuss the thermal conductivity behavior of the derived expressions (3.63 and 3.64) at three limits or special cases.

(I) In the case of perfect material or in the limit of small defect scattering, i.e. $A \rightarrow 0$, equation 3.63 (and 3.64) become equation 3.38 (and 3.53) which are expressions for thermal conductivity of pure, perfect materials that I have derived in section 3.4.

(II) In the limit of infinitely high temperature, i.e. $T \rightarrow \infty$, the first two terms in equation 3.63 (and 3.64) approaches zero, leaving the high temperature limit term, i.e. $\kappa \rightarrow \kappa_{limit}$.

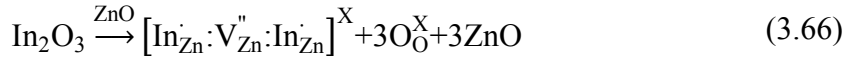
(III) At high temperatures and large defect scattering, equation 3.63 becomes,

$$\kappa_{pd} = \frac{k_B}{4\pi v_s C} A^{-\frac{1}{2}} T^{-\frac{1}{2}} - \frac{1}{6\pi^2} \frac{k_B \tau_{min}^{\frac{1}{4}}}{v_s} A^{-\frac{3}{4}} + \frac{1}{6\pi^2} \frac{\theta^3 k_B^4 \tau_{min}}{\hbar^3 v_s} \quad (3.65)$$

As compared with the Callaway and von Baeyer's model shown in equation 3.14, the first term is exactly same suggesting the same dependence ($T^{-\frac{1}{2}}$) on temperature and defect concentration or scattering strength ($A^{-\frac{1}{2}}$). The second term in equation 3.65 is an

additional correction term on defect scattering dependence and the third term is the high temperature saturation limit correcting the high temperature thermal conductivity behavior.

Numerical values for physical parameters for ZnO are mostly available: the sound velocity $v_s = 4008$ m/s [129], unit cell volume $\Omega_0 = 4.762 \times 10^{-29}$ m³, the Debye temperature $\theta = 370$ K [129] and the inverse time coefficient for phonon-phonon scattering processes $C = 1.30 \times 10^{-18}$ (SI units) that is derived from pure and undoped ZnO. The remaining unknown parameter is the point defect scattering strength factor Γ that characterizes the scattering strength of phonons by point defects. This was first introduced in equation 3.7 and 3.8. It depends on the type of the point defects and the corresponding fractions. In the case of indium doped ZnO, the defect reaction is as follows [90],



The above equation suggests that one chemical formula of In_2O_3 introduces two substitutional indium ions on zinc sites as well as one zinc vacancy for charge balance, all of which occur on zinc sites. Accordingly, the point defect scattering strength factor is written as,

$$\Gamma = x \frac{(M_{In} - \overline{M_{Zn}})^2}{2(\overline{M_{ZnO}})^2} + \frac{x}{2} \frac{(\overline{M_{Zn}})^2}{2(\overline{M_{ZnO}})^2} \quad (3.67)$$

where x is the indium concentration, M_{In} is the indium atomic mass, $\overline{M_{Zn}}$ is the average mass on the zinc site,

$$\overline{M_{Zn}} = \frac{2 - 3c}{2} M_{Zn} + c M_{In} + \frac{c}{2} M_{Vacancy} = 65.38 + 16.75x \quad (3.68)$$

and $\overline{M_{ZnO}}$ is the average mass of the unit cell,

$$\begin{aligned} \overline{M_{ZnO}} &= \frac{2 - 3c}{4} M_{Zn} + \frac{c}{2} M_{In} + \frac{c}{4} M_{Vacancy} + \frac{1}{2} M_O \\ &= 40.69 + 8.375x \end{aligned} \quad (3.69)$$

which gives

$$\begin{aligned} \Gamma &= \frac{1}{2(40.69 + 8.375x)^2} \left[\frac{2 - 3x}{2} (16.75x)^2 + x(49.44 - 16.75x)^2 \right. \\ &\quad \left. + \frac{x}{2} (65.38 + 16.75x)^2 \right] \end{aligned} \quad (3.70)$$

The first order approximation gives,

$$\Gamma \approx 1.38x \quad (3.71)$$

The calculated point defect scattering strength factor with indium concentration up to 0.10 is given Table 3.2.

Table 3.2: Calculated point defect scattering strength factor (SI units) for different indium concentrations based on equation 3.70 and 3.71.

[In]	0.02	0.05	0.08	0.10
Γ , eq. 3. 70	0.0274	0.0676	0.1066	0.132
Γ , eq. 3. 71	0.0276	0.0690	0.1104	0.138

The knowledge of Γ enables the calculation of A and thereby the complete numerical evaluations and calculations of the thermal conductivity of point defective

materials. The thermal conductivities of indium doped ZnO were calculated for a series of indium concentrations from 0.02 to 0.40 with the temperature range from 295 K to 1100 K based on my derived expressions (equation 3.63 or 3.64) as well as Callaway and von Baeyer's model (equation 3.11). Comparisons of the calculation results, together with measured values, are presented in Figure 3.3. It can be seen that at both low and high indium concentrations, the expression derived in this work (equation 3.63 or 3.64) predicts slightly higher thermal conductivity than Callaway and von Baeyer's model; however, two models appear to converge at intermediate indium concentration around 0.10.

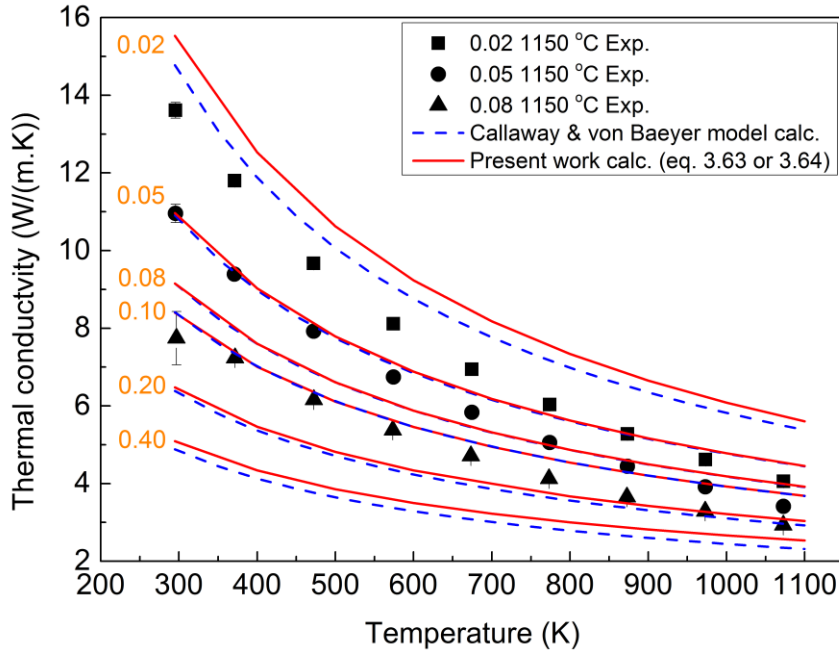


Figure 3.3: Thermal conductivity of ZnO solid solutions of indium with temperature for different indium concentrations (0.02 – 0.40). Calculations based on equation 3.63 or 3.64 are shown as red solid curves. Calculations based on Callaway and von Baeyer's model (equation 3.11) are shown as blue dashed curves. Measured values of [In] = 0.02, 0.05 and 0.08 doped ZnO annealed at 1150 °C for 1 day are also presented.

It is also of interest to evaluate each term in my derived expression as shown in equation 3.63 or 3.64. Calculation results of for 0.02 indium doped ZnO, as plotted in Figure 3.4. Also shown is the measured thermal conductivity of the samples after two annealing conditions. For a better reasonable comparison, the thermal conductivity of fully dense material κ_{dense} was obtained from the measured thermal conductivity $\kappa_{measured}$ by accounting for porosity, ϕ , according to the relation below [130-132],

$$\kappa_{dense} = \kappa_{measured} \frac{1}{(1 - 1.5\phi)} \quad (3.72)$$

where the porosity ϕ is determined from the measured and theoretical mass densities of the material². As seen from Figure 3.4, the calculations describe quite well both the thermal conductivity and the temperature dependence behavior. The first term basically characterizes the temperature dependence based on the intensity of phonon-phonon scattering which is dependent on the phonon density as well as the point defect scattering. The second term is a correction term reflective of point defect scattering; this term has much weaker temperature dependence. The third term is the high temperature thermal conductivity limit and is independent of temperature; it is the minimum thermal conductivity of the material when the phonon mean free path approaches the interatomic distance.

² It is relatively easier to determine the porosity or relative density of the ZnO sample with low indium concentration in which only solid solution phase forms; with increasing indium concentration, materials evolves to a mixture of multiple superlattice phases even with various orders. It is difficult to calculate the theoretical mass density especially without the knowledge of precise volume fractions of each phase as Rietveld refinement analysis cannot be performed due to the lack of atomic information on many $\text{In}_2\text{O}_3(\text{ZnO})_k$ superlattice phases.

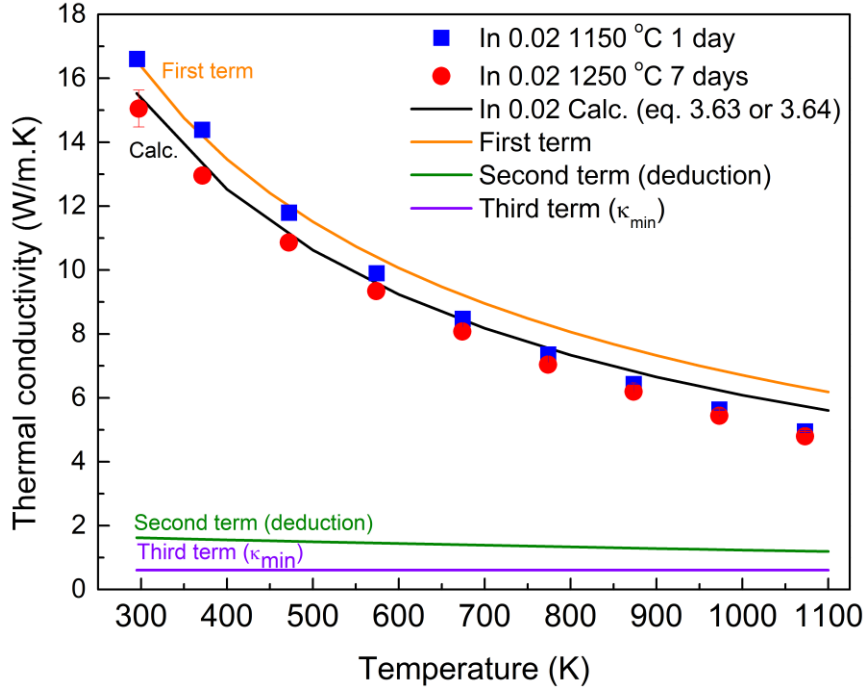


Figure 3.4: Numerical calculations of the thermal conductivity of 0.02 indium doped ZnO, with evaluations of three terms in equation 3.63 or 3.64. Thermal conductivity of fully dense materials obtained from measured results for two sets of annealing conditions (shown as scattered symbols) are also presented.

Examination of equation 3.63 reveals a competition between $C^2 T^2 \tau_{min}$ and $4A$. Recalling that the parameter C characterizes the phonon-phonon interaction processes (equation 3.18 and 3.19) and A represents the point defect scattering strength (equation 3.12), numerical comparison between the two terms indicate the relative significance of the two scattering mechanisms. Since phonon-phonon scattering is dependent on phonon density that increases with temperature, the term $C^2 T^2 \tau_{min}$ is calculated and plotted against temperature; $4A$ is then calculated and plotted against indium concentration with the assumption that all indium ions are incorporated into ZnO lattice forming point defects. The calculated results are plotted in Figure 3.5. The results clearly show that $4A$ is larger than $C^2 T^2 \tau_{min}$ at least by one order of magnitude even with one atomic percent

doping, suggesting that point defect scattering is more efficient in controlling thermal conductivity than phonon-phonon scattering.

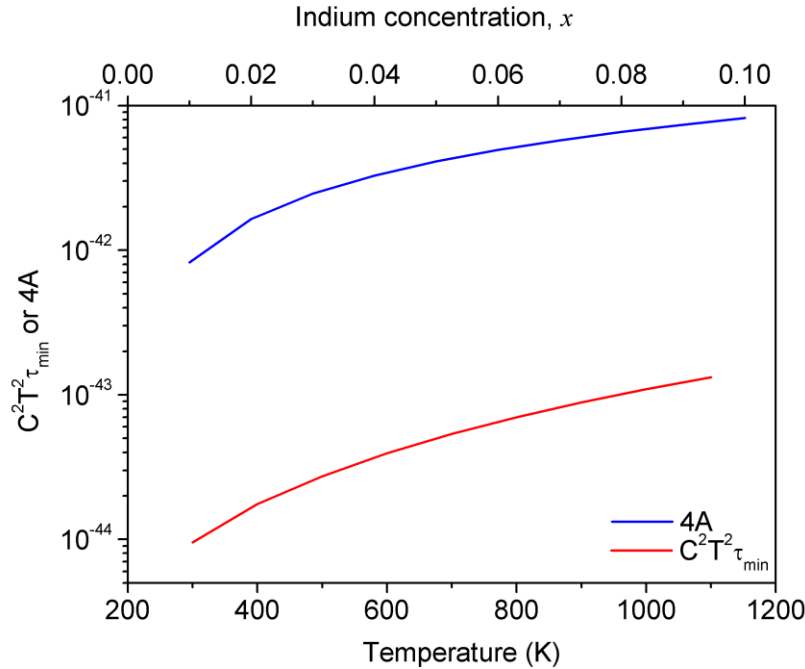


Figure 3.5: Significance of phonon-phonon scattering ($C^2 T^2 \tau_{\min}$) and point defect scattering ($4A$) over temperature and indium concentration in ZnO.

The thermal conductivity of indium doped ZnO is calculated up to 0.10 indium concentration in the temperature range of 300 K to 1073 K. The reason why calculations are only made up to the indium concentration of 0.10 is that this is about the indium solubility in ZnO, as revealed by our both structural characterization and thermal conductivity modeling. Details can be referred to Chapter 4. The calculations results are shown in Figure 3.6 together with measured results for samples with different annealing conditions. The calculated thermal conductivity seems to slightly overestimate, but describe reasonably well especially the 1150 °C 24 hours series data. Higher temperature annealing, i.e., 1250 °C 7 days, may initiate the formation of two-dimensional defects and therefore the thermal conductivity cannot be solely described by the point defect

scattering model. Nevertheless, our modeling calculations clearly show that the thermal conductivity decreases with indium concentration which is associated with the point defect concentration in this indium concentration range. Furthermore, the calculated thermal conductivity becomes less temperature dependent with indium concentration, which is also observed in the experimental results, suggesting that point defect scattering starts taking over the phonon-phonon scattering as the dominant mechanism.

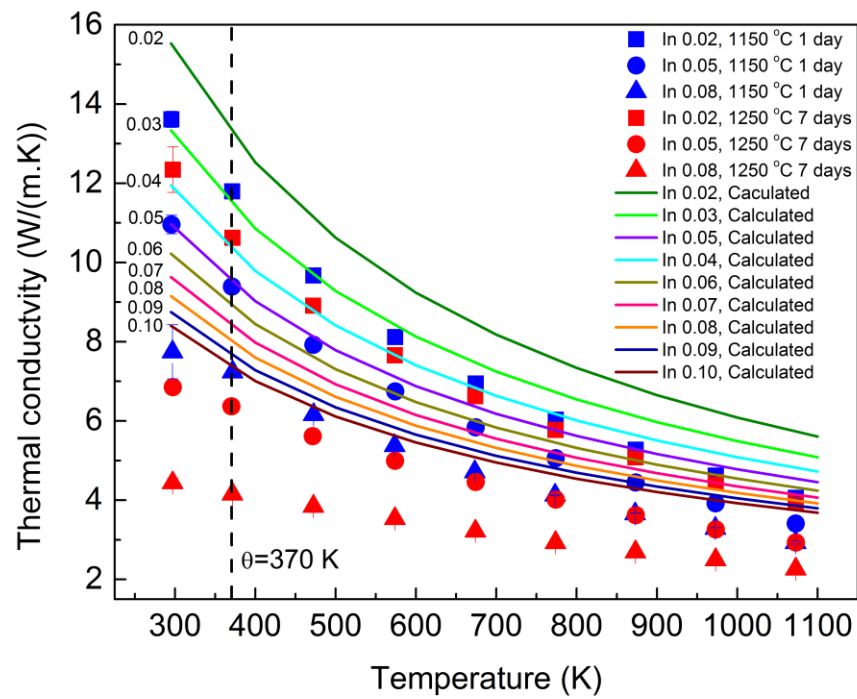


Figure 3.6: Calculations of thermal conductivity of indium doped ZnO based on equation 3.63 or 3.64 for the indium concentration range of 0.02 to 0.10 and in the temperature range of 300 K to 1073 K. Experimental results of two different annealing conditions (scattered symbols) are also shown for comparison. The Debye temperature of ZnO, $\theta = 370$ K, is shown as a dashed line on the figure.

3.6 Materials with Point Defects and Interfaces

When a high density of two-dimensional planar defects forms, for instance, high density of grain boundaries in nanograin structure materials, or superlattice structure, the phonon scattering by these boundaries need to be taken into account. In most cases, phonon scattering by these interfaces or boundaries becomes one of the dominant mechanisms in controlling thermal transport [27, 52, 53, 133-139]. This effect is reflected by adding the boundary scattering term to the combined phonon relaxation time,

$$\tau_c^{-1} = \tau_D^{-1} + \tau_P^{-1} + \tau_B^{-1} = Dx^4 + Ex^2 + \frac{v_s}{L} \quad (3.73)$$

where L is the average distance between boundaries or interfaces and $1/L$ then characterizes the boundary or interface density. The types of boundaries, depending on the typical periodic distance, could be (either synthetic or natural) superlattice interfaces ($L < 50$ nm), lamellar platelet structure or nano-size grain boundaries (50 nm $< L < 500$ nm), or grain / phase boundaries ($L > 500$ nm) in practice.

Introducing the minimum phonon relaxation time τ_{\min} and set the following conditions,

$$\tau(x) = \frac{1}{Dx^4 + Ex^2 + v_s/L}, \quad \text{if } \tau(x) > \tau_{\min}; \quad (3.74)$$

$$\tau(x) = \tau_{\min}, \quad \text{if } \tau(x) < \tau_{\min} \quad (3.75)$$

Accordingly, the original integral breaks into two parts,

$$\kappa = \frac{k_B}{2\pi^2 v_s} \left(\frac{k_B T}{\hbar} \right)^3 \left(\int_0^{x_1} \tau(x) \frac{x^4 e^x}{(e^x - 1)^2} dx + \int_{x_1}^{\theta} \tau_{\min} \frac{x^4 e^x}{(e^x - 1)^2} dx \right) \quad (3.76)$$

where x_1 is set such as

$$\tau(x_1) = \frac{1}{Dx_1^4 + Ex_1^2 + v_s/L} = \tau_{min} \quad (3.77)$$

Solving the above equation and choosing the solution of real values,

$$x_1 = \frac{1}{2} \sqrt{\frac{2DL\tau_{min} \left(\sqrt{E^2L^2\tau_{min}^2 - 4DL\tau_{min}^2v_s + 4DL^2\tau_{min}^2} - EL\tau_{min} \right)}{DL\tau_{min}}} \quad (3.78)$$

Substituting this into the integral in equation 3.76 and integrates, the symbolic analytical form for κ is enormously long and complicated, even not presentable. Nevertheless, numerical calculations and evaluations can still be performed, from which we can look into the physical implications.

Using the indium doped ZnO system as an example, experimental results suggested that the superlattice structure forms when indium concentration reaches around 0.10 that is about the solubility of indium in ZnO lattice. Accordingly, when we consider the material with superlattice interfaces, the indium concentration in ZnO is assumed to be saturated about 0.10, based on which the point defect scattering strength factor Γ was calculated to be 0.132 (SI units) and will be used in the following calculations. Figure 3.7 presents the numerical calculations of equation 3.76 for the thermal conductivity of indium doped ZnO with complete considerations of phonon scatterings by phonons, point defects and superlattice interfaces. The calculations were performed for a range of superlattice interface spacing L from 2.5 nm to 5000 nm. Also shown in the figure is the measured thermal conductivity of indium doped ZnO with indium concentration from 0.10 to 0.22, in which superlattice structure were observed. When the superlattice

interface spacing L is less than 100 nm, the calculated thermal conductivity becomes almost temperature independent. A similar trend is also observed in the measured data shown in the figure, where increasing indium concentration suggests increasing density of interfaces and thereby the decreasing interface spacing.

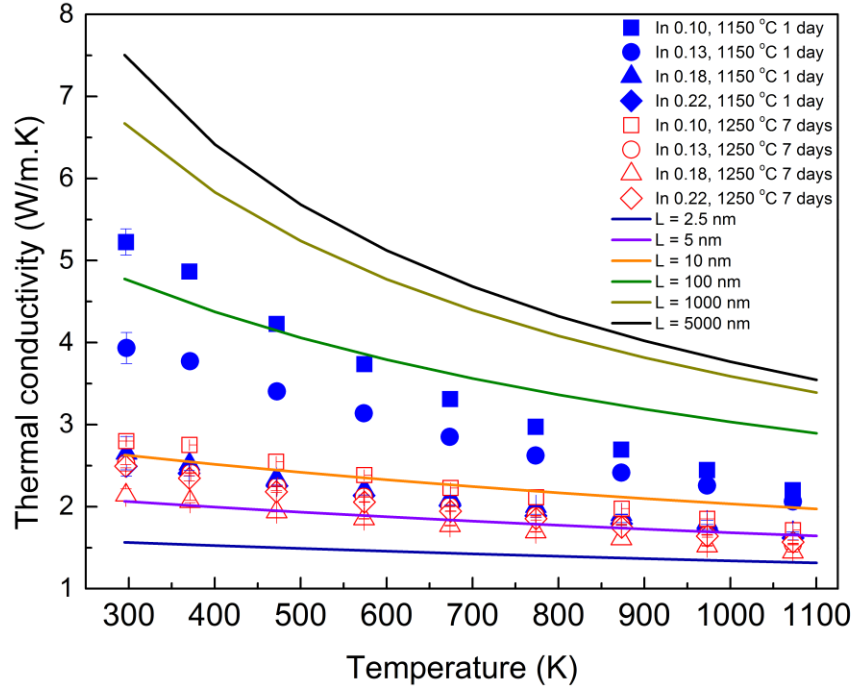


Figure 3.7: Calculated thermal conductivity of indium doped ZnO with different superlattice interface spacing ($L = 2.5 \sim 5000$ nm). Also shown is the measured thermal conductivity of indium doped ZnO with superlattice structure.

The thermal conductivity of indium doped ZnO with a large range of interface spacing, L from 2.5 nm to 500 μm for four different temperatures was calculated according to equation 3.76, and is shown as connected open symbols in Figure 3.8. As seen from the figure, thermal conductivity decreases with decreasing interface spacing, suggesting the important role of interface or boundaries on scattering phonons. The reduction of thermal conductivity at large interface spacing (above 10^3 nm) is less at high temperature than lower ones, implying the relative significance between phonon-phonon

scattering and interface scattering. Nevertheless, a significant drop in thermal conductivity occurs for all these different temperatures when $L < 10^3$ nm, above which thermal conductivity seems to plateau out and becomes less sensitive to interface spacing. This illustrates the effectiveness of nanostructural engineering on reducing thermal conductivity, which has been the basis for success in increasing thermoelectric figure of merit ZT over the past decade [17, 140].

Also shown in the figure are our measured thermal conductivities taken from samples of 0.22 and 0.05 indium doped ZnO after 1250 C 7 days' annealing, representing the interface spacing of 2.5 nm and 3000 nm, respectively. Although with limited experimental data on the interface spacing, the measured results seem to sit well in the scheme of our modeling calculations.

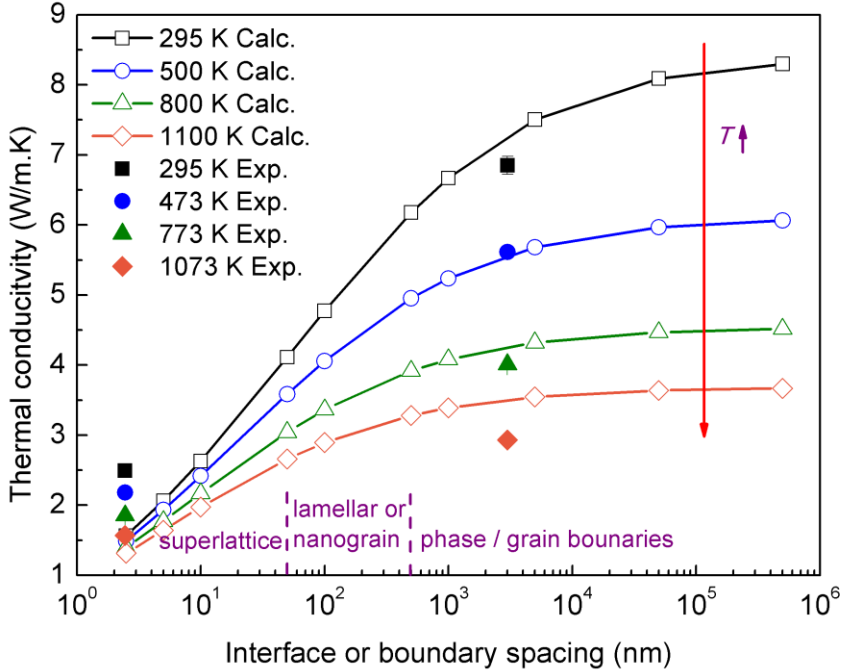


Figure 3.8: Calculated thermal conductivity of indium doped ZnO as a function of interface or boundary spacing at different temperatures, shown as connected open symbols. Also shown are experimental results for comparison.

3.7 Conclusions

In this chapter, the thermal conductivity of pure materials and its dependence on several physical parameters such as temperature and mean atomic mass was introduced and discussed. The physics of defect scattering are also briefly reviewed. The Callaway and von Baeyer's thermal conductivity model was recast by introducing the minimum phonon relaxation time τ_{\min} , followed by the detailed discussions and derivation for pure and perfect materials, point defective materials and material consisting of both point and planar defects. With this work on modifying the classical model, different expressions for thermal conductivity were unified. Comparisons with Callaway and von Baeyer's expressions are made and discussed; the consideration of minimum phonon relaxation

time (essentially the cut off phonon wavelength or frequency) introduces somewhat different temperature dependence plus the temperature independent term which is the high temperature thermal conductivity limit. Numerical calculations and evaluations were also made and found to be in reasonably good agreement with my experimental results of indium doped ZnO. In addition, the present modeling calculations also evidence that defect and nanostructure engineering are effective approaches to reduce the thermal conductivity and is beneficial for thermoelectric properties.

Chapter 4 Thermal (Kapitza) Resistance of Interfaces in Compositional Dependent ZnO-In₂O₃ Superlattices

Compositionally-dependent superlattices, In₂O₃(ZnO)_k, form in the ZnO-rich portion of the ZnO-In₂O₃ phase diagram, decreasing thermal conductivity and altering both the electron conductivity and Seebeck coefficient over a wide range of composition and temperature. With increasing indium concentration, isolated point defects first form in ZnO and then superlattice structures with decreasing interface spacing evolve. By fitting the temperature and indium concentration dependence of the thermal conductivity to the Klemens-Callaway model, incorporating interface scattering and accounting for conductivity anisotropy, the Kapitza resistance due to the superlattice interfaces is found to be $5.0 \pm 0.6 \times 10^{-10} \text{ m}^2\text{K/W}$. This finding suggests that selecting oxides with a compositionally-dependent superlattice structure can be a viable approach, unaffected by grain growth, to maintaining low thermal conductivity at high temperatures.

4.1 Introduction

Synthetic [50, 141-144] and natural superlattices [47, 145, 146] have been reported to exhibit very low thermal conductivities, in some cases close to or even below the minimum thermal conductivity [147]. Compositionally dependent superlattices, sometimes referred to as modular or polysomatic series in the mineralogical literature [148] and homologous series in the crystal chemistry literature [149], offer the opportunity to select the periodicity of phonon scattering interfaces through choice of composition and thereby the overall thermal conductivity. This possibility has been

demonstrated through atomistic simulations of the thermal conductivity of Ruddleston-Popper phases in SrO-SrTiO₃ system [150]. Furthermore, as the superlattice spacing is determined by composition, it is expected to be invariant with temperature and not coarsen. This is in contrast to microstructural approaches, such as decreasing grain size and plastic deformation, to decrease thermal conductivity. Over prolonged times at high temperatures these nanostructures coarsen, and their effect on reducing thermal conductivity and increasing ZT in thermoelectrics is lost.

Homologous series form in many oxides, including several semiconducting oxides such as ZnO, Ga₂O₃ and In₂O₃, at high alloying concentrations [151, 152]. Many of these oxides are of interest as prospective high-temperature thermoelectrics [153] since their electrical conductivity and *ZT* can be modified by aliovalent doping, their thermal conductivity can be modified by altering the superlattice spacing and they are thermodynamically stable to high temperatures. In contrast to synthetic, laboratory-grown superlattices which typically consist of alternating layers of finite thickness and composition, some of these natural superlattices consist of a periodically spaced, single or double atomic layer of one species, such as Sb or In, interleaved within another phase, such as ZnO. Most notable are superlattices in the ZnO-In₂O₃ system [154, 155]. In this system, the structure consists of single crystal wurtzite ZnO with single octahedrally-coordinated InO₂ sheets lying on the basal plane and separated by a spacing that depends on composition. Notionally, all the phases in this homologous series can be represented by the formula In₂O₃.(ZnO)_k where k is an integer [156]. (With trivalent dopants, such as Fe³⁺, Ga³⁺, these ions enter the InO₂ layer extending them into the third dimension in the phase diagram.) Ideally, as represented by the notional formula, the sheets are

periodically spaced, but high resolution microscopy reveals that they can often be irregularly spaced.

In this work, we demonstrate that the thermal (Kapitza) resistance of the InO₂ sheets can be derived from the temperature and indium concentration dependence of the thermal conductivity of the indium-doped ZnO. The values of the Kapitza resistance are found to be intermediate between those interfaces in epitaxial semiconductor superlattices and grain boundaries.

4.2 Experiments

Of particular interest is the ZnO-rich portion of the ZnO-In₂O₃ phase diagram [20]. As low concentrations of indium solute are added to ZnO, which is the usual range studied in the electronic doping of ZnO, the solute ion enters the crystal structure at random [21]. With further increases in solute concentration, individual InO₂ sheets form on the basal plane of ZnO and their spacing decreases until, at x=0.22 (k=7), a distinct, identifiable crystallographic compound Zn₇In₂O₁₀ forms [20]. So, in essence, a two-phase solid-solution region exists between pure ZnO and Zn₇In₂O₁₀ that, according to the phase diagram persists up to 1175oC. (Above this temperature a different superlattice spacing between the InO₂ sheets becomes stable [20]). While there remains some uncertainty as to the precise atomic arrangement in this compound, it is known to be rhombohedral (space group) and the InO₂ sheets are spaced 2.45 nm apart.

The materials studied in this work were bulk, polycrystalline oxides having compositions (Zn_{1-x}In_x)O for indium concentrations, x, over the range. They were

prepared by a two-step molecular mixing and combustion process followed by calcination and densification. Specifically, high purity solutions of zinc and indium nitrates were mixed with a concoction of arylamides and persulfate catalyst to form a combustible gel. After drying, the gel was crushed and then heated in a furnace at 600oC to initiate combustion. The powders were then further calcined at 825 oC for 2 hours to remove residual carbon. This wet chemistry method allows a uniform mixture of different ions to form at the molecular level, with the gel-combustion approach freezing the ratio of different types of ions. In combination these processes give good control of the composition. The powders were then densified into solid pellets 12.7 mm in diameter and 1 ~ 1.5 mm in thickness using a current assisted system at 900 oC for 5 min with an applied load of 125 MPa. Following densification, the samples were annealed in air at 900 oC for 2 hours to compensate the oxygen deficiency and further post-annealed at 1150 oC for 1 day. To avoid preferential evaporation of In and Zn, the pellets were embedded in oxide powders of the same composition during annealing. The pellets made this way were fully dense and exhibited no preferred crystallographic texture.

The thermal conductivity was determined from thermal diffusivity measurements of the pellets made by the laser flash method [22] (Netzsch LFA 457). Measurements were made from room temperature up to 800oC in flowing argon gas using a 1.06 m laser with a (350 μ s) pulse. The heat capacities were calculated from the compositions using the Kopp-Neumann rule based on literature data and the mass density measured using Archimedes method. Samples for TEM were made by standard ion-beam milling and samples for atom probe tomography (APT) were prepared by focused ion beam

milling and shaping from bulk samples. The atom probe tomography was carried out in a Cameca LEAP 4000X HR microscope using 355 nm pulsed laser excitation.

4.3 Results and Discussions

The measured thermal conductivities as a function of temperature are presented in Figure 1 indicating that the thermal conductivity decreases with increasing indium concentration and also become increasingly less temperature dependent. The lines through the data points correspond to the best fitting using the equations developed below. Figure 2 shows the dependence on indium doping concentration with reference to pure ZnO (made using the same process and post-annealed in air at 1150 °C for 24 hours). The figure clearly shows that alloying indium into ZnO significantly reduces its thermal conductivity as is expected as a result of solute additions but the reduction does not plateau out as has been reported for other solid-solution systems, such as Si-Ge alloys [23].

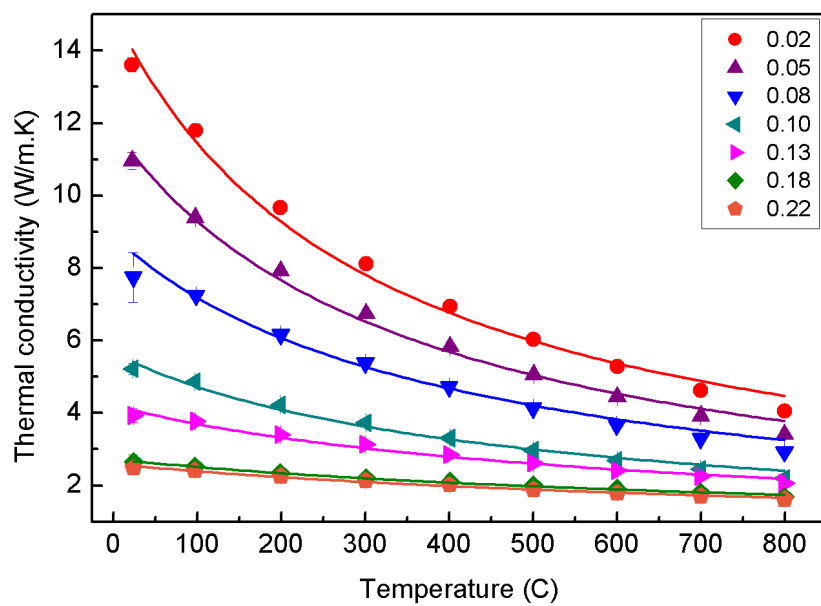


Figure 4.1: Thermal conductivity as a function of temperature for the indium concentrations indicated. The solid lines through the data correspond to the equation 4.3 in the text incorporating both point defect and interface scattering

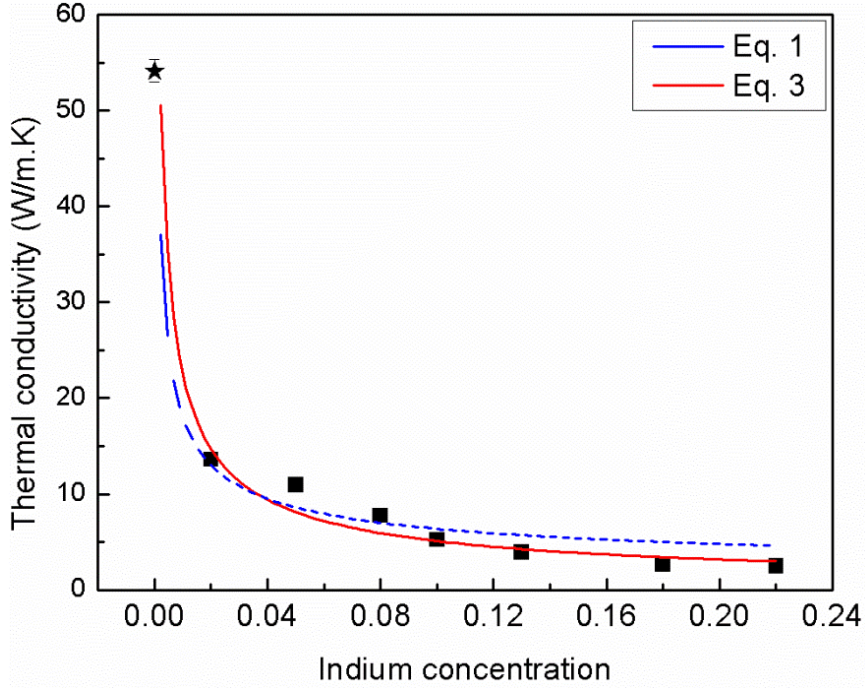


Figure 4.2: Room temperature thermal conductivity as a function of indium concentration. The two curves correspond to the Klemens-Callaway model with (equation 4.3) and without phonon scattering (equation 4.1) from superlattice compositionally-dependent superlattice spacing. The data point represented by * is that of pure, polycrystalline ZnO processed in the same way as the compositions containing indium.

The TEM images illustrate the existence of a superlattice structure, well established in numerous previous publications, for instance [13, 24]. Detailed analysis of the superlattice spacings indicate that their spacing averages to that expected from the composition based on individual InO_2 layers interspersed within the ZnO grains. TEM also indicates that no sheets are detectable at indium concentrations below about a composition of $\text{Zn}_{0.9}\text{In}_{0.1}\text{O}$. This is also the concentration at which the lattice parameter abruptly changes with composition, as shown in Figure 4.3, suggesting the onset of InO_2 sheet formation as distinct from a random solid solution.

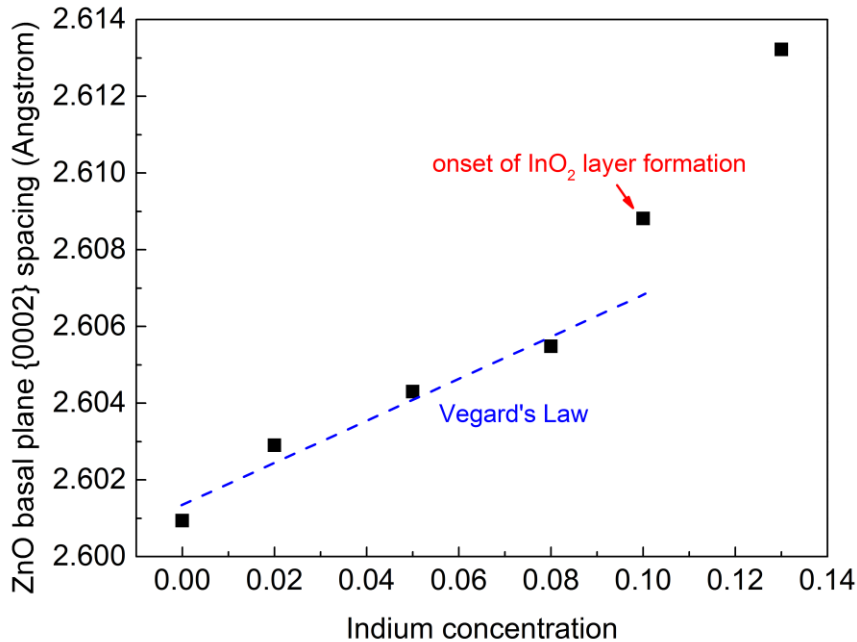


Figure 4.3: ZnO basal plane {0002} spacing measured by X-ray diffraction as a function of indium concentration. Below $x = 0.1$, the lattice parameter varies linearly with indium concentration, as consistent with Vegard's law, suggesting a random solid solution range. An abrupt change at $x = 0.1$ was observed, indicating the onset of InO_2 sheets formation.

In all the samples, the average size of the ZnO grains was 2-3 microns, much larger than that at which grain size usually affects thermal conductivity. The APT images, such as figure 3 (b), clearly reveal two important additional features: the indium ions not only form in sheets, as expected, but they are also randomly distributed within the ZnO blocks indicating a co-existing solid solution. In addition, some Zn ions are also located within the indium layers. Counting the individual Zn and In ions recorded and spatially mapping them, indicates that Zn ions are also substituted within the InO_2 sheets and not restricted to the ZnO blocks. (From these and similar images, we cannot determine whether the indium lie in a single or double sheet because of the difficultly in orienting the 3-D reconstruction to the precision necessary. Nevertheless, even if perfectly aligned, the FWHM of the concentration profiles indicates that the interface is no more than 0.7

nm wide, corresponding to a single InO_2 sheet with In also having some preference for occupying the adjacent planes of cations on either side). Taken together, the microscopies indicate that indium ions enter into the ZnO lattice at random and above about $x = 0.1$, they also form a superlattice consisting of quasi-equally spaced InO_2 sheets.

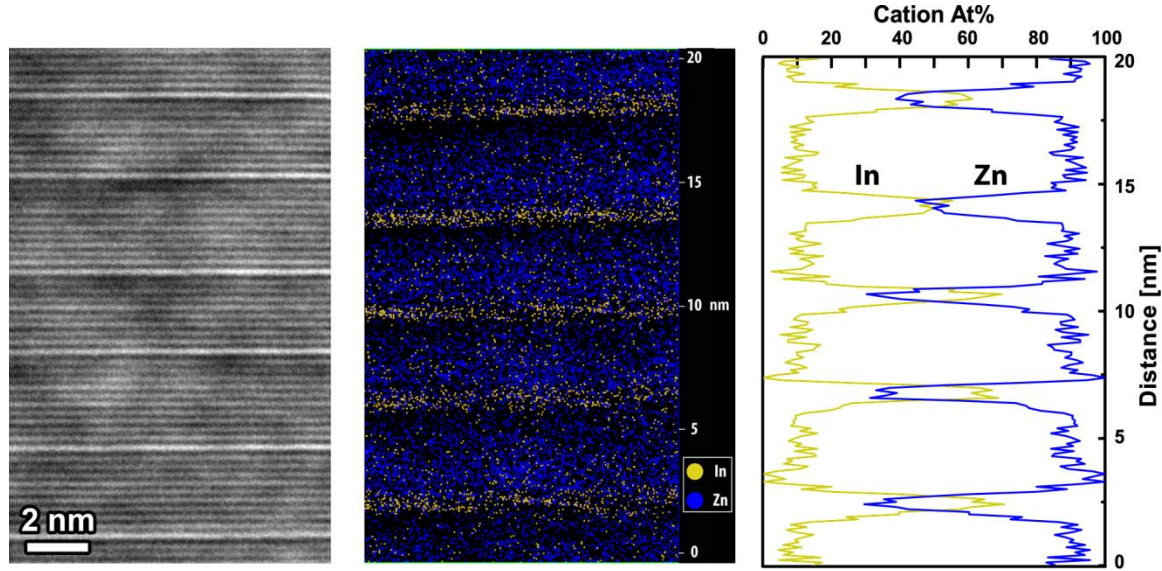


Figure 4.4: TEM and atom probe tomography (APT) images of ZnO containing 10 at. % indium ($\text{Zn}_{0.9}\text{In}_{0.1}\text{O}$). The TEM image indicates the presence of an almost periodic superlattice. The APT image (middle) reveals the existence of indium ions in solid solution in the ZnO blocks as well as the indium ions forming irregular InO_2 sheets. The yellow and blue dots representing indium and zinc ions, respectively (For clarity, the oxygen ions are not shown. Also the magnification is not the same as the TEM image). The compositional profile (right), obtained from the APT image perpendicular to the superlattice, quantifies the solubility of the indium ions in the ZnO blocks and the zinc ions in the InO_2 sheets.

In analyzing the thermal conductivity data, we find that for indium concentrations below about $x = 0.1$, the data are fully consistent with the Klemens-Callaway model [114] for thermal conductivity of crystals containing defects, incorporating a high-temperature limit, κ_{\min} . The high temperature limit corresponds to where the phonon wavelengths are equal to the interatomic spacing [49, 115]. At high temperature ($T > \theta$) and assuming a

Debye spectrum, (the electronic contribution is negligible and ignored in the present study), this relation is given by:

$$\kappa_i = \kappa_{min} + \frac{k_B \sqrt{v_s}}{\sqrt{\pi^3}} \frac{1}{\sqrt{\Omega_0 C \Gamma}} \frac{1}{\sqrt{T}} \tan^{-1} \left(\frac{k_B \theta}{\hbar} \left(\frac{\Omega_0 \Gamma}{4\pi v_s^3 C T} \right)^{\frac{1}{2}} \right) \quad (4.1)$$

where k_B is Boltzmann's constant, v_s the sound velocity of ZnO (4008 m/s [157]), Ω_0 the unit cell volume (4.762×10^{-29} m 3), θ the Debye temperature (370 K for ZnO [157]) and the constant C is the inverse time coefficient for phonon-phonon scattering processes in pure, un-doped ZnO [114]. Γ is the phonon scattering strength of point defects formed by indium solid solution alloying and depends on the mass variance due to doping at each atomic site. It is well established from computational and crystal chemical studies [158] that as indium ions are added to ZnO, they substitute onto the cation sites and are accompanied by the formation of cation vacancies (one for every two indium ions) to maintain charge neutrality. Consequently, the only defects that can cause phonon scattering are mass disorders associated with indium atoms and associated cation vacancies. The phonon scattering factor is then given by the sum of the mass variance [159] on the Zn site due to the presence of indium and vacancies on that site:

$$\Gamma = x \frac{(M_{In} - \overline{M_{ZnO}})^2}{2(\overline{M_{ZnO}})^2} + \frac{x}{2} \frac{(\overline{M_{Zn}})^2}{(\overline{M_{ZnO}})^2} \quad (4.2)$$

Where $\overline{M_{ZnO}}$ is the mean mass of the In-doped ZnO formula unit. To first order in indium concentration, x , and up to $x = 0.22$, Γ is given by: $\Gamma \cong 1.38x$. The constant, C , found by fitting the temperature dependence of pure, polycrystalline ZnO from 300 K to 1273 K, was found to have a value of 1.3×10^{-18} (R-square value of 0.99).

For indium concentrations greater than about $x = 0.1$, the fit of the Klemens-Callaway model to the data becomes progressively poorer as the indium concentration is increased. As this is the compositional range over which microscopy reveals that distinct superlattice interfaces form, we conclude that the InO_2 sheets also scatter phonons and further reduce the thermal conductivity. The superlattice sheets can be expected to introduce a thermal conductivity anisotropy so that the conductivity perpendicular to the sheets, κ_z , is different than the conductivity, $\kappa_x = \kappa_y$, parallel to them. (This latter in-plane conductivity, κ_x , is the same as the intrinsic conductivity, κ_i , introduced above to describe due to solute scattering). Assuming the contribution to thermal conductivity perpendicular to the sheets is as a thermal resistance in series with the In-doped ZnO blocks given by equation 4.1, the additional thermal resistance can be expressed as a Kapitza resistance, R_k :

$$\frac{1}{\kappa_z} = \frac{1}{\kappa_i} + \frac{R_k}{d_{SL}} = \frac{1}{\kappa_i} + \frac{R_k}{(k+1)d_{\{0002\}}} \quad (4.3)$$

where d_{SL} is the average interface spacing which, in turn, depends on the indium concentration according to the relationship:

$$d_{SL} \approx (k+1) \times d_{\{0002\}} \quad (4.4)$$

where $d_{\{0002\}}$ is the ZnO basal plane spacing (0.260 nm). (This macroscopic model [133, 160] is used rather than the microscopic phonon model incorporating interfaces since otherwise there are so many fitting parameters that there are multiple combinations of parameters that will fit the data). As discussed by Mityushov *et al.* [161], and more recently elaborated upon in Yang *et al.* [162], the effect of crystallographic thermal

anisotropy in polycrystalline materials containing randomly oriented, superlattice grains can be represented in terms of the conductivity anisotropy, $r = k_z/k_x$, by the :

$$\frac{\kappa^*}{\kappa_x} = \frac{r+3}{3} - \frac{2(r-1)^2}{9(r+2)} \quad (4.5)$$

where κ^* is the measured conductivity of the bulk, polycrystalline material as a function of indium concentration. When the Kapitza resistance of the superlattice interfaces is included to introduce a compositionally-dependent conductivity anisotropy, given by equations 3-5, the calculated thermal conductivity fits both the temperature and composition dependence extremely well as shown in Figures 4.1 and 4.2.

The value of the Kapitza resistance derived from fitting the equations 1-5 to the experimental data, $5.0 \pm 0.6 \times 10^{-10} \text{ m}^2\text{K/W}$ is comparable to those of epitaxial semiconductor interfaces (Table 4.1), and is also substantially smaller than grain boundaries in SrTiO₃ [163] and in yttria-stabilized zirconia [164] (both above their respective Debye temperatures), as well as interfaces in metallic nanolaminates. The temperature independence of the Kapitza resistance is consistent with the values reported for grain boundaries above room temperatures. [27, 139]. While no physical model adequately predicts the value of the Kapitza resistance for a single atomic layer interface, it is reasonable that our measured value is comparable to an epitaxial interface since the lattice is continuous across the superlattice interface apart from a possible lattice inversion when the sheet corresponds to an inversion layer boundary. Furthermore, the thermal conductivity model incorporating the interface scattering adequately represents that of the single phase, end member, Zn₇In₂O₁₀, ($x = 0.22$) as well as across the entire solid solution range, suggesting that the thermal conductivity can be well described by

the series conductances of the superlattice interfaces together with solid solution point-defect scattering.

Table 4.1: Examples of interfacial thermal resistances

Material	Interface Type	$R_k,$ $(10^{-10} \text{ m}^2\text{K/W})$	Temperature Range, K	Reference
ZnO-In ₂ O ₃	Superlattice (SL)	5.0	RT to 1073	This work
Si/Ge	Epitaxial SL	4.0	200	Lee [50]
AlN/GaN	Epitaxial SL	5 - 16	RT	Koh et al [143]
W/alumina	Nanolaminate	31.3	RT	Costescu et al [147]
Ni/Ti	Nanolaminate	19	RT	Clemens et al [142]
Ni/Zr	Nanolaminate	23	RT	Clemens et al
Si	Grain Boundaries	13	80-400 K	Cahill [165]
SrTiO ₃	Grain Boundaries	49.8- 34.1	300 - 1000	Wang et al [163]
YSZ	Grain Boundaries	45	373 - 1273	Limarga et al [164]

4.4 Conclusions

In conclusion, we observe that with increasing doping concentration, the microstructure of indium-doped ZnO evolves from isolated point defects to a combination of point defects and superlattice structures with decreasing interface spacing. It is also found that indium ions are present in solid solution in the ZnO blocks even when superlattice structure forms. Using this information, the thermal conductivity is fully described as a function of temperature (above room temperature) and concentration by the Klemens-Callaway model incorporating a Kapitza resistance of $5.0 \pm 0.6 \times 10^{-10} \text{ m}^2\text{K/W}$ for the scattering from the individual superlattice interfaces. This suggests that homologous series of compounds may be attractive, coarsening-resistant candidates in the search for high-temperature thermoelectrics.

Chapter 5 Relation between Thermoelectric Properties and Phase Equilibria in the ZnO-In₂O₃ Binary System

The electrical conductivities, Seebeck coefficients and thermal conductivities across the ZnO-In₂O₃ binary system are reported and related to the phase compositions and microstructures present at 1150 and 1250 °C. The ZnO-In₂O₃ binary system is of particular interest as it contains a variety of different types of phases, superlattice (modular) phases, solid solutions, two-phase regions and crystallographic features. Throughout much of the phase diagram, the thermal conductivities are less than 2 W/mK being limited by both solid solution disorder and thermal resistance due to the presence of InO/ZnO interfaces. Across the phase diagram, irrespective of the actual phases, the materials behave at high temperatures (800°C) as free-electron conductors with the Seebeck coefficient and electron conductivity satisfying the Jonker's relationship. In the two-phase regions of the phase diagram, the values of the power factor and figure of merit (ZT) are consistent with a simple law of mixtures, weighted according to the volume fractions of the two phases. Although the largest values of electrical conductivity and Seebeck coefficient occur over a range of composition centered at 40 m/o InO_{1.5}, the maximum ZT and power factors are observed at k = 4 (33 m/o InO_{1.5}). In contrast to the other modular phases at 1250 °C and below, this phase is hexagonal rather than rhombohedral.

5.1 Introduction

Studies of the thermoelectric properties of materials are usually restricted to a single composition or compound of interest and report on the effect of variables, such as doping concentration [62, 64, 65, 68, 69, 81, 82, 166], processing or grain size [167]. While such studies are essential once a promising material has been identified and provide invaluable information, they do not include the effect of compositional changes with the exception of simple solid solutions, for instance silicon-germanium [168]. In contrast, in this work we investigate the thermoelectric properties over the full compositional range of the ZnO-In₂O₃ binary system in order to explore systematic variations with composition. This oxide material system is of interest as the basis for high-temperature thermoelectrics [31, 34, 35, 40, 58] and because it exhibits a range of possible phases and microstructures [92]. These range from the pure compounds, simple solid solutions, two-phase regions, modular or natural superlattice (SL) compounds [148], as well as solid solution phases containing planar interfaces. This unusual variety provides an opportunity to quantify the effects of point defect scattering, interface scattering as well as phase content on the thermal and electrical conductivity all within the same system. Investigation of the two-phase compositions also enables us to compare with the mean-field predictions of the thermoelectric properties of two-phase, polycrystalline materials.

The thermal-to-electrical efficiency of thermoelectrics, η , is usually given in terms of a non-dimensional figure of merit, ZT :

$$\eta = \frac{T_H - T_C}{T_H} \left(\frac{(1 + ZT)^{\frac{1}{2}} - 1}{(1 + ZT)^{\frac{1}{2}} + T_C/T_H} \right) \quad (5.1)$$

where T_H and T_C are temperatures at hot and cold sides, respectively. The thermoelectric figure of merit ZT can be expressed in terms of the thermal conductivity, κ , Seebeck coefficient S and electronic conductivity σ by the relationship:

$$ZT = \frac{S^2\sigma}{\kappa} T \quad (5.2)$$

where the numerator term $S^2\sigma$ is defined as the thermoelectric power factor (*PF*). The difficulty in identifying promising thermoelectric materials is that these properties are not independent of one another. Furthermore, as illustrated by the graphs in the review by Snyder *et al.* [6], variations in them are sometimes contra-indicated. However, since the thermal conductivity is in the denominator it is often used as an initial screening parameter. It is also the easiest to estimate from existing models. For these reasons, there has been considerable attention given to microstructural modification, such as reduction in grain size, in order to decrease thermal conductivity of thermoelectric materials. In this work, we will quantify the effect of each of the parameters in equation 5.2. The majority of the results presented will be those measured at 800°C since these materials are primarily of interest as thermoelectrics at high temperatures in oxidizing atmospheres.

5.2 The ZnO-In₂O₃ Binary System

To provide a guide to the phases and compositions studied, the principal features of the ZnO-In₂O₃ binary in air are briefly reviewed using the phase diagram in Figure 5.1,

reproduced from the work of Moriga *et al.* [92]. The main features of interest are shaded and labeled. In addition to the two terminal compositions, ZnO and InO_{1.5}, there are a series of single phase, line compounds whose compositions are given by the formula In₂O₃(ZnO)_k where k is an integer. These compounds, sometimes referred to as modular compounds, or superlattice compounds, consist of a homologous series of alternating ZnO and In₂O₃ blocks, stacked along the *c*-axis direction of the ZnO wurtzite crystal structure, where k is the number of ZnO layers between each InO₂ layer. There remains some uncertainty about the detailed atomic arrangement of these compounds but all of them can be considered to consist of superlattices of individual InO₂ layers periodically interspersed within ZnO. Starting at the ZnO end of the phase diagram, the microstructure consists of a single phase solid solution of randomly distributed In³⁺ ions up until about 10 m/o and 5 m/o InO_{1.5} at 1150 °C and 1250 °C, respectively. With increasing indium concentration, pseudo-randomly distributed InO₂ layers form within ZnO grains. These InO₂ layers are crystallographically also inversion domain boundaries (IDBs) on account of the symmetry inversion that occurs across them. (Similar inversion domain boundaries have been reported in Sb-doped ZnO [83] and in ZnO-based varistors [89]).

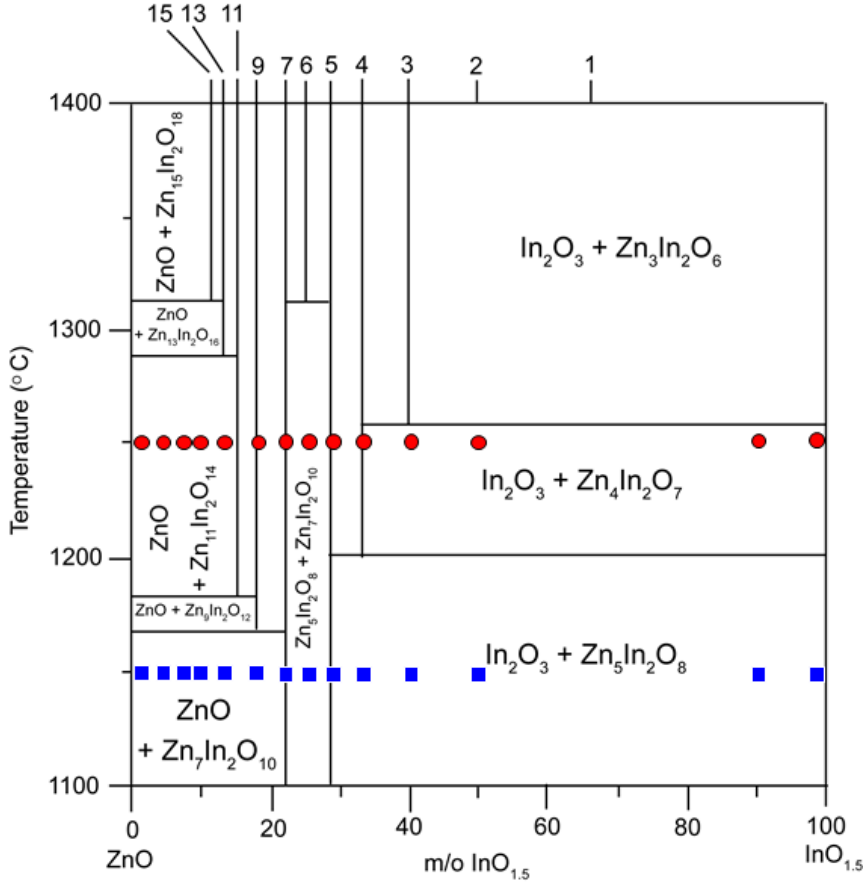


Figure 5.1: The compositions of the materials studied superimposed on the ZnO-In₂O₃ binary phase diagram [92]. Two sets of materials were annealed at 1150 °C for one day (circles) and at 1250 °C for seven days (squares). Phase regions of interests include In₂O₃ –rich two-phase regions, two-phase regime of In₂O₃(ZnO)₅ and In₂O₃(ZnO)₇ modular compounds, and the ZnO solid solution phase with individual InO₂ interfaces. In this and subsequent diagrams, the superlattice repeat value, *k*, is indicated along the top axis for phases stable below 1300 °C.

Starting with pure ZnO, the first single-phase modular compound forms at *k* = 7 (22 m/o InO_{1.5}) at 1150°C and *k* = 9 at 1250°C and then there are a series of modular compositions each distinguished by a discrete *k* value. The compounds are rhombohedral when the *k* values are odd. The phase diagram indicates that different compounds are stable over different ranges of temperature and that the higher the temperature the greater the number of equilibrium modular compounds. In between the line compounds, there are, notionally at least, two phase coexistence regions consisting of a mixture of two modular

compounds. At the In_2O_3 -rich portion of the diagram the two phase regions consist of a mixture of In_2O_3 and a modular compound whose composition depends on the temperature.

In this work we report on the properties of materials heat treated in air at either 1150 °C for 1 day or 1250 °C for 7 days; the compositions of samples synthesized and investigated are indicated on Figure 5.1. Based on our preliminary measurements, these two temperatures are sufficient to create stable microstructures. Annealing at higher temperature is possible but the increased volatility of both *Zn* and *In* makes it more difficult to ensure compositional homogeneity within samples.

5.3 Experimental Details

A series of compositions across the ZnO - In_2O_3 binary phase diagram were prepared from high purity nitrate powders, $\text{Zn}(\text{NO}_3)_2$ (99.999%, Sigma Aldrich®, USA) and $\text{In}(\text{NO}_3)_3$ (99.999%, Sigma Aldrich®, USA), dissolved in deionized and distilled water. Specific compositions were made by mixing appropriate nitrate solutions and heating them at 80 °C. Several organic fuels (acrylamide, N,N'-Methylene-bisacrylamide, 2,2'-Azobisisobutyro-nitrile and ammonium persulfate) were then mixed in converting the solutions into gels. They were then dried in the low temperature drying oven at 120 °C for 12 hours before grinding into fine particles and combusted by heating at 600 °C. The remaining mixture of oxide and carbon powders was then calcined at 825 °C for 2 hours to remove the residual carbon and other organic chemicals. The powders are then sintered into solid pellets 12.7 mm in diameter and 1 ~ 1.5 mm in thickness using

current assisted densification processing system (also known as spark plasma sintering) at 900 °C for 5 min at a constant pressure of 125 MPa. After the densification, the samples were annealed in air at 900 °C for 2 hours to restore the oxygen stoichiometry. The samples were then annealed at either 1150 °C for 1 day or 1250 °C for 7 days in order to achieve different phase equilibria and microstructures. To avoid evaporation of ZnO and In₂O₃, each of the sample pellets was embedded in oxide powders of the same compositions in a covered crucible. To serve as a reference, pellets of pure ZnO were made in the same way and annealed at 1150 °C for 1 day to fully oxidize the material.

X-ray diffraction analysis was performed with a Philips® PANalytical Multipurpose Diffractometer and the phases identified using PANalytical X’Pert HighScore Plus software connected to the 2011 ICDD PDF database [111]. To investigate the grain size and microstructure, the cross-sections of selected samples were ground and polished down to 1 µm, and were then thermally etched at 1050 °C for 30 min. Scanning electron microscopy imaging and elemental mapping were performed on Zeiss® Super VP55 FEG-SEM with an energy dispersive X-ray spectrometer (EDS). High resolution transmission electron microscopy (HRTEM) imaging and diffraction analysis were also made on selected samples to observe the detailed structures. Specimens for TEM observations were first thinned by polishing both sides until the thickness was reduced down to about 60 – 80 µm, and then thinned to electron transparency by ion-beam milling using a Fischione® 1010 Dual Beam Ion-Mill. After plasma cleaning in a Fischione® 110 Plasma Cleaner the samples were examined using a JEOL 2100 TEM and JEOL 2010 FEG-TEM.

The thermal conductivity (κ) was determined from the thermal diffusivity using the standard relationship:

$$\kappa = \alpha \cdot \rho \cdot C_p \quad (5.3)$$

The diffusivity (α) was measured from room temperature to 800 °C in flowing argon gas using the laser flash method (NETZCH Micro Flash® LFA 457) equipped with a 1.06 μm laser with a (350 μs) pulse. The heat capacities for each composition, C_p , were calculated using the Kopp-Neumann rule from literature data [112] and the mass density ρ measured using Archimedes method. The electrical conductivity and Seebeck coefficient were measured in air from room temperature to 800 °C on polycrystalline bars of dimensions $2 \times 2 \times 8$ mm using a ULVAC RIKO® ZEM 3 M10 unit.

5.4 Observations and Results

In this section, the electrical and thermal transport properties across the ZnO-In₂O₃ binary system are presented and related to the phase content and microstructures in the principal regions in the equilibrium phase diagram. The data are summarized in Figure 5.2 to Figure 5.5 for samples annealed at either 1150 °C for 1 day or 1250 °C for 7 days. Figure 5.2 and Figure 5.3 show the thermal conductivity against indium concentration measured at room temperature and 800 °C, respectively. Perhaps the most striking feature of the data is that the thermal conductivity is relatively independent of indium concentration above about 10 m/o InO_{1.5}. Figure 5.4 and Figure 5.5 report the electrical conductivity and Seebeck coefficient as a function of indium concentration measured at 800 °C, respectively. As can be seen from Figure 5.5, the Seebeck

coefficient is negative across the phase diagram indicating that all the compounds are *n*-type semiconductors.

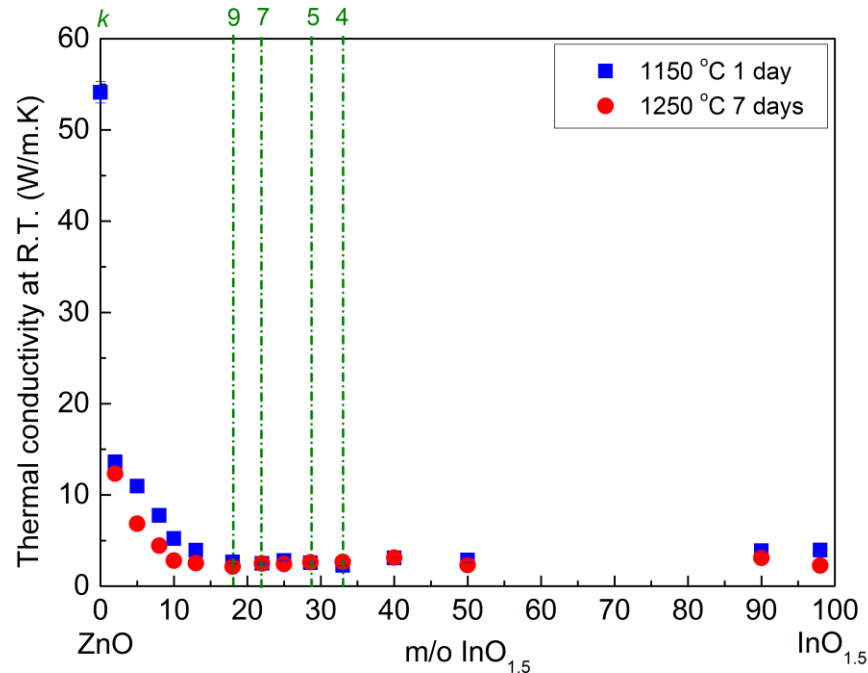


Figure 5.2: Room temperature thermal conductivity as a function of indium concentration for samples heat treated at either 1150 °C for 1 day (blue squares) or 1250 °C 7 days (red filled circles). In this and succeeding figures the compositions of the modular superlattice compounds $k = 4, 5, 7, 9$ stable below 1300 °C are indicated by the vertical dashed lines.

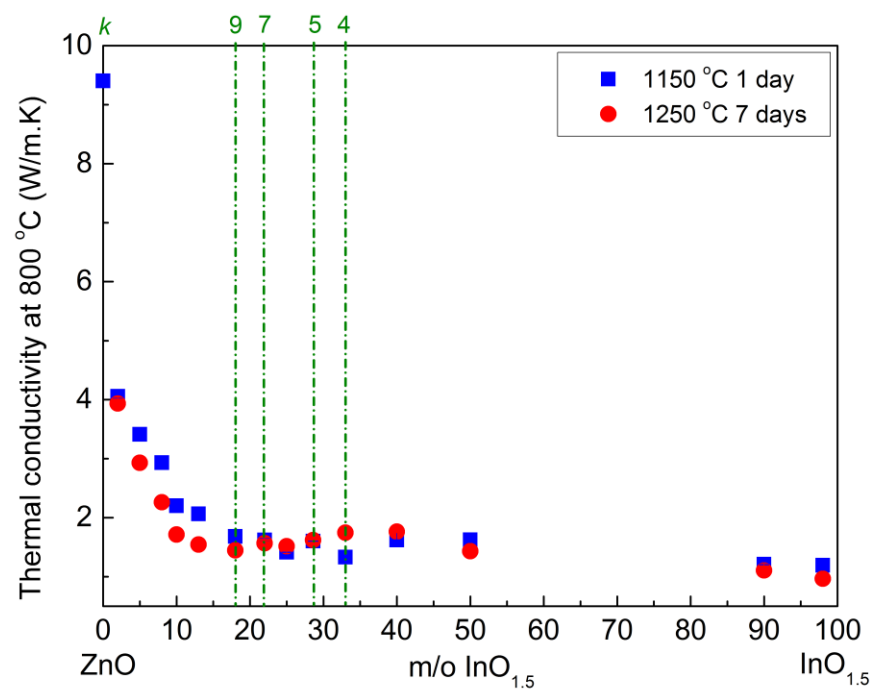


Figure 5.3: Thermal conductivity at 800 °C, for two sets of thermal treatments, 1150 °C 1 day (blue squares) and 1250 °C 7 days (red circles), respectively.

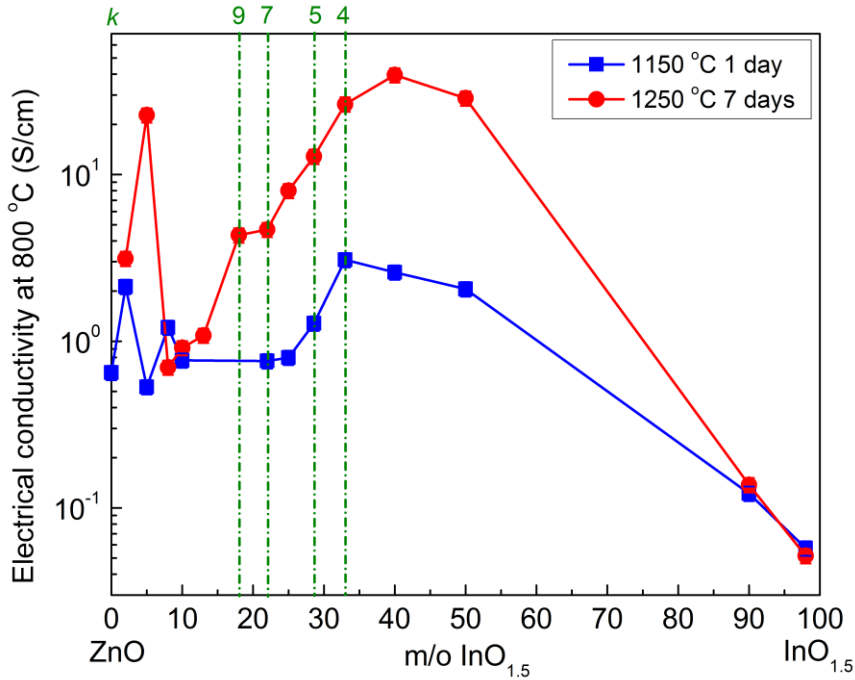


Figure 5.4: Electrical conductivity of $\text{ZnO}-\text{In}_2\text{O}_3$ oxide system as a function of indium concentration. Data presented are measurements made at $800\text{ }^\circ\text{C}$. The lines through the data points are guides to the eye.

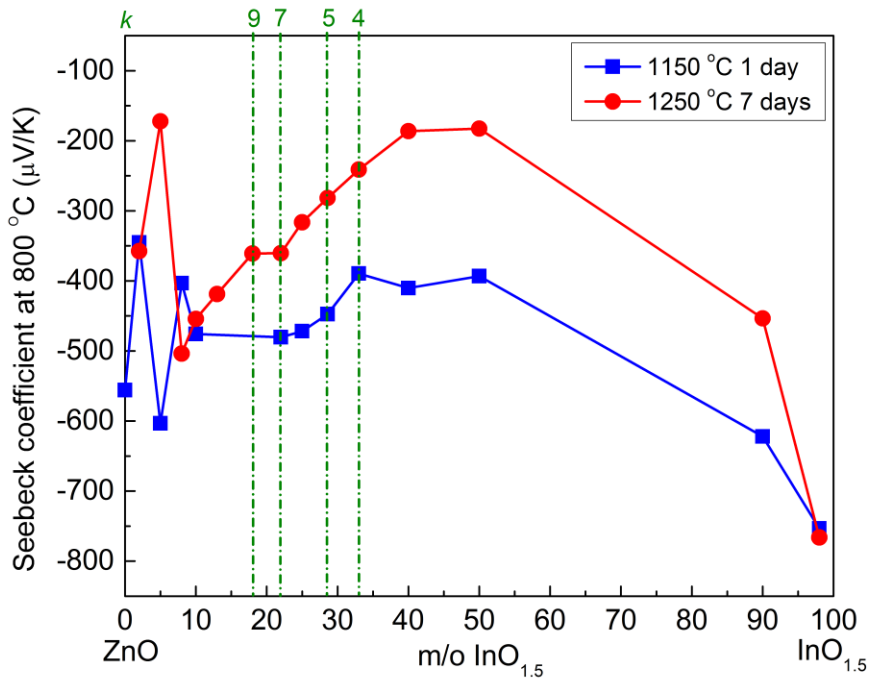


Figure 5.5: Seebeck coefficient at $800\text{ }^\circ\text{C}$ as a function of indium concentration.

5.4.1 ZnO Solid Solution Compositions

For the indium concentrations up to 8 or 10 m/o InO_{1.5} (at 1150 °C), the phase diagram indicates that the material is a solid solution consisting of indium ions dissolved in ZnO. Our microscopy is consistent with this expectation and the microstructure is featureless with a grain size of a few hundred nm. Over this solid solution region, the thermal conductivity rapidly decreases with increasing indium concentration from a room temperature value of 54 W/mK for the fully-densified pure material to less than 5 W/mK. The electrical conductivity and Seebeck coefficient also increase with increasing indium concentration in this compositional range after annealing at 1150 °C for 1 day. The increase in electrical conductivity with doping is consistent with the effect of other aliovalent dopants, such as Al³⁺ and Ga³⁺ in ZnO [62, 64-66, 87, 97]. The one notable exception is the unusually high conductivity of the 5 m/o InO_{1.5} annealed for 7 days at 1250°C, a very reproducible finding.

5.4.2 ZnO Solid Solution Containing Planar Crystallographic Interfaces

For indium concentrations above ~ 10 m/o InO_{1.5} annealed at 1150 °C and above about 5 m/o InO_{1.5} annealed at 1250°C, the solid solubility is exceeded and planar interfaces form on the basal plane of the ZnO grains. As remarked earlier these are believed to consist of individual InO₂ planes. An example is shown in Figure 5.6 (a) of the 10 m/o InO_{1.5} material after 1 day at 1150 °C. The superlattice structures are clearly seen but the interface spacing is apparently not constant. This is a common feature of these and other polytype homologous compounds as has been reported previously [169-173] and is attributed to the weak interaction between the InO₂ planes and slow kinetics required for long-range diffusion.

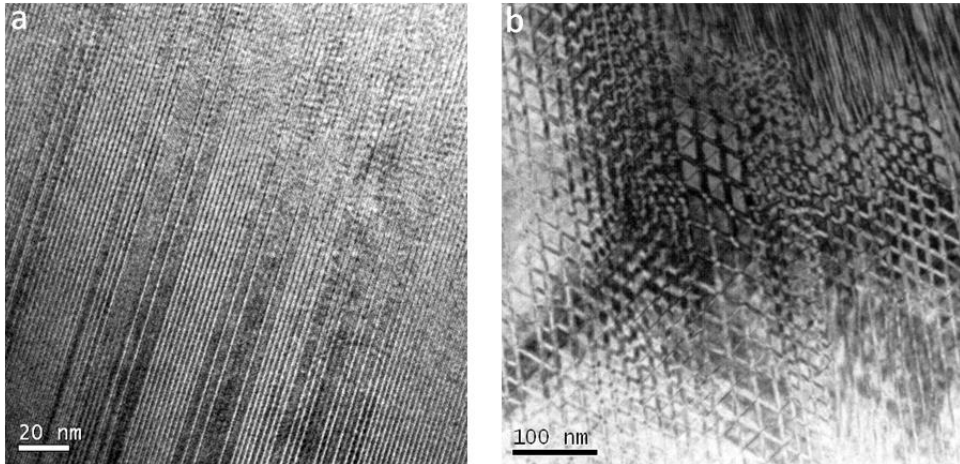


Figure 5.6: TEM micrographs of 10 m/o $\text{InO}_{1.5}$, after the post-annealing for (a) 1150 °C for 1 day and (b) 1250 °C for 7 days (b). The latter has a “chessboard” type pattern consisting two sets of superlattice structures of InO_2 sheets.

With further increasing indium concentration (from 10 up to 22 m/o $\text{InO}_{1.5}$), modular compounds become stable and appear in the solid solution phase of the phase diagram as planar interfaces associated with inversion domain boundaries. After higher temperature annealing (1250 °C for 7 days), however, the structure of each grain evolves into a “chessboard pattern” that essentially consists of two sets of intersecting interfaces within the same grain, as shown in Figure 5.6 (b).

The thermal conductivity of the solid solution phases containing InO_2 planes decrease with increasing indium concentration, at both room temperature (Figure 5.2) and 800 °C (Figure 5.3). However, the thermal conductivity becomes almost constant with indium concentration above about 18 m/o $\text{InO}_{1.5}$. Furthermore, it is also found that thermal conductivity becomes much less temperature-dependent as compared to the simple solid solution microstructure; the conductivity over the full temperature range (R.T. to 800 °C) has been published elsewhere [174]. Electrical conductivity in this phase region demonstrates slightly different dependence on indium concentration for two series

of thermally treated samples, as shown in Figure 5.4. The electrical conductivity of 1150 °C series sample is relatively constant with indium concentration whereas that of 1250 °C series sample increases with indium addition. The dependence of the Seebeck coefficient on the indium concentration has an opposite trend to that of electrical conductivity, as shown in Figure 5.5.

5.4.3 The Modular Compounds

The modular phases formed were as expected from the phase diagram. At 1150°C the single-phase modular compound formed at $k = 7$ and at 1250°C the stable modular compound formed at a smaller indium concentration, $k = 9$. High resolution microscopy indicated a well-ordered superlattice structure as shown in Figure 5.7 for the $k=7$ (22 m/o $\text{InO}_{1.5}$). Selected area diffraction patterns (presented in the inset) exhibited sharp, regular superlattice spots again indicative of a well-ordered structure. Together with XRD (not shown), this indicates that the $k = 7$ and $k = 9$ are largely single-phase compounds. In contrast, the modular compounds $k = 5$ and $k = 4$ consisted of mixed modular compounds.

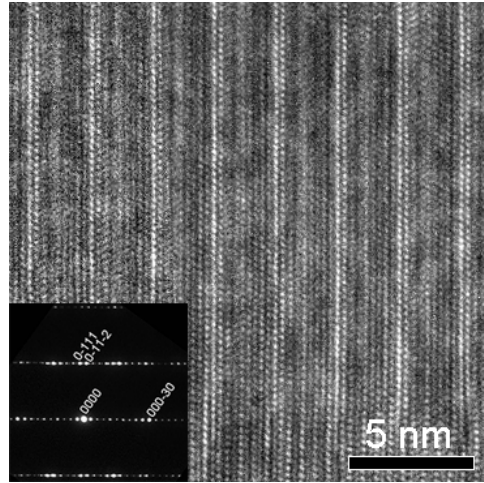


Figure 5.7: HRTEM image of 22 m/o $\text{InO}_{1.5}$ after the post-annealing of $1150\text{ }^\circ\text{C}$ for 1 day, showing the almost constant superlattice spacing; the inset is the selected area diffraction pattern taken with zone axis $<10\bar{1}0>$ where superlattice reflection spots are clearly captured. Both HRTEM image and indexing of diffraction pattern confirm the observed structure as $\text{In}_2\text{O}_3(\text{ZnO})_k$ phase.

5.4.4 Indium-rich Two-phase Regions

Consistent with the indium-rich end of the phase diagram, two different two-phase regions were found over the temperature range considered: (1) an In_2O_3 two-phase region and (2) the two superlattice compound mixture regions ($k = 5$ and 7). The 50 m/o $\text{InO}_{1.5}$ material annealed at $1250\text{ }^\circ\text{C}$ was identified by XRD as a two-phase mixture consisting of In_2O_3 and the $\text{In}_2\text{O}_3(\text{ZnO})_4$ compound. It has a typical microstructure consisting of two discrete phases as shown in Figure 5.8 (a). Elemental mapping reveals, as expected, indium-rich grains and a second, indium-poor phase, Figure 5.8 (b). The indium-poor phase is $\text{In}_2\text{O}_3(\text{ZnO})_4$ (the $k = 4$ phase). The proportion of the two phases is consistent with the Lever rule on the phase diagram at $1250\text{ }^\circ\text{C}$.

In the In_2O_3 -rich two-phase regions, the thermal conductivities were in the range of $2 \sim 3 \text{ W/m.K}$ at room temperature and were relatively constant with increasing indium concentration. Electrical conductivity increases monotonically with the fraction of second phase ($\text{In}_2\text{O}_3(\text{ZnO})_4$ or $\text{In}_2\text{O}_3(\text{ZnO})_5$) while, again, the Seebeck coefficient has the opposite dependence. High temperature annealing was found to significantly increase the electrical conductivity. In the region consisting of a mixture of two modular compounds, $k = 5$ and 7 , i.e. $0.25 \leq \text{In}O_{1.5} \leq 0.33$, the thermal conductivity also remained almost constant as shown in Figure 5.2 and Figure 5.3. Electrical conductivity in this region increased with indium concentration or the fraction of $\text{In}_2\text{O}_3(\text{ZnO})_5$ compound, as seen in Figure 5.4. In addition, the electrical conductivity of the 1250°C series samples was about one order of magnitude larger than those annealed at 1150°C .

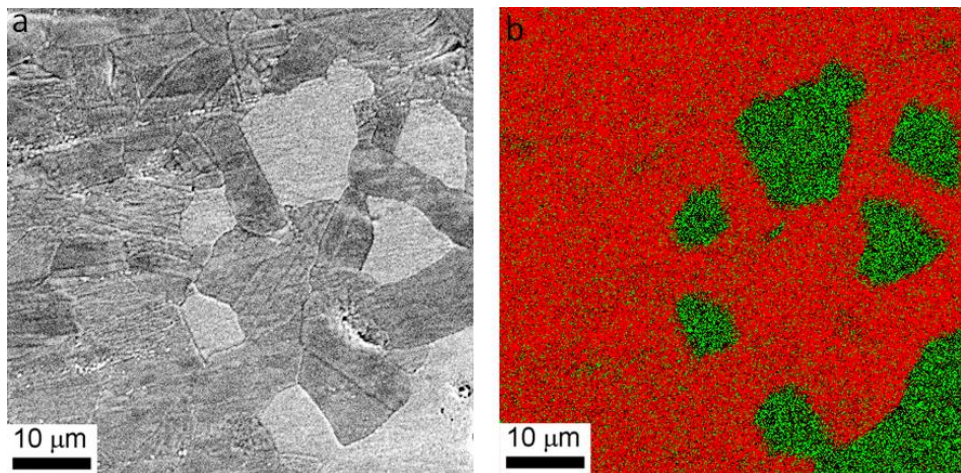


Figure 5.8: SEM image and elemental mapping of the cross-section microstructure of the 50 m/o $\text{InO}_{1.5}$ after 1250°C 7 days annealing: (a) SEM micrograph revealing the grain microstructure, (b) The corresponding EDS mapping showing the distribution of zinc (red) and indium (green).

5.5 Discussions

The data presented indicates that although the electrical conductivity and Seebeck coefficient exhibit large variations with indium concentration across the binary compositional range, the thermal conductivity is relatively independent once there is sufficient indium to form InO_2 sheets. To understand these contrasting behaviors we first discuss the variation in thermal conductivity in terms of the microstructures characteristic of the different phases in the $\text{ZnO}-\text{In}_2\text{O}_3$ system. This is then followed by a discussion of the electrical transport properties. Together, these set the stage for understanding the variation of the thermoelectric power factor and figure of merit with composition. Before doing this, though, we estimate the electronic contribution to the thermal conductivity using the Wiedemann-Franz relationship:

$$\kappa_e = L\sigma T \quad (5.4)$$

where κ_e is the electronic contribution to the thermal conductivity and L is the Lorentz factor typically $2.0 \times 10^{-8} \text{ J}^2\text{K}^{-2}\text{C}^{-2}$ for degenerate semiconductors [2]. Taking the highest value of the electrical conductivity measured, $\sim 40 \text{ S/cm}$ at 800°C for 40 m/o $\text{InO}_{1.5}$, the electronic thermal conductivity is calculated to be $\kappa_e \approx 0.08 \text{ W/m.K}$. This is more than an order of magnitude smaller than the thermal conductivities measured indicating that it is negligible compared to the lattice contribution to the phonon thermal conductivity. Based on this estimate, the following discussions of thermal conductivity are couched in terms of phonon scattering mechanisms alone.

5.5.1 ZnO Solid Solution Region – Point Defect Phonon Scattering

The rapid decrease in thermal conductivity with indium addition in the solid solution phase region is indicative of strong point defect scattering of phonons by indium ions substituting into the ZnO lattice. At temperatures above the Debye temperature, the thermal conductivity of crystalline materials can be expressed as:

$$\kappa = \frac{k_B\sqrt{v_s}}{\sqrt{\pi^3}} \frac{1}{\sqrt{\Omega_0 C \Gamma}} \frac{1}{\sqrt{T}} \tan^{-1} \left(\frac{k_B \theta}{\hbar} \left(\frac{\Omega_0 \Gamma}{4\pi v_s^3 C T} \right)^{\frac{1}{2}} \right) + \kappa_{min} \quad (5.5)$$

where the first term is the Callaway - van Baeyer description [114] of the effect of defect concentration and temperature on thermal conductivity and the second term is the high-temperature limit κ_{min} when the phonon wavelength approaches the interatomic distance [115, 118, 121]. k_B is Boltzmann's constant, v_s the sound velocity and Ω_0 is the unit cell volume. The constant C is the inverse time coefficient for phonon-phonon scattering processes in pure ZnO and is obtained by fitting equation 5 to the temperature dependence of pure ZnO. Γ is the phonon scattering strength of the point defects introduced by indium solid solution alloying. Indium is known to be a substitutional solute in ZnO, substituting for the Zn ion and creating cation vacancies for site and charge balance according to the overall defect reaction [90]:



Writing the indium concentration as, c , the formula for indium-doped ZnO can be expressed as:



In turn, the phonon scattering parameter Γ can be written as the mass variance on the cation site only since there are no defects on the anion lattice.

$$\Gamma = \frac{1}{2} \left(\frac{M_{Zn}}{\bar{M}} \right)^2 \Gamma(A) = \frac{1}{2} \left(\frac{M_{Zn}}{\bar{M}} \right)^2 \frac{\sum_j f_j (M_j - \bar{M}_{Zn})^2}{(\bar{M}_{Zn})^2} \quad (5.8)$$

where the summation is over the two different types of point defect, the substitutional and vacancy defects. To first order approximation in indium doping concentration,

$$\Gamma \approx 1.38c \quad (5.9)$$

Consistent with the data shown in Figure 5.2 and Figure 5.3, the conductivity κ decreases with indium concentration, c .

5.5.2 ZnO Solid Solution Containing Planar Interfaces

When the indium concentration exceeds its solid solubility in ZnO, our microscopy data, as well as that of others [37, 90], indicates that one-dimensional superlattice structures consisting of InO₂ planes inserted in the ZnO structure are formed. Their effect is to introduce additional phonon scattering, reducing the phonon mean free path while also introducing thermal conductivity anisotropy parallel and perpendicular to the InO₂ planes. The thermal conductivity of the ZnO solid solution containing these planar interfaces can then be written as:

$$\frac{1}{\kappa} = \frac{1}{\kappa_i} + \frac{R_k}{d_{SL}} \quad (5.10)$$

where κ_i is the thermal conductivity of the materials with point defects and the second term is the contribution of the thermal resistance associated with the InO/ZnO interfaces. d_{SL} is the average interface spacing which depends on the indium concentration, and is given by the following relation,

$$d_{SL} \approx (k + 1) \times d_{\{0002\}} \quad (5.11)$$

where $d_{\{0002\}}$ is the basal plane spacing of ZnO lattice (0.260 nm for pure ZnO). Accordingly, as the indium concentration increases, the interface density increases and the spacing d_{SL} decreases, leading to a reduction in thermal conductivity. Detailed analysis of the indium concentration and temperature dependence of this contribution to thermal conductivity has recently been quantified [174] and the important finding for this work is that the InO/ZnO interface is estimated to have a thermal (Kapitza) resistance R_k of $5.0 \pm 0.6 \times 10^{-10} \text{ m}^2\text{K/W}$.

Our microscopy observations indicate that after annealing at the higher temperature (1250 °C), a complex “chessboard” of intersecting InO₂ planes forms as shown in Figure 6(b). The effect of such intersecting faults on thermal conductivity has not been modeled in the literature. However, at the simplest level, one can assume that the InO/ZnO interfaces formed have the same thermal resistance as in the one-dimensional superlattice structures. Further, as they are arranged on different crystallographic planes, they will decrease the thermal conductivity anisotropy, further lowering the overall thermal conductivity. Lacking a detailed model, this would qualitatively cause a reduction in thermal conductivity of the materials annealed at 1250 °C relative to the same compositions annealed at 1150 °C. This is seen when the data measured at both room temperature and 800 °C are compared (Figure 5.2 and Figure 5.3).

5.5.3 Modular Compounds

As shown in Figure 5.2 and Figure 5.3, the thermal conductivities of the modular In₂O₃(ZnO)_k compounds ($k = 4, 5, 7, 9$) are similar, being in the range of 2 - 3 W/m.K at room temperature and 1.25 – 2.1 W/m.K at 800 °C. Since they only differ structurally by

the spacing of the InO_2 planes their thermal conductivities can be estimated from the spacing between the InO_2 planes and the thermal resistance of the InO/ZnO interface using equations 5.10 and 5.11. For example, when the periodicity of the InO_2 layers in the $k = 7$ compound, $\text{In}_2\text{O}_3(\text{ZnO})_7$, is used the thermal conductivity is calculated to be 2.3 W/m.K, very close to the measured value of 2.5 W/m.K. Repeating the calculation for the other modular compounds, the estimated values are close to those reported as summarized in Table 5.1.

Table 5.1: Calculated room temperature thermal conductivity of $\text{In}_2\text{O}_3(\text{ZnO})_k$ modular compounds based on InO/ZnO interface scattering (according to equations 5.10 and 5.11).

Also shown are the room temperature measurements in the present work (annealed at 1150 °C) and literature reported values.

k	Calculated values (R.T.)	Measured, present work (R.T.)	Literature (R.T)
4	1.74	2.26	3.50 [36];
5	1.95	2.80	2.60 [35]; 3.45 [36]
7	2.31	2.49	3.95 [36]
9	2.6	2.65	2.65 [35]; 4.65 [36]

5.5.4 Electrical Transport Properties

The most striking feature of the data in figures 4 and 5 is that the electrical conductivity and Seebeck coefficient exhibit opposite trends with indium concentration. This behavior is consistent with the correlation between the Seebeck coefficient and

electrical conductivity of a free electron semiconductor with a density of states at the conduction band edge, N_c :

$$S = -\frac{k_B}{e} \left[\ln \left(\frac{N_c}{n} \right) + A \right] \quad (5.12)$$

where $N_c = \left(\frac{2\pi m_e^* k_B T}{\hbar^2} \right)^{\frac{3}{2}}$, A is a transport constant that depends on the electron scattering mechanism and typically has a value in the range of 0 to 4 and where m^* is the effective mass of the electrons, n is the number of carriers and μ is the mobility:

$$\sigma = n e \mu \quad (5.13)$$

Consistent with these expectations is that the higher conductivities measured on the materials annealed at 1250°C are reflected by systematically lower values of the Seebeck coefficient. The one significant outlier is the data at a concentration of 5 m/o InO_{1.5} annealed at 1250 °C for 7 days. This data, which occurs at the onset of the formation of InO₂ planes, is very reproducible suggesting that there may be some unusual interactions effects with the InO₂ planes that we cannot explain.

The variation of the Seebeck coefficient with electron conductivity can also be represented by plotting the Seebeck coefficient as a function of the natural logarithm of electrical conductivity (a Jonker plot):

$$S = \frac{k_B}{e} (\ln (\sigma) - \ln(\sigma_0)) \quad (5.14)$$

where $\sigma_0 = N_c e \mu \exp(A)$. When our data, measured at 800 °C, is plotted this way across the full composition range of ZnO-In₂O₃ phase diagram for both annealing conditions a good correlation is obtained as shown in Figure 5.9. Furthermore, as

indicated by the dashed line with a slope of + 86.15 $\mu\text{V/K}$, corresponding to the value of k_B/e [2], the data is consistent with the Seebeck coefficient being determined by free electron transport in all the compositions. This is especially so for the materials annealed at 1250 °C. The intercept, $\ln(\sigma_0)$, sometimes referred to as the “DOS- μ ” product has a value of 10.0, similar to a recent assessment for some of the $\text{In}_2\text{O}_3(\text{ZnO})_k$ phases [94]. So, while the microstructure affects the actual values of the conductivity, the evidence is that across the phase diagram each of the phases is a free-electron semiconductor.

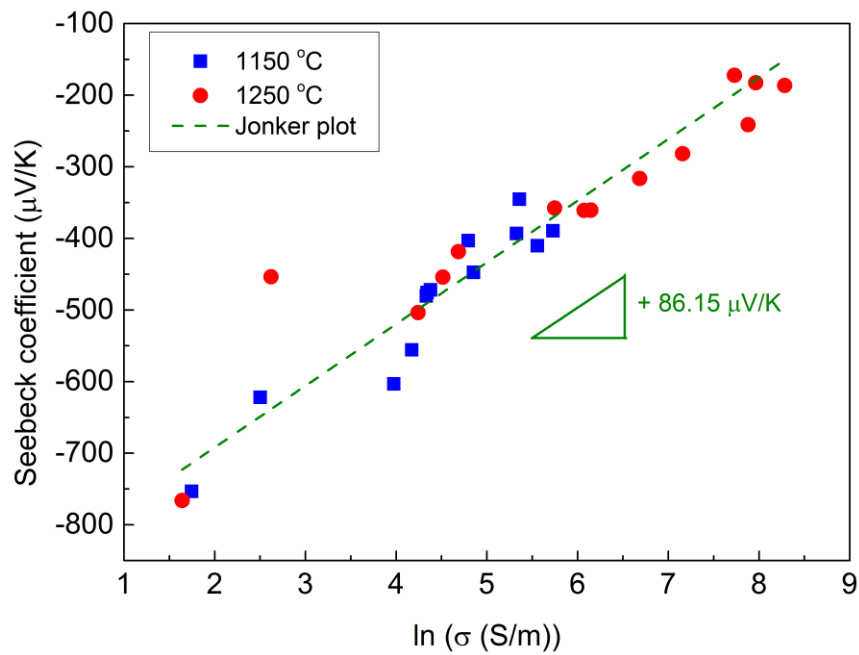


Figure 5.9: Jonker plot (Seebeck coefficient against natural logarithm of electrical conductivity) of $\text{ZnO}-\text{In}_2\text{O}_3$ materials measured 800 °C. The best fit of the data with a slope of + 86.15 $\mu\text{V/K}$ is shown as the dashed line.

Table 5.2 compares the electrical conductivity and Seebeck coefficient of the modular compounds studied in this work with values in the literature. One of the striking features of the electrical conductivity data is that it increases with the decreasing value of k (equivalently increasing indium concentration). In some cases, the conductivity is

comparable to, if not exceeds, the conductivity of the doped ZnO. Also of interest is that the thermoelectric properties of these modular compounds are monotonically increasing with decreasing order of superlattice, i.e. the k value. Clearly seen in Figure 5.10 and Figure 5.11, both power factor and ZT is increase almost linearly from $k = 9$ to 4. This may suggest that the low k compounds $\text{In}_2\text{O}_3(\text{ZnO})_k$ are more electrically conducting, which is consistent with the findings in literature that low k compound has large carrier concentration and mobility [92].

Table 5.2: Electrical conductivity and Seebeck coefficient of $\text{In}_2\text{O}_3(\text{ZnO})_k$ modular compounds measured at 800 °C. Also shown are literature reported values.

k	Electrical conductivity, S/cm		Seebeck coefficient, V/K	
	Present work	Literature	Present work	Literature
4	26.4	148 [36]	- 241.2	-175 [36]
5	12.8	203 [31]; 98 [36]; 200 [32]	- 281.7	-24 [31]; -193 [36]; -60 [32]
7	4.7	146 [31]; 70 [36]	- 360.5	-42 [31]; -198 [36]
9	4.3	98 [31]; 65 [36]	- 360.9	-82 [31]; -207 [36]

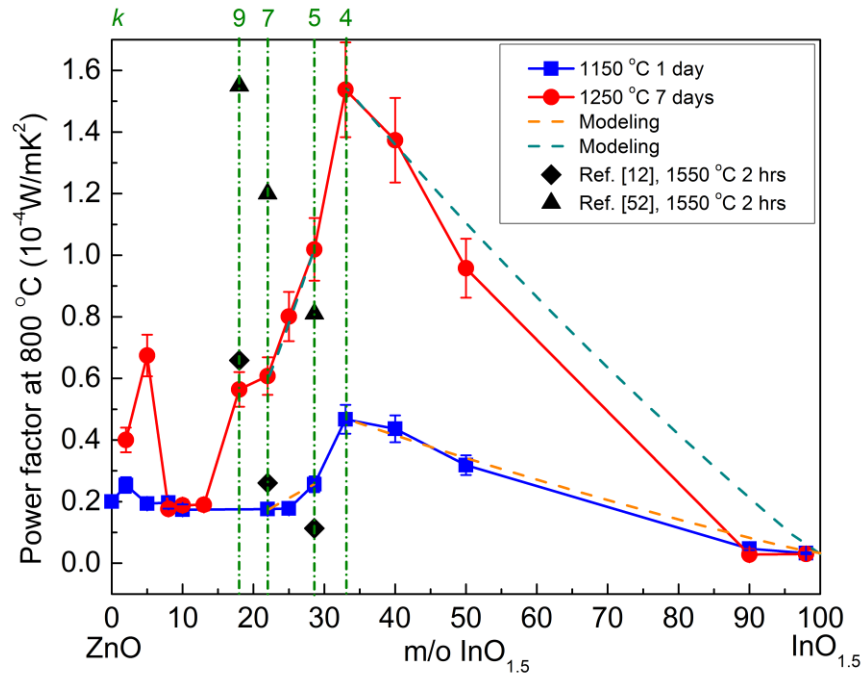


Figure 5.10: Thermoelectric power factor at 800 °C after annealing at 1150 °C for 1 day (blue squares) and 1250 °C for 7 days (red circles). Also shown are literature measurements for the $k = 5, 7, 9$ compounds measured at 800 °C [31, 32]. The dashed lines correspond to the Bergman effective medium model for two phase thermoelectrics [175, 176].

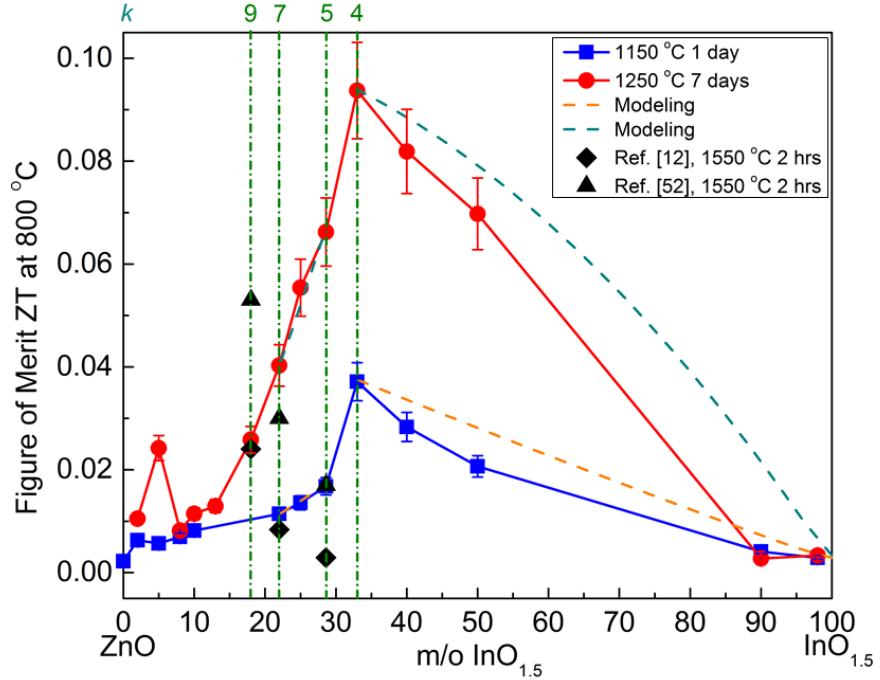


Figure 5.11: Thermoelectric figure of merit at 800 °C. Also shown are values from the literature for the $k = 5, 7, 9$ compounds measured at 800 °C [31, 32]. The dashed lines correspond to the Bergman effective medium model for two phase composite thermoelectrics [175, 176].

Apart from the variation in electrical conductivity with composition and the phase content, the other significant feature of the conductivity data is the consistently higher conductivities of the materials annealed for the longer time at higher temperature. This is attributed to the annealing out of point defects and local disorder at the higher temperature that reduce electron scattering. Indeed, many of the previous studies that report higher electrical conductivities [170, 177, 178] the materials were annealed at higher temperature and/or longer times. The effect on thermal conductivity is less striking but is nevertheless detectable at concentrations below which the modular compounds form. (At higher indium concentrations, the InO/ZnO interfaces are assumed to be more effective in phonon scattering and so the effect of annealing is less marked).

5.5.5 Two-phase Thermoelectrics

The relative insensitivity of the thermal conductivity to indium concentrations greater than about 10 m/o InO_{1.5}, means that the thermoelectric figure of merit ZT and the thermoelectric power factor $S^2\sigma$ exhibit similar dependence on indium concentration. These trends are shown in Figure 5.10 and Figure 5.11. The data indicates that the compounds k = 5 (at 1150 °C) and the k = 4 (at 1250 °C) have the largest values of both the thermoelectric power factor and ZT.

For compositions containing more indium than these compounds, the phase diagram, our X-ray diffraction and our SEM and EDS analyses all indicate that the materials are two phase. (There are also other two-phase regions consisting of mixtures of other modular compounds, albeit with a narrower range of composition, for instance between Zn₇In₂O₁₀ and Zn₅In₂O₈ compounds). A striking feature of the data is that the power factor and figure of merit vary almost linearly with concentration between the two phases suggesting that the thermoelectric properties obey the equivalent of the Lever rule with the value being a weighted average of the volume fractions of the two phases. It is, therefore, of interest to compare our data with the mean field model presented by Bergman *et al.* [175, 176] for the thermoelectric properties of a composite consisting of a randomly distributed mixture of two thermoelectric phases.

According to Bergman's model, the thermoelectric power factor of a random composite can be written in terms of the volume fraction, ϕ , and properties of the two phases, A and B, as:

$$PF = \frac{[(1 - \phi_B)(\sigma_A S_A - \sigma_B S_B) + \sigma_B S_B]^2}{(1 - \phi_B)(\sigma_A - \sigma_B) + \sigma_B} \quad (5.15)$$

(In the appendix, the volume fractions are computed from the molar phase fractions).

Figure 5.10 compares the predictions of the model to our data at 1150 °C and 1250 °C for both the In₂O₃ and Zn₄In₂O₇ two-phase system and for the mixture of Zn₇In₂O₁₀ and Zn₅In₂O₈ superlattice compounds. Reasonable agreement is obtained.

The same mean field model can be applied to the thermoelectric figure of merit by including the variation in thermal conductivity with composition. For this purpose, we express the effective thermal conductivity of a two-phase composite, including the thermal resistance of the grain boundaries, derived by Nan *et al.* [133] as

$$\kappa = \kappa_A \frac{\kappa_B(1 + 2\alpha) + 2\kappa_A + 2\phi_B[\kappa_B(1 - \alpha) - \kappa_A]}{\kappa_B(1 + 2\alpha) + 2\kappa_A - \phi_B[\kappa_B(1 - \alpha) - \kappa_A]} \quad (5.16)$$

where κ is the effective thermal conductivity of the composite, κ_A and κ_B are the thermal conductivity of each component with ϕ_B the volume fraction of component B. The parameter α is a dimensionless parameter determined by the shape of the second component, assumed to be elliptical, as well as the interface (Kapitza) thermal resistance R_k . For spherical particles, α is the ratio of two characteristic lengths, the thermal width of the interface $R_k \kappa_m$ and the particle radius, a :

$$\alpha = \frac{R_k \kappa_m}{a} \quad (5.17)$$

where κ_m is the thermal conductivity of the matrix phase.

In order to estimate an appropriate value of α , we use the following values: The typical grain size of the second phase is about 5 µm based on our microscopy

observations. The interfacial (Kapitza) thermal resistance R_k is about $5.0 \times 10^{-10} \text{ m}^2\text{K/W}$ for InO/ZnO interfaces [174]. The thermal conductivities of In_2O_3 and $\text{Zn}_4\text{In}_2\text{O}_7$ at 800 °C are about 1.5 W/m.K and 2 W/m.K, respectively. Either of the phases could be the matrix phase depending on the indium concentration. Using these values, $\alpha \sim 10^{-3}$ meaning that the grain boundary thermal resistance can be neglected and the effective thermal conductivity can be written as:

$$\kappa = \kappa_A \frac{\kappa_B + 2\kappa_A + 2\phi_B(\kappa_B - \kappa_A)}{\kappa_B + 2\kappa_A - \phi_B(\kappa_B - \kappa_A)} \quad (5.18)$$

By combining the mean field expressions (equations 5.15 and 5.18) and evaluating them for the individual phases, the variation in figure of merit (equation 5.2) over the two phase regions is shown by the dashed lines in Figure 5.11, for the 1150 °C and 1250 °C series, respectively. The experimental values for the figure of merit are again in reasonable agreement with the model, suggesting that Bergman's mean-field model is a reliable method of computing the thermoelectric properties of random two-phase mixtures.

5.5.6 Attaining Compositional and Structural Homogeneity

As remarked upon earlier, there have been a number of previous studies of the thermoelectric properties of some of the modular compounds [31, 35, 36] as well as variously doped ZnO and In_2O_3 materials [62, 64-66, 83, 84, 87, 179-183]. In comparing the results from the different studies, the largest variations are in the numerical values of the electrical conductivity and the smallest variations are in the thermal conductivities. The latter can be understood because the thermal conductivities are relatively insensitive to composition for indium concentrations > 15 m/o $\text{InO}_{1.5}$ and are determined by phonon

scattering from the InO/ZnO interfaces and solute scattering. Much of the reported variation in electrical conductivity can be attributed to the maximum temperature at which the materials have been equilibrated, annealing out extraneous point defects. Also related to these variations in electrical conductivity, it is believed, are compositional and structural inhomogeneities. The formation of the modular compounds with well-defined periodicity requires long-range diffusion and the larger the k -value the greater the distance over which diffusion must occur. Furthermore, if the temperature is changed, either during preparation of the materials or upon subsequent annealing, the kinetics of the change from one modular compound to another will also limit equilibration. One consequence of such kinetic limitations is that the lower temperature at which the modular compounds can form may be lower than indicated by the phase diagram in figure 1. A further consideration is that the modular compounds are line compounds and so it is difficult to make them single phase. For instance, Ohta *et al.* [31] measured the thermoelectric properties of the $k = 5, 7, 9$ compounds (sintered at 1550 °C for 2 hours) from 250 to 800 °C and found that the figure of merit was significantly larger than pure ZnO due to the increase in electrical conductivity and decrease in thermal conductivity. However, the periodicity in some of their materials is obviously not constant as shown in their TEM micrograph (e.g. their Figure 2B). It is apparent that the properties they measured are those for a mixture of $\text{In}_2\text{O}_3(\text{ZnO})_k$ compounds with varying k instead of a single one. We also note that our values systematically vary with indium concentration whereas Ohta's do not. It should also be noted that the difficulty in obtaining the single phase compounds has also been observed in other $\text{RMO}_3(\text{ZnO})_k$ homologous structure system [92, 169-172, 177]. Furthermore, in several papers, the reported value of k is the

ratio between zinc and indium ions in the starting materials rather than in the final materials, and so do not account for compositional losses associated with the volatility of Zn and In.

5.6 Conclusions

The ZnO-In₂O₃ binary system has proven to be a good model system for relating thermoelectric properties, including thermal conductivity, to the various phases and compositional fields that exist at 1150 and 1250 °C. At low concentrations of indium (< 10 m/o InO_{1.5}), the properties are relatively insensitive to the indium concentration except for the thermal conductivity that decreases very rapidly due to phonon scattering from substitutional indium ions. At higher concentrations, planar InO₂ sheets form and the thermal conductivity is almost independent of composition across the entire phase diagram at both 1150 and 1250 °C. At still higher indium concentrations, once modular compounds In₂O₃(ZnO)_k form, the electrical conductivity and Seebeck coefficient depend on the k value, with the changes being more pronounced for the 1250 °C series than the 1150 °C series of compositions. The largest values of both power factor and ZT occur at a composition corresponding to the k=4 compound, the only hexagonal compound in any of the compositional fields below 1320 °C. It is speculated this is because this compound does not contain crystallographic interfaces where there is a reversal in polarization and consequently electrostatic barriers to electron transport across them.

At still higher indium concentrations, the materials are two-phase consisting of In₂O₃ and a modular compound (k=5 at 1150 °C and k=4 at 1250 °C). In these two phase

compositions, the power factor and ZT decrease in proportion to the indium concentration and they are consistent with mean field estimates based on the random distribution of two thermoelectric phases. Across the phase diagram, the electrical conductivity is n-type and the Seebeck coefficient is proportional to the natural logarithm of the electrical conductivity. Careful studies of electron mobility as a function of composition are clearly needed, especially electron transport across the InO_2 planes.

In closing, we believe that similar studies relating thermoelectric properties to phase equilibria are extremely useful in understanding and potentially identifying high temperature oxide thermoelectric materials. Very few semiconductor modular compounds have been studied to date but they have the potential for crystal engineering to independently modify both the electrical conductivity and thermal conductivity. Furthermore, there is also the possibility of altering, through doping, the density of states of the interfaces to alter the Seebeck effect and enhance ZT .

5.7 Appendix: Conversion between Molar and Volume Fractions

The mole fraction x of the component B can be written in terms of its volume fraction as follows,

$$x = \frac{\phi_B \frac{\rho_B}{M_B}}{\phi_B \frac{\rho_B}{M_B} + (1 - \phi_B) \frac{\rho_A}{M_A}} \quad (5.19)$$

where ρ_i and M_i are the mass density and molecular weight of the each component.

For the In_2O_3 and $\text{Zn}_4\text{In}_2\text{O}_7$ two-phase composite system, we set In_2O_3 and $\text{In}_2\text{O}_3(\text{ZnO})_4$ as component A and B, respectively. The $\text{InO1.5} = 0.98$ sample with composition closest to the In_2O_3 end will represent the thermoelectric properties of In_2O_3 . The corresponding mass density and molecular weights are as follows. For In_2O_3 : $\rho_A = 7.179 \times 10^3 \text{ g/m}^3$ and $M_A = 277.64 \text{ g/mol}$; for $\text{Zn}_4\text{In}_2\text{O}_7$: $\rho_B = 6.193 \times 10^3 \text{ g/m}^3$ and $M_B = 603.27 \text{ g/mol}$. For the two-phase mixture of $\text{Zn}_7\text{In}_2\text{O}_{10}$ and $\text{Zn}_5\text{In}_2\text{O}_8$ superlattice compounds, we set $\text{In}_2\text{O}_3(\text{ZnO})_4$ and $\text{In}_2\text{O}_3(\text{ZnO})_5$ phases as component A and B, respectively, with their mass density and molecular weights as: for $k = 7$, $\rho_A = 6.034 \times 10^3 \text{ g/m}^3$ and $M_A = 847.26 \text{ g/mol}$; for $k = 5$, $\rho_B = 6.126 \times 10^3 \text{ g/m}^3$ and $M_B = 684.50 \text{ g/mol}$. The mass densities of $\text{In}_2\text{O}_3(\text{ZnO})_4$, $\text{In}_2\text{O}_3(\text{ZnO})_7$ and $\text{In}_2\text{O}_3(\text{ZnO})_5$ were calculated based on the lattice parameter reported in the literature[92].

For the two-phase composite consisting of In_2O_3 and $\text{In}_2\text{O}_3(\text{ZnO})_4$, the indium concentration can be further expressed in terms of mole fraction of component B as,

$$[\text{In}] = \frac{2x + 2(1-x)}{4x + 2x + 2(1-x)} \quad (5.20)$$

Similarly for the two-phase mixture of $\text{In}_2\text{O}_3(\text{ZnO})_7$ and $\text{In}_2\text{O}_3(\text{ZnO})_5$ superlattice compounds,

$$[\text{In}] = \frac{2x + 2(1-x)}{2x + 2(1-x) + 5x + 7(1-x)} \quad (5.21)$$

The above set of equations enables the two-phase composite thermoelectric power factor, which is originally expressed as a function of second phase volume fraction, to be expressed and modeled as a function of indium concentration.

Chapter 6 Thermoelectric Properties of Fe doped ZnO with High Temperature Grain Refinement

Thermoelectric properties of Fe doped ZnO materials are investigated and correlated with the phase and microstructural evolution. Both a ZnO solid solution phase and a ZnFe_2O_4 spinel phase are observed. By correlating the Seebeck coefficient with electrical conductivity, all the samples studied in the present work are found to behave as free electron semiconductors. In addition, the thermoelectric power factor and figure of merit are found to increase with the actual Fe content in ZnO lattices, due to the reduced thermal conductivity by point defect scattering of phonons and enhanced electrical transport via providing electron donors. The maximum achievable power factor of Fe doped ZnO material is estimated to be similar to that of ZnO-In₂O₃ system. Also of importance is the significant microstructural refinement of 18 m/o FeO_{1.5} doped ZnO after high temperature thermal treatment that leads to reduce thermal conductivity. This makes Fe doped ZnO as high temperature thermoelectric oxides.

6.1 Introduction

ZnO based oxide system has a rich variety of doping choices on altering the microstructure as well as tuning the transport properties. Fe doped ZnO system is one of such examples but not yet deeply explored. Light doping of Fe into ZnO was found not to cause any change of microstructure [77, 79]. Nevertheless, there were a few works on Fe highly doped ZnO reporting the formation of oxide defect structure including inversion domain structures[76] or anti-phase modulated structure [72], both of which were in the

scale of 10 nm. However, few efforts have been made to explore the thermoelectric properties of Fe doped ZnO, neither the thermal conductivity nor the electrical conductivity and the Seebeck coefficient. It is of interest in the present work to look into the relationship between phase equilibria, microstructural evolution and thermoelectric properties.

In the present work, 2, 4 and 18 m/o $\text{FeO}_{1.5}$ doped ZnO, with pure ZnO as reference, were synthesized to obtain different phase equilibria and investigate the thermoelectric properties. The 2 and 4 m/o $\text{FeO}_{1.5}$ doped ZnO were annealed at 1250 °C for achieving the solid solution phase. The 18 m/o $\text{FeO}_{1.5}$ doped ZnO was annealed at 1150 °C and 1350 °C to obtain the two-phase microstructure and highly Fe concentrated ZnO solid solution phase, respectively. The compositions and heat treatment temperatures of samples are indicated on the ZnO – $\text{FeO}_{1.5}$ binary phase diagram shown in Figure 6.1.

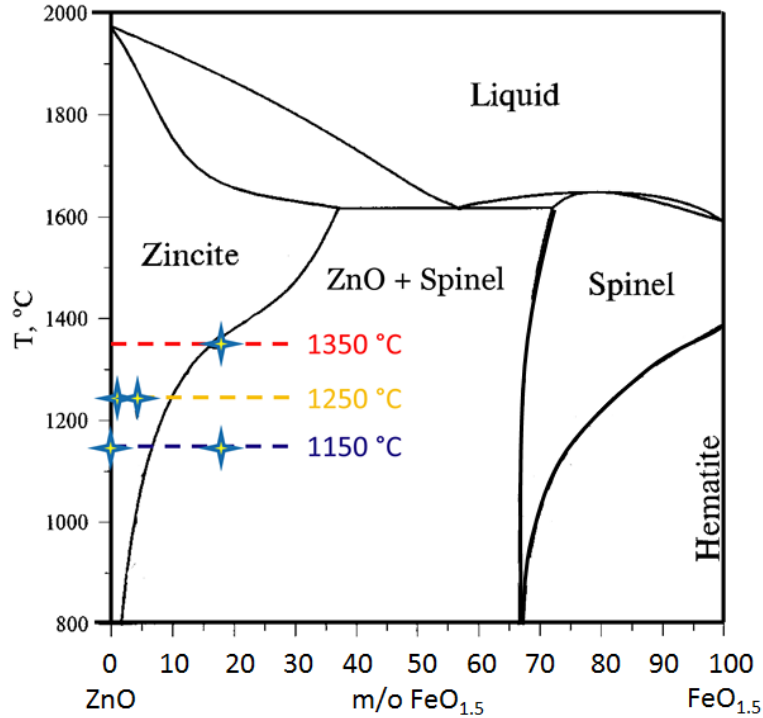


Figure 6.1: ZnO – FeO_{1.5} binary phase diagram adapted from Degterov et al.’s work[73]. The compositions of the material with different annealing temperatures are indicated on the figure.

6.2 Experimental

High purity commercial nitrate powders, Zn(NO₃)₂ (99.999%, Sigma Aldrich®, USA) and Fe(NO₃)₃ (99.99%, Sigma Aldrich®, USA), were used in the present study. The oxide powders with compositions of 2, 4, and 18 m/o FeO_{1.5} was prepared and synthesized using the combined wet chemistry and gel combustion approach and sintered into solid pellets at 900 °C for 5 min using CADPro system. Details about the synthesis and densification methods are the same as described in Chapter 2. The sintered solid samples were further annealed in furnace in air at different temperatures to achieve the expected phase equilibria. The 2 and 4 m/o FeO_{1.5} samples were annealed at 1250 °C for 1 day to form the ZnO solid solution phase. The 18 m/o FeO_{1.5} sample was annealed at

1150 °C for 1 day and 1350 °C for 3 days to obtain the expected two-phase microstructure and investigate the phase change. Pure ZnO was sintered in the same way and annealed at 1150 °C for 1 day as reference. All the heat treatments were followed by a furnace controlled cooling. X-ray diffraction analysis was performed ($2\theta = 10 \sim 70$ degree) to investigate the phase change under different annealing conditions. Both SEM and TEM imaging were made to investigate the microstructural evolution. STEM with EDS mapping was performed with the assistance of Dr. David C. Bell to study the elemental distribution on the fine structural features. Electrical and thermal transport properties were measured to obtain the thermoelectric properties; details of measurement approach can be referred to Chapter 2.

6.3 Results

6.3.1 Structural Characterization

X-ray diffraction results for Fe doped ZnO, including pure ZnO as reference, are presented in Figure 6.2. The X-ray scan of all the samples was made from 2θ of 10 to 70 degree, but spectra in the range of 2θ of 25 to 40 degree are presented as they are most representative of important phases and structure features. Characteristic peaks of each phase are labeled. Analysis of the X-ray diffraction results reveals several important features, as will be described in the followings.

With increasing $\text{Fe}/(\text{Fe}+\text{Zn})$ ratio up to 4 m/o $\text{FeO}_{1.5}$, a systematic shift of ZnO (002) peak towards smaller 2θ angle was observed indicating an increasing basal plane spacing, implying an increased incorporation of Fe ions into the ZnO lattice. A

continuous broadening of ZnO (101) peaks with increasing Fe concentration was also observed, as has also been reported in literature [184]. In addition, a ZnFe₂O₄ type of spinel phase (cubic, $Fd\bar{3}m$) but deficient in Fe, one example of which is a Zn_{0.945}Fe_{1.78}O_{3.71} phase (ICDD# 01-079-1500), was observed to form in both 2 and 4 m/o FeO_{1.5} doped ZnO annealed at 1250 °C. The 4 m/o FeO_{1.5} doped ZnO seems to have a smaller fraction of Zn_{0.945}Fe_{1.78}O_{3.71} spinel phase than the 2 m/o FeO_{1.5} sample but it has larger concentration of Fe in ZnO lattice, as seen from the larger shift of ZnO (002) peak as well as the ZnO (100) and (101) peaks.

The X-ray diffraction results shown in Figure 6.2 suggest the presence of both ZnO and ZnFe₂O₄ spinel phases in 18 m/o FeO_{1.5} doped ZnO annealed at 1150 °C, which is expected from the phase diagram shown in Figure 6.1. However, it is interesting that ZnO solid solution phase possesses a lower content of Fe, as clearly seen from its smaller shift of ZnO (002) peak as compared to 2 or 4 m/o FeO_{1.5} doped ZnO. As the 18 m/o FeO_{1.5} sample was further annealed at 1350 °C for 3 days, two ZnO solid solution phases were identified by two ZnO (002) peaks. One ZnO solid solution phase has the (002) peak close to the pure ZnO one, whereas the other one has a significant shift and identified as the (002) peak of Zn_{0.750}Fe_{0.171}O, a ZnO solid solution phase highly rich in Fe (ICSD# 155784) [184]. In addition, a tiny amount of Fe deficient ZnFe₂O₄ spinel phase was also observed in addition to the stoichiometric ZnFe₂O₄ spinel phase. Another feature is the peak broadening, especially the ZnO (101) peak, indicating the reduction in grain size.

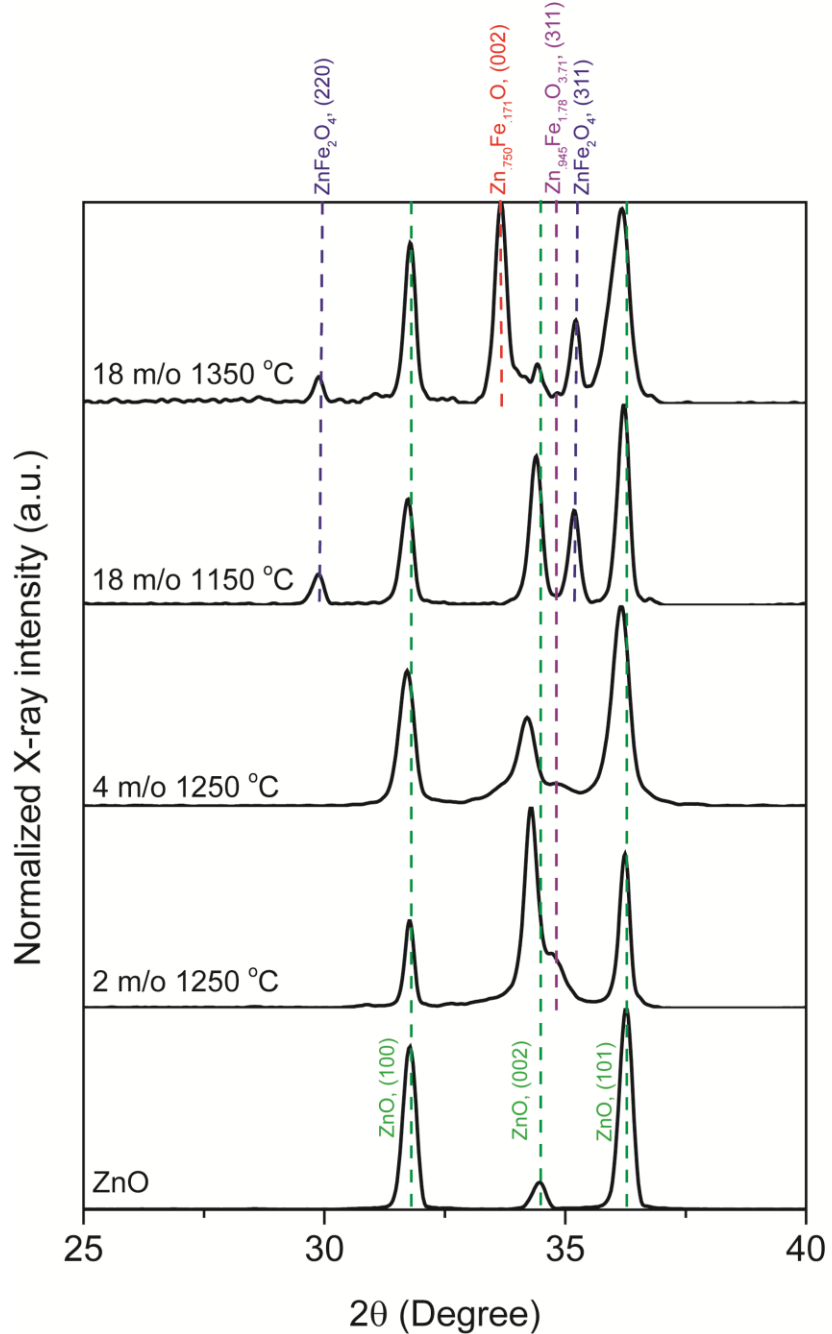
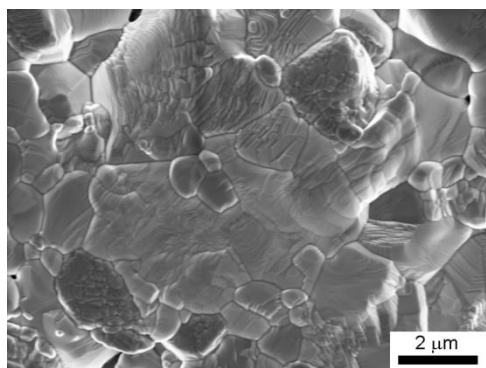


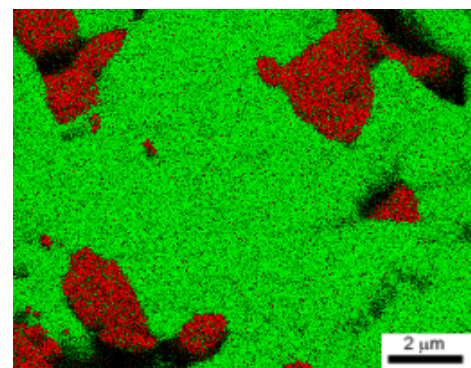
Figure 6.2: X-ray diffraction results of Fe doped ZnO with pure ZnO data also presented.
Characteristic peaks of each phase are labeled.

The 18 m/o $\text{FeO}_{1.5}$ doped ZnO, with plenty of features revealed by the X-ray diffraction, was further investigated under electron microscopy. The SEM cross-section micrograph of the sample after 1150 °C annealing is shown in Figure 6.3 (a). The typical

grain size was about $2 \sim 3 \mu\text{m}$. The corresponding EDS elemental mapping, as presented in Figure 6.3 (b), suggests the presence for ZnO solid solution phase and ZnFe_2O_4 spinel phase, as is consistent with the X-ray diffraction results. TEM micrograph as presented in Figure 6.4 (a) shows that the grain is clean without fine features and HRTEM lattice image of ZnO {002} basal planes shown in Figure 6.4 (b) suggests no defect contrast.

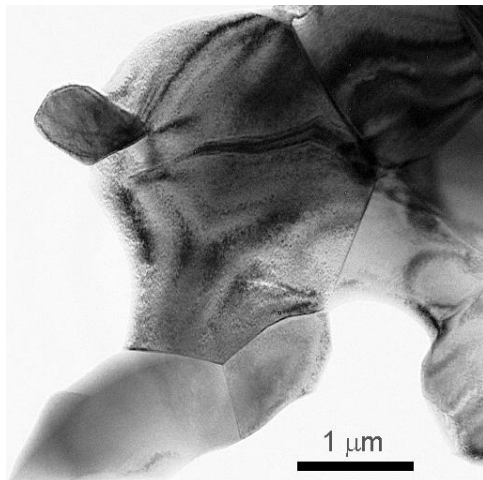


(a) SEM image

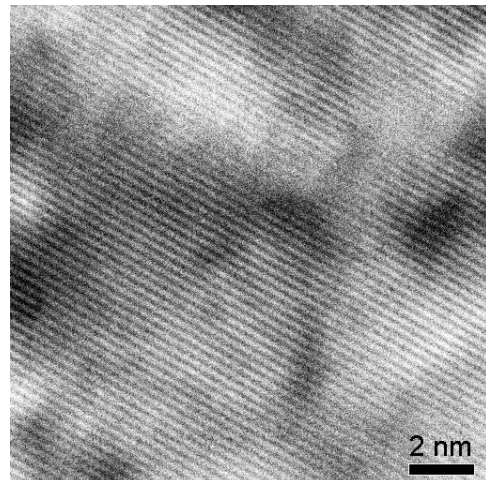


(b) EDS map: Zn L (green) and Fe L (red)

Figure 6.3: Cross-section microstructure of 18 m/o $\text{FeO}_{1.5}$ doped ZnO annealed at 1150°C for 1 day: (a) SEM micrograph; (b) EDS mapping with green and red colored data points representing Zn and Fe, respectively.



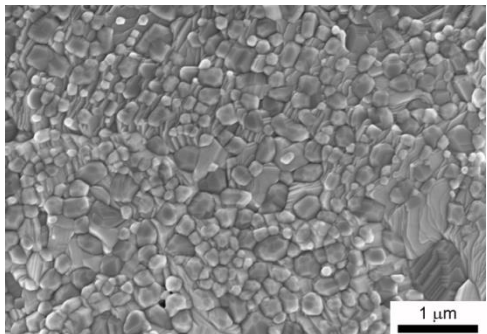
(a) TEM micrograph of grains



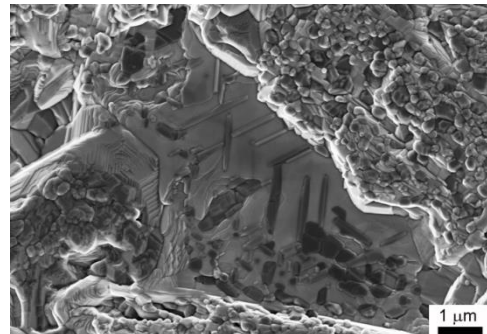
(b) HRTEM lattice image

Figure 6.4: TEM observations of microstructure in 18 m/o FeO_{1.5} doped ZnO annealed at 1150 °C for 1 day: (a) TEM micrograph of grains; (b) HRTEM lattice image of ZnO {002} basal planes.

After a further annealing of 18 m/o FeO_{1.5} sample at 1350 °C for 3 days, a significant structural change was observed, as seen from the SEM observations in Figure 6.5. The material evolves into two types of structures. One is fine grain structure with grain size reduced to about 200 nm, as shown in Figure 6.5 (a); the other is platelet or lamellar type structure embedded in a large grain as shown in Figure 6.5 (b). The SEM and the corresponding EDS elemental map in Figure 6.6 (a) and (b), which captures both types of structures, suggest that these fine grains and platelets are Fe-rich phases and therefore the ZnFe₂O₄ spinel phase in combination with X-ray diffraction results. Performing an imaging analysis of the EDS mapping gives a volume fraction of 0.17 for ZnFe₂O₄ spinel phase.

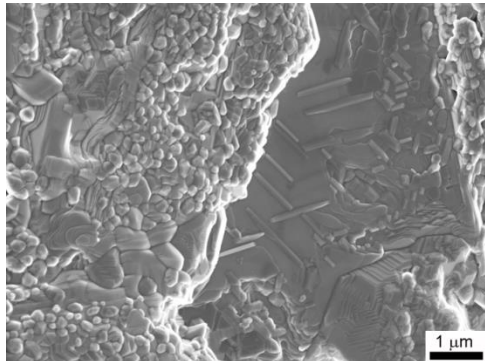


(a) Fine grain structure

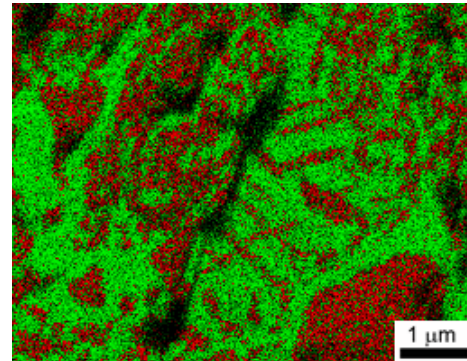


(b) Platelet structures

Figure 6.5: SEM micrographs of cross-section microstructure of 18 m/o $\text{FeO}_{1.5}$ doped ZnO annealed at 1350°C for 3 days: (a) Fine grain structures; (b) Platelet structures.



(a) SEM micrograph

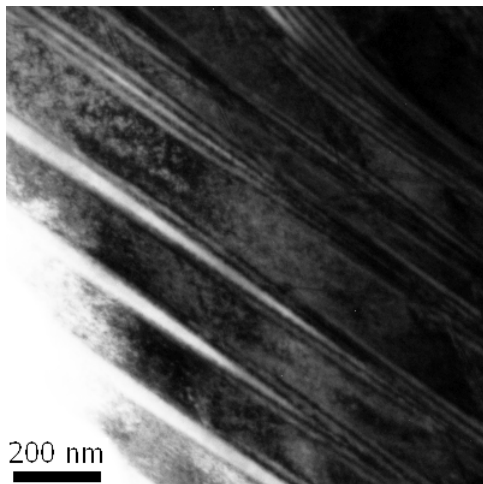


(b) EDS map: Zn (green) and Fe (red)

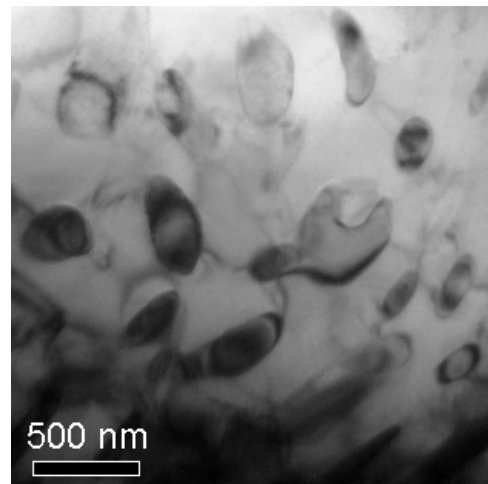
Figure 6.6: Cross-section microstructure of 18 m/o $\text{FeO}_{1.5}$ doped ZnO annealed at 1350°C for 3 days. (a) SEM image; (b) EDS mapping with green and red colored data points representing Zn and Fe, respectively.

Lamellar or platelet structures were observed on $\text{ZnO} \{002\}$ planes in my TEM investigations of the 18 m/o $\text{FeO}_{1.5}$ sample annealed at 1350°C , as shown in Figure 6.7 (a). Although there are a few literatures reporting the presence of superlattice structure (SL) or inverse domain boundaries (IDBs) in Fe doped ZnO where Fe-O layers or IDBs stack along c -axis of the ZnO [72, 76, 170-173], no such structures or related defect contrast were observed in this material even through the high resolution TEM observations of $\text{ZnO} \{002\}$ planes. In addition, it is noted that the average platelet spacing is about 200

nm which is much larger than the average superlattice or IDB spacing that is only about a few nm. Furthermore, the platelet is much thicker than superlattice interface or IDBs which are only one to two atomic layers thick. Fine grain structures, as have been seen in the SEM micrograph in Figure 6.5 (a), were also observed under TEM, as shown in Figure 6.7 (b).



(a) BF image of lamellar structure



(b) BF image of fine grain structure

Figure 6.7: TEM micrographs of typical microstructures in 18 m/o $\text{FeO}_{1.5}$ doped ZnO annealed at 1350 °C for 3 days. (a) Bright field image of lamellar structure; (b) Bright field image of fine grain structure.

A further STEM EDS elemental map was made for ZnO {002} planes, as shown in Figure 6.8, suggesting that the thin lamellar structures are enriched in Fe and therefore the ZnFe_2O_4 spinel phase in combination with our XRD results whereas the matrix is a ZnO solid solution phase. A line scan profile is presented in Figure 6.9, which provides semi-quantitative information on the Fe and Zn distribution in a direction perpendicular to the platelet structure. Since the scan was taken from the edge of the specimen towards inside (as indicated by the arrow on the image), the specimen thickness increases as away from the edge, leading to the increasing EDAX signal intensity for both zinc and iron. The counts ratio of Fe to Zn across these thin Fe-rich platelets is roughly two, which

basically corresponds to the Fe to Zn ratio in the ZnFe_2O_4 spinel compound. In addition, it is found that ZnFe_2O_4 platelets grow out of ZnO obeying to the previously reported crystallographic orientation relationship of ZnFe_2O_4 (111)[110] // ZnO (0001)[11 $\bar{2}$ 0] [185]. The STEM EDS elemental map was also made on the fine grain structures as shown in Figure 6.10. Elemental distribution results clearly show that these fine grains, which have the grain size of about 200 nm, are enriched in Fe and therefore the ZnFe_2O_4 spinel phase and the matrix is the ZnO solid solution phase.

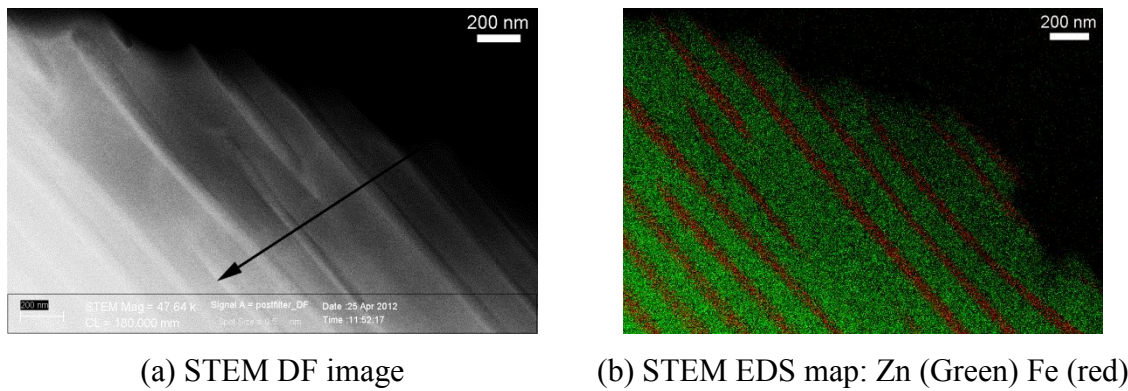


Figure 6.8: STEM image and elemental mapping of lamellar structure in 18 m/o $\text{FeO}_{1.5}$ doped ZnO annealed at 1350 °C for 3 days. (a) STEM dark field image with an arrow showing the line scan direction; (b) STEM EDS map with Zn and Fe represented by green and red colored data points, respectively.

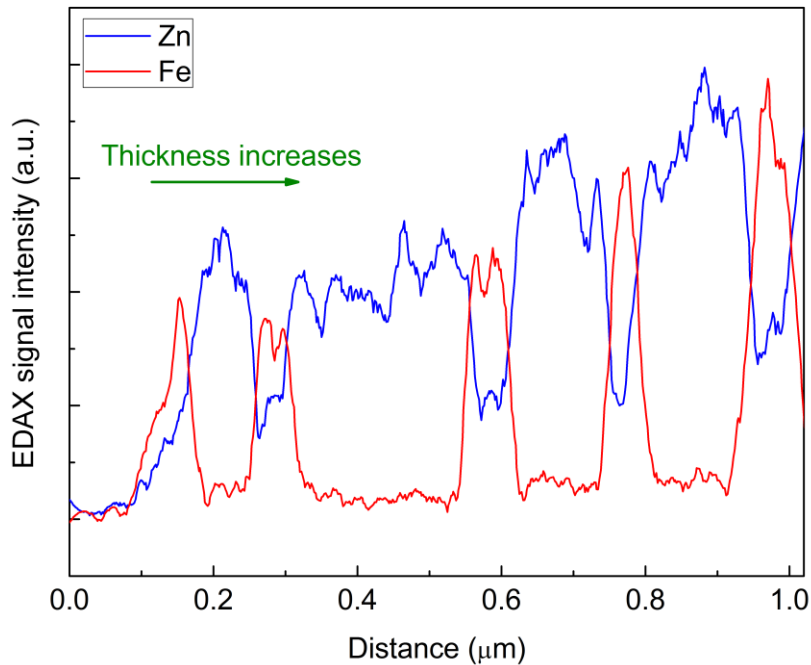


Figure 6.9: STEM EDS line scan across several platelets showing the Zn and Fe profile. Clearly, the thin lamellar structures are highly enriched in Fe, and the ratio of Fe to Zn is about two, in correspondence to ZnFe_2O_4 spinel phase.

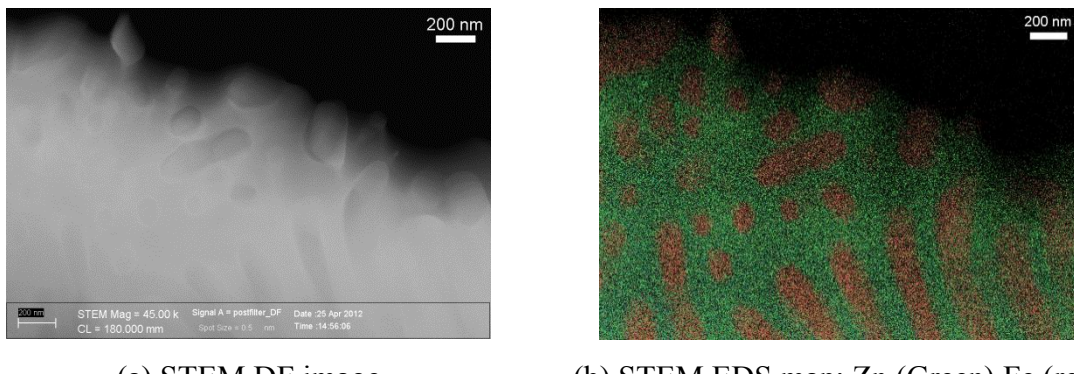


Figure 6.10: Aberration corrected STEM image and elemental mapping of fine grain structures in 18 m/o $\text{FeO}_{1.5}$ doped ZnO annealed at 1350 °C for 3 days. (a) STEM dark field image; (b) STEM EDS map with Zn and Fe represented by green and red colored data points, respectively.

6.3.2 Thermal and Electrical Transport Properties

Measured thermal conductivities of Fe doped ZnO with temperature up to 800 °C are presented in Figure 6.11. Doping ZnO with Fe results in both a significant drop in thermal conductivity as well as a reduced temperature dependence. It is also interesting to see that the 18 m/o Fe O_{1.5} sample annealed at 1150 °C has higher thermal conductivity than 2 or 4 m/o Fe O_{1.5} sample which are less Fe doped; however, a further annealing at 1350 °C reduces the thermal conductivity by a factor of more than two.

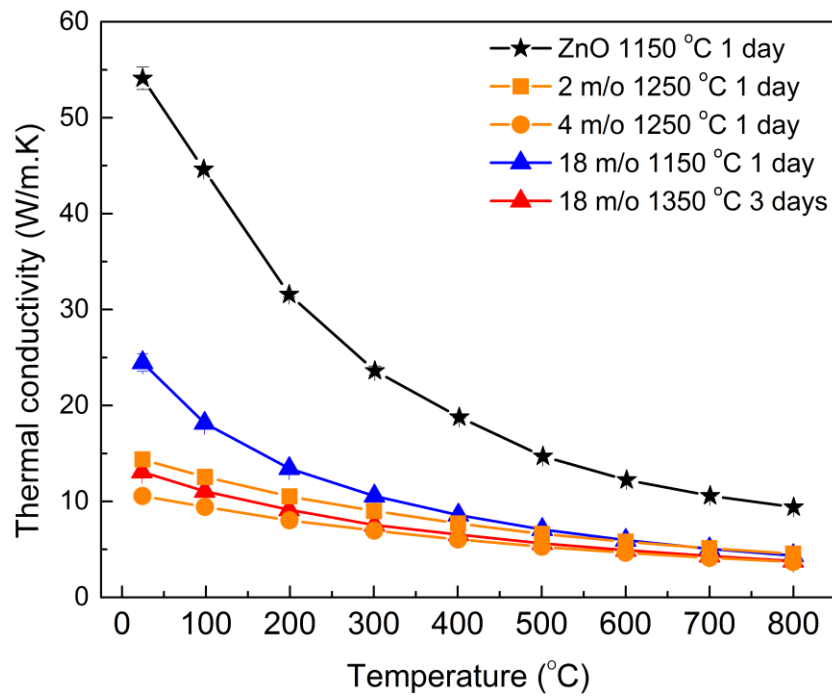


Figure 6.11: Thermal conductivity of Fe doped ZnO samples measured from room temperature up to 800 °C. The solid lines are for visual guide.

Electrical conductivity and Seebeck coefficient measurement results with temperature are presented in Figure 6.12 and Figure 6.13, respectively. Electrical conductivity of ZnO is significantly improved by Fe doping. In addition, for all the Fe doped ZnO, electrical conductivity increases with temperature. The 18 m/o FeO_{1.5} sample

annealed at 1350 °C has the highest electrical conductivity, followed by the 4 m/o, 2 m/o $\text{FeO}_{1.5}$ samples annealed at 1250 °C and the 18 m/o $\text{FeO}_{1.5}$ sample annealed at 1150 °C. For all the samples, Seebeck coefficient has exactly the opposite trend as to electrical conductivity, namely, the sample that demonstrates high electrical conductivity has small Seebeck coefficient. These findings suggest that all these samples are of typical free electron semiconductors.

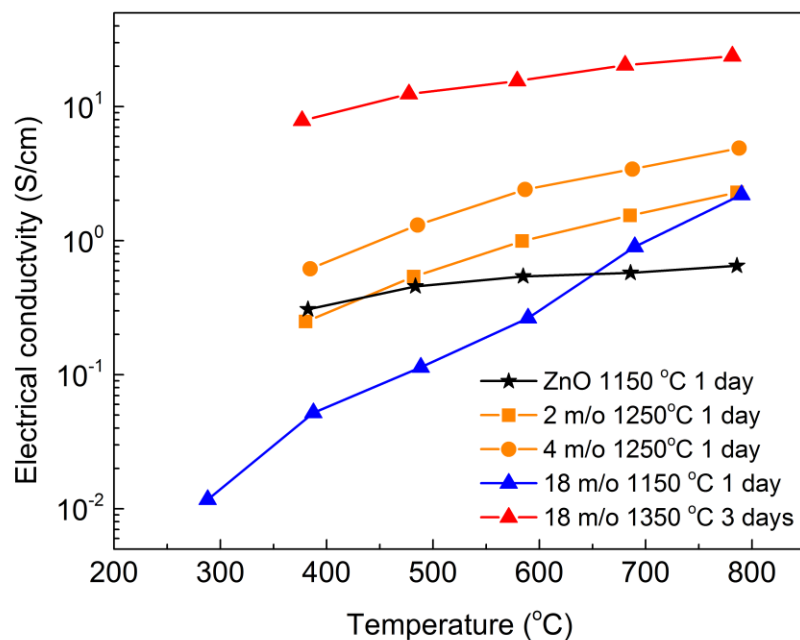


Figure 6.12: Electrical conductivity of Fe doped ZnO samples measured with temperature.

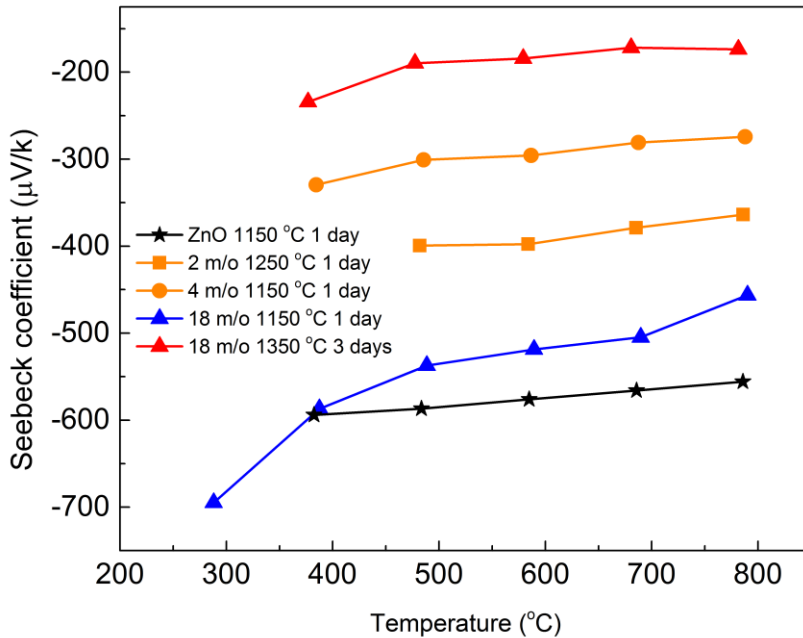


Figure 6.13: Seebeck coefficient of Fe doped ZnO samples measured with temperature.

6.4 Discussions

6.4.1 Phase Equilibria and ZnO Solid Solution

At relatively low Fe concentration, such as 2 and 4 m/o $\text{FeO}_{1.5}$ doped ZnO, both ZnO solid solution phase and a Fe deficient ZnFe_2O_4 spinel phase were observed. The phase diagram shown in Figure 6.1 predicts a ZnO solid solution phase in this compositional and temperature regime but not the formation of a Fe deficient $\text{Zn}_{0.945}\text{Fe}_{1.78}\text{O}_{3.71}$ spinel phase. In addition, a reduced fraction of Fe deficient ZnFe_2O_4 spinel phase and ZnO solid solution phase but with higher Fe concentration were observed in 4 m/o $\text{FeO}_{1.5}$ doped ZnO, suggesting a competition between the phase stabilities of ZnO and ZnFe_2O_4 spinel phases. The formation of Fe deficient ZnFe_2O_4 spinel phase possibly occur during cooling when passing through the ZnO/(ZnO+spinel)

phase boundary, when some of Fe ions left oversaturated ZnO and formed Fe deficient spinel phase that is energetically favored at low or room temperature.

It is also of interest when the 18 m/o $\text{FeO}_{1.5}$ doped ZnO was further annealed at 1350 °C and then cooled down to room temperature, two ZnO solid solution phases with different Fe concentration were formed. The Fe highly concentrated ZnO, $\text{Zn}_{0.750}\text{Fe}_{0.171}\text{O}$, which has a much larger fraction than the less Fe concentrated ZnO phase, was not found in the sample annealed at 1150 °C nor the 2 or 4 m/o $\text{FeO}_{1.5}$ sample. This is attributed to the fact that equilibrated at 1350 °C, the 18 m/o $\text{FeO}_{1.5}$ compositions is about at the phase boundary reaching the large solubility limit of Fe in ZnO lattices, as seen in the phase diagram in Figure 6.1. Both the stoichiometric and Fe deficient spinel phase formed in this sample, but the Fe deficient spinel phase only has a small fraction. It is apparent from the X-ray diffraction results of the 18 m/o $\text{FeO}_{1.5}$ sample annealed at 1350 °C that the fraction of Fe low concentrated ZnO as well as the Fe deficient spinel phase are minor phases. As 2 and 4 m/o $\text{FeO}_{1.5}$ sample (annealed at 1250 °C) consists of both less Fe concentrated ZnO and Fe deficient spinel phase, it is highly possible that the less Fe concentrated ZnO solid solution phase in 18 m/o $\text{FeO}_{1.5}$ sample annealed at 1350 °C was formed during cooling when equilibrium favors ZnO with less Fe content and the Fe solubility in ZnO lattice decreases. The formation of a small amount of Fe deficient spinel phase is also expected to occur during cooling and follow the similar scenario as of 2 or 4 m/o $\text{FeO}_{1.5}$ sample, which has been discussed previously. Detailed discussions on the phase and microstructure change in 18 m/o $\text{FeO}_{1.5}$ sample will be given in next section.

To evaluate the lattice parameter with the Fe concentration of the ZnO solid solution phase, the ZnO (002) basal plane spacing or $\frac{c}{2}$ where c is the unit cell lattice parameter, was obtained and calculated from the peak fitting of each X-ray diffraction data and plotted against m/o $\text{FeO}_{1.5}$ in Figure 6.14. Referring to the phase diagram in Figure 6.1, the 2 m/o and 4 m/o $\text{FeO}_{1.5}$ compositions equilibrated at 1250 °C fall in the ZnO solid solution regime. Accordingly, it is reasonable to assume the lattice parameter of these two samples annealed at 1250 °C follow the Vegard's law which suggests a linear dependence of lattice parameter with solute concentration [131]. Together with the undoped ZnO, a straight line can be fitted through the data representing the Vegard's law prediction, as shown by the dashed olive line on the figure. Imposing the ZnO (002) basal plane spacing or $\frac{c}{2}$ of ZnO solid solution phases in the 18 m/o $\text{FeO}_{1.5}$ sample onto the Vegard's law, the actual Fe content in these solution phases can be estimated, as shown in Figure 6.14. The ZnO solid solution in the 18 m/o $\text{FeO}_{1.5}$ doped ZnO annealed at 1150 °C has only about 1.0 m/o $\text{FeO}_{1.5}$ where much of Fe ions participate in the formation of ZnFe_2O_4 spinel phase. This can be attributed to the fact that Fe solubility goes down with decreasing temperature, as seen from the phase diagram in Figure 6.1. About 0.6 m/o $\text{FeO}_{1.5}$ content was estimated in the less Fe concentrated ZnO solution phase in the 18 m/o $\text{FeO}_{1.5}$ doped ZnO annealed at 1350 °C, which has a quite small fraction; on the other hand, the Fe highly concentrated ZnO solid solution, which is the major phase, is estimated to have about 16.0 m/o $\text{FeO}_{1.5}$.

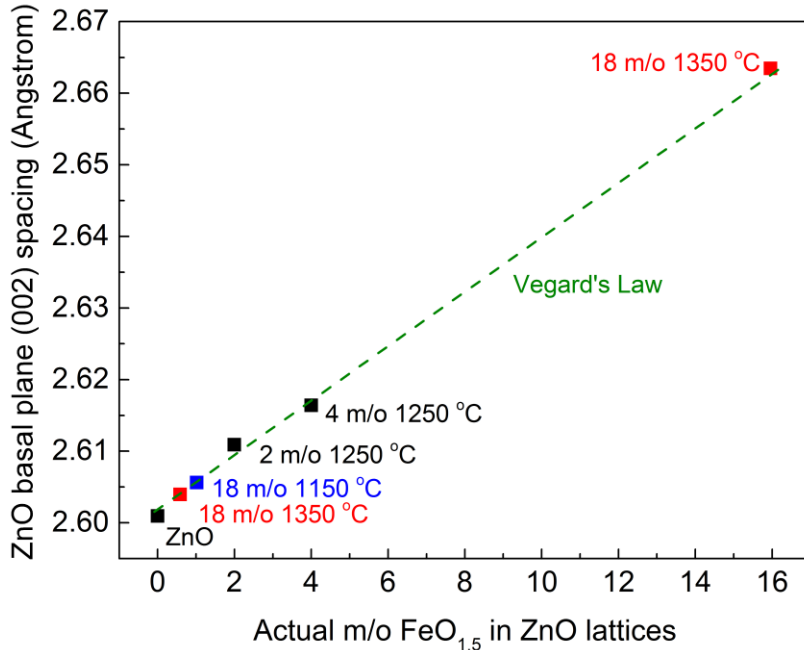


Figure 6.14: ZnO basal plane (002) spacing or $\frac{c}{2}$ measured by X-ray diffraction plotted as a function of actual m/o $\text{FeO}_{1.5}$ in ZnO lattices. The Vegard's law was determined based on the undoped ZnO, 2 and 4 m/o $\text{FeO}_{1.5}$ doped ZnO. The actual Fe content of ZnO solid solution in 18 m/o $\text{FeO}_{1.5}$ sample annealed at 1150 °C and 1350 °C were then estimated.

6.4.2 Microstructural Evolution of 18 m/o $\text{FeO}_{1.5}$ Sample

The microstructural and phase evolution of the 18 m/o $\text{FeO}_{1.5}$ sample annealed at 1150 and 1350 °C seems to be complex but can be understood as a sequence of two major steps. The first step is annealing at higher temperature, i.e. at 1350 °C in the single phase region. Clearly seen from the phase diagram in Figure 6.1, as temperature increases from 1150 to 1350 °C, the two-phase mixture of ZnO solid solution phase and ZnFe_2O_4 spinel phase are transforming to a ZnO solid solution phase with high Fe concentration. The second step is cooling down from 1350 °C to room temperature, during which a series of phase decomposition occur, as seen from our X-ray diffraction and electron microscopy observations. As cooling starts, the major phase change is the precipitation of

ZnFe_2O_4 spinel phase from the Fe highly enriched ZnO solid solution phase, obeying $(111)[110] // \text{ZnO}(0001)[11\bar{2}0]$ crystallographic relationship as observed from our electron microscopy studies. The EDS mapping of the 18 m/o $\text{FeO}_{1.5}$ sample annealed at 1350 °C suggests that the volume fraction of spinel phase is about 0.17, and the corresponding molar fraction is 0.09 after conversion; this molar fraction relates to about 1300 °C on the phase diagram according to the Lever rule. This finding also suggests that there was formation of ZnO solid solution phase with about 13 m/o $\text{FeO}_{1.5}$ when cooled down to this temperature. Nevertheless, a significant portion of Fe highly concentrated ZnO solid solution phase remained, which has about 16.0 m/o $\text{FeO}_{1.5}$ as discussed previously.

As the temperature decreases further on cooling, equilibrium favors the lower Fe concentration. It happens that a portion of ZnO solid solution phase changes to further lower Fe concentration, as cooling continuously carries on, the Fe solubility in ZnO decreases and ZnO with less Fe content is favored by equilibrium. This is indicated by the X-ray diffraction results that the less Fe concentrated ZnO phase in the sample annealed at 1350 °C has only about 0.6 m/o $\text{FeO}_{1.5}$. The Fe ions left the ZnO solid solution phase and form the Fe deficient spinel phase, as is the case of 2 or 4 m/o $\text{FeO}_{1.5}$ samples.

Based on the above discussions, the most striking finding on the 18 m/o $\text{FeO}_{1.5}$ sample that the grains are significantly refined after high temperature (1350 °C) annealing is explained. As the spinel phase grows from ZnO upon cooling from 1350 °C, either developing into the morphology of lamellar or platelet structures obeying the $(111)[110] // \text{ZnO}(0001)[11\bar{2}0]$ crystallographic relationship, or precipitating as fine

grains of 200 nm with limited further growth due to slowed diffusion process under cooling, original ZnO grains were segmented into much smaller grains and the average grain boundary spacing reduces from 2~3 μm to about 200 nm.

6.4.3 Thermal Conductivity

To facilitate the investigation of the compositional and structural role in thermal transport properties, the room temperature thermal conductivity was plotted against the actual m/o $\text{FeO}_{1.5}$ in ZnO lattices as shown in Figure 6.15. Fe addition and annealing temperature of each sample are indicated beside each symbol. As seen from the figure, thermal conductivity generally decreases with the actual Fe content in ZnO lattices. These observations on the effect of Fe addition on the thermal conductivity can be attributed to both the point defects introduced into the ZnO solid solution phase as well as the microstructural change such as new phase formation and morphological evolution. Point defects, which result in an atomic scale change, are normally more influential in affecting phonon transport as compared to microstructural change. In the current case of doping Fe_2O_3 into ZnO, the defect reaction is given by [76],



which suggests doping one molecule of Fe_2O_3 into ZnO creates two substitutional iron point defects on zinc sites and one zinc vacancy for charge balance. This is basically the same as the defect reaction when doping indium into ZnO. Following the similar scenario, the point defect scattering strength factor Γ can be calculated, and the first order approximation gives,

$$\Gamma \cong 0.67x \quad (6.2)$$

This suggests that with increasing Fe concentration x in ZnO lattice, the point defect phonon scattering is increasing. As a good approximation, the thermal conductivity κ is reversely proportional to Γ [126],

$$\kappa \propto \Gamma^{-\frac{1}{2}} \quad (6.3)$$

This suggests that the thermal conductivity decreases with the Fe content in the ZnO solid solution phase, which is basically seen from the experimental results as shown in Figure 6.15.

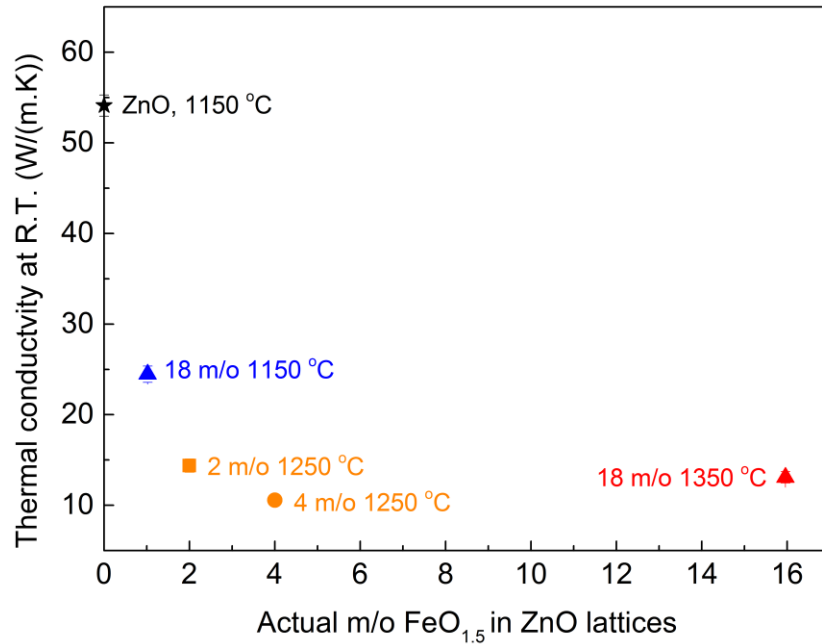


Figure 6.15: Room temperature thermal conductivity of Fe doped ZnO with actual m/o FeO_{1.5} in ZnO lattices. Each sample's composition and annealing temperature is indicated beside the symbol.

6.4.3 Thermoelectric Properties

In combination with my previous discussions on the actual Fe concentration in ZnO lattices based on the lattice parameter measurements, one may conclude that the electrical conductivities of all the samples, as shown in Figure 6.12, in general increases

with the actual Fe content in the ZnO solid solution phase. For instance, the 18 m/o $\text{FeO}_{1.5}$ doped ZnO sample annealed at 1350 °C, in which the ZnO solid solution phase has the largest Fe content among all the samples studied, demonstrates the highest electrical conductivity among all the samples.

This is especially true at high temperatures in the cases where all the electron donors are ionized and valance electrons jump from the donor defect states to the conduction band and therefore increase the free charge carrier concentration n . It is not clear about the role of ZnFe_2O_4 spinel phase, but at least it is not a very poor electrical conductor based on its measured band gap of ~ 2.5 eV [186]. Electrical conductivity σ and decreased Seebeck coefficient S , which have opposite dependence on n , are given by the following standard equations for the free electron semiconductors,

$$\sigma = ne\mu \quad (6.4)$$

$$S = -\frac{k_B}{e} \left[\ln \left(\frac{N_c}{n} \right) + A \right] \quad (6.5)$$

where e is the electronic charge and μ is the electron mobility. k_B is the Boltzmann's constant and N_c is the density of states at the conduction band edge given by $N_c = \left(\frac{2\pi m_e^* k_B T}{\hbar^2} \right)^{\frac{3}{2}}$ where m_e^* is the effective mass. A is a transport constant with a value in the range of 0 to 4 and depends on the electron scattering mechanism.

The Seebeck coefficient can be correlated with electrical conductivity by making a Jonker plot, in which the Seebeck coefficient is plotted against the natural logarithm of electrical conductivity [187], following the relationship below,

$$S = \frac{k_B}{e} (\ln(\sigma) - \ln(\sigma_0)) \quad (6.6)$$

where $\sigma_0 = N_c e \mu \exp(A)$. All the data measured at 800 °C were made in a Jonker plot and a reasonably good correlation between electrical conductivity and Seebeck coefficient is obtained with a linear slope of +86.15 μV/K, corresponding to the Seebeck value of classical free electron gas k_B/e [2], as shown in Figure 6.16. This suggests that the Seebeck coefficient of these Fe doped ZnO materials are determined by the free electron transport. The intercept, $\ln(\sigma_0)$, referred as “DOS-μ” product, was found to have a value of 10.0, very similar to the value of ZnO-In₂O₃ system. In addition, Ioffe plot analysis [94, 188, 189] suggests that the maximum achievable thermoelectric power factor PF_{\max} is dependent on $\ln(\sigma_0)$ given by the relation below,

$$\ln PF_{\max} = \ln \sigma_0 + \ln 4 \left(\frac{k_B}{e} \right)^2 - 2 \approx -19.33 + \ln \sigma_0 \quad (6.7)$$

This gives the $PF_{\max} \approx 0.9 \times 10^{-4}$ W/mK². Accordingly, one may foresee that with proper tuning of composition and structure, the Fe doped ZnO system has the potential of achieving similar level of thermoelectric power factor and figure of merit as that of ZnO-In₂O₃ system.

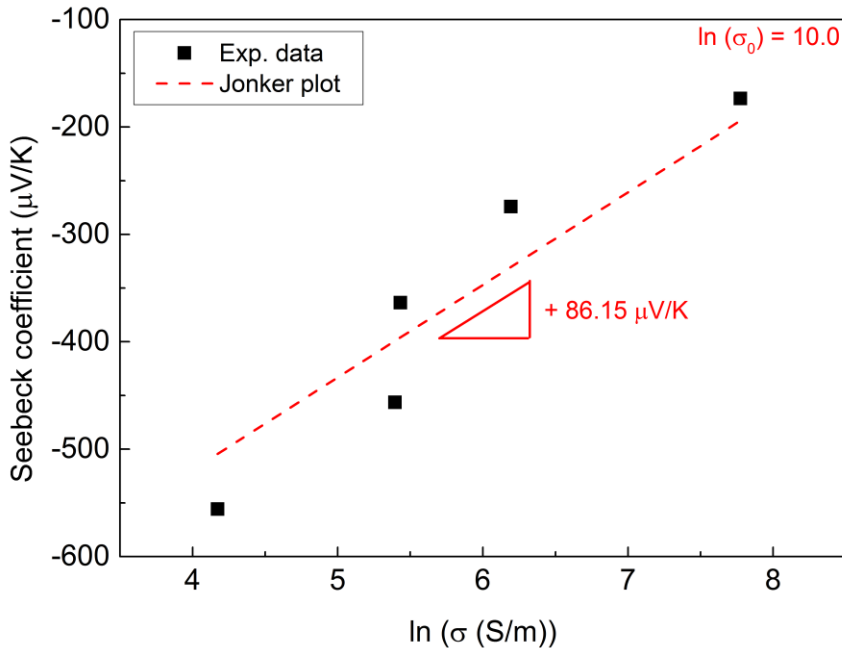


Figure 6.16: Jonker plot (Seebeck coefficient against natural logarithm of electrical conductivity) of Fe doped ZnO (including pure ZnO) measured at 800 °C. The best fit of the data with a slope of $+86.15 \mu\text{V/K}$ is shown as the dashed line.

The thermoelectric power factor PF and figure of merit ZT are calculated according to standard relation,

$$ZT = \frac{PF}{\kappa} T = \frac{S^2 \sigma}{\kappa} T \quad (6.8)$$

where κ is the measured thermal conductivity. Results of PF and ZT with temperature are presented in Figure 6.17 and Figure 6.18, respectively. The high temperature power factor basically increases with the actual Fe content in ZnO. The 18 m/o $\text{FeO}_{1.5}$ doped ZnO sample annealed at 1350 °C has the best power factor and figure of merit significantly superior to other samples in the range of medium to high temperatures. It also has the great advantage of keeping fine microstructures at high temperatures which are essential to maintain good thermoelectric properties. The 18 m/o $\text{FeO}_{1.5}$ doped ZnO

sample can be a promising high temperature thermoelectric oxide with further modification of electronic structure and/or microstructure by second doping.

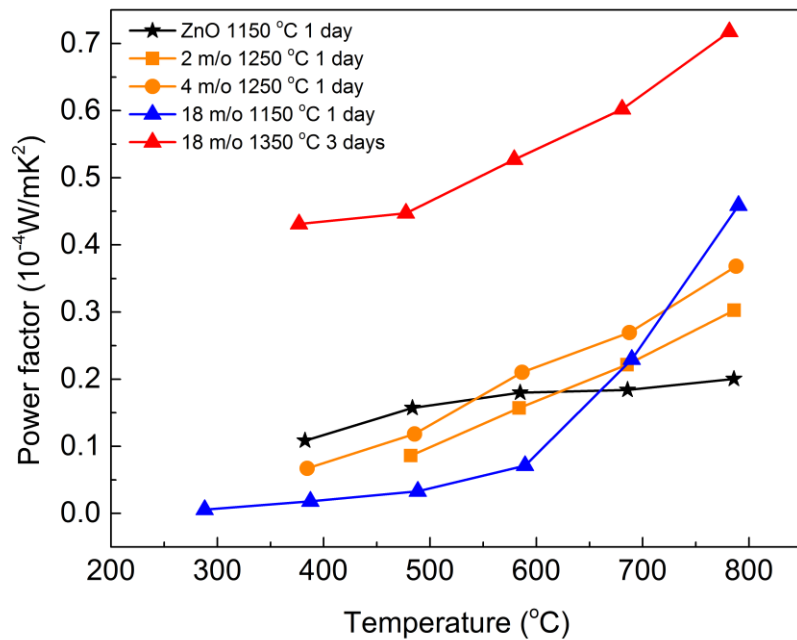


Figure 6.17: Power factor of Fe doped ZnO with temperature.

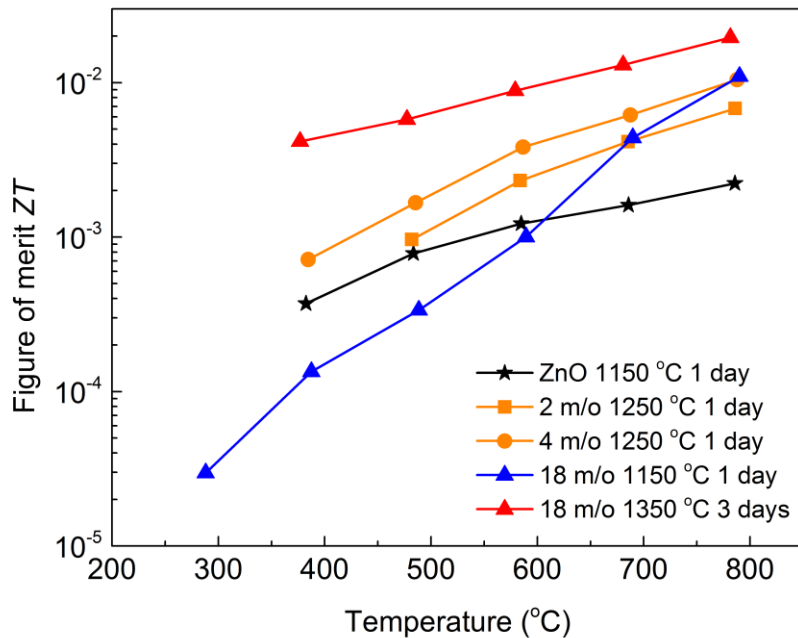


Figure 6.18: Figure of merit for Fe doped ZnO samples with temperature.

6.5 Conclusions

Systematic studies were made correlating the thermoelectric properties with phase and microstructure change of Fe doped ZnO materials. The Fe content in ZnO solid solution phase is strongly dependent on phase equilibria. Both thermal and electrical conductivity are observed to be sensitive to the actual Fe concentration in the ZnO phase. By properly choosing the composition and annealing temperature, the Fe highly concentrated ZnO solid solution phase can be produced, which significantly improves the overall thermoelectric properties by both reducing thermal conductivity (due to point defect scattering of phonons) and enhancing electrical conductivity (via providing electron donors).

All the samples investigated in the current work demonstrate free electron semiconductor behavior, as analyzed by correlating the Seebeck coefficient with electrical conductivity via a Jonker plot. The maximum achievable power factor of Fe doped ZnO is estimated to be comparable to that of ZnO-In₂O₃ system. In addition, significant structure refinement was observed in 18 m/o FeO_{1.5} doped ZnO sample after high temperature thermal treatment. These findings suggest that Fe doped ZnO can be a potential high temperature thermoelectric oxide system.

Chapter 7 Thermoelectric Properties of Ga Doped ZnO with Natural Nanostructures

In this chapter, the thermoelectric properties and structure of ZnO with several Ga concentrations were investigated. At low Ga concentration, the structure is a ZnO solid solution phase with fine structures and a significant reduction in thermal conductivity was observed. Electrical conductivity is substantially improved due to the creation of electron donors by Ga doping. With further increasing Ga addition beyond the solubility limit, both electrical and thermal conductivity decreases, due to the formation of a homologous $\text{Ga}_2\text{O}_3(\text{ZnO})_9$ natural superlattice structure with nanotwins and ZnGa_2O_4 spinel phase, both of which are less electrically conductive. The 18 m/o $\text{GaO}_{1.5}$ doped ZnO, the most heavily doped ZnO sample in the current work, demonstrates the lowest thermal conductivity due to the enhanced phonon scatterings by point defects and especially nanostructure interfaces. Calculated thermal conductivities with temperatures for both 2 and 18 m/o $\text{GaO}_{1.5}$ doped ZnO are consistent with measurements, which illustrate the critical role of nanostructure engineering in achieving very low thermal conductivity. All the Ga doped ZnO samples were found to be n-type semiconductors, and both electrical conductivity and Seebeck coefficient increases with temperature. A combined analysis of electrical conductivity and Seebeck coefficient with temperature implies a change of dominant electron scattering mechanism with Ga concentration. The Ga doped ZnO, with improved electrical conductivity due to introduced electron donors and reduced thermal conductivity arising from coarsening-resistant natural nanostructures, is believed to be a promising candidate for high temperature thermoelectric oxide materials.

7.1 Introduction

Similar to the electrical doping of ZnO with Al³⁺ [64, 66, 67, 190] and In³⁺ [31, 37, 39, 70], Ga³⁺ doping has also been widely applied to enhance the electrical conductivity of ZnO [96-98, 191]. This makes the Ga doped ZnO a possible candidate for thermoelectric oxides. In addition, homologous $\text{Ga}_2\text{O}_3(\text{ZnO})_k$ natural superlattice structures, in which k is an integral number basically denoting the number of Zn-O layers between Ga-O layers, have been reported in various studies [42-45, 177], especially in Ga highly doped ZnO. Belonging to the $\text{RMO}_3(\text{ZnO})_k$ type of homologous layered oxides [92, 170, 171, 173, 177], very low thermal conductivity can be expected due to the Zn(Ga)-O/Ga-O interfacial phonon scattering, which is a key factor in achieving high thermoelectric performance.

Nevertheless, a search of literature reveals that, except a few studies on the electrical and optical properties of Ga doped ZnO [45, 96, 97], few attempts have been made either on measuring the Seebeck coefficient or evaluating the thermal conductivity. In addition, no ZnO-Ga₂O₃ binary phase diagram exists to our knowledge which can be a useful guide to engineer the phase composition and structure. It is therefore the motivation of the present work to investigate the thermoelectric properties of ZnO with different Ga concentrations and then correlate the electrical and thermal transport properties with structure, especially the natural nanostructures.

7.2 Experiments

2, 4 and 18 m/o $\text{GaO}_{1.5}$ doped ZnO oxide powders were prepared from the high purity commercial nitrate powders, $\text{Zn}(\text{NO}_3)_2$ (99.999%, Sigma Aldrich®, USA) and $\text{Ga}(\text{NO}_3)_3$ (99.999%, Sigma Aldrich®, USA) using the wet chemistry - gel combustion method. After dehydrating the gel followed by the combustion process, the powders were further calcined and then were sintered into solid pellets in our current assisted densification processing system at 900 °C for 5 min. The entire sintering process was under vacuum with a constant compressive stress of 125 MPa. To compensate for the oxygen deficiency, all sintered samples were annealed at 1000 °C in air for 2 hours, followed by a post-annealing at 1150 °C for 1 day. During annealing, the samples were immersed in the powders of the same compositions and kept in a closed crucible to minimize the preferential evaporation of ZnO . Pure ZnO solid pellets were sintered from high purity commercial powders (99.999%, Sigma Aldrich®, USA) and annealed at 1150 °C for 1 day as reference. Synthesis and sintering details can be referred to Chapter 2.

X-ray diffraction data were recorded at a Bruker® D8 Discover Diffractometer and the phase compositions were analyzed using 2011 ICDD PDF database [111]. Raman spectra were collected from all the samples at room temperature with an excitation laser at 532 nm. SEM with EDS elemental mapping and HRTEM investigations were made on the 18 m/o $\text{GaO}_{1.5}$ doped ZnO sample. Thermal conductivity, electrical conductivity and Seebeck coefficient were measured for all the samples from room temperature up to 800 °C. Experimental details can be found in Chapter 2.

7.3 Results

X-ray diffraction results of all the samples annealed at 1150 °C for 1 day are presented in Figure 7.1, with the characteristic peaks of identified phases indicated at the bottom. Unlike ZnO with hexagonal structure, the ZnGa₂O₄ spinel phase has a cubic structure (ICDD# 00-038-1240). It has a few X-ray diffraction peaks which are most distinguishable from ZnO in the present scan range, as indicated by the red dashed lines in assistance of identifying its presence in the samples. The 2 m/o GaO_{1.5} doped ZnO basically has the ZnO solid solution phase without the formation of ZnGa₂O₄ spinel phase. However, apparent broadening of ZnO (103) peak (2θ at about 63 degree) was observed, suggesting the presence of fine structures, which are possibly nanotwin boundaries as reported in the 2 m/o GaO_{1.5} doped ZnO [192]. No ZnGa₂O₄ spinel phase was found in 4 m/o GaO_{1.5} sample but a homologous superlattice phase Ga₂O₃(ZnO)₉ was formed which has the orthorhombic structure (ICDD# 00-050-0448), in addition to the ZnO solid solution phase. Both Ga₂O₃(ZnO)₉ superlattice structure and ZnGa₂O₄ spinel phase were identified in the 18 m/o GaO_{1.5} doped ZnO where Ga₂O₃(ZnO)₉ has a dominant phase fraction.

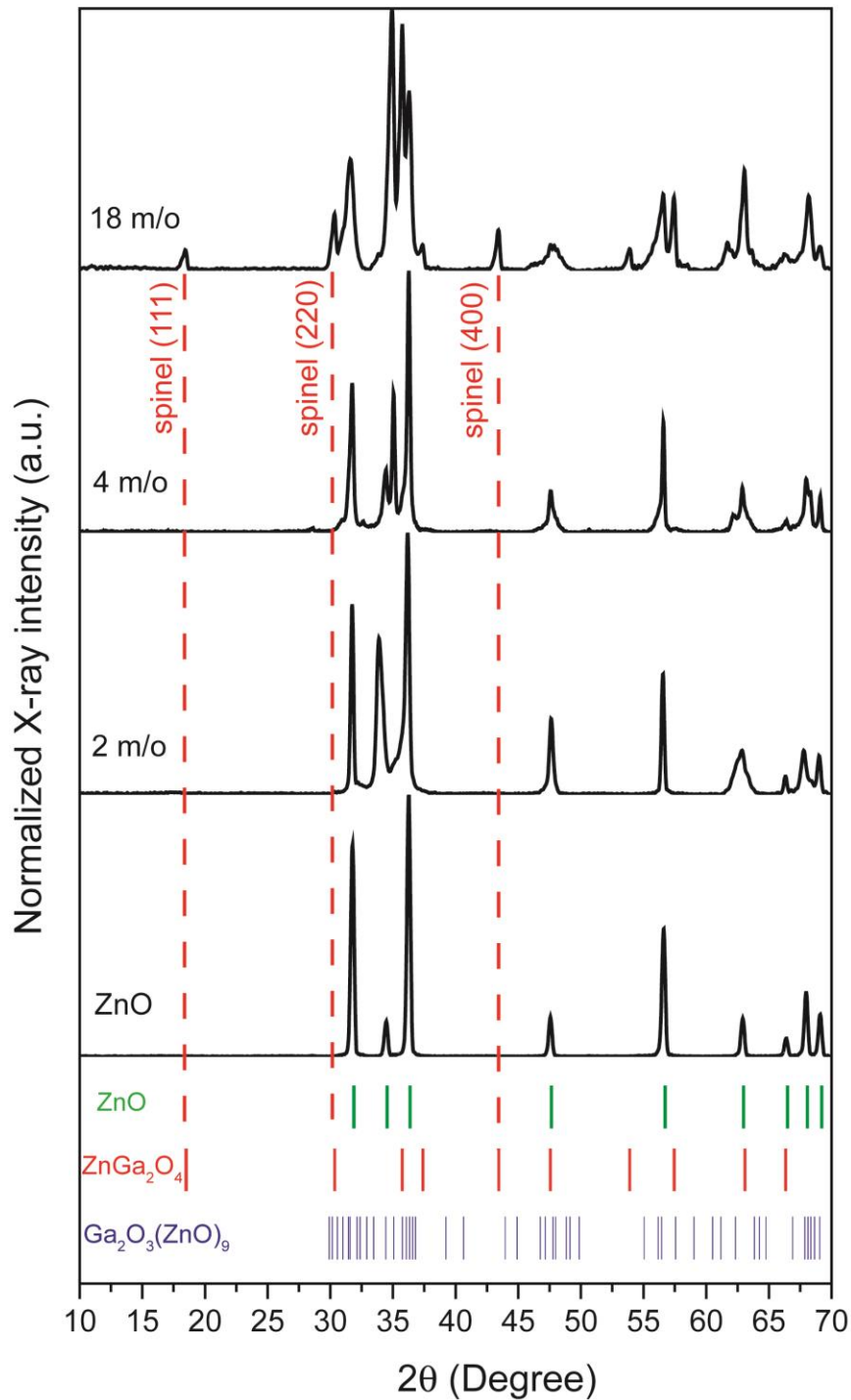


Figure 7.1: X-ray diffraction of Ga doped ZnO after 1150 °C 1 day thermal treatment. The characteristic peaks of $\text{Ga}_2\text{O}_3(\text{ZnO})_9$, ZnGa_2O_4 spinel and ZnO phases are indicated at the bottom of the figure. A few ZnGa_2O_4 spinel X-ray diffraction peaks as distinguished from other phases are indicated.

Raman spectra of all the samples are presented in Figure 7.2, with characteristic Raman modes of ZnO [193] and ZnGa₂O₄ [194] structure indicated on the spectra represented by the labels or dashed lines of olive and red colors, respectively. With increasing gallium addition, the Raman spectrum basically remains most of the ZnO characteristic Raman modes, whereas a systematic broadening and shift of ZnO Raman modes such as E₂ modes at 101 and 438 cm⁻¹ were observed. Characteristic Raman modes of ZnGa₂O₄ spinel structure with notation of “s” are labeled on the figure according to Van Gorkom *et al*’s report [194]; however, both T_{2g} at 611 cm⁻¹ and E_g mode at 636 cm⁻¹ were not observed by Preudhomme and Tarte [195], and there was also discrepancy between two references on whether the T_{1u} mode position is at 570 or 593 cm⁻¹. However, both peaks at 576 cm⁻¹ and 636 cm⁻¹, although with much reduced Raman intensity, were also observed in both 2 and 4 m/o GaO_{1.5} doped ZnO samples in which the spinel phases were not detected by X-ray diffraction. In addition, these Raman peaks appear much broader than those reported in the literature [194].

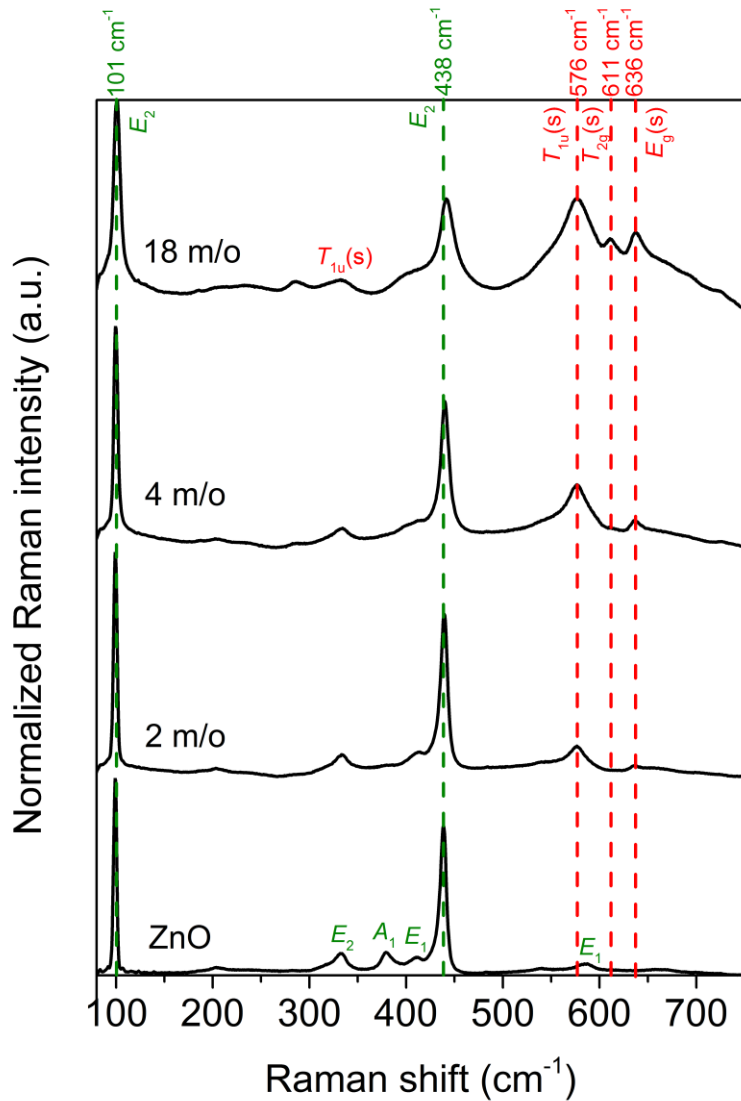


Figure 7.2: Raman spectra of Ga doped ZnO annealed at 1150 °C for 1 day; pure ZnO data was also enclosed. The characteristic Raman modes for ZnO and ZnGa₂O₄ spinel phase (s) are indicated by olive and red colored labels, respectively. Raman modes of significant interests in the present work are also indicated by the dashed lines across all the spectra.

Figure 7.3 presents the cross-section SEM image and EDS elemental mapping of typical microstructure observed in the cross-section of the 18 m/o GaO_{1.5} doped ZnO sample. Several gallium enriched grains of about ~ 1 μm size were observed in the matrix which is zinc rich phase. In combination with X-ray diffraction results, the zinc rich matrix phase is possibly the Ga₂O₃(ZnO)₉ modular phase and the gallium-rich grains are

ZnGa_2O_4 spinel phase. The homologous superlattice structures revealed by the high resolution TEM are shown in Figure 7.4, where nanotwin nanostructures were also observed. The twinning relationship with a crystallographic angle of 60° was clearly characterized from both the image and the corresponding diffraction pattern shown in the inset; this is consistent with literature findings that twin boundaries in Ga doped ZnO are on $\{01\bar{1}3\}$ planes of ZnO [42, 192]. The diffuse streaks of superlattice reflection spots corresponding to the planar faults or interfaces were also revealed in the electron diffraction pattern. In addition, the nanotwin boundary spacing is found to vary with locations, but has a typical length scale of $2 \sim 5$ nm.

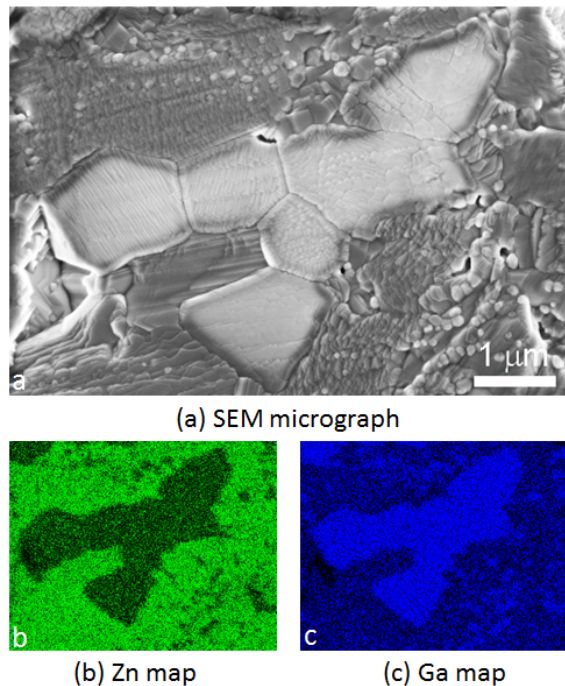


Figure 7.3: SEM image and corresponding EDS elemental mapping of cross-sectional microstructure in 18 m/o $\text{GaO}_{1.5}$ doped ZnO. (a) SEM image; (b) Zn map; (c) Ga map.

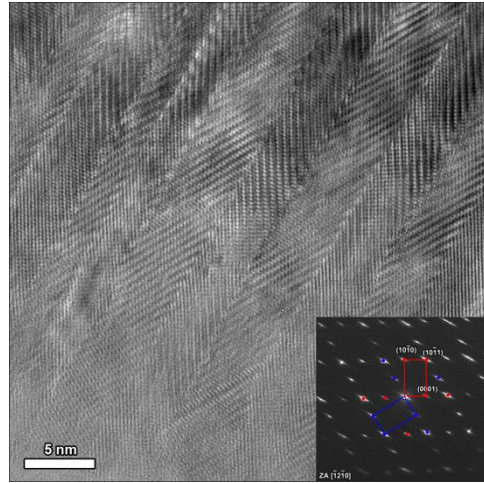


Figure 7.4: HRTEM image and the corresponding diffraction pattern (shown in the inset) of superlattice structures with nanotwins in 18 m/o $\text{GaO}_{1.5}$ doped ZnO . The HRTEM image reveals the nanotwin boundary with a crystallographic angle of about 60° . The electron diffraction pattern was taken along the $\bar{1}2\bar{1}0$ direction, which consists of two sets of lattices; in addition, diffuse superlattice reflection streaks were also observed.

Measured thermal conductivity of Ga doped ZnO from room temperature up to 800°C are presented in Figure 7.5. Also shown are the data of undoped ZnO and 18 m/o $\text{FeO}_{1.5}$ doped ZnO for comparison. All the samples presented here were annealed at 1150°C for 1 day. A significant reduction of thermal conductivity was observed even with a 2 m/o $\text{GaO}_{1.5}$ addition. With increasing addition of $\text{GaO}_{1.5}$, the thermal conductivity decreases and the temperature dependence is drastically reduced. As seen on the figure, the thermal conductivity of 18 m/o $\text{GaO}_{1.5}$ doped ZnO is virtually independent on temperature. Electrical conductivities measured with temperature up to 800°C are shown in Figure 7.6. All the Ga doped ZnO have much improved electrical conductivity than the undoped ZnO , and the 2 m/o $\text{GaO}_{1.5}$ doped ZnO demonstrates highest electrical conductivity whereas the 4 and 18 m/o $\text{GaO}_{1.5}$ doped ZnO samples have similar values in the temperature range measured. In addition, electrical conductivity increases with temperature for the 2 m/o $\text{GaO}_{1.5}$ doped ZnO but less noticeable for the 4 and 18 m/o

$\text{GaO}_{1.5}$ doped ZnO samples. Figure 7.7 presents the Seebeck coefficient measured with temperature. Across the entire temperature range of measurements, all the samples studied were found to be n-type semiconductors as seen from their negative values of Seebeck coefficient. In addition, Seebeck coefficient of all the Ga doped ZnO samples increases with temperature.

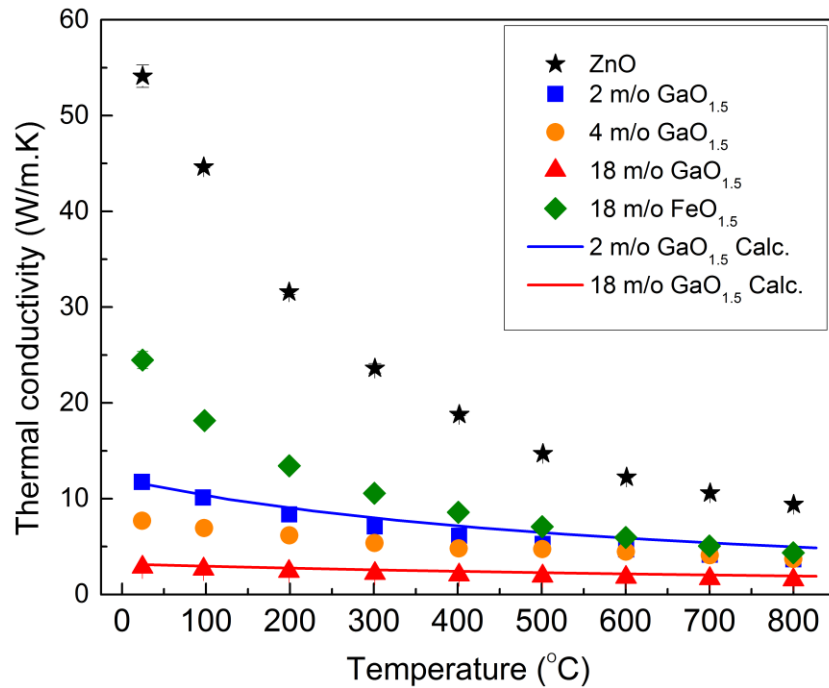


Figure 7.5: Thermal conductivity measured with temperature for Ga doped ZnO samples with date of undoped ZnO well as 18 m/o $\text{FeO}_{1.5}$ doped ZnO shown for comparisons, all represented by scattered symbols. All the samples presented on this figure were annealed at 1150 °C for 1 day. The blue and red solid curves represent the calculation results for the 2 m/o and 18 m/o $\text{GaO}_{1.5}$ doped ZnO samples, respectively.

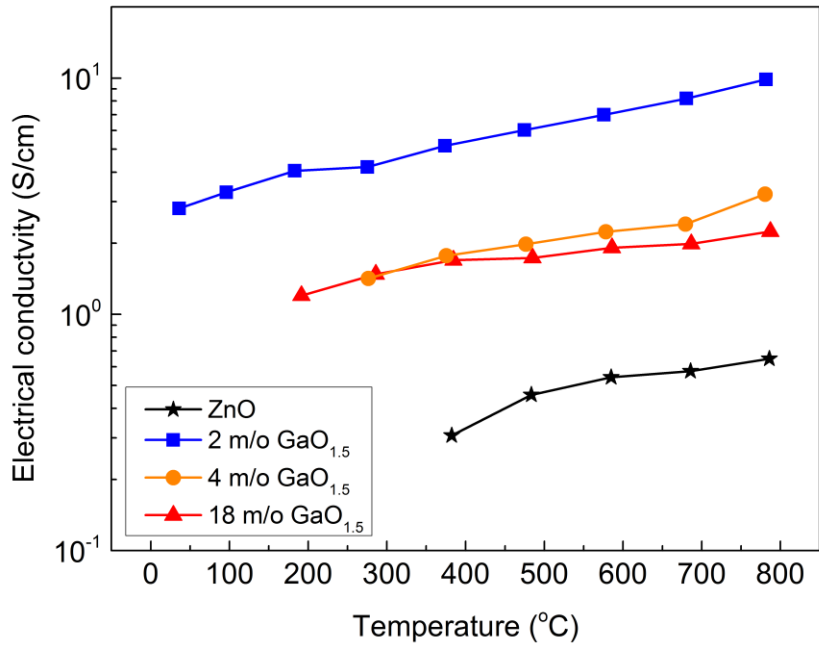


Figure 7.6: Electrical conductivity of Ga doped ZnO measured with temperature up to 800 °C. Pure ZnO data are also indicated. The lines through the data points are guides to the eye.

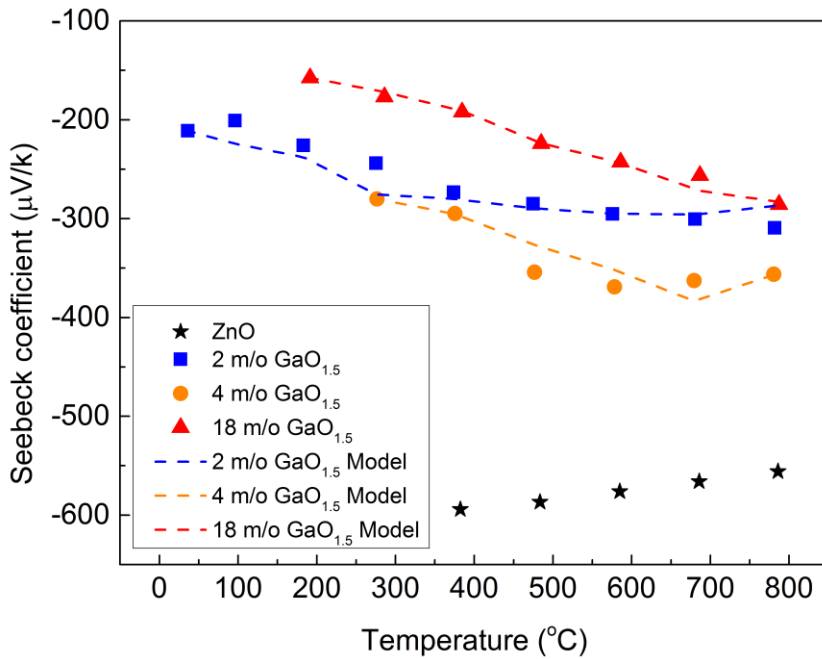


Figure 7.7: Seebeck coefficient of Ga doped ZnO measured with temperature up to 800 °C. The experiment results are shown as scattered symbols, and the modeling fits of the measured data are represented by dashed lines with the same colors of the measurement data symbols.

7.4 Discussions

7.4.1 Solid Solution and Nanostructures of Ga doped ZnO

It is important to clarify the phases or microstructures present in these samples, as an important clue to understand the thermoelectric properties. It is unambiguous from the combined results of X-ray diffraction and Raman spectroscopy that there are $\text{Ga}_2\text{O}_3(\text{ZnO})_9$ like homologous superlattice structures and ZnGa_2O_4 spinel phase (may also with a small amount of ZnO solid solution phase) present in the 18 m/o $\text{GaO}_{1.5}$ doped ZnO . The X-ray diffraction results clearly exclude the presence of spinel phases in both 2 and 4 m/o $\text{GaO}_{1.5}$ doped ZnO samples. However, the broad Raman peaks at 576 and 636 cm^{-1} , which were assigned to T_{1u} and E_g modes of ZnGa_2O_4 spinel phase by Van Gorkom *et al.* [194], were observed in all the three Ga doped ZnO samples as seen in Figure 7.2. It is in question whether they arise from the ZnGa_2O_4 spinel structure, considering that T_{2g} mode at 611 cm^{-1} and E_g mode at 636 cm^{-1} were not observed by Preudhomme and Tarte [195] as well as a non-negligible discrepancy on the peak position of Raman mode at 576 cm^{-1} . Since in both references [194, 195] the ZnGa_2O_4 spinel phase was made from solid state reactions of ZnO and Ga_2O_3 powders, it is not impossible that homologous superlattice compounds $\text{Ga}_2\text{O}_3(\text{ZnO})_k$ were formed and some of their Raman modes were assigned to the ZnGa_2O_4 spinel phase such as those at 576 and 638 cm^{-1} . Also of importance is that these Raman peaks in our samples are much broader than those reported by Van Gorkom *et al.* [194]; this is similar to what we have observed in the Raman spectra of $\text{In}_2\text{O}_3(\text{ZnO})_k$ superlattices.

Furthermore, in combination with X-ray diffraction results, only the Raman peak at 611 cm^{-1} may be undoubtedly recognized as the T_{2g} mode of ZnGa_2O_4 spinel phase. As

both 4 and 18 m/o $\text{GaO}_{1.5}$ doped ZnO are found to have $\text{Ga}_2\text{O}_3(\text{ZnO})_9$ superlattice structures by X-ray diffraction analysis, together with the HRTEM observations of the nanostructures, it therefore further increases the possibility that the two broad peaks centered at 576 and 636 cm^{-1} could be characteristic Raman modes of these superlattice nanostructures instead of ZnGa_2O_4 spinel phase. These two Raman peaks, with much reduced Raman intensity, are also observed in the 2 m/o $\text{GaO}_{1.5}$ doped ZnO sample. With literature findings on the HRTEM observations of nanotwin boundaries in a 2 m/o $\text{GaO}_{1.5}$ doped ZnO [192], as well as the X-ray (103) peak broadening we observed in this sample, we may conclude that nanostructures are also present in the 2 m/o $\text{GaO}_{1.5}$ doped ZnO . In addition, a systematic shift and broadening of ZnO Raman modes with increasing Ga addition, such as E_2 mode at 101 and 438 cm^{-1} , also indicates an increasing strained or defective lattice.

These findings may also suggest that the Ga solubility in ZnO could be around 2 m/o, similar to the findings by Wang *et al.* [96] which reports a 2.7 m/o Ga solubility in ZnO in the temperature range of 1000 to 1200 °C. Exceeding the Ga solubility in ZnO phase may result in one or both of the following two consequences: the formation of ZnGa_2O_4 spinel phase as similar to the Al doped ZnO system [62, 64-66, 196], and/or the homologous $\text{Ga}_2\text{O}_3(\text{ZnO})_k$ superlattice compounds which have been reported in literatures [42, 43, 45, 177], as similar to the indium doped ZnO system [90-92, 197].

7.4.2 Thermal Transport Properties

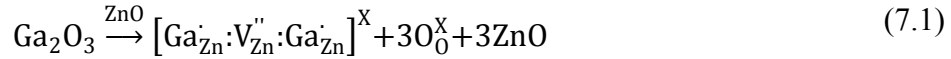
Since electrical conductivities of all the samples across the measurement temperatures are not high enough to consider the electronic contribution to the thermal conductivity by Wiedemann-Franz law, as shown in Figure 7.6, only lattice or phonon thermal conductivity will be considered in the following discussions.

Drastic reduction of thermal conductivity with Ga addition was observed suggesting the enhanced phonon scatterings due to the introduction of defects. In addition, the significantly reduced temperature dependence of thermal conductivity with Ga addition implies the switching of dominant phonon scattering from phonon – phonon scatterings, which is temperature dependent, towards a combination of point defect and interface scatterings. Although the ZnGa_2O_4 spinel phase was present in 18 m/o $\text{GaO}_{1.5}$ doped ZnO , but its effect on reducing thermal conductivity can be much less critical considering its minor phase fraction (at most ~ 0.20 in the 18 m/o $\text{GaO}_{1.5}$ sample) as well as its grain size of about $1 \mu\text{m}$, as seen in Figure 7.3. This is in contrast with either point defects acting at atomic scale or superlattice and nanotwins at nanometer scale. Accordingly, with the lack of the knowledge on the intrinsic thermal conductivity of ZnGa_2O_4 spinel phase, it is not inappropriate to assume that the role of ZnGa_2O_4 spinel phase is much less significant in scattering phonons, and much emphasis will be placed on the point defects and nanostructure interfaces due to Ga doping.

To evaluate and investigate the role of point defects and nanostructures on thermal conductivity, I will apply the thermal conductivity model based on phonon transport that I have developed and described in Chapter 3 to both 2 and 18 m/o $\text{GaO}_{1.5}$ doped ZnO . The lengthy list of mathematic equations of the thermal conductivity model

employed will not be repeated here, but can be found in Chapter 3 for detailed physical and mathematical derivations and calculations.

The point defects introduced by doping ZnO with gallium includes gallium substitutional ions on zinc sites as well as zinc vacancies for charge compensation while there are no defects on anion sites. The corresponding defect reaction is given by [198],



Following the same calculation procedure for the indium or iron doped ZnO (Chapter 4 and 6), the point defect scattering strength parameter Γ , to the first order approximation, is obtained as

$$\Gamma \approx 0.65x \quad (7.2)$$

where x is the gallium concentration x in ZnO lattice. Inputting the gallium concentration $x = 0.02$ for 2 m/o GaO_{1.5} doped ZnO, the point defect scattering strength parameter is obtained as $\Gamma = 1.31 \times 10^{-2}$ (SI units). In addition, the lower bound for the average Ga₂O₃(ZnO)_k superlattice interface spacing L can be estimated based on the Ga addition, as what we did for the In₂O₃(ZnO)_k superlattices (which can be referred to Chapter 4). A value of $L = 25.7$ nm was obtained for the 2 m/o GaO_{1.5} doped ZnO.

The solubility limit of gallium in ZnO has been reported to be around 2.7 atomic percent at the synthesis temperature of 1000 to 1200 °C [96], which suggests that ZnO solid solution phase is saturated with gallium in the 18 m/o GaO_{1.5} doped ZnO sample. It is therefore reasonable to use the solubility limit of $x = 0.027$ to calculate the point defect scattering strength parameter Γ according to equation 7.2, which was obtained as 1.77×10^{-2} (SI units). Furthermore, the average spacing L of Ga₂O₃(ZnO)₉ superlattice

interfaces or nanotwin boundaries needs to be estimated in order to perform calculations for the 18 m/o $\text{GaO}_{1.5}$ doped ZnO . Our microscopy reveals that the average nanotwin boundary spacing is about ~ 3 nm; however, the interfacial spacing of Ga-O layers in the $\text{Ga}_2\text{O}_3(\text{ZnO})_9$ superlattice phase is smaller about $\frac{c_0}{2} \approx 1.65$ nm where c_0 is the unit cell parameter of $\text{Ga}_2\text{O}_3(\text{ZnO})_9$ modular compound [42, 177]. This suggests that the superlattice interfaces have a higher density than nanotwin boundaries and therefore are more representative of interface scattering in the 18 m/o $\text{GaO}_{1.5}$ doped ZnO sample. Accordingly, it is appropriate to choose an average interface spacing $L = \frac{c_0}{2} = 1.65$ nm to carry on the calculations.

Substituting these values into the thermal conductivity model (equation 3.76) that I have derived in Chapter 3, the thermal conductivities of the 2 and 18 m/o $\text{GaO}_{1.5}$ doped ZnO with randomly distributed point defects and planar interfaces were calculated with temperature, as represented by the blue and red solid curves in Figure 7.5. As seen from the figure, there are excellent agreements between the calculation and measurement results. This suggests that the point defect and nanoscale interfaces play a dominant role in controlling phonon transport processes in this Ga heavily doped ZnO with natural nanostructures. Furthermore, as the interface spacing reduces from 25.7 to 1.65 nm, the calculated room temperature thermal conductivity (as also representative of measurements) decreases from 11.6 to 3.1 W/mK; this is about four-fold reduction, clearly revealing the crucial effect of nanostructure interfaces on phonon scattering.

7.4.3 Electrical Transport Properties

All the Ga doped ZnO samples demonstrate greater electrical conductivity as compared to the undoped ZnO, as seen in Figure 7.6. This suggests that the doped Ga ions provide the electron donors and therefore increase the charge carrier concentration. However, through the entire measurement temperature, the electrical conductivity basically decreases with the increasing Ga addition, with 18 m/o Ga_{1.5} doped ZnO having the lowest electrical conductivity. The systematic decrease of electrical conductivity with Ga addition can be correlated with the change in phase compositions and structure. As has been discussed previously, based on various characterization techniques, there is no doubt that ZnGa₂O₄ spinel phase formed in the 18 m/o Ga_{1.5} doped ZnO. This spinel phase is a less electrical conducting phase than pure ZnO, due to its large band gap of 4.0 eV and electrical conductivity of 10⁻¹ S/cm at 290 K [199] as compared with the band gap of 3.3 eV for ZnO [95]. This is very similar to the observations on Al doped ZnO where electrical conductivity initially increases with Al addition but drops when the Al solubility in ZnO lattice is reached and a less conducting ZnAl₂O₄ spinel phase forms [190]. Furthermore, the content of superlattice or nanotwin interfaces increases with Ga addition; these nanostructures can also scatter electrons to some extent and induce an increase in electrical resistivity [45].

Also of interest is that all the Ga doped ZnO samples investigated in the present work demonstrate an increase of both electrical conductivity and Seebeck coefficient with temperature, especially the 2 m/o Ga_{1.5} doped ZnO. This finding is opposite to the behavior of the undoped ZnO where electrical conductivity and Seebeck coefficient normally behaves in an opposite trend with temperature as the former one increases with

carrier concentration whereas the latter decreases [6]. In addition, the Seebeck coefficient of a semiconducting material normally decreases with temperature according to the following relation with the band gap E_g [2],

$$S \approx \left(\frac{k_B}{e}\right) \frac{E_g}{k_B T} \quad (7.3)$$

where k_B is the Boltzmann's constant and e is the electronic charge. Our observations that the Seebeck coefficient of Ga doped ZnO materials does not follow the temperature dependence given by equation 7.3 suggest that there are other transport parameters which needs to be considered. In order to understand and interpret our observations, a more complete expression for Seebeck coefficient needs to be used which incorporates both influence of temperature T as well as the carrier concentration n , as given by the following relation [2, 6],

$$S \approx \frac{2k_B^2}{e\hbar} m^* T (3\pi^2 n)^{-\frac{2}{3}} \quad (7.4)$$

where m^* is the effective mass of charge carriers which are electrons in n-type semiconductors. The above equation suggests that the Seebeck coefficient is mostly controlled by the change in temperature and carrier concentration, i.e.

$$S \propto T \cdot n(T)^{-\frac{2}{3}} \quad (7.5)$$

It is noted that the carrier concentration $n(T)$ is also dependent on temperature T , which can be extracted from the temperature dependence of electrical conductivity $\sigma(T)$, according to the following standard equation,

$$\sigma(T) = n(T) e \mu(T) \quad (7.6)$$

where $\mu(T)$ is the electron mobility and is also a function of temperature [200],

$$\mu(T) = \frac{4}{3\pi^{\frac{1}{2}}} \Gamma\left(r + \frac{5}{2}\right) \frac{e\tau_0(k_B T)^r}{m^*} \quad (7.7)$$

where Γ here is the gamma function, $\tau_0(k_B T)^r = \tau_e$ is the electron relaxation time where τ_0 and r are constants for a given scattering process. The important constant in this equation is r which reflects the temperature dependence of carrier mobility. The two bounds or extreme values of r are $-3/2$ for electron scattering dominated by lattice vibrations or phonons, and $3/2$ for ionized impurities dominated scattering, respectively. In compilation of the equations 7.2 to 7.7 and with experimental data of electrical conductivity, we are able to model the temperature dependence of Seebeck coefficient with r as the only fitting parameter. As shown in Figure 7.7, the best modeling fit of the temperature dependence of Seebeck coefficient for all the Ga doped ZnO are represented by the dashed lines with same colors of the scattered symbols of measurements. The model describes reasonably well the temperature dependence of Seebeck coefficients measured in all the Ga doped ZnO. Since normally more than one source of scattering is present, for instance, both lattice phonons and impurities in the current case, the derived value of r is a reflection of a combination of both electron scattering mechanisms; however, which one is relatively more dominant in the material can be indicated based on its sign and value.

Lattice (phonon) scattering, which mostly dominates in the undoped or lightly doped materials, is found to be the primary electron scattering mechanism in the 2 m/o $\text{GaO}_{1.5}$ doped ZnO for which a negative value of $r = -0.1$ was obtained. This suggests that electron mobility decreases with temperature, as at higher temperatures there are

more phonons and therefore increased phonon scattering that tends to reduce mobility. Ionized impurity scattering, which is normally observed in the heavily doped materials, is found to be governing in the 4 and 18 m/o GaO_{1.5} samples, both of which have a derived value of 0.32 for r . When ionized impurities are the main source of scattering, electron mobility increases with temperature as the thermal speeds of the carriers increase with temperature and therefore spends less time near an ionized impurity leading to the reduced scattering effect by the ions. The above combined analysis of electrical conductivity and Seebeck coefficient with temperature suggests a transition in the dominant electron scattering mechanism with Ga doping concentration, i.e. from lattice or phonon scattering to ionized impurity scattering.

7.4.4 Thermoelectric properties

Thermoelectric power factor PF and figure of merit ZT were calculated based on the measured thermal conductivity κ , electrical conductivity σ and Seebeck coefficient S , according to the definition equation,

$$ZT = \frac{PF}{\kappa} T = \frac{S^2 \sigma}{\kappa} T \quad (7.8)$$

where T is the absolute temperature. The results plotted against temperature are shown in Figure 7.8 and Figure 7.9, respectively. The 2 m/o GaO_{1.5} sample demonstrates highest power factor over the measurement temperature range due to its large electrical conductivity and intermediate level of Seebeck coefficient. With its considerably lower thermal conductivity, it also has the highest figure of merit as seen in Figure 7.9. The power factor of 18 m/o GaO_{1.5} sample is even smaller than the undoped ZnO due to the presence of ZnGa₂O₄ and superlattice compounds which are less electrically conducting

phases or structures. Nevertheless, its drastically lower thermal conductivity makes it superior to the undoped ZnO and appears as comparable to the 4 m/o GaO_{1.5} sample.

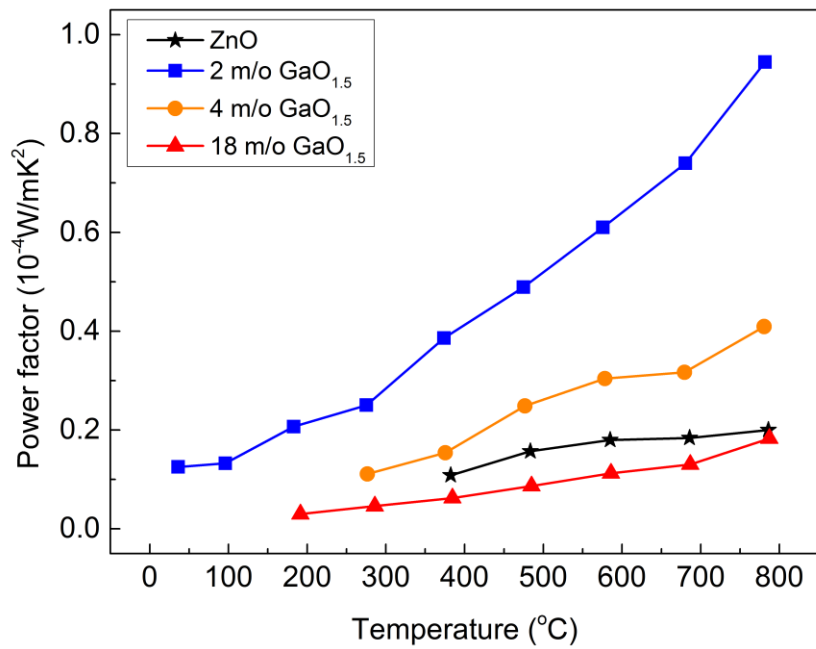


Figure 7.8: Power factor of Ga doped ZnO as a function of temperature; the undoped ZnO data are also enclosed. The lines through the data points are guides to the eye.

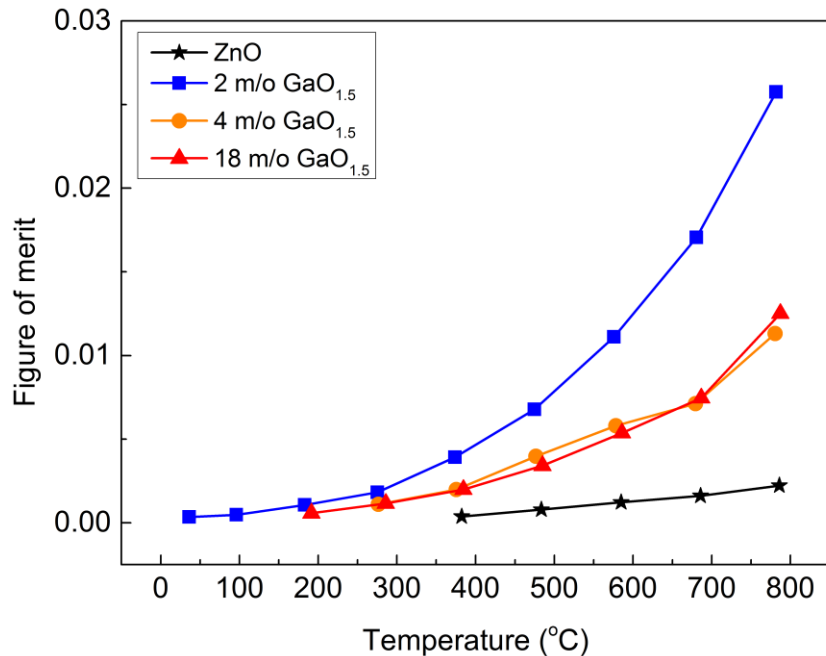


Figure 7.9: Figure of merit of Ga doped ZnO with temperature, with the undoped ZnO data also enclosed. The lines through the data points are guides to the eye.

7.5 Conclusions

In conclusion, correlation between thermoelectric properties and the microstructure of Ga doped ZnO were investigated. At low Ga addition, the structure is a ZnO solid solution phase but with the presence of fine structures based on a combination of X-ray diffraction and Raman spectroscopy studies. The presence of these fine structures was found to result in a drastic reduction in thermal conductivity. On the other hand, a significant enhancement in electrical conductivity was observed due to the creation of electron donors by Ga doping.

With further increasing Ga addition beyond its solubility in ZnO, a $\text{Ga}_2\text{O}_3(\text{ZnO})_9$ homologous superlattice structure with nanotwins as well as ZnGa_2O_4 spinel phase are

formed, both of which are less electrically conductive, leading to the decreasing electrical conductivity with Ga addition. The thermal conductivity, due to the introduced point defect and nanostructure interfaces, were significantly lowered. Modeling also performed on for the 2 and 18 m/o $\text{GaO}_{1.5}$ doped ZnO, with the role of point defect and especially the nanostructure interface scatterings of phonons clearly illustrated.

In addition, a combined analysis of electrical conductivity and Seebeck coefficient with temperature suggests the different operating electron scattering mechanisms. With increasing Ga addition, we observed a transition in the dominant scattering mechanism from lattice (phonon) scattering to ionized impurity scattering.

All the Ga doped ZnO demonstrate significantly improved thermoelectric properties as compared to the undoped ZnO. The 2 m/o $\text{GaO}_{1.5}$ doped ZnO was found to have the highest power factor and figure of merit due to its highest electrical conductivity and relatively large Seebeck coefficient. The 18 m/o $\text{GaO}_{1.5}$ doped ZnO, although with a small power factor, has a figure of merit comparable to 4 m/o $\text{GaO}_{1.5}$ doped ZnO due to its very low thermal conductivity arising from strong nanostructure interface scattering of phonons. Similar to the ZnO-In₂O₃ system, the Ga doped ZnO is also a promising high temperature thermoelectric oxide based on its natural nanostructures, which are coarsening-resistant, as well as the improved electrical transport properties via electron doping.

Chapter 8 Conclusions and Outlook

In this chapter, I will summarize and conclude the findings on the structure and thermoelectric properties of ZnO based materials, mainly focusing on the trivalent doping of ZnO including In^{3+} , Ga^{3+} and Fe^{3+} . Future work of this subject will then be suggested.

8.1 Phase Equilibria, Nanostructure and Thermoelectric Properties of Trivalent Elements Doped ZnO Oxides

Doping of ZnO with trivalent elements, indium, gallium, iron and aluminum (not presented) have been investigated. All the elements have certain solid solubility in ZnO, below which all these solute ions form randomly distributed substitutional point defects while creating the zinc vacancies for charge balance. These point defects significantly reduce the thermal conductivity due to the mass and size mismatch at atomic scale. Within the solubility range, the thermal conductivity decreases with increasing point defect concentration directly related to the dopant content in ZnO. Electrical conductivity generally increases with solute concentration as well, especially at elevated temperatures, due to the increased number of carriers arising from the activated dopant ions as electron donors. All the materials investigated are identified as n-type semiconductors as seen from their negative values of Seebeck coefficient. The thermoelectric power factor and figure of merit, the latter of which has the coupling of electrical and thermal transport, general increases with both doping concentration as well as temperature within the solubility regime.

When the solubility is exceeded, the phase and structure as well as thermoelectric properties vary with the specific dopant element. Generally, there are two possible consequences of exceeding the solubility: the formation of (a) spinel phase and (b) natural nanostructures like $M_2O_3(ZnO)_k$ homologous superlattice phases. Whether either or both of them occur depends on the specific dopant species. In the case of aluminum doped ZnO, as the Al addition goes beyond the solubility (which depends on sample preparation and post-treatment but generally believed to be around 1 or 2 m/o), the $ZnAl_2O_4$ spinel phase forms which is a less electrically conductive phase than ZnO. The electrical conductivity decreases with increasing fraction of the $ZnAl_2O_4$ spinel phase [190]; however, the drop of electrical conductivity with the formation of $ZnAl_2O_4$ spinel phase is not substantial in my observations up to 4 m/o Al doping. This may be explained by the fact that the band gap of $ZnAl_2O_4$ spinel, which is about 3.8 eV [201, 202], is close to that of ZnO with a value of 3.3 eV [95]. A summary of band gap for several zinc oxide spinel phases are presented in Table 8.1. In addition, although a recent study reports that nanoparticles of $ZnAl_2O_4$ spinel phase is effective in lowering thermal conductivity [203], my experiment results (not shown) suggest little effect of this spinel phase on the thermal conductivity. Accordingly, the increase of thermoelectric figure of merit with Al doping can be largely attributed to the enhancement of electrical conductivity.

Table 8.1: Summaries of band gap for several zinc spinel phases.

Phase	Band gap, eV
ZnO	3.3 [95]
ZnAl ₂ O ₄	3.8 [201, 202]
ZnFe ₂ O ₄	2.43 – 2.61 [186]
ZnGa ₂ O ₄	4.0 [199]; 5.0 [204]

The Fe doped ZnO is similar. A ZnFe₂O₄ spinel phase forms when the Fe solubility is exceeded. Due to the lack of the knowledge on the intrinsic thermal conductivity of this spinel phase, it is not clear how this spinel phase affects the overall thermal conductivity. It seems from my experimental results that the actual Fe content in the ZnO plays a central role in controlling both the electrical and thermal conductivity. In addition, the 18 m/o FeO_{1.5} heavily doped sample, which has the largest fraction of ZnFe₂O₄ spinel phase (about 0.17 in volume fraction) among all the Fe doped ZnO samples studied, demonstrates the highest electrical conductivity. This may imply that the ZnFe₂O₄ spinel phase is at least not a poor electrical conducting phase. In fact, it is reported that the ZnFe₂O₄ spinel phase has a band gap of about 2.5 eV [186], even smaller than that of ZnO.

In the case of indium doped ZnO, we have observed a solubility of about 0.05 at 1250 °C and 0.10 at 1150 °C. However, when the solubility is exceeded, no ZnIn₂O₄ spinel phase was observed; instead, homologous In₂O₃(ZnO)_k superlattice phases start

forming. At relatively low indium concentration, the structure consists of ZnO solid solution with planar faults or inverse domain boundaries associated with the disordered superlattice structure where the interface spacing normally varies with locations. Further increasing indium concentration or temperature, ordered $\text{In}_2\text{O}_3(\text{ZnO})_k$ modular phases become stable where the interface spacing tends to be more constant. The thermal conductivity is further decreased due to the phonon scatterings by these superlattice interfaces, in addition to the randomly distributed point defects. The thermal (Kapitza) resistance of $\text{In}_2\text{O}_3(\text{ZnO})_k$ superlattice interfaces is found to be $5.0 \pm 0.6 \times 10^{-10}$ m²K/W by fitting the temperature and indium concentration dependence of the thermal conductivity to the Klemens-Callaway's thermal conductivity model. Electrical conductivity generally increases with indium addition, even above the indium solubility, and irrespective of the formation of $\text{In}_2\text{O}_3(\text{ZnO})_k$ modular phases. This may also be correlated with relatively smaller band gap of $\text{In}_2\text{O}_3(\text{ZnO})_k$ phase, $\sim 2.7 - 2.9$ eV, as has been summarized and listed in Table 1.1 in Chapter 1. These investigations suggest that the superlattice interfaces associated with the $\text{In}_2\text{O}_3(\text{ZnO})_k$ phases are capable of blocking phonons while relatively permissive to electrons, leading to a reduced thermal conductivity and enhanced electrical conductivity, therefore a substantially increased thermoelectric figure of merit.

Exceeding the solubility of Ga in ZnO lattices yields both ZnGa_2O_4 spinel and $\text{Ga}_2\text{O}_3(\text{ZnO})_k$ homologous superlattice phases. The formation of $\text{Ga}_2\text{O}_3(\text{ZnO})_k$ homologous superlattices and nanotwin boundaries, which provides strong interfacial scattering of phonons, significantly reduces the thermal conductivity. The role of ZnGa_2O_4 spinel phase on thermal conductivity is not clear without the knowledge of its

intrinsic thermal conductivity. Nevertheless, considering its grain size of micrometers, its effect on thermal conductivity seems not to be critical as compared to nanostructures. The electrical conductivity decreases with the formation of nanostructures like $\text{Ga}_2\text{O}_3(\text{ZnO})_k$ homologous superlattices and nanotwins as well as the ZnGa_2O_4 spinel phase. The ZnGa_2O_4 spinel phase is a less electrical conducting phase than ZnO , due to its large band gap of $4.0 - 5.0$ eV [199, 204]. In addition, the $\text{Ga}_2\text{O}_3(\text{ZnO})_k$ superlattice interfaces are found not only to scatter phonons but electrons as well [45]. This is in contrast with $\text{In}_2\text{O}_3(\text{ZnO})_k$ superlattice structures which allow electrons through while filtering phonons out. The consequence is the decrease of both electrical and thermal conductivity with the formation of $\text{Ga}_2\text{O}_3(\text{ZnO})_k$ superlattices. Nevertheless, the very low thermal conductivity due to the presence of such nanostructures can compensate for the loss of electrical conductivity in terms of overall thermoelectric properties, which brings the figure of merit significantly higher than the undoped ZnO .

8.2 Achieving Low Thermal Conductivity by Nanostructure Engineering

By recasting the Callaway and von Baeyer's thermal conductivity model and performing numerical calculations, the role of defect scatterings of phonons are clearly illustrated and revealed. Increasing defect concentrations not only decreases thermal conductivity but also reduce the temperature dependence, which is attributed to the switch of the dominant phonon scattering mechanism from phonon – phonon interactions to the defect scatterings. As important, the nanostructure interfaces possess strong phonon scattering strength and can further lower the thermal conductivity in addition to

point defect scattering. Calculations of thermal conductivity as a function of interface spacing L at different temperatures suggest that irrespective of temperatures, the most substantial drop of the thermal conductivity occurs as the interface spacing is below $\sim 10^3$ nm. This provides the basis for achieving very low thermal conductivity by engineering the structure into nanoscale, by which the figure of merit can be increased.

8.3 Comments on Electrical Conductivity and Seebeck Coefficient

For the materials that I have investigated, differing temperature dependence of electrical conductivity σ and Seebeck coefficient S was observed. Generally, the electrical conductivity either increases or remains relatively unchanging with temperature. Irrespective of which, it is noted that both carrier concentration n and mobility μ , which together determine the electrical conductivity and Seebeck coefficient, are dependent on temperature. Accordingly, the variation of electrical conductivity with temperature is essentially a coupled temperature dependence of carrier concentration $n(T)$ and mobility $\mu(T)$, whereas the temperature change with the consequent change of carrier concentration $n(T)$ together affects the Seebeck coefficient.

In most cases of doped materials, the carrier concentration $n(T)$ increases with temperature T due to the increasing number of activated electron donors. On the other hand, the temperature dependence of mobility is essentially determined by the dominant electron scattering mechanism which is affected by the impurity concentration. Generally, lattice or phonon scatterings dominate in the pure or lightly doped materials, in which mobility $\mu(T)$ decrease with temperature; whereas ionized impurity scattering governs in

the heavily doped ones and $\mu(T)$ increases with temperature. In general, it is a combination of the two scattering mechanisms or plus possibly others. An illustration of the change in the dominant electron scattering mechanism with doping concentration has been made for the Ga doped ZnO and can be found in Chapter 7.

8.5 Outlook for the Future Work

Variation of phases and microstructures with dopant species offer us rich opportunities of tuning the thermoelectric properties by properly choosing a combination of dopant species. On one hand, one dopant species can be appropriately chosen to alter the electronic structure by creating donors states close to the conduction band edge. On the other hand, since thermal conductivity is sensitive to microstructure, a second dopant species which produce natural superlattice structures can be used. With proper tuning of compositions and structures, the dual doped ZnO can be expected to demonstrate very low thermal conductivity but with significantly enhanced electrical conductivity. A drastic improvement in figure of merit of Al and Ga dual doped ZnO has been recently reported [205]. However, reproducibility and interpretation of the results are needed, especially in correlation with the electronic structure and microstructure, in order to provide a useful guide in designing high temperature thermoelectric oxides.

Hall measurements are needed to obtain the charge carrier mobility and therefore the carrier concentration in combination with the electrical conductivity measurements. By distinguishing the role between carrier concentration and mobility in electrical transport, better understanding of Seebeck coefficient becomes possible, which can

further provide clues to modify the existing oxides or develop new materials for large thermoelectric figure of merit. Furthermore, investigations of electron mobility as a function of composition are useful to facilitate the understanding of electronic transport across the superlattice interfaces, which is helpful in identifying nanostructure interfaces that have good electron transparency.

Appendix: Combined X-ray Diffraction and Raman Spectroscopy

Characterization of $\text{In}_2\text{O}_3(\text{ZnO})_k$ Natural Superlattice Structures

The $\text{In}_2\text{O}_3(\text{ZnO})_k$ natural superlattice structure phases have Zn-O/In-O superlattice interfaces in addition to randomly distributed point defects in ZnO blocks. One may expect that such features can result in the changes of lattice vibration behaviors, which can be detected by Raman spectroscopy. In addition, there is also a lack of Raman spectroscopy characterization of oxide superlattice structures in literatures. It is of interest to track the evolution in Raman spectra of ZnO-In₂O₃ system in combination with X-ray diffraction analysis, by which the Raman spectral features of $\text{In}_2\text{O}_3(\text{ZnO})_k$ superlattice structures can be identified.

The X-ray diffraction results of ZnO-In₂O₃ system with two thermal treatments, 1150 °C for 1 day and 1250 °C for 7 days, are presented in Figure A.1 and Figure A.2, respectively. Although the X-ray scans were made for 2θ of 10 to 70 degree, much emphases are placed on the 2θ range of 10 to 30 degree where most distinguishable peaks of different $\text{In}_2\text{O}_3(\text{ZnO})_k$ superlattice structures fall. Characteristic peaks of each specific $\text{In}_2\text{O}_3(\text{ZnO})_k$ superlattice phase are labeled by the vertical dashed line with *k* value indicated on the top of the figure, according to a combination of 2011 ICDD PDF database [111] as well as literature reports [31, 92]. It is interesting to observe the peak shift for some $\text{In}_2\text{O}_3(\text{ZnO})_k$ superlattice phases, which can be indicative of variations of the indium content in the ZnO blocks with compositions. A couple of $\text{In}_2\text{O}_3(\text{ZnO})_k$ superlattice phases equilibrated at high temperatures, such as $\text{In}_2\text{O}_3(\text{ZnO})_6$ and $\text{In}_2\text{O}_3(\text{ZnO})_{11}$, appear in a few compositions after the thermal treatment at 1250 °C.

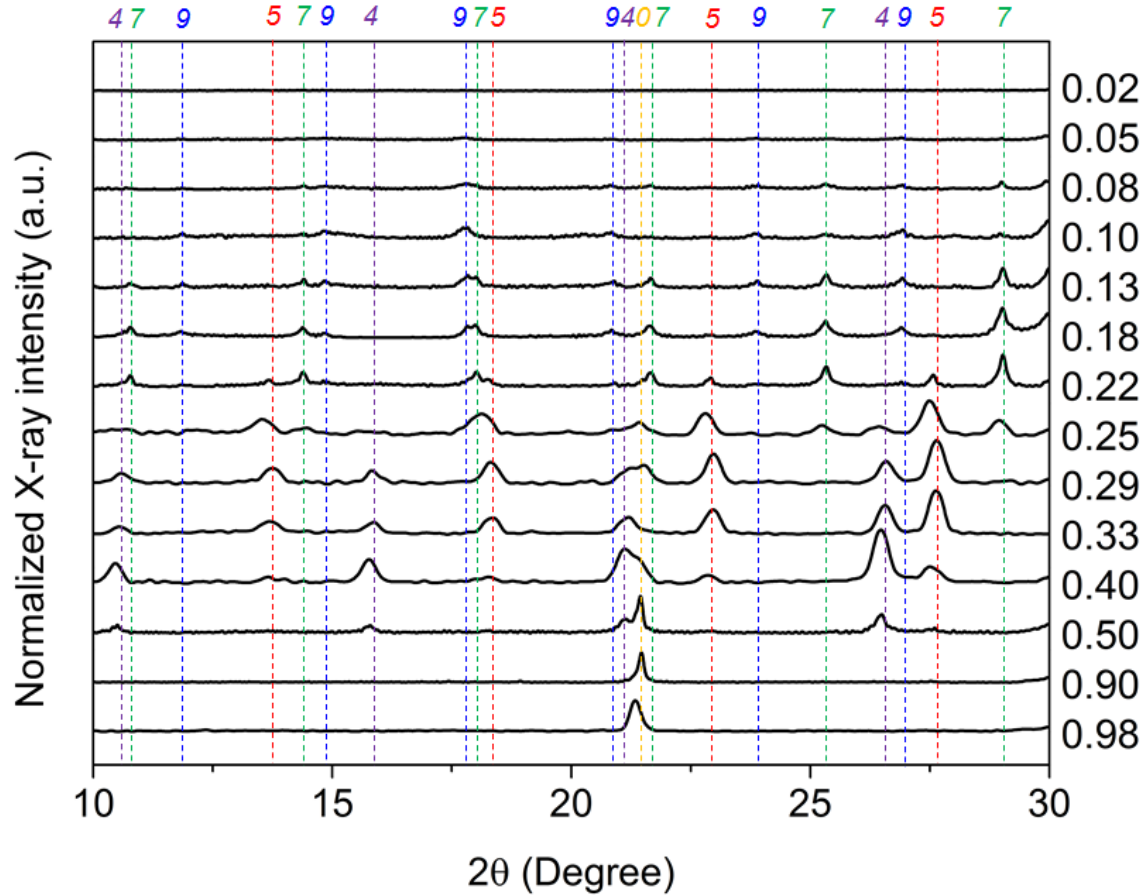


Figure A.1: X-ray diffraction results of $\text{ZnO}-\text{In}_2\text{O}_3$ binary system annealed at 1150°C for 1 day. The 2θ range of $10 - 30$ degree where most of $\text{In}_2\text{O}_3(\text{ZnO})_k$ superlattice reflections lie are presented. The $\text{InO}_{1.5}$ concentration is indicated to right of the figure. The characteristic diffraction peaks of different $\text{In}_2\text{O}_3(\text{ZnO})_k$ superlattices are indicated by the dashed lines of different colors with k values shown on the top of the figure.

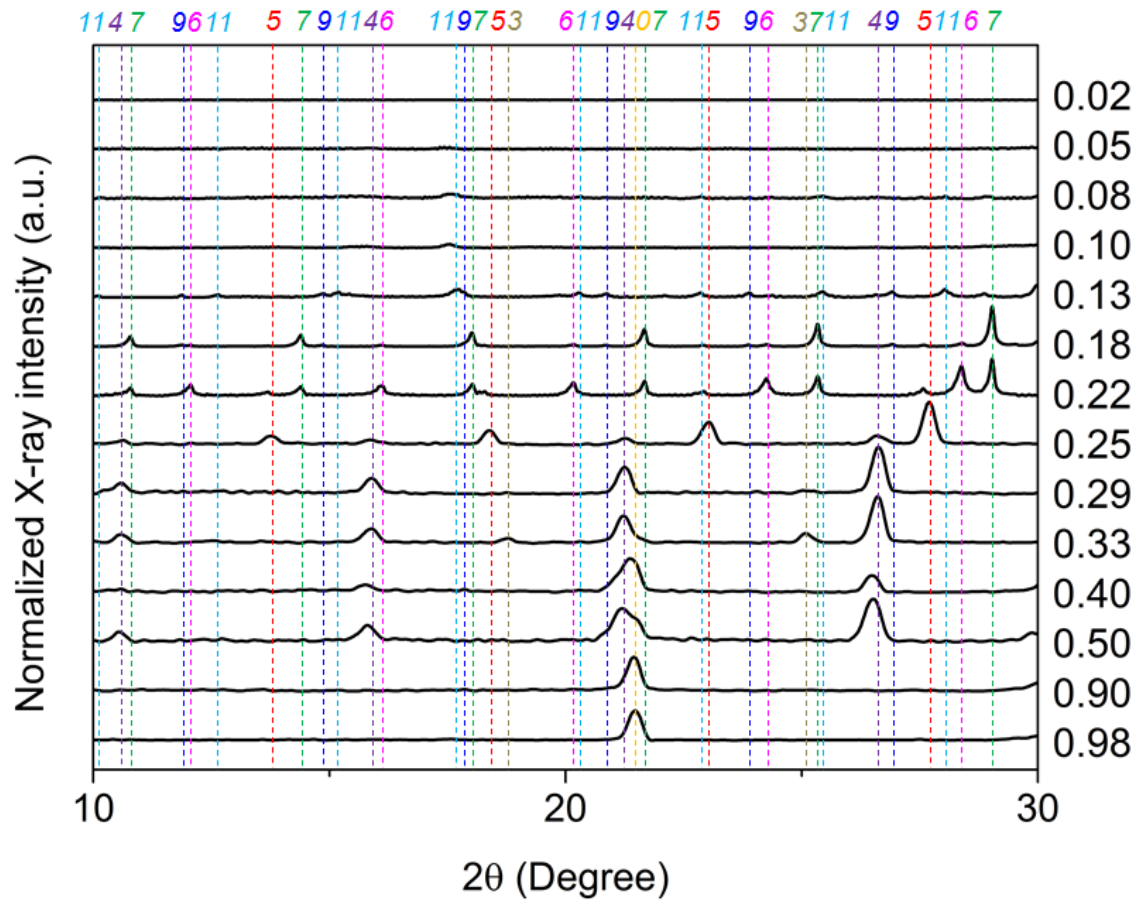


Figure A.2: X-ray diffraction results of ZnO-In₂O₃ binary system annealed at 1250 °C for 7 days.

Raman spectra data are shown in Figure A.3 and Figure A.4, for the two thermal treatments, respectively. According to literature, characteristic Raman peaks of ZnO [193] and In₂O₃ [206] are labeled by the vertical dashed lines of green and red colors, respectively, with active Raman modes shown on the top of the figure. A systematic change of Raman spectra with increasing indium concentration (as shown on the right of the figure) is observed. The most striking feature is the appearance of significant peak broadening in the range of 550 – 650 cm⁻¹. Combined with the X-ray diffraction results, these broad Raman bands can be related to In₂O₃(ZnO)_k superlattice structures.

Systematic changes of Raman spectra with composition were observed for the ZnO-In₂O₃ system annealed at 1150 °C. As shown in Figure A.3, distinct ZnO Raman modes remain up to 0.18 InO_{1.5}. However, at 0.22 InO_{1.5}, ZnO Raman modes become quite diminished whereas no In₂O₃ modes appear. With further increasing indium addition above 0.25 InO_{1.5}, Raman modes characteristic of In₂O₃ show up and their intensities become stronger with indium concentration. Furthermore, broad Raman band over 550 - 650 cm⁻¹ appears with the highest Raman intensity over the entire spectrum. Such broad Raman band at 550 – 650 cm⁻¹ was basically observed in the composition range of 0.10 to 0.50 InO_{1.5}, where In₂O₃(ZnO)_k superlattices were distinctly detected by the X-ray diffraction. Similar evolution of Raman spectra was also observed for the series of ZnO-In₂O₃ materials annealed at 1250 °C. The Raman modes of ZnO remain up to 0.18 InO_{1.5}, but disappear with further increasing InO_{1.5} addition. In addition, a consistent shift of Raman peak at 101 cm⁻¹ as well as the broadening of the peak at 437 cm⁻¹, both of which belong to ZnO E₂ modes, were observed with increasing indium concentration. Raman modes of neither ZnO nor In₂O₃ were observed in the InO_{1.5} concentration range of 0.22 – 0.29 and the major feature of the Raman spectra is the broad band at 550 – 650 cm⁻¹. From 0.33 InO_{1.5} and above, Raman modes of In₂O₃ appear and the intensity increases with increasing InO_{1.5} concentration.

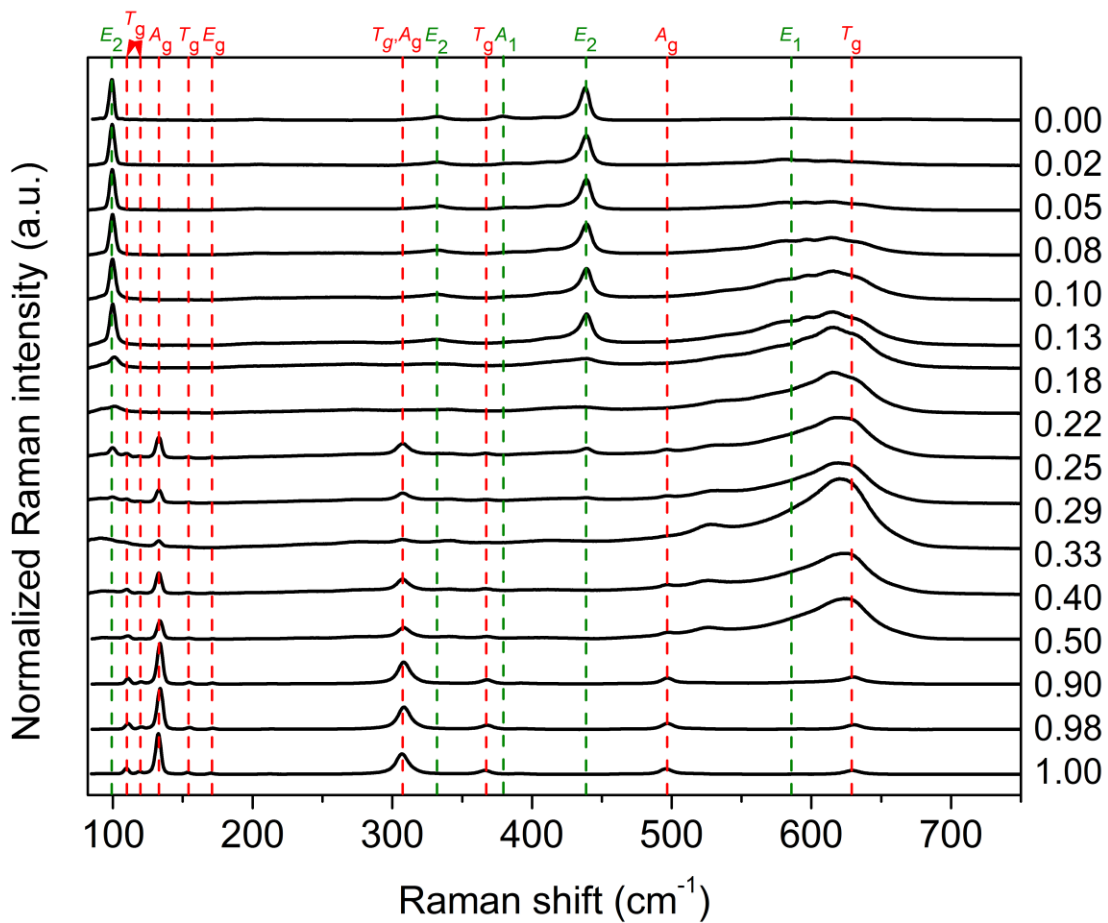


Figure A.3: Raman spectra of ZnO-In₂O₃ binary system annealed at 1150 °C for 1 day; InO_{1.5} concentration is indicated on the right of the figure. The characteristic Raman modes of ZnO and In₂O₃ are labeled by the dashed lines of green and red colors, with vibration modes indicated on the top of the figure.

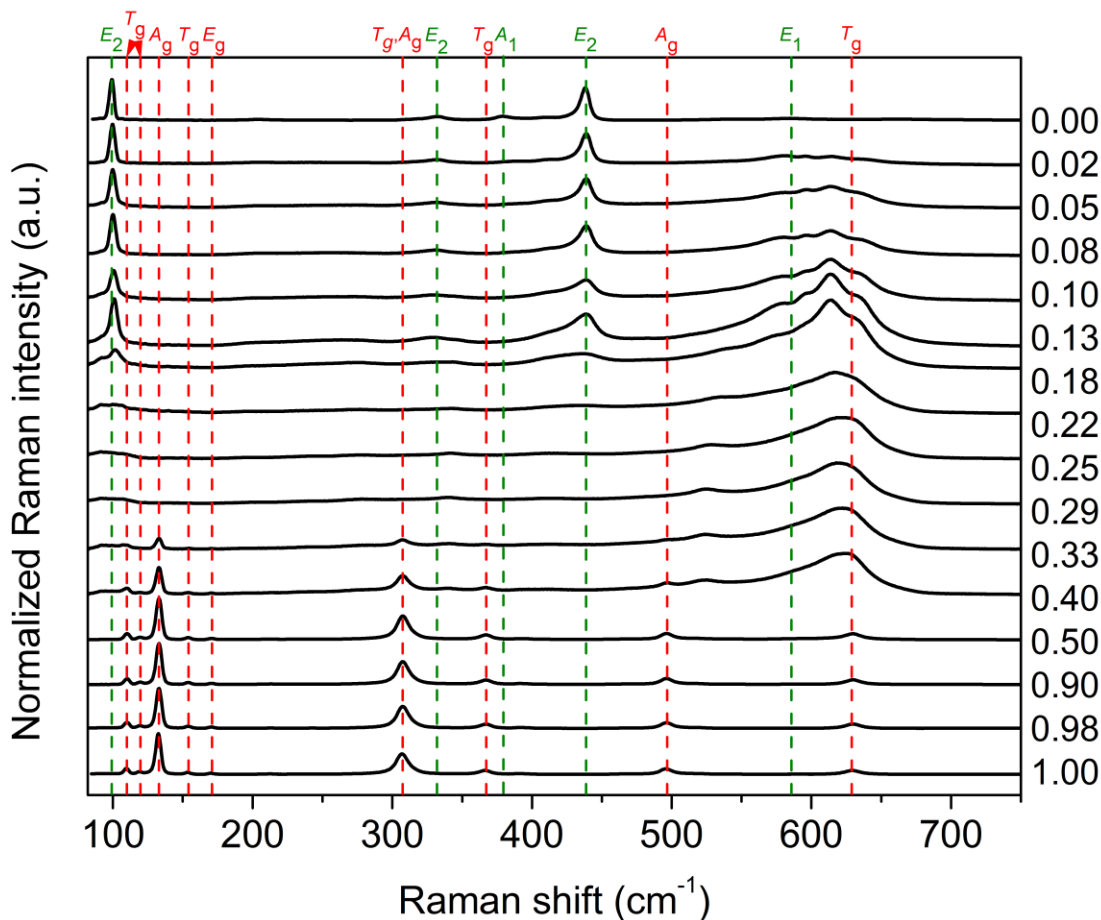


Figure A.4: Raman spectra of ZnO-In₂O₃ binary system annealed at 1250 °C for 7 days.

The evolution of Raman spectra with indium concentration, for both thermal treatments, is generally consistent with the phase equilibria and microstructure identified by X-ray diffraction or predicted from the ZnO-In₂O₃ binary phase diagram. The Raman spectroscopy results clearly present the phase and structural transition with indium addition, basically following the route of ZnO solid solution → ZnO solid solution with superlattice structures → superlattices mixtures → a two-phase composite consisting of In₂O₃ and modular superlattice compound, and finally → the In₂O₃ solid solution close to the In₂O₃ end.

The most striking feature is that the presence and intensity of the broad band observed at $550 - 650 \text{ cm}^{-1}$ are consistently related to the presence and fractions of $\text{In}_2\text{O}_3(\text{ZnO})_k$ superlattice structures as detected by the X-ray diffraction. These broad features are related to the optical phonon confinement due to the presence of superlattice interfaces. Future work such as collecting the information on the distribution of superlattice interface spacings is needed, which enables us to perform the phonon confinement model calculations.

References

1. Shakouri, A., *Recent Developments in Semiconductor Thermoelectric Physics and Materials*, in *Annual Review of Materials Research*, Vol 41, D.R. Clarke and P. Fratzl, Editors. 2011. p. 399-431.
2. Tritt, T.M., *Thermoelectric Phenomena, Materials, and Applications*, in *Annual Review of Materials Research*, Vol 41, D.R. Clarke and P. Fratzl, Editors. 2011. p. 433-448.
3. Yang, J.H. and T. Caillat, *Thermoelectric materials for space and automotive power generation*. Mrs Bulletin, 2006. **31**(3): p. 224-229.
4. Tritt, T.M., H. Boettner, and L. Chen, *Thermoelectrics: Direct solar thermal energy conversion*. Mrs Bulletin, 2008. **33**(4): p. 366-368.
5. Kittel, C., *Introduction to Solid State Physics*. 8th ed2005: Wiley.
6. Snyder, G.J. and E.S. Toberer, *Complex thermoelectric materials*. Nature Materials, 2008. **7**(2): p. 105-114.
7. DiSalvo, F.J., *Thermoelectric Cooling and Power Generation*. Science, 1999. **285**(5428): p. 703-706.
8. Bell, L.E., *Cooling, heating, generating power, and recovering waste heat with thermoelectric systems*. Science, 2008. **321**(5895): p. 1457-1461.
9. Homm, G. and P.J. Klar, *Thermoelectric materials - Compromising between high efficiency and materials abundance*. Physica Status Solidi-Rapid Research Letters, 2011. **5**(9): p. 324-331.
10. Bux, S.K., et al., *Nanostructured Bulk Silicon as an Effective Thermoelectric Material*. Advanced Functional Materials, 2009. **19**(15): p. 2445-2452.

11. Kanatzidis, M.G., *Nanostructured Thermoelectrics: The New Paradigm?* Chemistry of Materials, 2009. **22**(3): p. 648-659.
12. Prytz, O., et al., *Reduction of lattice thermal conductivity from planar faults in the layered Zintl compound SrZnSb₂*. Journal of Applied Physics, 2011. **109**(4): p. 043509.
13. Toberer, E.S., A. Zevalkink, and G.J. Snyder, *Phonon engineering through crystal chemistry*. Journal of Materials Chemistry, 2011. **21**(40): p. 15843-15852.
14. Toberer, E.S., L.L. Baranowski, and C. Dames, *Advances in Thermal Conductivity*. Annual Review of Materials Research, 2012. **42**(1): p. 179-209.
15. Takahata, K., et al., *Low thermal conductivity of the layered oxide (Na,Ca)Co₂O₄: Another example of a phonon glass and an electron crystal*. Physical Review B, 2000. **61**(19): p. 12551-12555.
16. Minnich, A.J., et al., *Bulk nanostructured thermoelectric materials: current research and future prospects*. Energy & Environmental Science, 2009. **2**(5): p. 466-479.
17. Koumoto, K., et al., *Oxide Thermoelectric Materials: A Nanostructuring Approach*, in *Annual Review of Materials Research, Vol 40* 2010. p. 363-394.
18. Chernatynskiy, A., D.R. Clarke, and S.R. Phillpot, *Thermal Transport in Nanostructured Materials*, 2012, CRC.
19. Nolas, G.S., J.W. Sharp, and H.J. Goldsmid, *Thermoelectrics: Basic Principles and New Materials Developments* 2001, Berlin/Heidelberg: Springer.
20. Li, D.Y., et al., *Thermal conductivity of Si/SiGe superlattice nanowires*. Applied Physics Letters, 2003. **83**(15): p. 3186-3188.
21. Poudel, B., et al., *High-thermoelectric performance of nanostructured bismuth antimony telluride bulk alloys*. Science, 2008. **320**(5876): p. 634-638.

22. Lan, Y., et al., *Enhancement of Thermoelectric Figure-of-Merit by a Bulk Nanostructuring Approach*. Advanced Functional Materials, 2010. **20**(3): p. 357-376.
23. Dresselhaus, M.S., et al., *New directions for low-dimensional thermoelectric materials*. Advanced Materials, 2007. **19**(8): p. 1043-1053.
24. Kosuga, A., et al., *Thermal Conductivity Characterization in Bulk Zn(Mn,Ga)O₄ with Self-Assembled Nanocheckerboard Structures*. Japanese Journal of Applied Physics, 2009. **48**(1).
25. Ohta, S., et al., *High-temperature carrier transport and thermoelectric properties of heavily La- or Nb-doped SrTiO₃ single crystals*. Journal of Applied Physics, 2005. **97**(3).
26. Okuda, T., et al., *Large thermoelectric response of metallic perovskites: Sr_{1-x}LaxTiO₃ (0 <= x <= 0.1)*. Physical Review B, 2001. **63**(11).
27. Limarga, A.M. and D.R. Clarke, *The grain size and temperature dependence of the thermal conductivity of polycrystalline, tetragonal yttria-stabilized zirconia*. Applied Physics Letters, 2011. **98**(21): p. 211906-3.
28. Androulakis, J., et al., *Spinodal decomposition and nucleation and growth as a means to bulk nanostructured thermoelectrics: Enhanced performance in Pb_{1-x}Sn_xTe-PbS*. Journal of the American Chemical Society, 2007. **129**(31): p. 9780-9788.
29. Gelbstein, Y., et al., *High Thermoelectric Figure of Merit and Nanostructuring in Bulk p-type Ge-x(SnyPb1-y)(1-x)Te Alloys Following a Spinodal Decomposition Reaction*. Chemistry of Materials, 2010. **22**(3): p. 1054-1058.
30. Sondergaard, M., et al., *Thermoelectric and microstructural properties of Pb_{0.9-x}Sn_{0.1}GexTe compounds prepared by spinodal decomposition*. Journal of Solid State Chemistry, 2011. **184**(5): p. 1172-1175.
31. Ohta, H., W.S. Seo, and K. Koumoto, *Thermoelectric properties of homologous compounds in the ZnO-In₂O₃ system*. Journal of the American Ceramic Society, 1996. **79**(8): p. 2193-2196.

32. Kazeoka, M., et al., *Improvement in thermoelectric properties of (ZnO)(5)In₂O₃ through partial substitution of yttrium for indium*. Journal of Materials Research, 1998. **13**(3): p. 523-526.
33. Li, C., et al., *Relation between In ion ordering and crystal structure variation in homologous compounds InMO₃(ZnO)_m (M=Al and In; m=integer)*. Micron, 2000. **31**(5): p. 543-550.
34. Masuda, Y., et al., *Structure and thermoelectric transport properties of isoelectronically substituted (ZnO)(5)In₂O₃*. Journal of Solid State Chemistry, 2000. **150**(1): p. 221-227.
35. Hirano, S., et al., *Electrical and thermal transport properties in layer-structured (ZnO)(m)In₂O₃ (m=5 and 9) ceramics*. Japanese Journal of Applied Physics Part 1-Regular Papers Short Notes & Review Papers, 2002. **41**(11A): p. 6430-6435.
36. Kaga, H., R. Asahi, and T. Tani, *Thermoelectric properties of doped (ZnO)(m)In₂O₃*. Japanese Journal of Applied Physics Part 1-Regular Papers Short Notes & Review Papers, 2004. **43**(6A): p. 3540-3543.
37. Harvey, S.P., K.R. Poeppelmeier, and T.O. Mason, *Subsolidus Phase Relationships in the ZnO-In₂O₃-SnO₂ System*. Journal of the American Ceramic Society, 2008. **91**(11): p. 3683-3689.
38. Yoshinari, A., et al., *Crystal and electronic band structures of homologous compounds ZnkIn₂Ok+3 by Rietveld analysis and first-principle calculation*. Materials Research Bulletin, 2009. **44**(2): p. 432-436.
39. Hoel, C.A., et al., *Transparent Conducting Oxides in the ZnO-In₂O₃-SnO₂ System*. Chemistry of Materials, 2010. **22**(12): p. 3569-3579.
40. Hopper, E.M., et al., *Electronic and thermoelectric analysis of phases in the In(2)O(3)(ZnO)(k) system*. Journal of Applied Physics, 2011. **109**(1): p. 6.
41. Peng, H.W., et al., *Possible n-type carrier sources in In₂O₃(ZnO)(k)*. Chemistry of Materials, 2012. **24**(1): p. 106-114.

42. Li, C., et al., *Structure analysis of new homologous compounds $Ga_2O_3(ZnO)_m$ ($m = \text{integer}$) by high-resolution analytical transmission electron microscopy*. Acta Crystallographica Section B, 1999. **55**(3): p. 355-362.
43. Barf, J., T. Walther, and W. Mader, *Twin boundaries in zinc oxide with additions of gallium oxide*. Interface Science, 2004. **12**(2-3): p. 213-226.
44. Michiue, Y., N. Kimizuka, and Y. Kanke, *Structure of $Ga_2O_3(ZnO)_6$: a member of the homologous series $Ga_2O_3(ZnO)_m$* . Acta Crystallographica Section B, 2008. **64**(5): p. 521-526.
45. Yoon, S.W., et al., *Ga Ordering and Electrical Conductivity in Nanotwin and Superlattice-Structured Ga-Doped ZnO*. Crystal Growth & Design, 2012. **12**(3): p. 1167-1172.
46. Yeo, S., et al., *Solid state self-assembly of nanochckerboards*. Applied Physics Letters, 2006. **89**(23).
47. Shen, Y., D.R. Clarke, and P.A. Fuierer, *Anisotropic thermal conductivity of the Aurivillus phase, bismuth titanate, $(Bi_4Ti_3O_{12})$: A natural nanostructured superlattice*. Applied Physics Letters, 2008. **93**(10).
48. Majumdar, A., *Thermoelectricity in semiconductor nanostructures*. Science, 2004. **303**(5659): p. 777-778.
49. Cahill, D.G., S.K. Watson, and R.O. Pohl, *Lower limit to the thermal conductivity of disordered crystals*. Physical Review B, 1992. **46**(10): p. 6131-6140.
50. Lee, S.M., D.G. Cahill, and R. Venkatasubramanian, *Thermal conductivity of Si-Ge superlattices*. Applied Physics Letters, 1997. **70**(22): p. 2957-2959.
51. Costescu, R.M., M.A. Wall, and D.G. Cahill, *Thermal conductance of epitaxial interfaces*. Physical Review B, 2003. **67**(5): p. 054302.
52. Costescu, R.M., et al., *Ultra-low thermal conductivity in W/ Al_2O_3 nanolaminates*. Science, 2004. **303**(5660): p. 989-990.

53. Chiritescu, C., et al., *Ultralow thermal conductivity in disordered, layered WSe₂ crystals*. Science, 2007. **315**(5810): p. 351-353.
54. Koh, Y.K., et al., *Heat-Transport Mechanisms in Superlattices*. Advanced Functional Materials, 2009. **19**(4): p. 610-615.
55. Narayanamurti, V., et al., *Selective transmission of high-frequency phonons by a superlattice: the "dielectric" phonon filter*. Physical Review Letters, 1979. **43**(27): p. 2012-2016.
56. Chen, G., *Phonon transport in low-dimensional structures*, in *Recent Trends in Thermoelectric Materials Research Iii*, T.M. Tritt, Editor 2001. p. 203-259.
57. Wang, H., et al., *Weak electron–phonon coupling contributing to high thermoelectric performance in n-type PbSe*. Proceedings of the National Academy of Sciences, 2012. **109**(25): p. 9705-9709.
58. Koumoto, K., I. Terasaki, and R. Funahashi, *Complex oxide materials for potential thermoelectric applications*. Mrs Bulletin, 2006. **31**(3): p. 206-210.
59. Venkatasubramanian, R., et al., *Thin-film thermoelectric devices with high room-temperature figures of merit*. Nature, 2001. **413**(6856): p. 597-602.
60. Boukai, A.I., et al., *Silicon nanowires as efficient thermoelectric materials*. Nature, 2008. **451**(7175): p. 168-171.
61. Hochbaum, A.I., et al., *Enhanced thermoelectric performance of rough silicon nanowires*. Nature, 2008. **451**(7175): p. 163-U5.
62. Ohtaki, M., et al., *High-temperature thermoelectric properties of (Zn_{1-x}Al_x)O*. Journal of Applied Physics, 1996. **79**(3): p. 1816-1818.
63. Park, K.C., D.Y. Ma, and K.H. Kim, *The physical properties of Al-doped zinc oxide films prepared by RF magnetron sputtering*. Thin Solid Films, 1997. **305**(1-2): p. 201-209.

64. Tsubota, T., et al., *Thermoelectric properties of Al-doped ZnO as a promising oxide material for high-temperature thermoelectric conversion*. Journal of Materials Chemistry, 1997. **7**(1): p. 85-90.
65. Cai, K.F., et al., *Preparation and thermoelectric properties of Al-doped ZnO ceramics*. Materials Science and Engineering B-Solid State Materials for Advanced Technology, 2003. **104**(1-2): p. 45-48.
66. Qu, X.R., et al., *Thermoelectric properties and electronic structure of Al-doped ZnO*. Solid State Communications, 2011. **151**(4): p. 332-336.
67. Fujishiro, Y., et al., *Effect of Microstructural Control on Thermoelectric Properties of Hot-Pressed Aluminum-Doped Zinc Oxide*. Journal of the American Ceramic Society, 2003. **86**(12): p. 2063-2066.
68. Park, K., et al., *Zn_{1-x}BixO (0 < x < 0.02) for thermoelectric power generations*. Journal of Alloys and Compounds, 2009. **485**(1-2): p. 532-537.
69. White, M.A., S.T. Ochsenbein, and D.R. Gamelin, *Colloidal Nanocrystals of Wurtzite Zn_{1-x}CoxO (0 < x < 1): Models of Spinodal Decomposition in an Oxide Diluted Magnetic Semiconductor*. Chemistry of Materials, 2008. **20**(22): p. 7107-7116.
70. Minami, T., T. Kakumu, and S. Takata, *Preparation of transparent and conductive In₂O₃-ZnO films by radio frequency magnetron sputtering*. Vol. 14. 1996: AVS. 1704-1708.
71. Orikasa, Y., N. Hayashi, and S. Muranaka, *Effects of oxygen gas pressure on structural, electrical, and thermoelectric properties of (ZnO)(3)In₂O₃ thin films deposited by rf magnetron sputtering*. Journal of Applied Physics, 2008. **103**(11): p. 7.
72. Li, C., et al., *Antiphase Modulated Structure of Fe₂O₃(ZnO)₁₅ Studied by High-Resolution Electron Microscopy*. Journal of Solid State Chemistry, 1999. **142**(1): p. 174-179.
73. Degterov, S.A., et al., *Experimental study of phase equilibria and thermodynamic optimization of the Fe-Zn-O system*. Metallurgical and Materials Transactions B-Process Metallurgy and Materials Processing Science, 2001. **32**(4): p. 643-657.

74. Hansson, R., P. Hayes, and E. Jak, *Experimental study of phase equilibria in the Al-Fe-Zn-O system in air*. Metallurgical and Materials Transactions B, 2004. **35**(4): p. 633-642.
75. Hansson, R., P. Hayes, and E. Jak, *Phase equilibria in the system Fe-Zn-O at intermediate conditions between metallic-iron saturation and air*. Metallurgical and Materials Transactions B, 2005. **36**(2): p. 179-185.
76. Köster-Scherger, O., et al., *ZnO with Additions of Fe₂O₃: Microstructure, Defects, and Fe Solubility*. Journal of the American Ceramic Society, 2007. **90**(12): p. 3984-3991.
77. Liu, H. and et al., *Structure and magnetic properties of Fe-doped ZnO prepared by the sol-gel method*. Journal of Physics: Condensed Matter, 2009. **21**(14): p. 145803.
78. Sawalha, A., M. Abu-Abdeen, and A. Sedky, *Electrical conductivity study in pure and doped ZnO ceramic system*. Physica B: Condensed Matter, 2009. **404**(8-11): p. 1316-1320.
79. Liu, H. and et al., *Structure, magnetic, and optical properties in Zn_{0.98}Cu_{0.02}Fe_xO diluted magnetic semiconductors*. Physica Status Solidi (a), 2010: p. n/a.
80. Li, X., et al., *Synthesis and magnetic properties of Al doped Zn_{0.995}Mn_{0.005}O powers*. Vol. 94. 2009: AIP. 252501.
81. Park, K., J.K. Seong, and G.H. Kim, *NiO added Zn_{1-x}Ni_xO (0 < x < 0.05) for thermoelectric power generation*. Journal of Alloys and Compounds, 2009. **473**(1-2): p. 423-427.
82. Colder, H., et al., *Preparation of Ni-doped ZnO ceramics for thermoelectric applications*. Journal of the European Ceramic Society, 2011. **31**(15): p. 2957-2963.
83. Park, K., J.K. Seong, and S. Nahm, *Improvement of thermoelectric properties with the addition of Sb to ZnO*. Journal of Alloys and Compounds, 2008. **455**(1-2): p. 331-335.

84. Park, K., et al., *Influence of SnO₂ addition on the thermoelectric properties of Zn_{1-x}Sn_xO (0.01 ≤ x ≤ 0.05)*. Materials Research Bulletin, 2008. **43**(1): p. 54-61.
85. Park, K. and J.K. Seong, *Influence of simultaneous addition of Sb₂O₃ and SnO₂ on thermoelectric properties of Zn_{1-x-y}Sb_xSn_yO prepared by tape casting*. Journal of Alloys and Compounds, 2008. **464**(1-2): p. 1-5.
86. Seo, D.K., et al., *Drastic improvement of oxide thermoelectric performance using thermal and plasma treatments of the InGaZnO thin films grown by sputtering*. Acta Materialia, 2011. **59**(17): p. 6743-6750.
87. Yamaguchi, H., et al., *Thermoelectric Properties of ZnO Ceramics Co-Doped with Al and Transition Metals*. Journal of Electronic Materials, 2011. **40**(5): p. 723-727.
88. Cannard, P.J. and R.J.D. Tilley, *New intergrowth phases in the ZnO-In₂O₃ system*. Journal of Solid State Chemistry, 1988. **73**(2): p. 418-426.
89. McCoy, M.A., R.W. Grimes, and W.E. Lee, *Inversion domain boundaries in ZnO ceramics*. Journal of Materials Research, 1996. **11**(8): p. 2009-2019.
90. McCoy, M.A., R.W. Grimes, and W.E. Lee, *Planar intergrowth structures in the ZnO-In₂O₃ system*. Philosophical Magazine a-Physics of Condensed Matter Structure Defects and Mechanical Properties, 1997. **76**(6): p. 1187-1201.
91. Yan, Y., et al., *Polytypoid structures in annealed In₂O₃-ZnO films*. Applied Physics Letters, 1998. **73**(18): p. 2585-2587.
92. Moriga, T., et al., *Phase relationships and physical properties of homologous compounds in the zinc oxide-indium oxide system*. Journal of the American Ceramic Society, 1998. **81**(5): p. 1310-1316.
93. King, P.D.C., et al., *Band gap, electronic structure, and surface electron accumulation of cubic and rhombohedral In₂O₃*. Physical Review B, 2009. **79**(20): p. 205211.
94. Hopper, E.M., et al., *Electronic and thermoelectric analysis of phases in the In₂O₃(ZnO)(k) system*. Journal of Applied Physics, 2011. **109**(1).

95. Srikant, V. and D.R. Clarke, *On the optical band gap of zinc oxide*. Journal of Applied Physics, 1998. **83**(10): p. 5447-5451.
96. Wang, R.P., A.W. Sleight, and D. Cleary, *High conductivity in gallium-doped zinc oxide powders*. Chemistry of Materials, 1996. **8**(2): p. 433-439.
97. Bhosle, V., A. Tiwari, and J. Narayan, *Electrical properties of transparent and conducting Ga doped ZnO*. Journal of Applied Physics, 2006. **100**(3).
98. Serier, H., A. Demourgues, and M. Gaudon, *Investigation of Ga Substitution in ZnO Powder and Opto-Electronic Properties*. Inorganic Chemistry, 2010. **49**(15): p. 6853-6858.
99. Major, S., A. Banerjee, and K.L. Chopra, *Highly transparent and conducting indium-doped zinc oxide films by spray pyrolysis*. Thin Solid Films, 1983. **108**(3): p. 333-340.
100. Kikkawa, S., S. Hosokawa, and H. Ogawa, *Preparation of Transparent Conductive (ZnO)_mIn₂O₃ Fine Powder by Gel-Combustion Reaction*. Journal of the American Ceramic Society, 2005. **88**(2): p. 308-311.
101. Omori, M., *Sintering, consolidation, reaction and crystal growth by the spark plasma system (SPS)*. Materials Science and Engineering a-Structural Materials Properties Microstructure and Processing, 2000: p. 183-188.
102. Shen, Z.J., et al., *Spark plasma sintering of alumina*. Journal of the American Ceramic Society, 2002. **85**(8): p. 1921-1927.
103. Zhan, G.D., et al., *Alumina-based nanocomposites consolidated by spark plasma sintering*. Scripta Materialia, 2002. **47**(11): p. 737-741.
104. Anselmi-Tamburini, U., et al., *Spark plasma sintering and characterization of bulk nanostructured fully stabilized zirconia: Part II. Characterization studies*. Journal of Materials Research, 2004. **19**(11): p. 3263-3269.
105. Anselmi-Tamburini, U., et al., *Spark plasma sintering and characterization of bulk nanostructured fully stabilized zirconia: Part I. Densification studies*. Journal of Materials Research, 2004. **19**(11): p. 3255-3262.

106. Anselmi-Tamburini, U., J.E. Garay, and Z.A. Munir, *Fundamental investigations on the spark plasma sintering/synthesis process III. Current effect on reactivity*. Materials Science and Engineering a-Structural Materials Properties Microstructure and Processing, 2005. **407**(1-2): p. 24-30.
107. Anselmi-Tamburini, U., et al., *Fundamental investigations on the spark plasma sintering/synthesis process - II. Modeling of current and temperature distributions*. Materials Science and Engineering a-Structural Materials Properties Microstructure and Processing, 2005. **394**(1-2): p. 139-148.
108. Chen, W., et al., *Fundamental investigations on the spark plasma sintering/synthesis process - I. Effect of dc pulsing on reactivity*. Materials Science and Engineering a-Structural Materials Properties Microstructure and Processing, 2005. **394**(1-2): p. 132-138.
109. Bernard-Granger, G. and C. Guizard, *Spark plasma sintering of a commercially available granulated zirconia powder: I. Sintering path and hypotheses about the mechanism(s) controlling densification*. Acta Materialia, 2007. **55**(10): p. 3493-3504.
110. Bernard-Granger, G., et al., *Spark plasma sintering of a commercially available granulated zirconia powder-II. Microstructure after sintering and ionic conductivity*. Acta Materialia, 2008. **56**(17): p. 4658-4672.
111. ICDD (2011). PDF-4+ 2011 (Database), International Centre for Diffraction Data: Newtown Square, PA, USA.
112. Barin, I., *Thermochemical data of pure substances*1989, Weinheim: VCH.
113. Klemens, P.G., *Theory of the thermal conductivity of solids*. Thermal Conductivity, ed. R.P. Tye1968, New York: Academic Press.
114. Callaway, J. and H.C. von Baeyer, *Effect of Point Imperfections on Lattice Thermal Conductivity*. Physical Review, 1960. **120**(4): p. 1149-1154.
115. Roufosse, M.C. and P.G. Klemens, *Lattice Thermal Conductivity of Minerals at High Temperatures*. J. Geophys. Res., 1974. **79**(5): p. 703-705.

116. Mevrel, R., et al., *Thermal diffusivity and conductivity of Zrl-xYxO2-x/2 (x=0, 0.084 and 0.179) single crystals*. Journal of the European Ceramic Society, 2004. **24**(10-11): p. 3081-3089.
117. Limarga, A.M., et al., *Effect of high-temperature aging on the thermal conductivity of nanocrystalline tetragonal yttria-stabilized zirconia*. Acta Materialia, 2012. **60**(15): p. 5417-5424.
118. Clarke, D.R., *Materials selection guidelines for low thermal conductivity thermal barrier coatings*. Surface and Coatings Technology, 2003. **163–164**(0): p. 67-74.
119. Grimvall, G., *Thermalphysical Properties of Materials*1999, Amsterdam: North Holland.
120. Glassbrenner, C.J. and G.A. Slack, *Thermal conductivity of silicon and germanium from 3 K to melting point*. Physical Review a-General Physics, 1964. **134**(4A): p. 1058-&.
121. Cahill, D.G. and R.O. Pohl, *Lattice Vibrations and Heat Transport in Crystals and Glasses*. Annual Review of Physical Chemistry, 1988. **39**(1): p. 93-121.
122. Dugdale, J.S. and D.K.C. Macdonald, *Lattice thermal conductivity*. Physical Review, 1955. **98**(6): p. 1751-1752.
123. Lawson, A.W., *On the high temperature heat conductivity of insulators*. Journal of Physics and Chemistry of Solids, 1957. **3**(1-2): p. 155-156.
124. Berman, R., *Thermal Conductivity in Solids*1976: Oxford University Press.
125. Ziman, J.M., *Electrons and Phonons*1960, Oxford: Clarendon Press.
126. Qu, Z., et al., *Thermal conductivity of the gadolinium calcium silicate apatites: Effect of different point defect types*. Acta Materialia, 2011. **59**(10): p. 3841-3850.
127. Klemens, P.G., *The scattering of low-frequency lattice waves by static imperfections*. Proceedings of the Physical Society of London Section A, 1955. **68**(12): p. 1113-1128.

128. Klemens, P.G., *Thermal Resistance due to Point Defects at High Temperatures*. Physical Review, 1960. **119**(2): p. 507-509.
129. Robie, R.A. and J.L. Edwards, *Some Debye temperatures from single-crystal elastic constant data*. Journal of Applied Physics, 1966. **37**(7): p. 2659-&.
130. Schlichting, K.W., N.P. Padture, and P.G. Klemens, *Thermal conductivity of dense and porous yttria-stabilized zirconia*. Journal of Materials Science, 2001. **36**(12): p. 3003-3010.
131. Kingery, W.D., *Introduction to Ceramics*. 2nd Edition ed1976, New York: Wiley Interscience.
132. Winter, M.R. and D.R. Clarke, *Oxide Materials with Low Thermal Conductivity*. Journal of the American Ceramic Society, 2007. **90**(2): p. 533-540.
133. Nan, C.W., et al., *Effective thermal conductivity of particulate composites with interfacial thermal resistance*. Journal of Applied Physics, 1997. **81**(10): p. 6692-6699.
134. Nan, C.-W. and R. Birringer, *Determining the Kapitza resistance and the thermal conductivity of polycrystals: A simple model*. Physical Review B, 1998. **57**(14): p. 8264-8268.
135. Kiselev, A.A., K.W. Kim, and M.A. Stroscio, *Thermal conductivity of Si/Ge superlattices: A realistic model with a diatomic unit cell*. Physical Review B, 2000. **62**(11): p. 6896-6899.
136. Yang, H.-S., et al., *Interfacial thermal resistance in nanocrystalline yttria-stabilized zirconia*. Acta Materialia, 2002. **50**(9): p. 2309-2317.
137. Yang, R. and G. Chen, *Thermal conductivity modeling of periodic two-dimensional nanocomposites*. Physical Review B, 2004. **69**(19): p. 195316.
138. Chernatynskiy, A., et al., *Crossover in thermal transport properties of natural, perovskite-structured superlattices*. Applied Physics Letters, 2009. **95**(16).

139. Wang, Y.F., et al., *Interfacial Thermal Resistance and Thermal Conductivity in Nanograined SrTiO₃*. Applied Physics Express, 2010. **3**(3): p. 031101.
140. Lawless, W.N. and T.K. Gupta, *Thermal properties of pure and varistor ZnO at low temperatures*. Journal of Applied Physics, 1986. **60**(2): p. 607-611.
141. Costescu, R.M., M.A. Wall, and D.G. Cahill, *Thermal Conductance of Epitaxial Interfaces*. Physical Review B, 2003. **67**: p. 054302.
142. Clemens, B.M., G.L. Eesley, and C.A. Paddock, *Time-Resolved Thermal Transport in Compositionally Modulated Metal Films*. Physical Review B, 1988. **37**(3): p. 1085-1096.
143. Koh, Y.K., et al., *Heat Transport Mechanisms in Superlattices*. Advanced Functional Materials, 2009. **19**(4): p. 610-615.
144. Josell, D., A. Cezairliyan, and J.E. Bonevich, *Thermal Diffusion Through Multilayer Coatings: Theory and Experiments*. International Journal of Thermophysics, 1998. **19**(2): p. 525.
145. Sparks, T.D., P.A. Fuierer, and D.R. Clarke, *Anisotropic Thermal Diffusivity and Conductivity in La-Doped Strontium Niobate*. Journal of the American Ceramic Society, 2010. **93**(4): p. 1136-1141.
146. Wan, C.L., et al., *Thermal Conductivity of the Rare-Earth Strontium Aluminates*. Journal of the American Ceramic Society, 2010. **93**.
147. Costescu, R.M., et al., *Ultra-Low Thermal Conductivity in W/Al₂O₃ Nanolaminates*. Science, 2004. **303**: p. 989-990.
148. Veblen, D.R., *Polysomatism and Polysomatic Series: A Review and Applications*. American Mineralogist, 1991. **76**: p. 801-826.
149. Tilley, R.J.D., *Crystals and Crystal Structures* 2008, Hoboken: Wiley.
150. Chernatynskiy, A., et al., *Cross-Over in Thermal Transport Properties of Natural, Perovskite Structured Superlattices*. Applied Physics Letters, 2009. **95**: p. 161906.

151. Kimizuka, N. and T. Mohri, *Structural classification of $RAO_3(MO)_n$ compounds ($R = Sc, in, Y, or lanthanides; A = Fe(III), Ga, Cr, or Al; M = divalent cation; n = 1-11$)*. Journal of Solid State Chemistry, 1989. **78**(1): p. 98-107.
152. Kimizuka, N., E. Takayama, and K. Siratori, *The Systems $R_2O_3-M_2O_3-M' O$* , in *Handbook on the Physics and Chemistry of Rare Earths*, K.A. Gschneidner and L. Eyring, Editors. 1990, North-Holland: Amsterdam. p. 283-383.
153. Ohta, H., W.-S. Seo, and K. Koumoto, *Thermoelectric Properties of Homologous Compounds in the $ZnO-In_2O_3$ System*. Journal of the American Ceramic Society, 1996. **79**: p. 2193-2196.
154. Cannard, P.J. and R.J.D. Tilley, *New Intergrowth Phases in the $ZnO-In_2O_3$ System*. Journal of Solid State Chemistry, 1988. **73**: p. 418-426.
155. Nakamura, M., N. Kimizuka, and T. Mohri, Journal of Solid State Chemistry, 1991. **93**: p. 298.
156. Kimizuka, N., M. Isobe, and M. Nakamura, *Syntheses and Single Crystal Data of Homologous Compounds $In_2O_3(ZnO)_m$, $InGaO_3(ZnO)_3$ and $Ga_2O_3(ZnO)_m$ in the $In_2O_3-ZnGa_2O_4-ZnO$ System*. Journal of Solid State Chemistry, 1995. **116**: p. 170-178.
157. Robie, R.A. and J.L. Edwards, Journal of Applied Physics, 1966. **37**(7): p. 2659.
158. McCoy, M.A., R.W. Grimes, and W.E. Lee, *Planar Intergrowth Structures in the $ZnO-In_2O_3$ System*. Philosophical Magazine A, 1997. **76**(6): p. 1187-1201.
159. Berman, R., E.L. Foster, and J.M. Ziman, *Thermal Conductivity of Dielectric Crystals*. Proceedings of the Royal Society of London Series A-Mathematical Physical and Engineering Sciences.
160. Nan, C.W. and R. Birringer, *Determining the Kapitza Resistance and the Thermal Conductivity of Polycrystals: A Simple Model*. Physical Review B, 1998. **57**(14): p. 8264-8268.
161. Mityushov, E.A., R.A. Adamesku, and P.V. Gel'd, *Relation Between Kinetic Properties of Single Crystals and of Oriented Polycrystalline Materials*. InzheneroFizicheskii Zhurnal, 1984. **47**: p. 1052-1056.

162. Yang, F., et al., *Effective thermal conductivity of polycrystalline materials with randomly oriented superlattice grains*. Journal of Applied Physics, 2010. **108**(3): p. 034310.
163. Wang, Y., et al., *Interfacial Thermal Resistance and Thermal Conductivity in Nanograined SrTiO₃* Applied Physics Express, 2010. **3**: p. 031101.
164. Limarga, A.M. and D.R. Clarke, *The Grain Size and Temperature Dependence of the Thermal Conductivity of Polycrystalline, Tetragonal Yttria-Stabilized Zirconia*. Applied Physics Letters, 2011. **98**: p. 211906.
165. Cahill, D.G., M. Katiyar, and J.R. Abelson, *Thermal Conductivity off a-Si:H Thin Films*. Physical Review B, 1994. **50**: p. 6077-6081.
166. Park, K. and K.Y. Ko, *Effect of TiO₂ on high-temperature thermoelectric properties of ZnO*. Journal of Alloys and Compounds, 2007. **430**(1-2): p. 200-204.
167. Kishimoto, K. and T. Koyanagi, *Preparation of sintered degenerate n-type PbTe with a small grain size and its thermoelectric properties*. Journal of Applied Physics, 2002. **92**(5): p. 2544-2549.
168. Slack, G.A. and M.A. Hussain, *The maximum possible conversion efficiency of silicon-germanium thermoelectric generators*. Journal of Applied Physics, 1991. **70**(5): p. 2694-2718.
169. Nakamura, M., N. Kimizuka, and T. Mohri, *The phaes relations in the In₂O₃-Ga₂ZnO₄-ZnO system at 1350 degree C*. Journal of Solid State Chemistry, 1991. **93**(2): p. 298-315.
170. Nakamura, M., N. Kimizuka, and T. Mohri, *The phase relations in the In₂O₃-Fe₂ZnO₄-ZnO system at 1350 degree C*. Journal of Solid State Chemistry, 1990. **86**(1): p. 16-40.
171. Kimizuka, N., et al., *Syntheses and crystallographic data of the homologous compounds InFeO₃(ZnO)_m (m = 1, 2, 3, 7, 11, 13, 15, and 19) and Fe₂O₃(ZnO)_m (m = 8 and 9) in the In₂O₃-ZnFe₂O₄-ZnO system*. Journal of Solid State Chemistry, 1993. **103**(2): p. 394-402.

172. Kimizuka, N., et al., *Syntheses and Crystallographic Data of the Homologous Compounds InFeO₃(ZnO)_m, (m = 1, 2, 3, 7, 11, 13, 15, and 19) and Fe₂O₃(ZnO)_m (m = 8 and 9) in the In₂O₃-ZnFe₂O₄-ZnO System*. Journal of Solid State Chemistry, 1993. **103**(2): p. 394-402.
173. Uchida, N., et al., *High-resolution electron-microscopy of homologous compounds InFeO₃(ZnO)_m*. Journal of Electron Microscopy, 1994. **43**(3): p. 146-150.
174. Liang, X., M. Baram, and D.R. Clarke, *Thermal (Kapitza) Resistance of interfaces in compositional dependent ZnO-In₂O₃ superlattices*. Applied Physics Letters, 2013.
175. Bergman, D.J. and O. Levy, *Thermoelectric properties of a composite medium*. Journal of Applied Physics, 1991. **70**(11): p. 6821-6833.
176. Bergman, D.J. and L.G. Fel, *Enhancement of thermoelectric power factor in composite thermoelectrics*. Journal of Applied Physics, 1999. **85**(12): p. 8205-8216.
177. Kimizuka, N., M. Isobe, and M. Nakamura, *Syntheses and Single-Crystal Data of Homologous Compounds, In₂O₃(ZnO)_m (m = 3, 4, and 5), InGaO₃(ZnO)₃, and Ga₂O₃(ZnO)_m (m = 7, 8, 9, and 16) in the In₂O₃-ZnGa₂O₄-ZnO System*. Journal of Solid State Chemistry, 1995. **116**(1): p. 170-178.
178. Nakamura, M., et al., *The phase relations in the In₂O₃-Al₂ZnO₄-ZnO system at 1350 degree C*. Journal of Solid State Chemistry, 1993. **105**(2): p. 535-549.
179. Ohtaki, M., et al., *High-temperature thermoelectric properties of In₂O₃-based mixed oxides and their applicability to thermoelectric power generation*. Journal of Materials Chemistry, 1994. **4**(5): p. 653-656.
180. Berardan, D., et al., *In₂O₃:Ge, a promising n-type thermoelectric oxide composite*. Solid State Communications, 2008. **146**(1-2): p. 97-101.
181. Liu, Y., et al., *Effect of Transition-Metal Cobalt Doping on the Thermoelectric Performance of In₂O₃ Ceramics*. Journal of the American Ceramic Society, 2010. **93**(10): p. 2938-2941.

182. Cheng, B., et al., *Thermoelectric Performance of Zn and Ge Co-Doped In₂O₃ Fine-Grained Ceramics by the Spark Plasma Sintering*. Journal of the American Ceramic Society, 2011. **94**(8): p. 2279-2281.
183. Liu, Y., et al., *Thermoelectric Performance of Zn and Nd Co-doped In₂O₃ Ceramics*. Journal of Electronic Materials, 2011. **40**(5): p. 1083-1086.
184. Yamashita, T., R. Hansson, and P.C. Hayes, *The relationships between microstructure and crystal structure in zincite solid solutions*. Journal of Materials Science, 2006. **41**(17): p. 5559-5568.
185. Zhou, S.Q., et al., *Crystallographically oriented magnetic ZnFe₂O₄ nanoparticles synthesized by Fe implantation into ZnO*. Journal of Physics D-Applied Physics, 2007. **40**(4): p. 964-969.
186. Sultan, M. and R. Singh, *Structural and optical properties of RF-sputtered ZnFe 2 O 4 thin films*. Journal of Physics D: Applied Physics, 2009. **42**(11): p. 115306.
187. Jonker, G.H., *Application of combined conductivity and seebeck-effect plots for analysis of semiconductor properties*. Philips Research Reports, 1968. **23**(2): p. 131-&.
188. Ioffe, A.F., *Semiconductor Thermoelements and Thermoelectric Cooling* 1957, London: Infosearch Ltd.
189. Zhu, Q.M., et al., *Combined Jonker and Ioffe Analysis of Oxide Conductors and Semiconductors*. Journal of the American Ceramic Society, 2011. **94**(1): p. 51-57.
190. Guilmeau, E., A. Maignan, and C. Martin, *Thermoelectric Oxides: Effect of Doping in Delafossites and Zinc Oxide*. Journal of Electronic Materials, 2009. **38**(7): p. 1104-1108.
191. Palmer, G.B. and K.R. Poeppelmeier, *Phase relations, transparency and conductivity in Ga₂O₃-SnO₂-ZnO*. Solid State Sciences, 2002. **4**(3): p. 317-322.
192. Barf, J., T. Walther, and W. Mader. *Twin boundaries in zinc oxide with additions of gallium oxide*. 2004.

193. Damen, T.C., S.P.S. Porto, and B. Tell, *Raman Effect in Zinc Oxide*. Physical Review, 1966. **142**(2): p. 570-574.
194. Van Gorkom, G.G.P., J.H. Haanstra, and H. v. d. Boom, *Infrared and Raman spectra of the spinel ZnGa₂O₄*. Journal of Raman Spectroscopy, 1973. **1**(5): p. 513-519.
195. Preudhomme, J. and P. Tarte, *Infrared studies of spinels—III: The normal II–III spinels*. Spectrochimica Acta Part A: Molecular Spectroscopy, 1971. **27**(9): p. 1817-1835.
196. Yoon, M.H., et al., *Solid solubility limits of Ga and Al in ZnO*. Journal of Materials Science Letters, 2002. **21**(21): p. 1703-1704.
197. Liang, X., M. Baram, and D.R. Clarke, *Thermal (Kapitza) resistance of interfaces in compositional dependent ZnO-In₂O₃ superlattices*. Applied Physics Letters, 2013. **102**(22): p. 223903.
198. Uematsu, T. and H. Hashimoto, *Excess electron concentration of pure and doped zinc oxides*. Journal of Catalysis, 1977. **47**(1): p. 48-54.
199. Yan, Z., H. Takei, and H. Kawazoe, *Electrical Conductivity in Transparent ZnGa₂O₄: Reduction and Surface-Layer Structure Transformation*. Journal of the American Ceramic Society, 1998. **81**(1): p. 180-186.
200. Goldsmid, H.J., *Introduction to Thermoelectricity*. Springer Series in Materials Science2010, Berlin, Heidelberg: Springer.
201. Sampath, S.K. and J.F. Cordaro, *Optical Properties of Zinc Aluminate, Zinc Gallate, and Zinc Aluminogallate Spinels*. Journal of the American Ceramic Society, 1998. **81**(3): p. 649-654.
202. Mathur, S., et al., *Single-Source Sol-Gel Synthesis of Nanocrystalline ZnAl₂O₄: Structural and Optical Properties*. Journal of the American Ceramic Society, 2001. **84**(9): p. 1921-1928.
203. Jood, P., et al., *Al-Doped Zinc Oxide Nanocomposites with Enhanced Thermoelectric Properties*. Nano Letters, 2011. **11**(10): p. 4337-4342.

204. Omata, T., et al., *New ultraviolet-transport electroconductive oxide, ZnGa₂O₄ spinel*. Applied Physics Letters, 1994. **64**(9): p. 1077-1078.
205. Ohtaki, M., K. Araki, and K. Yamamoto, *High Thermoelectric Performance of Dually Doped ZnO Ceramics*. Journal of Electronic Materials, 2009. **38**(7): p. 1234-1238.
206. Garcia-Domene, B., et al., *High-pressure lattice dynamical study of bulk and nanocrystalline In₂O₃*. Journal of Applied Physics, 2012. **112**(12): p. 123511-123511-7.